The Pennsylvania State University

The Graduate School

College of Earth and Mineral Sciences

HYBRID LASER-ARC WELDING OF NI-BASE ALLOY 690

A Dissertation in

Materials Science and Engineering

by

Jared J. Blecher

Submitted in Partial Fulfillment
of the Requirements
for the Degree of

Doctor of Philosophy

May 2019

The dissertation of Jared J. Blecher was reviewed and approved* by the following:

Tarasankar DebRoy
Professor of Materials Science and Engineering
Dissertation Co-Advisor
Co-Chair of Committee

Todd A. Palmer
Professor of Engineering Science and Mechanics and Materials Science and Engineering
Dissertation Co-Advisor
Co-Chair of Committee

Long-Qing Chen
Hamer Professor of Materials Science and Engineering

Allison Beese
Assistant Professor of Materials Science and Engineering and Mechanical Engineering

Robert Voigt
Professor of Industrial and Manufacturing Engineering

Suzanne Mohney
Professor of Materials Science and Engineering and Electrical Engineering
Chair of Graduate Program

*Signatures are on file in the Graduate School

Abstract

The welding of Ni-base alloy Inconel™ 690 is commonly required during the construction and refurbishing of nuclear power plants. The tubing and control rod drive mechanism housing, located in the steam generator and reactor, respectively, are both fabricated form Alloy 690 and vary in thickness from 1 mm to greater than 25 mm. However, during conventional multi-pass welding of Alloy 690 in this thickness range, micro-cracking in the form of ductility dip cracking (DDC) and solidification cracking can occur, causing significant delays in an already expensive industry. DDC depends on the underlying weld microstructure and grain boundary characteristics. Solidification cracking requires a large difference in solidus and liquidus temperatures. The solutions to these welding defects reduce productivity or introduce additional difficulties (e.g. adding alloying elements to eliminate DDC but increasing susceptibility to solidification cracking). Hybrid laser-arc welding can significantly reduce the number of passes necessary to weld thick sections and, at the same time, lower the risk of forming DDC and solidification cracking.

Significant advantages can be achieved by welding with laser and arc energy sources in close proximity. The high intensity laser forms a vapor cavity, or keyhole, leading to a large increase in weld depth, and welding speed is typically higher during laser welding. On the other hand, an arc creates a wide weld pool, which is useful for bridging gaps between plates, and can add material to the weld with a consumable electrode. However, hybrid laser-arc welding can lead to unique defects not found in conventional arc welding, including keyhole porosity and root defects. Porosity from keyhole instability and collapse can lead to very large bubbles (> 1 mm) becoming trapped as pores in the weld metal during partial penetration welds, while, during full penetration welds, weld metal can fall out of the weld and solidify as nuggets, a form of root defect.

Because solidification microstructure has been the primary region of weld defects in the past and because laser and hybrid laser-arc welding can introduce novel defects, these topics are the primary focus of this work. The effects of welding parameters and solidification parameters on the fusion zone sub-grain structure is investigated with the assistance of a three-dimensional heat transfer and fluid flow model. The solidification parameters, including temperature gradient, solidification rate, cooling rate, and morphology parameter, are calculated for all locations on the liquidus temperature contour. Using weld fusion zone micrographs, these data are correlated to

the experimental scale and morphology (e.g. cells and columnar dendrites) of the solidification microstructure features. With this combined dataset, a solidification map for Alloy 690 is constructed with axes of temperature gradient and solidification rate, showing regions where cells and columnar dendrites form and curves of constant cell or secondary dendrite arm spacing. Among other uses, the minimum secondary dendrite arm spacing can be estimated from the map.

Low carbon steel plates of differing thicknesses and laser and hybrid laser-arc welding are used to investigate the formation of root defects. In addition to plate thickness and welding technique, the effect of surface tension is varied by modifying the bottom surface of the plate, which had an oxide scale. As expected greater plate thicknesses, hybrid laser-arc welding, and the presence of an oxide scale increase the chances of root defects. This behavior is modeled using the experimental weld dimensions and estimated surface tensions. The model accurately predicts all but one of the cases. Root defects are found to be a competition between the liquid metal weight in the pool and the surface tension, which is influenced by the thermophysical properties of the liquid metal, the width of the pool at the bottom of the plate, and the presence of dissolved oxygen, a surface active element that reduces surface tension. The liquid metal weight is primarily affected by the plate thickness. To assist practicing engineers, root defect maps are constructed for plain carbon steel, stainless steel, titanium alloys, and magnesium alloys from previously published research. The maps show that a non-dimensional heat input range can be used for plates up to 10 mm thick for all alloy classes.

Keyhole porosity is another novel defect found in laser and hybrid laser-arc welding. Laser and hybrid welds are fabricated in Inconel Alloy 690 with two different welding speeds and three different laser powers and subjected to X-ray computed tomography. The porosity in each weld is characterized by location and size of all pores. While the laser welds are found to have extensive porosity at all laser powers, the hybrid laser-arc welds only have significant porosity at laser powers less than 4kW. Comparing the weld dimensions to the modeled region of consumable electrode impingement show that the deeper welds (e.g. higher laser powers) have more potential room for bubble escape. Heat transfer and fluid flow modeling confirm this finding that deeper pools had significant space between the impingement region and the bottom of the weld pool for bubble escape. Another compelling piece of evidence is that all of the pores in the low power hybrid weld are in the bottom two thirds of the weld, while pores are more evenly dispersed in low

laser power laser welds. Using the volumetric heat source model for the impingement region and the trend of weld depth with laser power, a process map showing the region where porosity is not expected to exist is constructed.

Keyhole porosity originates at the bottom of an unstable keyhole, which is constantly fluctuating. So, a tool for probing keyhole dynamics is very valuable. Inline coherent imaging (ICI) uses a probe beam and reference beam in an interferometric construction to measure the keyhole depth two hundred thousand times a second to within a few microns. During laser welding experiments in five different structural alloys, ICI is validated with micrographs, showing good agreement between the two measurements for four of the five alloys. With the validated tool, keyhole dynamics at the beginning of the weld are investigated, and the keyhole growth rate in the first ms is measured as 1 m/s for every alloy except aluminum, which did not form a keyhole until 1.5 ms after the start of welding. Order of magnitude estimation of the keyhole growth rate confirmed that the measured values are reasonable.

Table of Contents

List of Figures

xvi

List of Tables

Acknowledgements

I would first like to thank my advisors Prof. Tarasankar DebRoy and Prof. Todd A. Palmer for their guidance and patience in mentoring me. Many of my achievements and milestones during my graduate studies would not have been possible without their support. They have instilled in me a desire to mentor and educate others in the private sector regarding the materials science of additive manufacturing. I am also grateful to my dissertation committee members, Prof. Long-Qing Chen, Prof. Allison Beese, and Prof. Robert Voigt.

I would also like to thank the past and present members of the group, including Dr. Brandon Ribic, Dr. Amit Arora, Dr. Rohit Rai, Dr. Ashwin Raghavan, Prof. Huiliang Wei, Dr. Vinaya Manvatkar, Dr. Snehanshu Pal, Mr. Tuhin Mukherjee, and Mr. James Zuback. This work would not been possible without the assistance of Mr. Ed Good with preparation of metallographic samples, Mr. Jay Tressler and Mr. Corey Dickman with assistance with the welding experiments, Mr. Griffin Jones for training on the X-ray CT equipment, and Dr. Richard Martukanitz with providing access to his lab.

I am also very grateful for the love and support my parents, brother, and girlfriend have provided during my graduate studies.

Chapter 1 – Introduction

1.1 Alloy 690 and the Nuclear Industry

Nuclear power is an important 21st century energy source with global use expected to increase between 87% and 156% over 2012 levels by 2040 [1]. Currently, it remains competitively priced with conventional energy, such as fossil fuels and hydropower [2]. Despite several high profile accidents over the last 40 years, nuclear energy remains one of the safest forms of energy. In terms of deaths per unit of energy generated (both workplace and pollution related deaths), nuclear energy and wind have the lowest values by 1 to 3 orders of magnitude compared to fossil fuels and renewable energy sources, such as solar and hydropower [3]. However, unlike wind energy, which relies on intermittent natural forces, nuclear energy is dispatchable and can increase or decrease output on demand to balance the energy load in a local region [2].
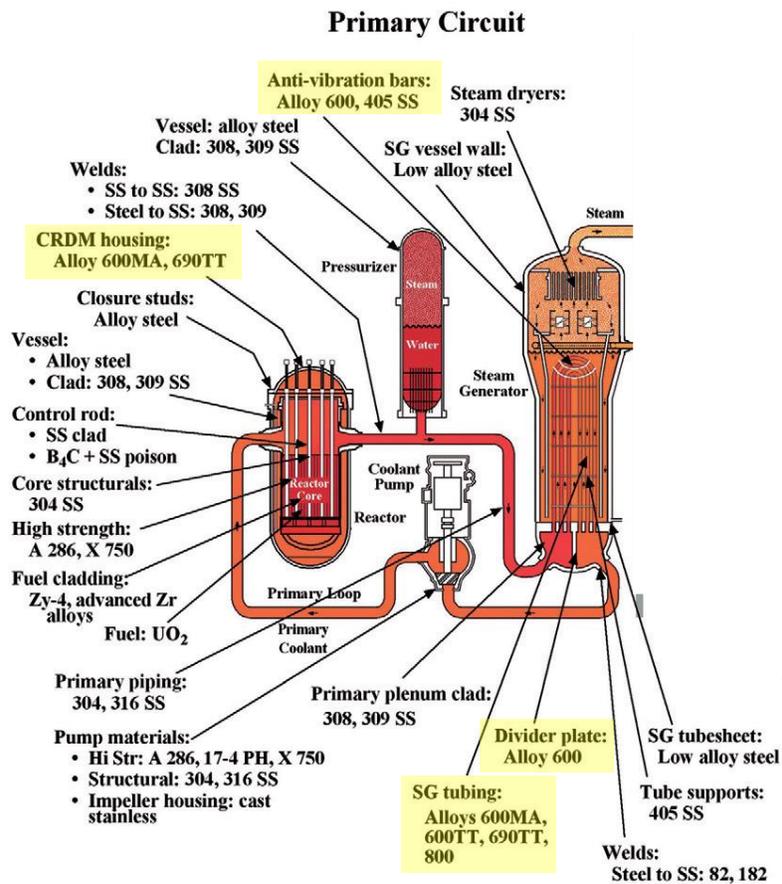
Figure 1: The primary water circuit of a nuclear reactor contains several components fabricated with Alloy 600 and Alloy 690 [4].

A range of materials are used to construct nuclear power plants as shown in Figure 1 [4], which depicts the major features of the primary water circuit in a pressurized water reactor (PWR). Current generations of light water reactors, which include PWRs, experience maximum temperatures of approximately 590 K and pressures of 160 atm at the reactor coolant outlet under normal operating conditions [4]. To handle these intense conditions, advanced materials have been used in the designs. However, these alloys have degraded in unexpected ways over several decades of operation, and new alloys have been integrated into both existing as well as newly constructed plants. For example, the high strength regions of primary circuit coolant pumps were initially fabricated with precipitation hardenable stainless steels (i.e. A286 and 17-4 PH), but they have been replaced by a more corrosion resistant Ni-base precipitation hardenable alloy, X-750 [4].

Next generation reactors will need materials that can handle different coolants, including lead and sodium, and temperatures and pressures up to 1270 K and 250 atm [4]. However, the high barrier to entry of new materials into this highly regulated industry requires that current materials be utilized to their greatest potential under increasingly extreme processing conditions. High temperature nickel-base alloys represent one alloy system of interest. Inconel® Alloy 600 and its replacement, Alloy 690, are used in various parts of pressurized water reactor (PWR) nuclear power stations. These alloys are used primarily at locations, where high temperature stress corrosion cracking resistance is required, including the control rod drive mechanism (CRDM) housing and steam generator (SG) tubing.

Figure 2: Thick sections of Alloy 690 are joined with multi-pass arc welds. (Courtesy of EPRI)

Nickel-base Alloy 690 is a high chromium variant of Alloy 600, containing 30 wt.% chromium compared to 20% for Alloy 600. Developed in the 1970's to be less susceptible to stress corrosion cracking [5,6], Alloy 690 is expected to remain in service for several decades, given the projected average lifespan of 60 to 80 years for some current power plants [7] and planned new construction. For reference, in the United States, 81 reactors have received 20 year extensions to the their 40 year operating licenses, 11 more have applied for the extension, and six of the
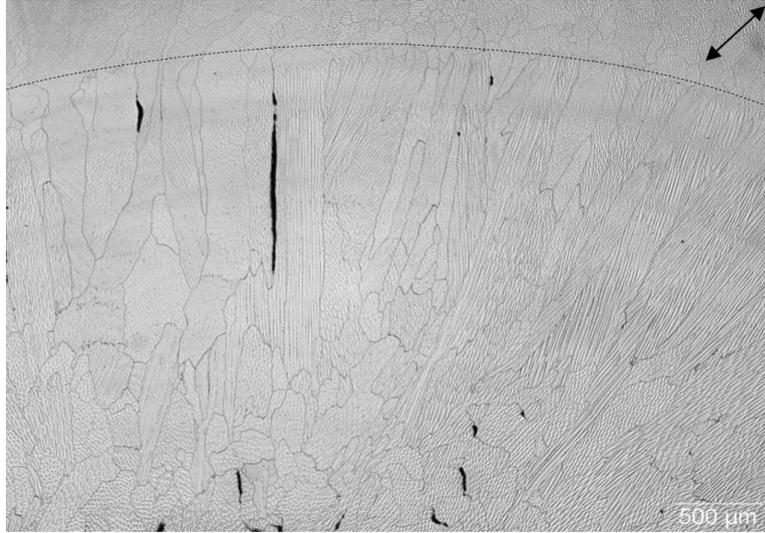
Figure 3: Ductility dip cracks form along the grain boundaries as shown here after a strain to fracture test [15].

remaining seven have informed the regulatory authority that they will apply by 2022 [8]. So, understanding and mitigating material failures is critical for maintaining this important energy source over the longer term.

During construction and repair of nuclear power plants, Alloy 690 is commonly fusion welded, which can lead to the formation of critical defects, requiring expensive and time-consuming repairs [9-14]. A multi-pass weld in an 80 mm thick section of Alloy 690 is shown in Figure 2. During multi-pass gas tungsten arc welding (GTAW) or submerged arc welding (SAW), Alloy 690 can suffer from ductility dip cracking and other characteristics of poor weldability, resulting in welds with defects that can lead to pre-mature failures.

An example of DDC related defects formed during a strain to fracture test of a GTA spot weld is shown in Figure 3 [15]. These solid state cracks form along the relatively straight grain boundaries of previously solidified weld metal during successive weld passes at relatively high temperatures around 900°C [9]. A pre-existing fusion zone solidification microstructure (relatively long, straight grain boundaries), high temperatures (900°C ± 100°C), and mechanical strain (≥ 2%) are required for DDC, and all of these conditions are commonly found in conventional multi-pass arc welds. Grain boundary sliding and crack nucleation at grain triple points have been identified as the most likely DDC mechanisms [10,16-20], while grain boundary orientation [21], nucleation of $M_{23}C_6$ during cooling [22], and combined sulfur and phosphorus contents in excess of 30 ppm have been identified as other possible mechanisms [23-28].
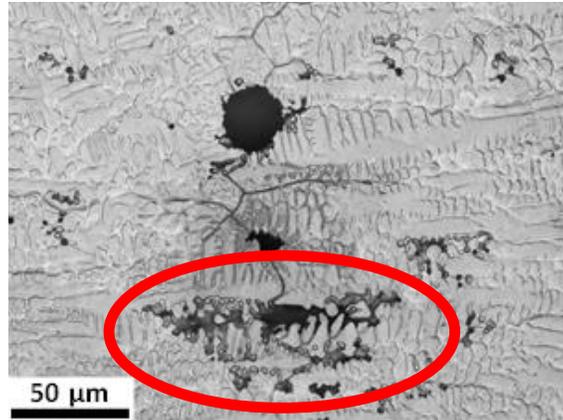
Figure 4: Solidification cracks can form with the addition of Nb and Mo, which are added to avoid DDC.

While, the mechanisms for DDC have been studied extensively, little progress has been made in identifying remedies for DDC defects in these alloys. Lower heat inputs per pass will reduce the likelihood for cracking but require more passes and lower productivity [29]. Other remedies have concentrated on the use of high Nb and Mo content filler metals, which lower DDC susceptibility [10, 11, 19] but increase solidification cracking susceptibility [13,14], as shown in Figure 4. Overall, conventional arc welding is ultimately limited by the physics of the process. The resulting molten pool geometry and relatively low depth of penetration require many passes to successfully weld thick sections. High intensity beam welding with the capability of producing deep penetration welds on the order of 25 mm [30] can overcome the propensity of these alloys to fail through DDC by avoiding multi-pass welding all together.

1.2 Overcoming the Limitations of Conventional Arc Welding

High intensity (10 kW/mm^2) laser beam welding (LBW) and hybrid laser-arc welding (HLAW) are not limited by conventional GTAW and gas metal arc welding (GMA) characteristics, such as slow weld speeds, high heat input, and low depth of penetration. In fact, LBW and HLAW are characterized by a very large depth of penetration, and depth-to-width or aspect ratios larger than 1. The weld depth for a single pass is several times greater than that in conventional GTAW, under comparable heat inputs [31]. In the same study, the weld depths during laser and hybrid welding were comparable, while the hybrid welds consistently produced wider pools [31]. A schematic of the hybrid welding process is shown in Figure 5 [32]. In HLAW, an electric arc, with or without a consumable electrode, is added to the laser welding process in such a way as to produce a synergistic effect between the arc and the laser [31]. Plates with
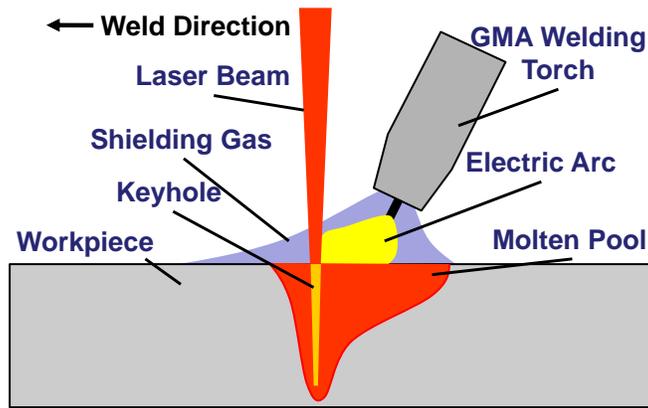
Figure 5: The schematic shows hybrid laser-arc welding and the important components [32].

thicknesses of 10 mm and greater can be joined in a full penetration single pass with a defect free weld in most structural alloys [33-38]. These single pass welds eliminate the need for multi-pass welding and the possibility of producing arc related defects or cracks in certain alloys. Welding speeds can also be several times faster than conventional arc welding, resulting in higher productivity [39]. The addition of an arc increases the weld pool width significantly, making HLAW capable of bridging large gaps between two plates and making the process more versatile for welding in the field.

In many lower intensity laser welding processes (e.g. low laser power and/or large beam), the welding mode is known as conduction mode, in that heating and melting occurs through conduction from the top surface, where the beam is incident on the weldment. The deep weld pools in LBW and HLAW are produced through a mechanism in which a vapor filled cavity, or keyhole, is formed by the high energy density of the laser heat source. When operating in the keyhole mode, the laser rapidly heats, melts, and evaporates the metal, and if the intensity (i.e. fluence and power density) exceeds $10\,\mathrm{kW/mm^2}$, a vapor cavity or keyhole will form. The keyhole is held open against surface tension and hydrostatic forces in the surrounding molten pool by vapor pressure and the recoil force of the evaporating liquid metal [40]. While the keyhole can be exploited for greater weld depths, the keyhole itself is very unstable and can result in high amounts of porosity [41], with amounts, sizes, and morphologies differing between alloys.
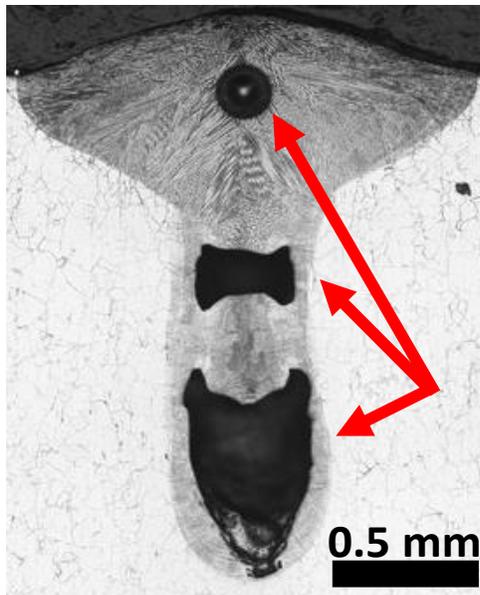
Figure 6: High levels of porosity were observed in some laser welds of Alloy 690.

Keyhole induced porosity has been identified as a serious problem in laser welding of Alloy 690, significantly reducing its effectiveness as a remedy of DDC [42]. Because the keyhole is unstable and fluctuates frequently, bubbles can form at the bottom of the keyhole [41]. If these bubbles do not escape from the molten pool, the bubbles are captured as pores in the weld metal during solidification [41], as identified by the arrows in Figure 6. The state of the art strategies for avoiding porosity are primarily empirical and require trial and error experiments to select the appropriate welding parameters, such as weld speed, power modulation frequency, and shielding gas composition [41, 43-45]. Appropriate defocusing, welding speeds, and power modulation strategies can decrease porosity but cannot completely eliminate it in Alloy 690 laser weldments. Some studies show a decrease in porosity during hybrid welding compared to laser welding [46].

Alloy 690 is particularly susceptible to keyhole porosity [42] and more easily forms porosity than stainless steel [47]. The relationship between alloy composition and susceptibility to keyhole porosity is illustrated in Figure 7, which shows the equilibrium vapor pressures as a
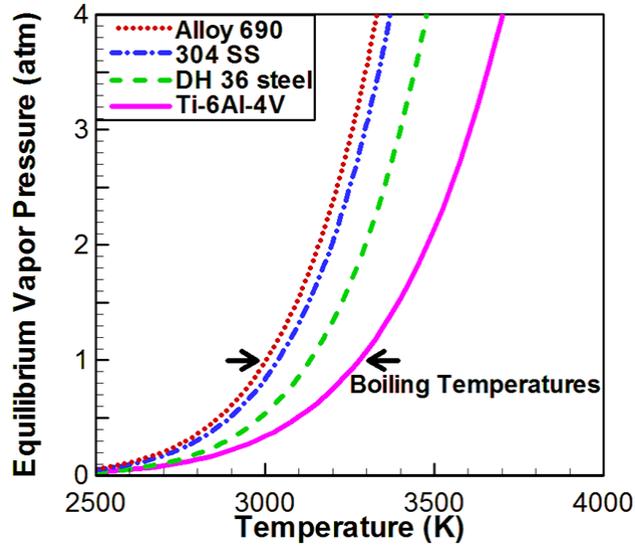
Figure 7: The equilibrium vapor pressure curves of various alloys can by used to qualitatively to compare the susceptibility of different alloys to keyhole porosity.

function of temperature for Alloy 690, 304 stainless steel, low carbon steel, and Ti-6Al-4V. An ideal solution is assumed for the calculation of vapor pressure, which is the sum of the product of the alloying element mole fraction and the vapor pressure for the pure substance (i.e. Fe, Cr, Ni, Ti, Al, and V) at each temperature [48,49]. At the boiling temperatures (i.e. 1 atm), the vapor

Figure 8: A root defect formed in a laser weld of 16 mm thick plate of 304 stainless steel [50].

7

pressure curve of Alloy 690 has a greater slope compared to the other alloys, indicating a more unstable keyhole and higher susceptibility to keyhole porosity.

In addition, the single pass full penetration welds enabled by the keyhole can produce root defects [50]. Another common defect in high intensity full penetration laser welds is the formation of small globules of weld metal along the weld root, as shown in Figure 8 [50]. Root defects can occur in both LBW and HLAW [51,52] and have various names, including chain of pearls [53], dropping [54], and root humping [55]. Root defects of this type result in a weaker weld, and stress concentrators form at the edges of the solid globules, reducing fatigue life in steel and stainless steel welds. Similar to keyhole collapse porosity, the mechanisms behind the remedies are not well understood and require trial and error experiments to select appropriate parameters.

1.3 Motivation

Laser beam and hybrid laser arc welding are promising technologies for producing high speed single pass thick section joints, increasing productivity through time and automation without ductility dip and solidification cracking. However, effective implementation of LBW and HLAW requires an understanding of the heat transfer and fluid flow governing the solidification behavior and defect formation and evolution during these high intensity laser welding processes. Figure 9 shows a schematic diagram of the laser and hybrid welding with regions of interest highlighted. The various physical processes (i.e. keyhole formation and solidification) and defect initiation and
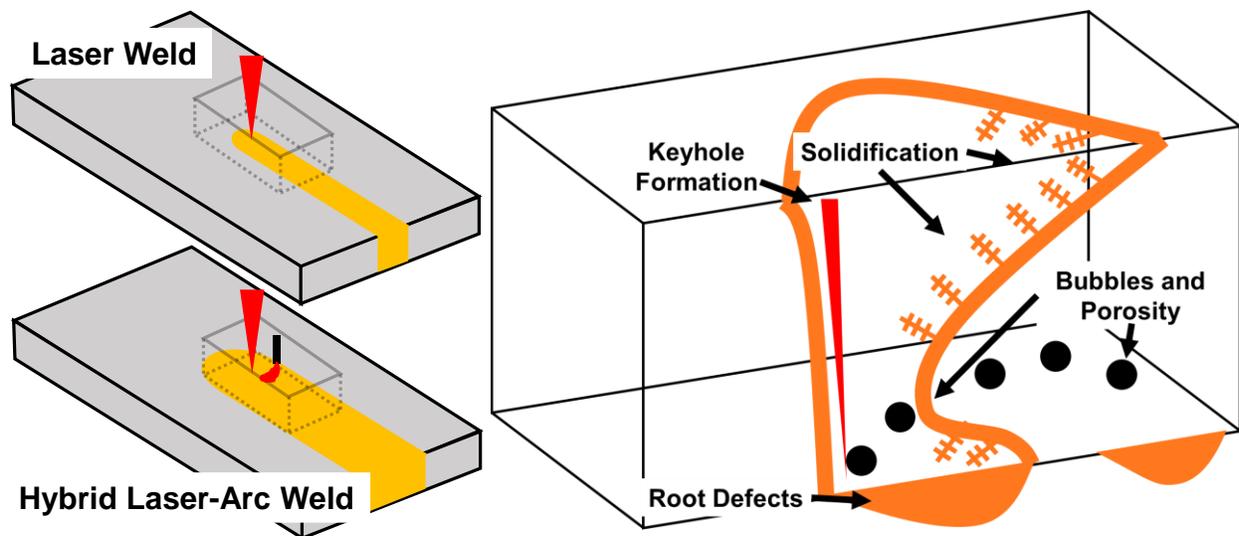
Figure 9: The laser and hybrid laser-arc weld schematics show the region of interest for the weld pool schematic on the right side of the image. The weld pool schematic shows the connections between the various physical processes investigated in this thesis.

evolution (i.e. bubbles and porosity and root defects) that occur in a typical weld pool are also identified. The important processes that affect the formation of defects and ultimate weld quality in LBW and HLAW occur in and around the molten pool. So, understanding the weld pool and associated governing physics is important for the formation of a quality laser and hybrid laser-arc weld joint.

1.4 Research Objectives

Alloy 690 suffers from poor weldability due to micro-cracking susceptibility during conventional multipass arc welding of thick sections. Laser and hybrid laser-arc welding have been identified as potential solutions for this alloy system, but there are other issues, which arise and produce different defect structures. This research seeks to quantitatively understand the formation and mitigation of defects during LBW and HLAW of Alloy 690. Heat transfer and fluid flow control weldment temperature fields, keyhole formation, and pool geometry, which directly impact solidification, formation of trapped porosity and root defects, and keyhole evolution. The unique temperature fields and pool geometries lead to the novel solidification characteristics and defects only found in laser and hybrid laser-arc welding. Specifically, this research seeks to understand:

1. The solidification characteristics during laser welding are examined and qualified. Since the solidification microstructure leads to most of the weldability issues during conventional welding, differences produced during LBW are examined.
2. Keyhole porosity is a direct result of bubbles formed at the keyhole tip not escaping the pool and becoming trapped, leading to porosity defects.
3. Root defects are specific to the laser and hybrid welding processes and are directly related to the temperature fields and pool geometries formed during these welding processes.
4. Keyhole formation and growth is not quantitatively understood at the precision necessary to model the process accurately.

This research utilizes a unique set of tools to understand heat transfer and fluid flow, monitor their effects, and characterize the resulting defects. A 3D heat transfer and fluid flow mathematical model is used to calculate the temperature fields, fluid velocity fields, and pool geometries. A very fast process monitoring tool, inline coherent imaging (ICI) is used to determine the keyhole depth and is used to measure keyhole growth rates at the initiation of welding. X-ray

computed tomography (CT) measures characteristics of pores, resulting from keyhole porosity, with unrivalled resolution. The combination of these experimental tools allows a more complete understanding of the underlying physics and corresponding effects during welding.

1.5 Thesis Structure

This work seeks to understand the physical phenomena impacting the formation of common defects during the laser and hybrid laser-arc weldling of Alloy 690. These welding processes are expected to mitigate current issues encountered during the arc welding of Alloy 690, such as DDC and solidification cracking, but they present challenges of their own. Heat transfer and fluid flow and their combined effects on pool geometry, temperature fields, keyhole formation and evolution, and defects are examined. This thesis is laid out to address these various effects.

The underlying background and motivation of this thesis are laid out in Chapter 1, which also details the research objectives and the thesis layout.

In Chapter 2, a critical review of previously published studies is undertaken. Studies on laser welding of Alloy 690, keyhole collapse porosity, root defects, and mathematical modeling of heat transfer and fluid flow are reviewed to develop an understanding of the fundamental physical phenomena governing laser and hybrid-laser arc welding.

Chapter 3 describes the solidification characteristics of Alloy 690 under laser welding conditions, since most defects associated with Alloy 690 have been identified in the solidification microstructure of the fusion zone. Laser welding experiments and solidification morphology characterization are combined with 3D mathematical modeling of heat transfer and fluid flow. The solidification structure size and morphology are mapped as a function of position in the laser weld fusion zones. Solidification parameters, including temperature gradient, solidification rate, cooling rate, and morphology parameter, are calculated for the entire molten pool from the temperature fields and pool geometry. The calculated cooling rates and morphology parameters are correlated to the observed solidification structures, and an Alloy 690 solidification map is constructed based on the results.

Laser and laser-arc hybrid welding experiments designed to investigate root defect formation are described in Chapter 4. Root defects were intentionally formed during full penetration welding experiments in order to study the conditions under which they formed. A simple pool geometry model was developed to understand the role of pool size and melt pool

composition on root defect formation. The effect of oxygen on reduced surface tension was tested with and without oxide scale on the bottom side of the plate at the weld root. Root defect maps were assembled for steel, stainless steel, titanium alloys, and magnesium alloys.

In Chapter 5, the effects of pool size and arc characteristics on porosity in laser and hybrid laser-arc welds are investigated. Welding parameters were chosen to induce a large amount of porosity in the welds, X-ray CT was used to detect and characterize porosity without sectioning the welds, and heat transfer and fluid flow modeling was used to calculate the temperature fields and molten pool size. At higher laser powers, hybrid welds produced much lower porosity compared to laser welds because the molten pool was large enough that the electrode-molten pool interaction volume was not able to impede upward bubble motion and eventual escape from the pool.

Experimental measurements of keyhole initiation and growth in several engineering alloys are presented in Chapter 6. Measurements were undertaken using inline coherent imaging (ICI), a coaxial depth sensing technique with potential applications in defect detection (i.e. the initiation of bubbles at the keyhole tip). The results show that an aluminum alloy is the slowest to initiate and grow a keyhole, while the high temperature alloys, such as a plain carbon steel, 304 stainless steel, Alloy 690, and Ti-6Al-4V, exhibited growth rates on the order of 1 m/s, which are almost twice that observed in the aluminum alloy.

1.6 References

[1] International Energy Agency. 2015. Key World Energy Statistics. Accessed 9 September 2018. <https://www.oecd-ilibrary.org/docserver/key_energ_stat-2015-en.pdf?expires=1536958349&id=id&accname=ocid195625&checksum=2496798A7017E1FCCA58B1B8B5E85EE7>

[2] U.S. Energy Information Administration. 2015. Levelized cost and levelized avoided cost of new generation resources in the annual energy outlook 2015. Accessed 9 September 2018. <https://www.eia.gov/outlooks/archive/aeo15/pdf/0383(2015).pdf> 9/14/2018

[3] Conca, J. How deadly is your kilowatt? We rank the killer energy sources. *Forbes*, 10 June 2012, accessed 9 October 2017. <https://www.forbes.com/sites/jamesconca/2012/06/10/energys-deathprint-a-price-always-paid/>

[4] Allen, T., Busby, J., Meyer, M., and Petti, D. 2010. Materials challenges for nuclear systems. *Mater. Today* 13 (12): 14-23.

[5] Patel, S.J. 2006. A century of discoveries, inventors, and new nickel alloys. *JOM* 58 (9): 18-20.

[6] Hodge, F.G. 2006. The history of solid-solution-strengthened Ni alloys for aqueous corrosion service. *JOM* 58 (9): 28-31.

[7] Voosen, P. 2009. How long can a nuclear reactor last. *Scientific American* 20 November 2009, accessed 9 October 2017, www.scientificamerican.com.

[8] Nuclear Engery Institute, 'Fact sheets: License renewal of nuclear power plants, November 2016, accessed 9 October 2017, www.nei.org.

[9] Nissley, N.E. and Lippold, J.C. 2008. Ductility-dip cracking susceptibility of nickel-based weld metals part 1: strain-to-fracture testing. *Weld. J.* 87 (10): 257s-264s.

[10] Nissley, N.E. and Lippold, J.C. 2009. Ductility-dip cracking susceptibility of nickel-based weld metals: part 2-microstructural characterization. *Weld. J.* 88 (6): 131s-140s.

[11] Unfried, J.S. and Ramirez, A.J. 2012. Intergranular cracking in alloy 690 with Nb, Mo, and Hf additions: in situ SEM high temperature deformation study. *Mater. Sci. Forum* 706-709: 945-950.

[12] McCracken, S.L., Alexandrov, B.T., Lippold, J.C., Sowards, J.W., and Hope, A.T. 2010. Hot cracking study of high chromium nickel-base weld filler metal 52MSS (ERNiCrFe-13) for nuclear applications. *Proc. ASME Press. Vessels Pip. Conf. 2010*. 6: 879-889.

[13] Alexandrov, B.T. and Lippold, J. 2011. Further development of the cast pin tear test for evaluating solidification cracking in Ni-base alloys. *3rd Workshop on Hot Cracking Phenomena Welds*, eds: Lippold, J., Bollinghaus, T., and Cross, C.E., Columbus OH, March 2010. 317-331.

[14] Yushchenko, K., Savchenko, V., Chervyakov, N., Zvyagintseva, A., and Guyot, E. 2011 Comparative hot cracking evaluation of welded joints of alloy 690 using filler metals Inconel® 52 and 52 MSS. *Weld. World* 55 (9-10): 28-35.

[15] Nissley, N.E. 2008. Ductility-dip cracking susceptibility of nickel-based weld metals part 1: strain-to-fracture testing. The Ohio State University, PhD Dissertation.

[16] Chen, J.-Q., Lu, H., and Cui, W. 2011. Study on ductility dip cracking susceptibility in filler metal 82 during welding. *Front. Mater. Sci.* 5 (2): 203-208.

[17] Noecker II, F.F. and Dupont, J.N. 2009. Metallurgical investigation into ductility dip cracking in Ni-based alloys: part II. *Weld. J.* 88 (1): 62s-77s.

[18] Ramirez, A.J., Sowards, J.W., and Lippold, J.C. 2006. Improving the ductility-dip cracking resistance of Ni-base alloys. *J. Mater. Process. Technol.* 179(1-3): 212-218.

[19] Ramirez, A.J. and Garzon, C.M. 2008. Thermodynamic and kinetic approach to ductility-dip cracking resistance improvement of Ni-base alloy ERNiCrFe-7: effect of Ti and Nb additions. *2nd International Workshop on Hot Cracking Phenomena in Welds*, eds: Bollinghaus, T., Herold, H., Cross, C.E., and Lippold, J.C., Berlin, Germany, 5-6 March 2007, 427-453.

[20] Unfried, J.S., Torres, E.A., and Ramirez, A.J. 2011. In situ observations of ductility-dip cracking mechanism in Ni-Cr-Fe alloys. *3rd Workshop on Hot Cracking Phenomena Welds*, eds: Lippold, J., Bollinghaus, T. and Cross, C.E., Columbus OH, March 2010, 295-315.

[21] Dave, V.R., Cola, M.J., Kumar, M., Schwartz, A.J., and Hussen, G.N.A. 2004. Grain boundary character in alloy 690 and ductility-dip cracking susceptibility. *Weld. J.* 83 (1): 1s-5s.

[22] Young, G.A., Capobianco, T.E., Penik, M.A., Morris, B.W., and McGee, J.J. 2008. The mechanism of ductility dip cracking in nickel-chromium alloys. *Weld. J.* 87 (2): 31s-43s.

[23] Nakao, Y. , Shinozaki, K., Ogawa, T., and Sakurai, H. 1993. Fractography on microcracks in Ni-base multipass weld metals – Study on microcracks in multipass weld metals of Ni-base alloys (Part 1). *Trans. Jpn. Weld. Soc.* 24 (2): 94-100.

[24] Nakao, Y., Shinozaki, K., Ogawa, T., and Sakurai, H. 1993. Effects of Cr and S on ductility-dip cracking susceptibilities in the reheated weld metals of Ni-Cr-Fe ternary alloys – Study on microcracks in multipass weld metals of Ni-base alloys (Part 2). *Trans. Jpn. Weld. Soc.* 24 (2): 101-106.

[25] Nishimoto, N., Saida, K., and Okauchi, H. 2006. Microcracking in multipass weld metal of alloy 690 part 1 – microcracking susceptibility in reheated weld metal. *Sci. Technol. Weld. Joining*. 11 (4): 455-461.

[26] Nishimoto, N., Saida, K., Okauchi, H., and Ohta, K. 2006. Microcracking in multipass weld metal of alloy 690 part 2 – microcracking mechanisms in reheated weld metal. *Sci. Technol. Weld. Joining* 11 (4): 462-470.

[27] Nishimoto, N., Saida, K., Okauchi, H., and Ohta, K. 2006. Microcracking in multipass weld metal of alloy 690 part 3 – prevention of microcracking in reheated weld metal by addition of La to filler metal. *Sci. Technol. Weld. Joining* 11 (4): 471-479.

[28] Saida, K., Nomoto, Y., Okauchi, H., Ogiwara, H., and Nishimoto, K. 2012. Influences of phosphorus and sulphur on ductility dip cracking susceptibility in multipass weld metal of alloy 690. *Sci. Technol. Weld. Joining* 17 (1): 1-8.

[29] Dupont, J.N., Lippold, J.C., and Kiser, S.D. 2009. Welding metallurgy and weldability of nicke-base alloys. John Wiley & Sons, Hoboken, NJ.

[30] Sokolov, M., Salminen, A., Kuznetsov, M., and Tsibulskiy, I. 2011. Laser welding and weld hardness analysis of thick section S355 structural steel. *Mater. Des.* 32 (10): 5127-5131.

[31] Ribic, B., Rai, R., and DebRoy, T. 2008. Numerical simulation of heat transfer and fluid flow in GTA/laser hybrid welding. *Sci. Technol. Weld. Joining* 13 (8): 683-693.

[32] The Lincoln Electric Company. Hybrid Laser GMAW: The Next Generation of Welding Technology. www.lincolnelectric.com, accessed 24 December 2016.

[33] Sokolov, M., Salminen, A., Kuznetsov, M., and Tsibulskiy, I. 2011. Laser welding and weld hardness analysis of thick section S355 structural steel. *Mater. Des.* 32 (10): 5127-5131.

[34] Zhang, M., Chen, G., Zhou, Y., and Liao, S. 2014. Optimization of deep penetration laser welding of thick stainless steel with a 10 kW fiber laser. *Mater. Des.* 53: 568-576.

[35] Ramasamy, S. and Albright, C.E. 2001. CO_2 and Nd-YAG laser beam welding of 5754-O aluminium alloy for automotive applications. *Sci. Technol. Weld. Joining* 6 (3): 182-190.

[36] Costa, A., Miranda, R., Quintino, L., and Yapp, D. 2007. Analysis of beam material interaction in welding of titanium with fiber lasers. *Mater. Manuf. Process.* 22 (7-8): 798-803.

[37] Osoba, L.O. and Ojo, O.A. 2012. Influence of laser welding heat input on HAZ cracking in newly developed Haynes 282 superalloy. *Sci. Technol. Weld. Joining* 28 (4): 431-436.

[38] Wang, Z., Gao, M., Tang, H., and Zeng, X. 2011. Characterization of AZ31B wrought magnesium alloy joints welded by high power fiber laser. *Mater. Charact.* 62 (10): 943-951.

[39] Reutzel, E.W., Sullivan, M.J., and Mikesic, D.A. 2006. Joining pipe with hybrid laser-GMAW process: weld test results and cost analysis. *Weld. J.* 85 (6): 66-71.

[40] Ribic, B., Tsukamoto, S., Rai, R., and DebRoy, T. 2011. Role of surface-active elements during keyhole-mode laser welding. *J. Phys. D: Appl. Phys.* 44 (48): 485203.

[41] Matsunawa, A., Kim, J.-D., Seto, N., Mizutani, M., and Katayama, S. 1998. Dynamics of keyhole and molten pool in laser welding. *J. Laser Appl.* 10 (6): 247-254.

[42] Tucker, J.D., Nolan, T.K., Martin, A.J., and Young, G.A. 2012. Effect of travel speed and beam focus on porosity in alloy 690 laser welds. *JOM* 64 (12): 1409-1417.

[43] Kuo, T.-Y. 2005. Effects of pulsed and continuous Nd-YAG laser beam waves on welding of Inconel alloy. *Sci. Technol. Weld. Joining.* 10 (5): 557-565.

[44] Kuo, T.-Y. and Lin, Y.-D. 2007. Effects of different shielding gases and power waveforms on penetration characteristics and porosity formation in laser welding of Inconel 690 alloy. *Mater. Trans.* 48 (2): 219-226.

[45] Elmer, J.W., Vaja, J., Carlton, H.D., and Pong, R. 2015. The effect of Ar and N_2 shielding gas on laser weld porosity in steel, stainless steels, and nickel. *Weld. J.* 94 (10): 313s-325s.

[46] Ribic, B., Palmer, T.A., and DebRoy, T. 2009. Problems and issues in laser-arc hybrid welding. *Int. Mater. Rev.* 54 (4): 223-244.

[47] Kuo, T.Y. and Jeng, S.L. 2005. Porosity reduction in Nd-YAG laser welding of stainless steel and Inconel alloy by using a pulsed wave. *J. Phys. D: Appl. Phys.* 38 (5): 722-728.

[48] Smithells, C. 2004. Smithells metals reference book. 8th ed. Boston: Elsevier Butterworth Heinemann.

[49] Yaws, C. L. 2007. The Yaws handbook of vapor pressure : Antoine coefficients. Houston: Gulf Publishing Company.

[50] Kaplan, A.F.H. and Wiklund, G. 2009. Advanced welding analysis methods applied to heavy section welding with a 15 kW fibre laser. *Weld. World* 53: 295-300.d

[51] Ohnishi, T., Kawahito, Y., Mizutani, M., and Katayama, S. 2013. Butt welding of thick, high strength steel plate with a high power laser and hot wire to improve tolerance to gap variance and control weld metal oxygen content. *Sci. Technol. Weld. Joining* 18 (4): 314-322.

[52] Piili, H., Salminen, A., Harkko, P., and Lehtinen, J. 2008. Study of phenomenon of fibre-laser-mig/mag-hybrid-welding. *ICALEO 2008 – 27th Int. Congr. Appl. Lasers Electro-Opt.* Laser Inst. of America: 506-515.

[53] Salminen, A., Piili, H., and Purtonen, T. 2010 The characteristics of high power fibre laser welding. *Proc. IMechE, Part C J. Mech. Eng. Sci.* 224 (C5): 1019-1029.

[54] Havrilla, D., Rominger, V., Holzer, M., Harrer, T., and Andreev, A. 2013. Advanced welding techniques with optimized accessories for high brightness 1 μm lasers. *Proc. SPIE* 8603: 86030N.

[55] Ilar, T., Eriksson, I., Powell, J., and Kaplan, A. 2012. Root humping in laser welding – an investigation based on high speed imaging. *7th Conf. Laser Assist Net Shape Eng./Int. Conf. Photonic Eng.* eds. M. Schmidt, F. Vollertsen, and M. Geiger, Elsevier Sci.: 27-32.

Chapter 2 – Literature Review

2.1 Defect Generation in Deep Penetration Laser Welding

Keyhole porosity in partial penetration welds and root defects in full penetration welds are the two most deleterious defects limiting the use of laser and hybrid laser arc welding for fabrication of thick, welded structures. These defects are primarily process based, although the alloy being welded may be more or less susceptible to keyhole porosity or root defects, depending on the thermophysical properties of the alloy. Fabricating high quality single pass welds in Alloy 690 requires understanding of keyhole porosity and root defects.

During partial penetration laser and hybrid laser-arc welding, keyhole porosity initiates at the bottom of the unstable keyhole as bubbles, which then become trapped in the solidification front as large pores. Multiple strategies have been developed to mitigate porosity formation, but the practical implementation of these strategies are not always possible. Process parameter control strategies with straightforward implementation (e.g. power modulation) have been identified in specific cases but have not been generalized to variations in alloy composition and desired weld depth. Several authors have concluded that hybrid laser-arc welding can reduce porosity in most cases, however the mechanism of porosity reduction is not well understood [1,2].

Root defects remove metal from the joint and can form during full penetration welding of thick plates. The mechanism is not entirely understood but appears to be a competition between the surface tension and weight of the liquid metal in the pool, so thicker plates and wider weld pools promote root defects. Few practical strategies exist for mitigating root defects. The best strategy is to select an alloy with a low susceptibility to root defects and thinnest plate practical and optimize laser power and welding speed. This application specific strategy results from the dearth of practical mitigation strategies.

2.2 Keyhole Collapse Porosity

2.2.1 Laser Energy Absorption and Keyhole Formation

Two laser-material interaction mechanisms are shown schematically in Figure 10. Conduction-mode welding occurs at lower laser intensities in laser welding during which the energy is distributed to the weldment through conduction mechanisms, resulting in generally wide and shallow weld pools. The aspect ratio (depth/width) of the pool is always less than 0.5, which

is the highest value that can be achieved during conduction mode welding with a point heat source. Heat conduction will spread the laser energy evenly and create a pool width that is double the depth in the absence of fluid flow, however, with fluid flow will generally lead to a wider and shallower pool. When the laser intensity, power density, is below 1 kW/mm^2 [3], these types of processes are common. At laser intensities between of 3 and 10 kW/mm^2 [3], the welding mode changes to keyhole. The keyhole is a very high ratio (~0.5 mm wide, >10 mm deep) vapor cavity formed by the forces associated with rapid evaporation. The associated weld pool has an aspect ratio greater than 1 in most cases.
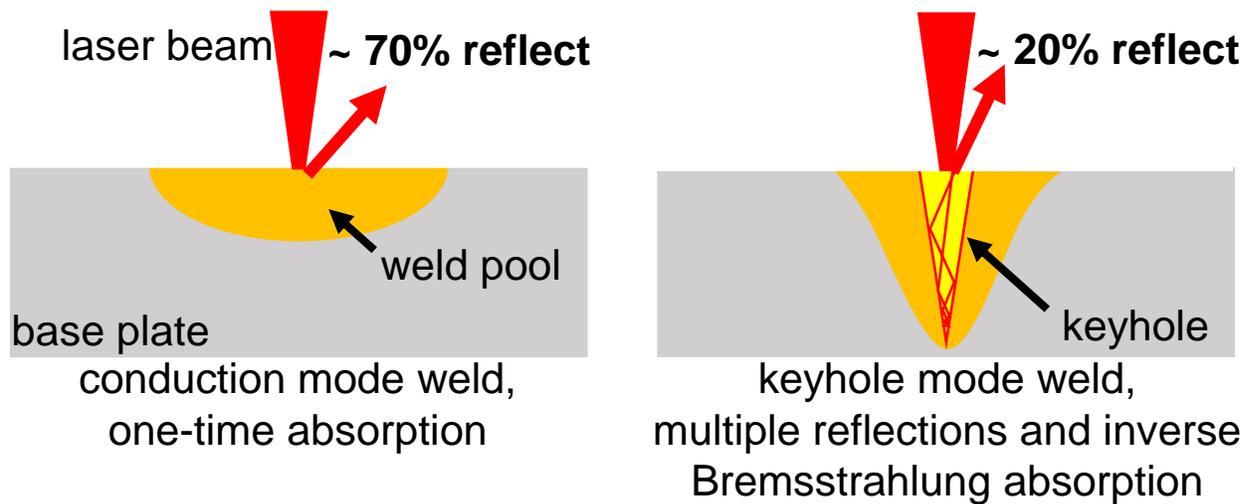
Figure 10: The two primary welding modes are conduction and keyhole and result in different amounts of laser absorption.

The deep weld pools formed during keyhole mode welding are only partly related to the higher laser intensities, which can be obtained through a combination of higher laser powers and smaller beam sizes. For Fe-, Ni-, and Ti-based alloys, a liquid metal pool only absorbs about 30% of the energy of a 1070 nm wavelength laser beam. The other 70% is reflected. In a conduction mode weld pool, this reflected energy is lost and cannot be used for deeper pools. However, during keyhole mode welding, the laser energy is incident on the walls of the keyhole and reflected down the keyhole, undergoing multiple reflections along the depth and enhancing energy absorption [4-9].

There are several ways to determine the effective absorption during keyhole mode welding. The number of reflections and effective absorption has been computed by Kaplan [4] based on reflection and a triangular keyhole geometry. For example, an 80% effective absorption angle

required 12 reflections and a 4° keyhole wall angle for a 10.6 μm wavelength laser beam. Ki et al. [5] calculated a 60% effective absorption in a 1.5 mm deep keyhole. Other researchers have looked into the energy distribution along the keyhole wall after explicit ray tracing calculations. Solana and Negro [6] performed the calculation for Gaussian and top hat beams and iterated to the final keyhole geometry, which was assumed radially symmetric. In both cases, a very high intensity was found at the center of the keyhole, as expected for a Gaussian beam, but with a complex behavior away from the center of the keyhole (e.g. 5 to 6 local maxima). Jin [7] performed ray tracing calculation using a keyhole profile obtained during high speed imaging of welds in clear glass. These welds displayed a much more complex shape with the bottom bent backwards and opposite the welding direction (positive x-direction), as shown in Figure 11. The multiple reflection analysis showed that laser energy only reached the bottom of the 2.5 mm deep keyhole after reflection. The maximum intensity was found at a height of 1.5 mm above the bottom of the keyhole.
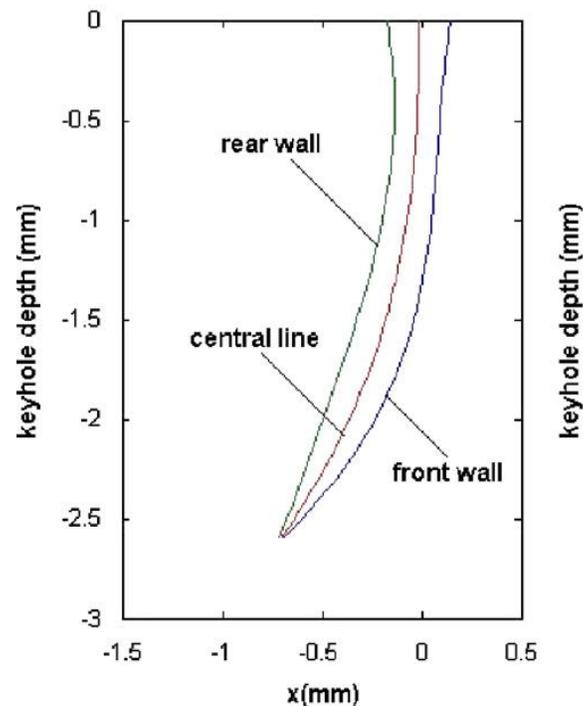
Figure 11: Ray tracing of a laser beam in a complex experimental keyhole shape shows laser energy does not reach the bottom in the absence of reflection [7].

A more direct or experimental based method for determining effective absorption is direct calorimetric measurement. Wang et al. [8] performed the measurements for partial and full penetration welds in 304 stainless steel with a 1070 nm laser operating at 6 kW. The partial

penetration welds exhibited an absorptivity between 71% and 58% for welding speeds between 50 and 150 mm/s, respectively. Keyhole depths ranged from 6.4 to 3.1 mm in 9 mm thick plate. In the case of full penetration welds, absorption increased from 36% to 57% when the welding speed increased from 50 mm/s to 150 mm/s due to greater inclination of the front keyhole wall, shallower initial reflection angle, and less light escaping through the keyhole. In another study that varied parameters from conduction mode to keyhole mode welding, Trapp et al. [9] fabricated low laser power (32 W to 540 W) and high speed (100 mm/s to 1500 mm/s) welds in 316 austenitic stainless steel with a 1070 nm wavelength laser. In the conduction mode regime, the absorptivity varies from 25% to 30%. As the power increased, the absorptivity peaked at 75% to 80% at welding speeds of 100 mm/s and 500 mm/s and laser powers between 100 W and 350 W. At the highest welding speed of 1500 mm/s, the absorptivity increased with power to 68% at 540 W but never reached a local maximum.

Higher effective absorption levels in keyhole mode welding are also possible through inverse Bremsstrahlung (IB) absorption, which occurs in the metal vapor and weakly ionized plasma (metal and shielding gas) directly above and inside the keyhole. The degree of absorption by the metal vapor and plasma depends on the wavelength of the laser beam. When welding with a one micron wavelength laser (e.g. 1064 nm Nd:YAG laser or 1070 nm Yb-doped fiber laser), absorption of less than 4% of the total laser power is expected [10]. The other primary laser wavelength for material processing is 10.6 μm (e.g. CO_2 laser). While the amount of absorption has not been measured directly for this wavelength, significant amounts of laser energy is absorbed through the IB mechanism at the 10.6 μm wavelength. The laser radiation remaining after absorption may not be enough to keep the keyhole at a consistent depth, and, in extreme cases, the keyhole may completely close periodically [11,12]. In fact, IB is one basis for keyhole stability during CO_2 laser welding, and controlling the vapor and plasma near the top of the keyhole with a high flow shielding gas can result in quality welds.

2.2.2 Heat Balance at the Keyhole Walls and Keyhole Shape

Understanding the keyhole shape is important for simulating multiple reflections and computing the pressure balance. An important welding characteristic, weld depth, is primarily controlled by keyhole depth during keyhole mode laser welding. Typically, the heat balance is used to compute the keyhole geometry, including depth, width, and length. All proposed

calculations are done on a point-by-point bases at the keyhole wall (e.g. local keyhole geometry) and include incident laser intensity and heat flux through the keyhole wall [4,6,13-17]. Kaplan [4] and Rai et al. [14] extended this further to the following heat balance equation, which includes the evaporation heat flux and terms in I_a to account for multiple reflections and IB absorption,

$$\tan(\theta) = \frac{I_c}{I_a - I_v} \tag{1}$$

where θ is the local keyhole wall angle relative to the vertical axis, I_c is the radial heat flux conducted through the keyhole wall, I_a is the absorbed laser energy, and I_v is the evaporation heat flux. So, the local wall angle is adjusted to make the fluxes equal as shown in Figure 12. The radial heat flux is defined as

$$I_c(r, \varphi) = -\lambda \frac{\partial T(r, \varphi)}{dr} \tag{2}$$

where λ is the thermal conductivity, T is temperature, and r and φ are the radial coordinates in the x,y plane. The temperature field in Equation 2 is defined as

$$T(r, \varphi) = T_a + \frac{P'}{2\pi\lambda} K_0\left(\frac{Ur}{2\kappa}\right) e^{\frac{-Ur}{2\kappa}\cos\varphi} \tag{3}$$

where P' is the power per unit length (or line source strength), K_0 is the second kind and zero order modified Bessel function, U is welding speed, and κ is thermal diffusivity. The second heat flux in the heat balance at the keyhole wall is the absorbed laser intensity, which can be calculated with the following equation
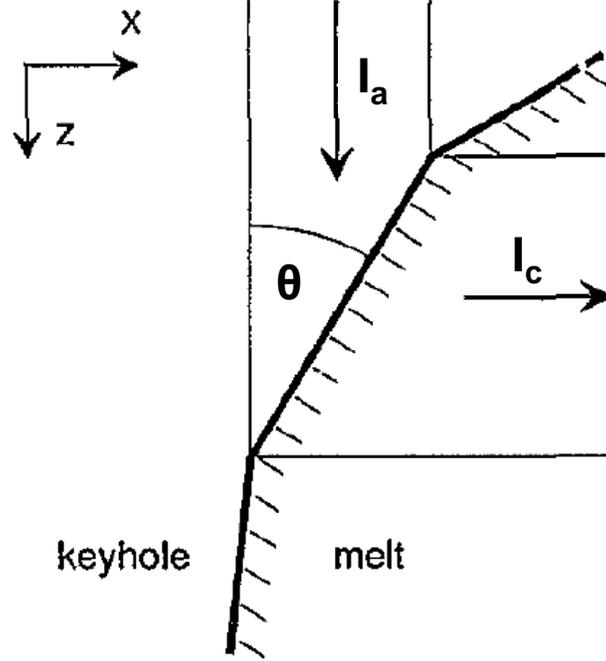
Figure 12: The heat balance is used to calculate the local wall angle and includes terms for incident laser energy, heat flux, and energy for evaporation. Adapted from [4].

$$I_a = e^{-\beta L}\left(1 - (1 - \alpha)^{1+\pi/4\theta}\right)I_0$$

(4)

where β is the plasma attenuation coefficient and accounts for inverse Bremsstrahlung absorption, L is the average path of the laser beam and can be assumed to be the keyhole depth, α is the absorption coefficient of the liquid metal, and I_0 is the incident laser intensity. The second exponent in Equation 4 accounts for the multiple reflections, using the average keyhole wall angle. Instead of using Equation 4, the absorbed laser intensity can include the effect of the keyhole wall angle on the absorption coefficient and explicit calculation of the multiple reflections as described by Solana and Negro [6]. The last energy flux in the heat balance is the evaporative heat flux, which is described by the equation [14]

$$I_v = \sum_{i=1}^{n} \frac{a_i P_{v,i}^0}{7.5} \sqrt{\frac{M_i}{2\pi R T_b}} \Delta H_i$$

(5)

where a_i is the activity of alloy component i, $P_{v,i}$ is the partial pressure of component i, M_i is the molecular weight of component i, R is the gas constant, T_b is the boiling point of the alloy, and ΔH_i is the heat of evaporation of component i.

2.2.3 Keyhole Mechanics and Pressure Balance

During keyhole mode laser welding, the laser does not vaporize a volume of material equal to the keyhole volume. Rapid evaporation of a small volume of liquid metal (much less than the keyhole volume) and resulting forces from the metal vapor open up and maintain the keyhole shape against the opposing closing pressures. The pressure balance is suspected to be the primary cause of keyhole collapse and porosity, and the balance is commonly manipulated during industrial welding processes to reduce porosity.

The various opening and closing pressures present in the keyhole [13,18] are shown in Figure 13. The pressure balance results from the forces exerted by the metal vapor on the keyhole wall, which is close to the boiling point of the alloy. The equilibrium vapor pressure and the recoil pressure from evaporation exert the primary opening forces. On the closing side of the balance are atmospheric pressure, hydrostatic pressure, and surface tension of the liquid metal. Hydrodynamic forces may play a role (e.g. 10% of atmospheric pressure) at very high welding speeds, exceeding 1700 mm/s for alloys with liquid metal densities of 7000 kg/m^3.

A pressure balance at the keyhole wall is assumed to be the driving force for maintaining an open keyhole. The full pressure balance with most of the possible terms is described in the relationship below [13,18]

$$P_0 + \frac{\gamma}{R_c} + \rho_l g h + \frac{1}{2}\rho U^2 = \sum a_i P_{v,i} + \sum \frac{J_i^2}{\rho_{v,i}} + P_{gas}$$

(6)

where the left side of equation is the keyhole closing pressures and the right side is the opening pressures. In Equation 6 on the left side, the first term is the ambient pressure, the second term is the surface tension pressure, the third term is the hydrostatic pressure, and the fourth term is the hydrodynamic pressure. On the same side of Equation 6, γ is surface tension, R_c is the radius of curvature of the keyhole, ρ_l is density of the liquid, g is acceleration due to gravity, h is depth below the top of the keyhole, and U is the welding speed. The hydrodynamic pressure term is the maximum value, and additional terms account for the keyhole shape [13,19].
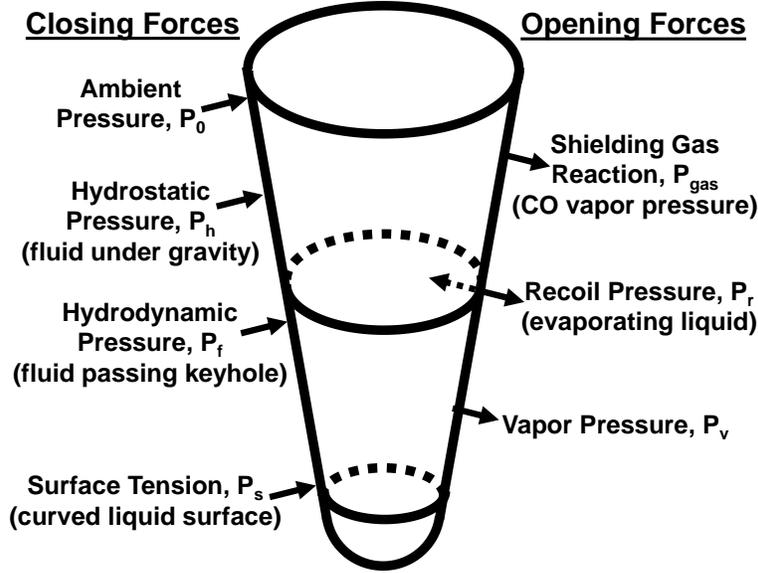
Figure 13: The closing and opening keyhole forces are diagramed.

On the right side of Equation 6, the first term is the vapor pressure, the second term is the recoil pressure, and the third term accounts for possible reactions between the shielding gas and alloy components. In steels welded with small amounts of oxygen added to the shielding gas, the carbon and oxygen in the liquid weld pool can react, forming carbon monoxide [18,20]. An example of carbon monoxide formation and vapor pressure affecting the keyhole stability and associated calculations are described by Ribic et al. [18]. In Equation 6, a_i is the activity of alloy component i, $P_{v,i}$ is the partial pressure, J_i is the evaporation mass flux, $\rho_{v,i}$ is the density of the evaporating gas, and P_{gas} is a place holder variable for the equations to calculate the vapor pressure of other gases, such as carbon monoxide. The evaporation mass flux is expressed as

$$J_i = \frac{a_i P_{v,i}}{n} \sqrt{\frac{M_i}{2\pi RT}} \tag{7}$$

where n accounts for evaporation outside of a vacuum and is taken as 7.5 [21-23]. The density of the evaporating gas is expressed as

$$\rho_{v,i} = \frac{a_i P_{v,i} M_i}{RT} \tag{8}$$

24

Ribic et al. [18] reported the calculated pressures at the keyhole wall during laser welding of mild steel with oxygen in the shielding gas. For a 9 mm deep weld with no oxygen in the weld pool, the pressures were calculated at 4.5 mm depth and are shown in Table 1. In terms of opening pressures, vapor pressure was the highest at 0.924 atm, followed by carbon monoxide vapor pressure at 0.103 atm, and recoil pressure was the lowest at 0.002 atm. On the closing side, ambient pressure was the highest at 1 atm, followed by surface tension at 0.026 atm, and hydrostatic pressure was the lowest at 0.003 atm. As expected at this depth, the vapor pressure and atmospheric pressure are the dominant terms for opening and closing the keyhole, respectively. The gas formation also has a significant impact as an opening term, but the other terms are one or more orders of magnitude less than the dominant terms. These terms change with the depth of the keyhole, and if they were calculated closer to the tip, the surface tension would be higher.

Table 1: Ribic et al. [18] calculated the pressures along the keyhole wall at the half-depth of the weld.

Term	Symbol	Value (atm)
Keyhole Opening Terms		
Equilibrium Vapor Pressure	P_v	0.92400
CO Vapor Pressure	P_{CO}	0.10300
Recoil Pressure	P_r	0.00208
Keyhole Closing Terms		
Ambient Pressure	P_0	1.00000
Surface Tension Pressure	P_γ	0.02570
Hydrostatic Pressure	P_h	0.00303

2.2.4 Keyhole Instability and Porosity

The keyhole is inherently unstable and will fluctuate in depth during welding. This instability, especially near the keyhole tip, can lead to the formation of keyhole porosity.
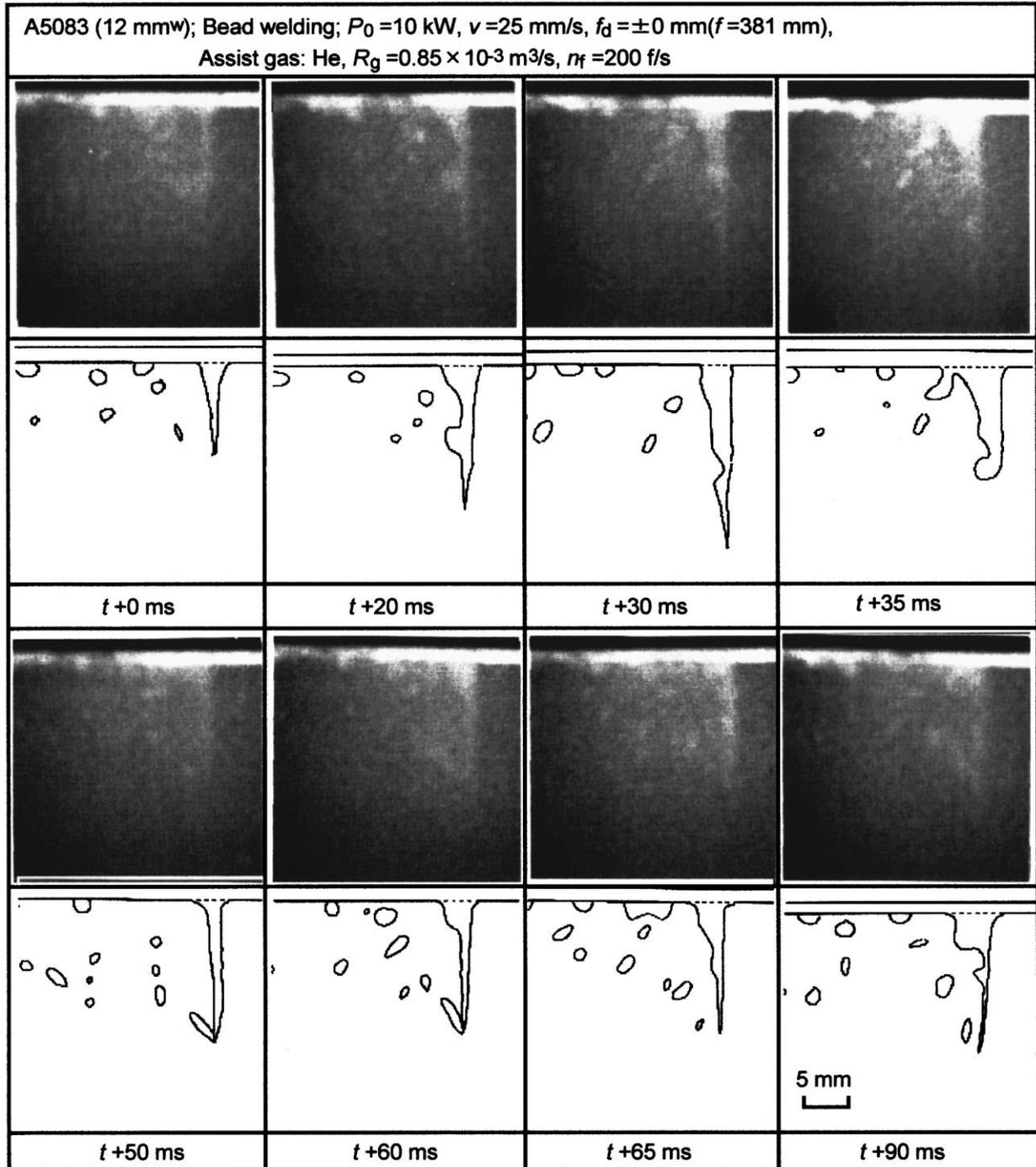
Figure 14: X-ray videography and the authors' interpretation of the frames [24] is shown. Keyhole porosity results from the pinching off of the bottom of the keyhole, forming a bubble that gets trapped in the solidifying metal as a pore.

Researchers [10,20,24-27] have relied heavily on X-ray videography to capture keyhole dynamics at high speeds. Matsunawa et al. [24] performed the earliest of this type of research by welding an aluminum alloy with a 10.6 μm wavelength CO_2 laser. Frames from the videography and accompanying schematic representations of the frames are shown in Figure 14. As shown, the keyhole changes dramatically in depth and shape over the 5 to 25 ms time period between frames. For example, a bulge in the keyhole wall disappears from the 20 ms to 30 ms slide, and the pinching at the bottom of the keyhole in the 35 ms slide forms into a bubble by the 50 ms slide. This pinching is expected to cause the formation of most of the porosity observed in laser and hybrid laser-arc welds. The keyhole is most unstable at the tip because the keyhole curvature (i.e. small keyhole radius) and surface tension forces are very high, requiring higher keyhole wall temperatures and vapor and recoil pressures. Without these higher temperatures and pressures, the tip pinches off, as shown in Figure 14, and forms a bubble, which is then either trapped in the solidification front as a pore or, through buoyancy forces, escapes from the pool.

While the formation of keyhole porosity initiating at the tip of the keyhole is the most prevalent type, the mechanism can vary with modern fiber lasers, which operate at high powers with smaller beam sizes and at a wavelength of 1070 nm. In a series of studies, Kawahito et al. [25,26] investigated the use of a fiber laser operating at 6 and 10 kW to weld 304 stainless steel. When welding at a laser power of 6 kW, keyhole porosity formed at the tip of the keyhole in a
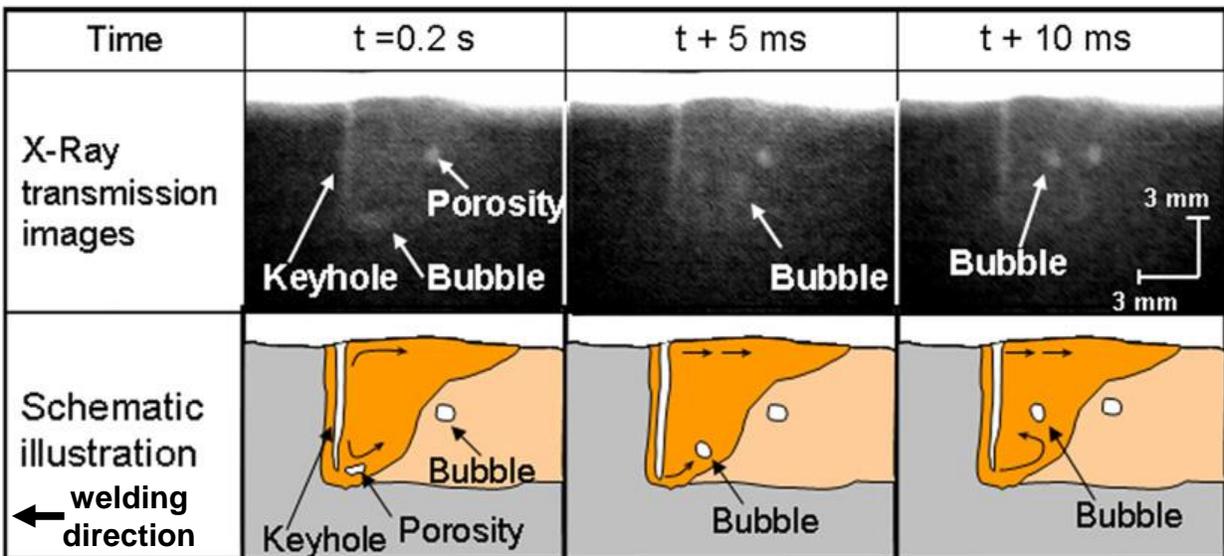
Figure 15: The same keyhole porosity mechanisms exist during fiber laser welding of stainless steel with 6 kW of laser power [26]. Bubbles form at the bottom of the keyhole and get trapped in the solid metal.

Time	$t_1 = 1.2$ s	$t_1 + 7$ ms	$t_1 + 10$ ms
X-Ray transmission images	Keyhole		1 mm 1 mm
Schematic illustration	Welding direction Keyhole		Bubble
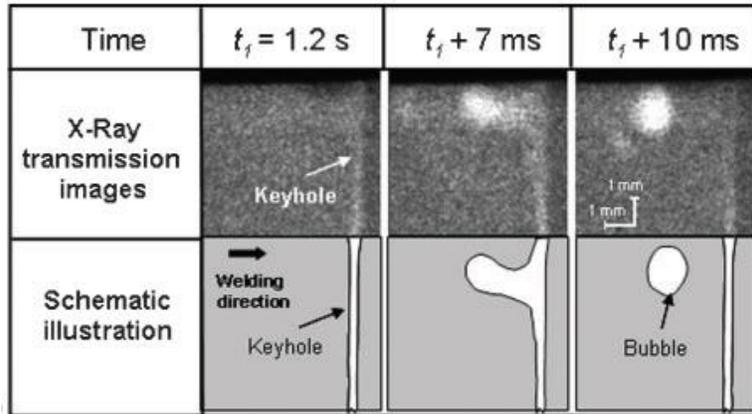
Figure 16: During fiber laser welding at higher powers of 10 kW, the bubble formation mechanism can change, producing bubbles at the top of the keyhole [25].

similar way [26]. Figure 15 shows the X-ray videography frames and representative schematics over a 10 ms exposure. Porosity is clearly forming at the tip and moving up and to the right (i.e. opposite the welding direction). This porosity behavior is similar to the earlier research with a CO_2 laser. When the power is increased to 10 kW, bubble formation has been observed both at the bottom and near the top of the keyhole as shown in Figure 16. In this case, a bulge initiates in a little less than 6 ms, and within another 4 ms, the bulge has pinched off and formed a very large bubble, which is]about 1 mm in diameter. This new mechanism (bubbles forming at the top of keyhole) was not studied in detail, but the authors concluded that it may result from a lack of defocus of the laser beam relative to the workpiece and resulting very high laser intensity in the top half of the keyhole, causing instabilities above the tip.

2.2.5 Pressure Balance Analysis of Keyhole Stability

Accounting for the pressure balance, heat balance, and laser absorption through multiple reflections and inverse Bremsstrahlung in the calculation of the keyhole geometry is non-trivial. An analytical solution does not exist and an iterative numerical solution is required because certain terms are required before others can be solved (e.g. local keyhole geometry before heat and pressure balances and full keyhole geometry before multiple reflection solution). This difficulty has resulted in a poor understanding of the pressure balance over the entire keyhole under various processing conditions, including low ambient pressure and low surface tension (two known mechanisms for reducing porosity).

However, if the geometry of the keyhole is known in advance, then the pressure balance is only a function of temperature and can be solved for the various pressure components. The three

28
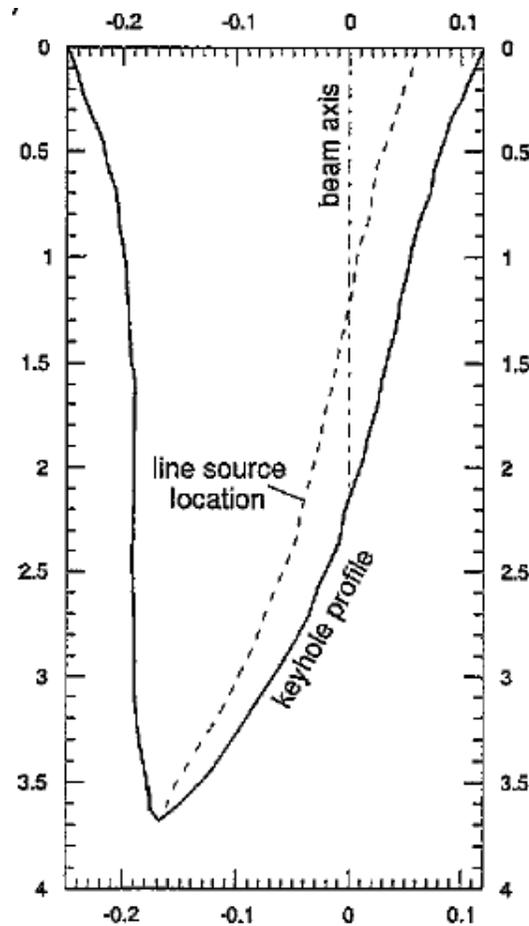
Figure 17: Kaplan [4] calculated the keyhole geometry. Beam axis indicates the center of the beam. The calculation uses a line heat source, which is also indicated in the figure.

different conditions that will be tested here are unmodified surface tension and atmospheric ambient pressure, low ambient pressure, and low surface tension. The unmodified surface tension and atmospheric ambient pressure case represents the typical laser welding conditions with no special precautions taken to reduce keyhole porosity. The low ambient pressure case would represent welding in a relatively weak vacuum to avoid keyhole porosity, while a low surface tension would represent welding with a high concentration of a surface active species present and would also be expected to reduce porosity. The computed keyhole geometry has been taken from Kaplan [4] and is shown in Figure 17.

Without the hydrodynamic and gas pressure terms, Eq. 6 was solved for the remaining four pressure terms. The only temperature dependent term kept constant was the density of the liquid metal. Pure iron physical properties were used. The temperature was solved for by assuming a pressure balance of atmospheric pressure, surface tension, hydrostatic pressure, vapor pressure,
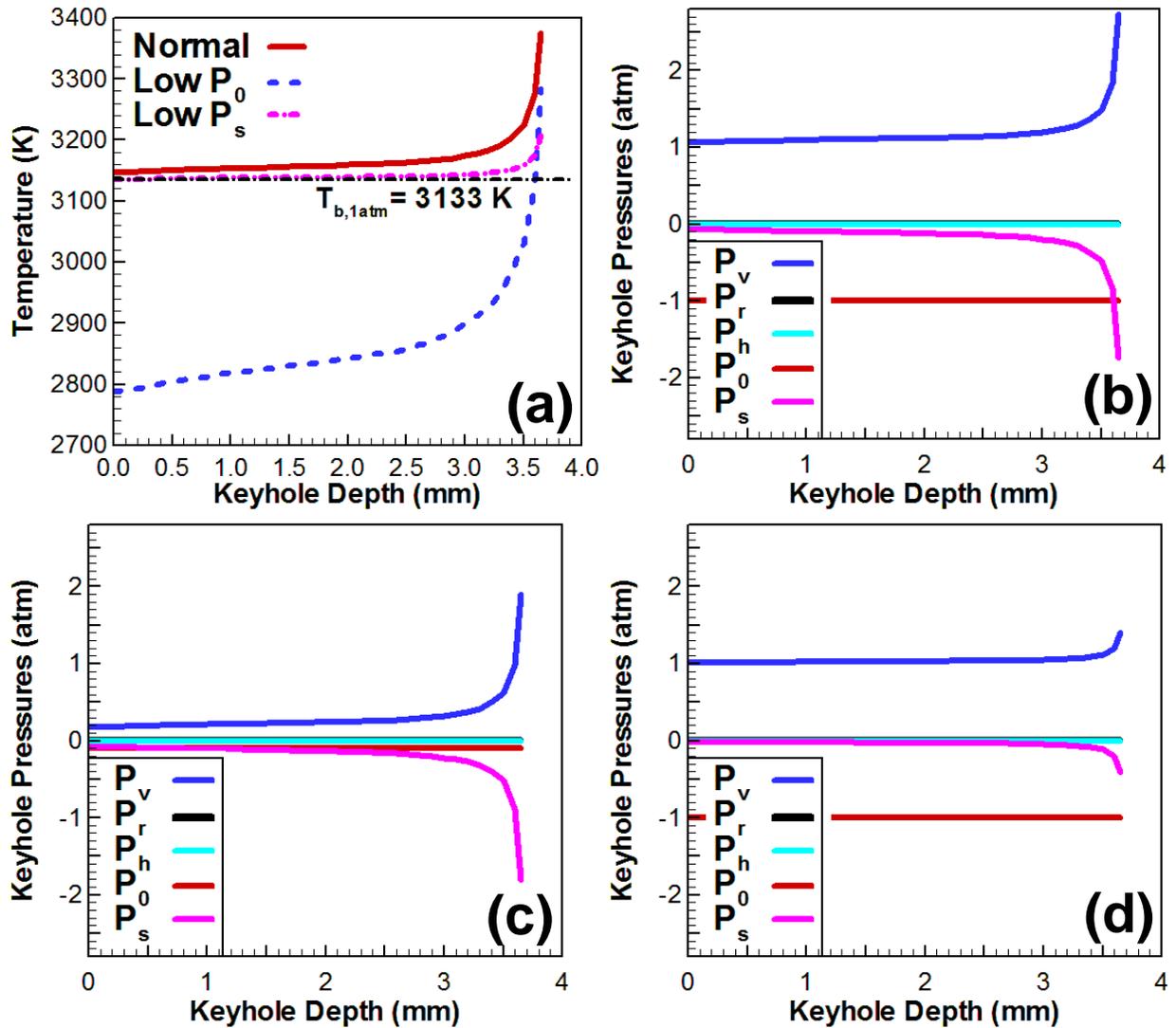
Figure 18: The keyhole wall pressure balance has been calculated for three cases: (b) normal ambient pressure and surface tension, (c) 0.1 atm ambient pressure, and (d) low surface tension. The wall temperatures that satisfied the pressure balance are shown in (a).

and recoil pressure at every position along the keyhole depth. The calculated keyhole wall temperature profiles are shown in Figure 18a. For nominal values of atmospheric pressure and surface tension (e.g. nominal P_0 and P_s), the temperature at the top of the keyhole is 10 K above the boiling point at 1 atm. The temperature rises gradually until the last 0.5 mm of depth, where temperature rises about 200 K. During welding in low atmospheric pressure (low P_0), the temperature at the top of the keyhole is approximately 350 K below the boiling point at one atmosphere. The temperature rises another 120 K to 2900 K in the first 3 mm of depth. In the remaining 0.5 mm, the temperature increases nearly 400K to 3285 K. In the low surface tension case (low P_s), the keyhole wall temperature remains with 10 K of the boiling point for the first 3

mm of depth and then increases to 3210 K in the last 0.5 mm at the bottom of the keyhole. The primary difference between the normal case and the other two cases that are known to produce low keyhole porosity welds is higher average temperature along the keyhole walls. However, a relatively sharp increase in temperature near the bottom of the keyhole is a feature in all cases.

To better understand why different techniques produce fewer porosity defects, the pressure terms for each case are plotted in Figure 18b, c, and d. For clarity, the opening pressures, vapor and recoil pressure, are plotted with positive values, and the closing pressures, atmospheric, surface tension, and hydrostatic, are plotted with negative values. Clearly, the recoil and hydrostatic pressures play almost no role in the pressure balance for pure iron, but recoil pressure may play a role in alloys containing high vapor pressure elements, such as Mn, Mg, and Al. Each force never reached more than 0.01 atm. This finding is at odds with some works, such as those by Semak and Matsunawa [16,28], which assumed the recoil pressure is the primary keyhole opening force. However, in those works, recoil pressure is defined as 55% of the equilibrium vapor pressure based on an undefined calculation of evaporation in vacuum versus evaporation at a high ambient pressure. In the analysis presented here, recoil pressure is defined as the square of the evaporation mass flux divided by the density of the evaporating gas (J^2/ρ_v), which reduces to $P_{v,Fe}/(2\pi n^2)$ and effectively 0.3% of the equilibrium vapor pressure.

For the three cases considered, the determining factors for keyhole wall temperature at the top and bottom of the keyhole differ. At the top of the keyhole, the temperature depends on the ambient pressure since the surface tension is relatively low in all cases due to the wide, low curvature keyhole opening. However, at the bottom of the keyhole, surface tension drives the temperature because the keyhole is narrowing and curvature is approaching infinity. The maximum pressures reached in the nominal case are 2 atm for the surface tension and more than 2.5 atm for the vapor pressure. In the other cases (e.g. low defect cases), the pressures never exceeded 2 atm, and, especially in the low surface tension case, the maximum pressures never exceeded 1.5 atm. The magnitude of the pressures on the keyhole walls may play an important role in keyhole stability.

Another consideration for keyhole stability is the temperature and spatial gradients of the pressure terms at different locations in the keyhole. Knowing how each pressure term changes with temperature and local keyhole diameter provides additional insight into how a bubble could

form. On the iron equilibrium vapor pressure curve, Figure 19 illustrates how vapor and surface tension pressures vary with temperature and keyhole diameter at the top and bottom of the keyhole cavity. While the magnitudes of each term are important, the most valuable takeaway from this figure is that the pressure balance at the keyhole wall is very susceptible to small changes in temperature and keyhole diameter. For example, if the temperature at the bottom of the keyhole, under nominal conditions, increases 1 K, the vapor pressure increases 11 mbar, and surface tension decreases 1 mbar. If the pressure balance was self-correcting, each term should have the same sign and the same magnitude. If the small temperature increase is accompanied by a small increase in keyhole diameter (e.g. a fraction of a micron), then the closing pressure will drop dramatically, possibly leading to a rapid increase in keyhole diameter at the bottom. At some point, the laser
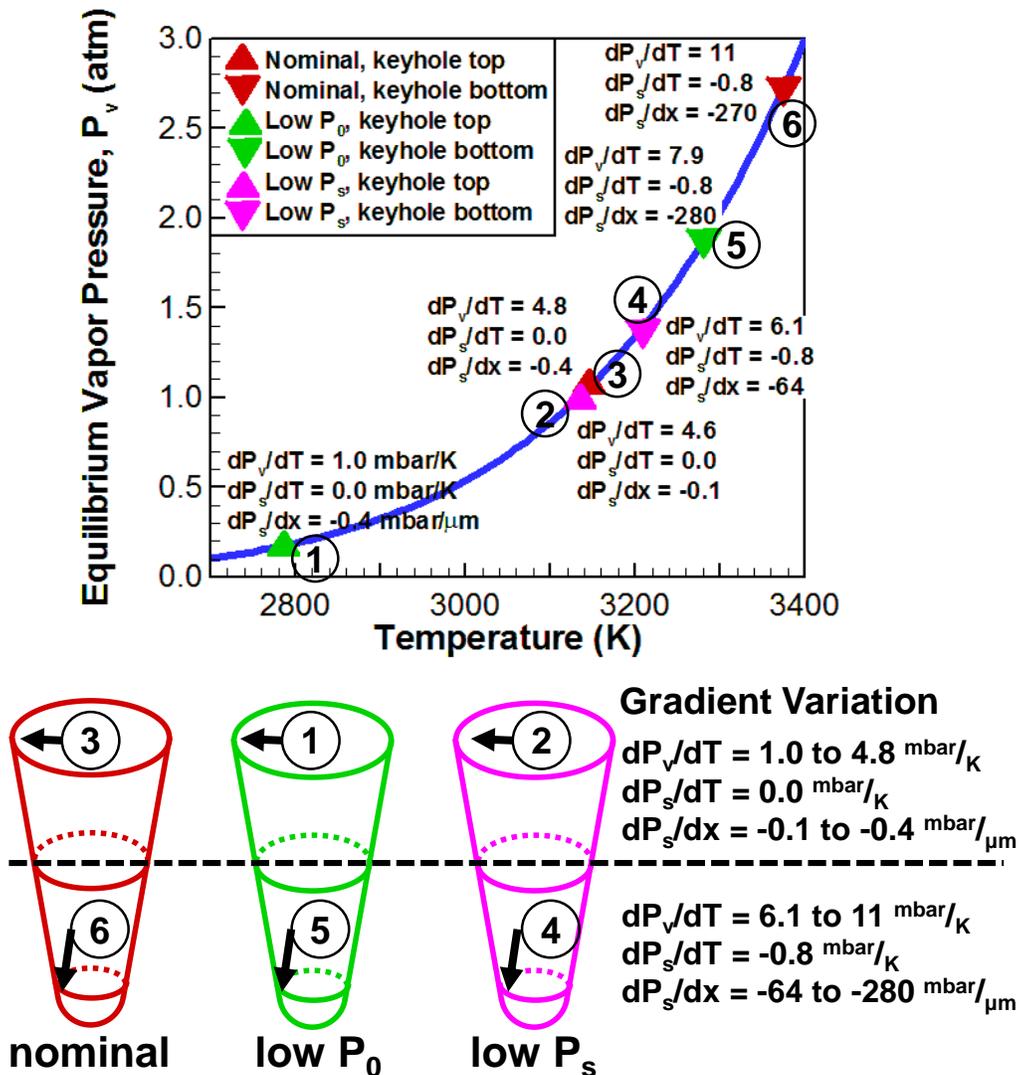
Figure 19: The spatial and temperature gradients of vapor pressure and surface tension pressure for different ambient pressure and surface tension conditions.

intensity will not be able to maintain the keyhole width, and the closing forces will increase dramatically as the keyhole diameter decreases.

2.3 Techniques for Reducing Keyhole Porosity

Due to its nature as a defect, keyhole porosity formation dynamics have been extensively studied [12,18,20,24,26,27,29], and solutions for reducing and eliminating porosity have been developed [20,26,27,30,31-34,35-38]. The solutions vary widely in their degree of complexity and their feasibility on the shop floor or in the field. Their qualitative effectiveness depends on the alloy being welded and can differ widely from a small reduction in porosity to complete elimination. The variation in solutions includes (1) process parameter optimization, (2) process environment optimization, and (3) implementation of an electric arc for a hybrid laser-arc process. In (1), a combination of laser power, welding speed, and power modulation parameters is selected to produce a defect free weld. Reactive shielding gases and welding in a weak vacuum are examples of (2). A leading or trailing arc in (3) significantly alters the welding physics and adds more process parameters for selection and optimization.

2.3.1 Optimizing Laser Power and Scan Speed

As two of the most fundamental and easily adjustable parameters, laser power and welding speed are commonly optimized to reduce porosity [25,26,30,39,40]. For 304 stainless steel, Kawahito et al. [25,26], in two studies, investigated the effect of welding speed, laser power, and beam size on the laser material interaction mode, which was characterized as keyhole porosity, defect free welds, humping of the free surface, or underfill at the top of the weld. Kawahito et al. evaluated the role of laser power of 6 and 10 kW on the interaction mode. The laser beam propagation characteristics were measured directly with a beam diagnostic tool. The resulting process maps from these studies are show in Figure 20. The general trend at each laser power is the same. Below a critical welding speed, porosity formation occurs. Once the critical welding speed reaches a level between 75 to 83 mm/s, welds without porosity can be fabricated with two laser beam diameters of 360 μm and 560 μm.. This reduction in porosity is attributed to the stabilization of the keyhole. At faster welding speeds beyond 100 to 170 mm/s (depending on laser power), humping [41] and underfill defects dominate and are differentiated by the laser beam size. While there are similarities, laser power has a large impact on the size of the process window with the higher power producing a much smaller process window.
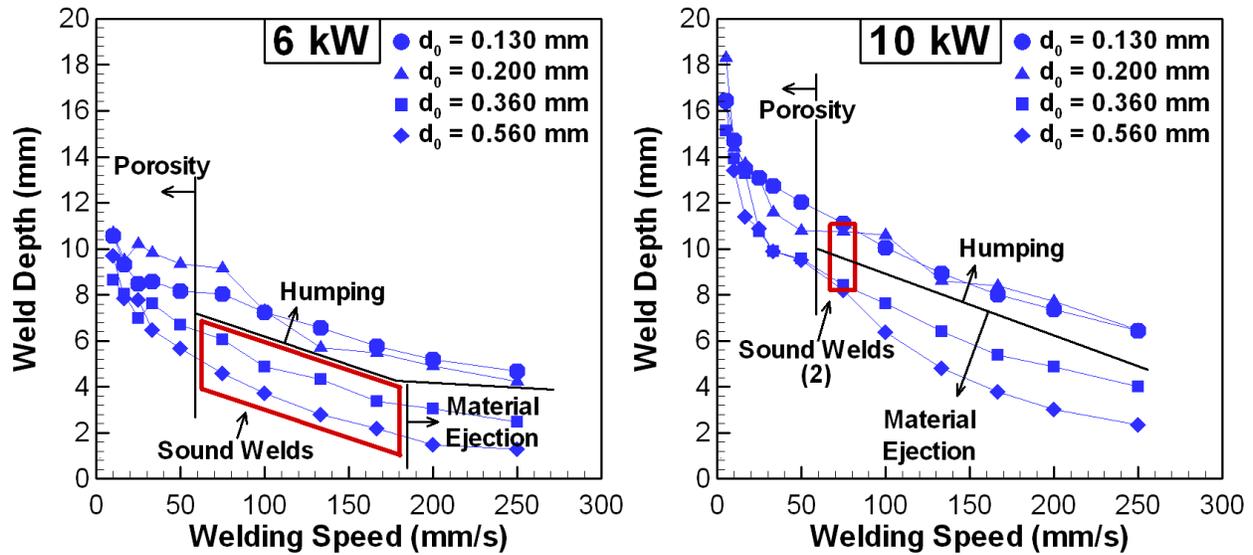
Figure 20: Optimizing laser power and scan speed for various beam sizes can reduce porosity, however, the process window shrinks dramatically when power increases from 6 kW (left pane) to 10 kW (right pane) [25,26].

At the lower laser power, the process window for welds without porosity spans 83 to 167 mm/s. When the power is increased 10 kW, only welds fabricated with welding speeds of 75 mm/s produced welds without porosity or other defects. Laser power dictates which beam sizes produce defect free welds. In the 6 kW case, usable laser diameters include 360 and 560 μm. The 560 μm diameter no longer produces defect free welds when the power is increased to 10 kW. Now, beam diameters are 200 and 360 μm for defect free welds. The tightly focused beam with a spot diameter of 130 μm never produces a defect free weld.

Optimizing the laser power and scan speed can produce sound welds, but a relatively high welding speed must be used. These high welding speeds significantly reduce the maximum achievable penetration depth compared to the low speed welds. For example, in the 6 kW welds, maximum penetration depth without defects is 6 mm, which is 45% less than the maximum achievable depth. The result is similar in the 10 kW welds with 11 mm as the highest penetration depth without defects and 19 mm with defects. So, penetration depth is reduced significantly to produce welds without defects, but laser power and weld speed are readily adjustable in most production environments. While it is known that high welding speeds reduce porosity, the exact reason why the keyhole stabilizes is unclear. The geometry of the keyhole would be expected to change significantly when increasing weld speed (e.g. shallower incline of the front wall), but the effect of this geometry change on stability is not understood.

2.3.2 Modulating Laser Power

The rapid oscillation in delivered laser power in the frequency range from 10 Hz to 500 Hz has been identified as a technique for reducing keyhole porosity during laser welding [20,24,31-33]. When power modulation is used instead of a constant laser power, additional process parameters must be selected, including peak power, base power, frequency, duty cycle, and waveform (e.g. square, sine, triangle, etc.). A selection of these parameters is shown in Figure 21. Matsunawa et al. [24] demonstrated the utility of power modulation in aluminum alloy 5182. The researchers used a peak power of 5 kW and a base power of zero and varied the duty cycle from 100% (continuous wave) to 50% (equal time at base power) at 100 Hz. X-ray images of the welds are shown in Figure 22. At a duty cycle of 70%, the combined parameters produced a porosity
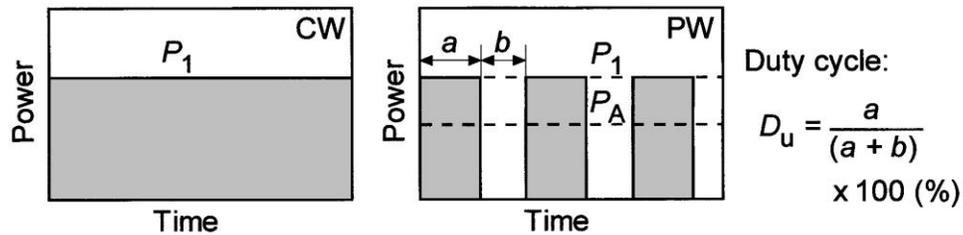
Figure 21: The base and peak powers and duty cycle are explained for the pulsed welding (PW) case compared to the continuous wave (CW) case [24].

Figure 22: Proper selection of peak power, base power, duty cycle, and frequency can produce porosity free power modulated welds in aluminum [24].

free weld. The authors attributed the reduced porosity to removal of porosity by succeeding pulses if the proper overlap is selected and to forced oscillation causing more stable keyhole motion.

Zhao et al. [20] studied keyhole porosity during power modulated laser welds in plain carbon steel with a fiber laser. Frequency was varied from 10 to 125 Hz, and base power and peak power were maintained at 3 and 7 kW, respectively. Duty cycle was dependent on frequency and varied from 5% to 63%. The researchers found that porosity was not completely eliminated but was reduced by 85% from the continuous wave value when operating at 60 Hz and 30% duty cycle. These results are shown in Figure 23. The authors attributed the low porosity to matching the power modulation frequency with the natural oscillation frequency of the weld pool.
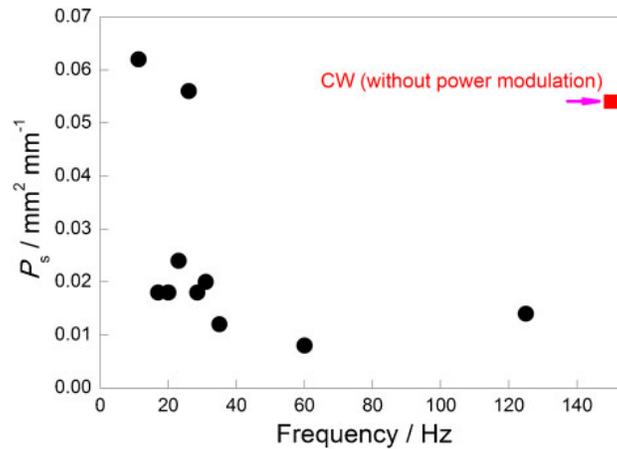
Figure 23: Frequencies greater than 35 Hz produce low keyhole porosity welds in plain carbon steel [20].

Compared to the other techniques, power modulation does not require a sacrifice in penetration depth, alloy chemistry, or weldment size. However, four new process parameters are created with this technique, and each one must be optimized and controlled for quality. Any optimized parameters may not produce defect free welds when one of the other common process parameters, such as weld speed or beam size, is modified. Previous research does not provide detailed guidance on how porosity is reduced with power modulation or how the natural weld pool oscillation frequency changes with process parameters or alloy composition.

2.3.3 Operating at Low Ambient Pressures

Welding in reduced ambient pressure is regularly performed for electron beam welds due to the requirements of the process (i.e. electrons must be incident on the part being welded). The benefits of this process include deeper weld penetration and reduced keyhole porosity. Laser welds can also be fabricated at lower ambient pressures but do not require the extremely low vacuum

environments necessary for electron beam welding (i.e. 4 mbar vs. 0.0001 mbar, respectively). When performed at these ambient pressures, laser welds gain the same attributes (i.e. deeper penetration and reduced porosity) [27 ,29,34].

Katayama et al. [27] studied the effects of low ambient pressure on the penetration depth and keyhole porosity in laser welds of 5083 aluminum and 304 stainless steel, using CO_2 and YAG laser systems. The authors also used X-ray videography to observe the keyhole dynamics during welding. When welding in ambient pressures varying from 1000 mbar to 0.3 mbar, porosity disappeared at pressure of 4 mbar or less for both laser welding systems. During CO_2 welding, the keyhole depth in both alloys did not increase significantly at low ambient pressure compared to atmospheric pressure. This lack of increase may be due to the higher evaporation rates under low ambient pressures and, therefore, higher laser absorption in the metal vapor and plasma. On the other hand, during YAG welds, the penetration depth in aluminum increased from 2.5 mm to 7 mm when ambient pressure decreased from atmospheric pressure to 4 mbar, and the penetration depth in stainless steel increased from 6 mm to 7.5 mm over the same pressure range. During welding at low pressure, no bubbles formed, however, a bulge in the rear keyhole wall was observed. This behavior and a schematic depicting the bulge are shown in Figure 24. The bulge fluctuates with time but does not disappear or pinch off to form a bubble.
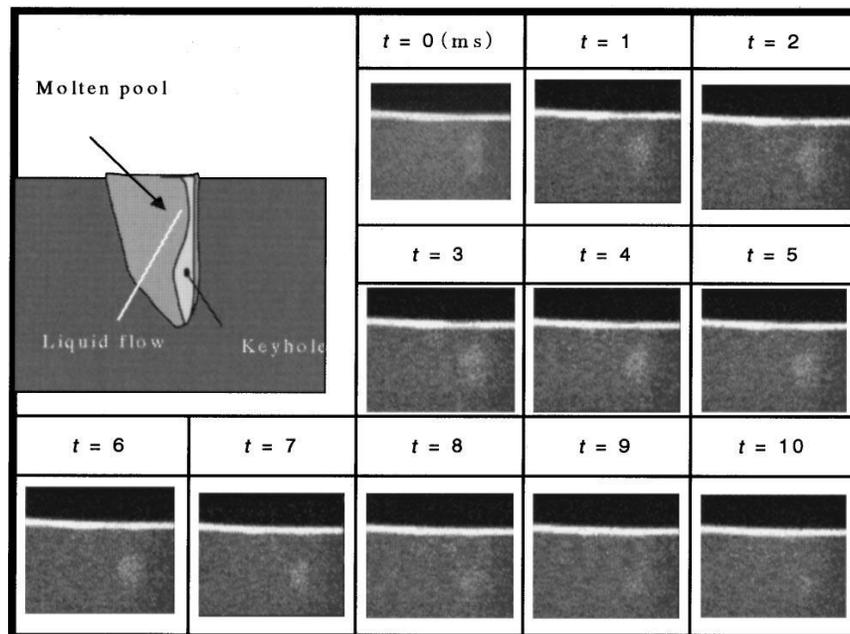
Figure 24: X-ray videography of laser welds performed in low ambient pressures shows that bubbles do not form, which limits keyhole porosity [27].

Elmer et al. [34] studied the variation of the ambient pressure from atmospheric pressure to 0.1 mbar during laser welding of commercially pure titanium and nickel with a disk laser, operating at 1030 nm wavelength. Resulting keyhole porosity was measured with X-ray computed tomography, and the pores were characterized by size, location, and shape. Figure 25 shows the porosity in nickel welds under the two different ambient pressures. Clearly, the porosity is reduced in size at lower pressures. The total porosity volume in the low pressure weld was 11% of that observed in the atmospheric pressure weld, even with a greater number of pores (117 vs. 218). The pores are also confined to the lower portion of the weld, with very few pores near the top of the weld in the low ambient pressure weld. The porosity results for titanium laser welded under the two different pressure conditions are shown in Figure 26. When welded in lower pressure, titanium produce virtually no pores (i.e. just one at the weld root) and had only 3% of the porosity of the higher pressure weld. Comparing titanium and nickel, nickel had much more porosity than titanium under similar welding conditions.

Welding in reduced amibient pressure of 4 mbar or less provides significant benefits for laser welding. For similar conditions, welding under a lower pressure produces deeper penetration welds and lower porosity, although porosity may not be entirely eliminated for every alloy. In fact, the ability to reduce porosity depends on the alloy being welded. Keyhole porosity free or nearly free welds are fabricated in Al-, Fe-, and Ti-base alloys, but the same is not possible for commercially pure nickel. Why the weak vacuum does not affect nickel similar to the other alloys
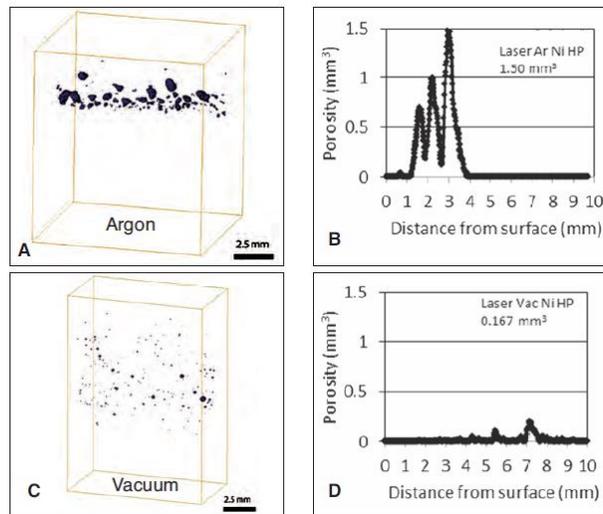
Figure 25: The (a) X-ray CT of Ni welded in argon, (b) the porosity distribution Ni welded in argon, (c) X-ray CT of Ni welded in vacuum, and (d) the porosity distribution of Ni welded in vacuum are shown [34].
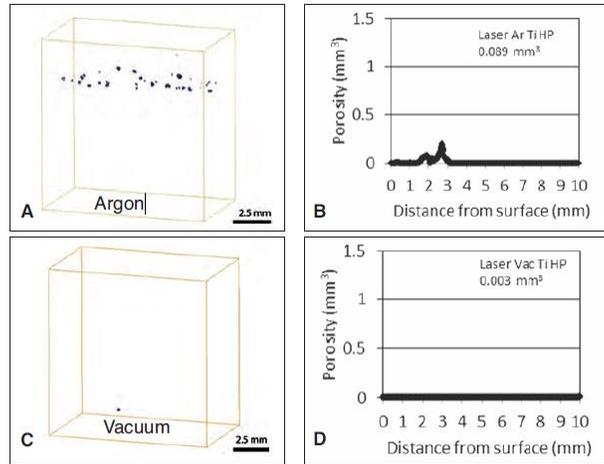
Figure 26: The (a) X-ray CT of Ti welded in argon, (b) the porosity distribution Ti welded in argon, (c) X-ray CT of Ti welded in vacuum, and (d) the porosity distribution of Ti welded in vacuum are shown [34].

is unclear. The technique is relatively simple and does not require tuning of multiple variables before quality welds can be fabricated. The major downside is that a vacuum chamber is required, with the largest systems able to handle a maximum weldment size of 5.8 m x 1.2 m area and 1.2 m high [42]. Aircraft frame parts easily fit in this envelope, but construction of large machinery, ships, and power plants do not benefit from the technolgy and would require other means for reducing porosity.

2.3.4 Welding in Nitrogen-rich Environments

Nitrogen rich shielding gases have been proven to reduce keyhole porosity in certain alloys [25,35-37]. Kawahito et al. [25] recognized the effects of nitrogen as a shielding gas during laser beam welding of 304 stainless steel. When welding with a 1070 nm wavelength laser under argon shielding gas at 50 mm/s welding speed and 10 kW laser power, porosity was identified throughout the weld. When the same weld was made with nitrogen shielding gas, X-ray videography revealed a stable keyhole with no porosity generation as shown in Figure 27, and the authors concluded that nitrogen was absorbed in the liquid metal and stabilized the keyhole. An increase in N content in the steel of 100 ppm supports their conclusion. In addition to reducing porosity, the penetration depth of 12 mm was maintained when the shielding gas was switched from argon to nitrogen.

While 304 stainless steel exhibits reduced porosity when welding with nitrogen shielding gas, the effect on other alloys was unknown. Elmer et al. [35] studied the effects of shielding gas and process parameters on keyhole porosity in four different alloys, including 304 stainless steel,

39
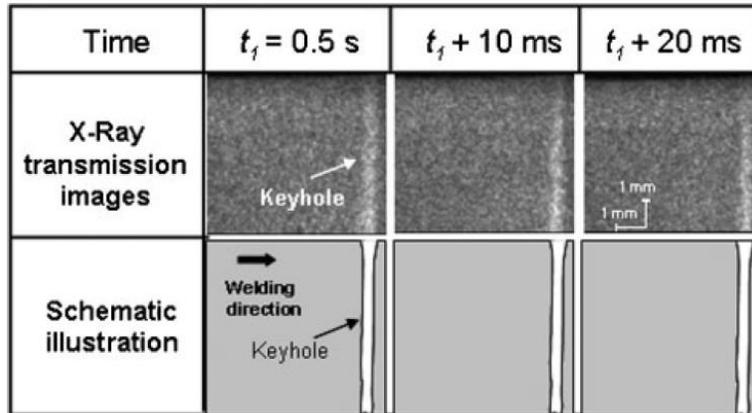
Figure 27: X-ray videography shows that the use of N₂ reduces porosity by eliminating the formation of bubbles [25].

A36 steel, 21-6-9 stainless steel, and pure nickel. In terms of processing parameters, the authors demonstrated that higher welding speeds lead to less porosity, which is in agreement with many other studies [25,26]. Under argon shielding gas, high levels of porosity were observed in pure nickel, moderate porosity occurred in 304 stainless and A36 steels, and very low to zero porosity was found in 21-6-9 stainless steel. When the same welds were fabricated under nitrogen shielding gas, no change was observed in nickel (i.e. still high) and 21-6-9 stainless steel (still low). On the other hand, the 304 stainless and A36 steel exhibited less porosity than welds fabricated under argon.

The authors attributed the reduction in porosity to the high solubility of nitrogen in iron and concluded that nitrogen stabilized the keyhole or that nitrogen bubbles formed in the liquid were quickly absorbed by the molten steel. In the case of 21-6-9 stainless steel, the authors believed that the high manganese content increased the vapor and recoil pressures, stabilizing the keyhole, regardless of the shielding gas. Because the pure nickel does not dissolve nitrogen in any significant quantities and had no high vapor pressure alloying elements, the authors concluded that there were no special factors to increase the stability of the keyhole or to absorb bubbles.

The use of nitrogen as a shielding gas presents a unique technique for reducing porosity during laser welding. Unlike parameter optimization, which requires high welding speeds and a sacrifice in penetration depth, nitrogen shielding gas does not result in a lower penetration depth and can be easily implemented into most weldments. However, higher nitrogen content in the weld metal is a consequence and may not be acceptable for some applications. In the case of Kawahito et al. [25], nitrogen content increased by 100 ppm during welding in an N₂ shielding

gas. This increase represents a minimum 10% increase if the starting nitrogen content of the alloy is within the 1000 ppm limit for 304 stainless steel. The exact mechanism for enhanced keyhole stability is unclear. Nitrogen will reduce the surface tension of the weld metal, resulting in a lower closing pressure, but the effect needs to be quantified through experiments or calculations for any conclusions to be drawn. The view that nitrogen shielding gas results in an unstable keyhole and that the resulting nitrogen bubbles are absorbed seems unlikely given the X-ray videography evidence of every low porosity weld having a very stable keyhole.

2.3.5 Welding with an Oxygen-rich Shielding Gas

Similar to nitrogen, oxygen-rich shielding gases have exhibited low porosity laser welds [18,20,38]. Zhao et al. [20] tested the effects of oxygen in argon and helium shielding gases in plain carbon steel. The results of these experiments are shown in Figure 28. In these experiments, porosity was measured radiographically along the longitudinal side of the weld and is reported as porosity area per unit length of weld measured (P_s in Figure 28). For helium, porosity reduces to zero after 10% O_2 addition. On the other hand, in argon, the porosity never fully decreases to zero, and there is a slight increase at 2.5% O_2 before a continuous decrease begins. The differences in behavior between argon and helium are attributed to the higher density and momentum of argon possibly contributing to porosity formation at the keyhole wall. In any case, X-ray videography showed the oxygen stabilized the keyhole and no bubbles were formed. Figure 29 shows welds with and without the addition of 10% O_2 in helium shielding gas. The keyhole maintains a steady shape in the case of O_2.
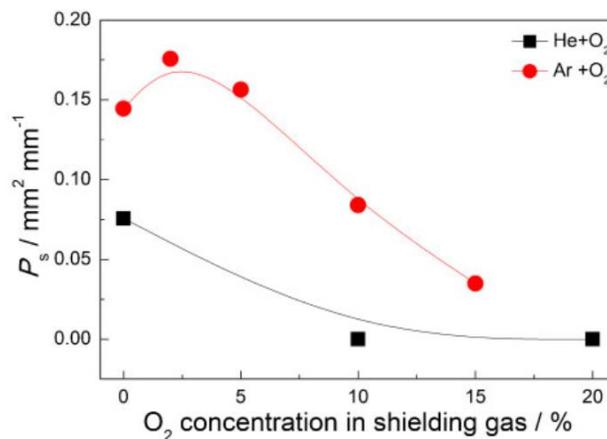
Figure 28: The addition of oxygen to an inert shielding gas results in lower porosity, measured along the longitudinal side of the weld as porosity area per unit length of weld [20].

41
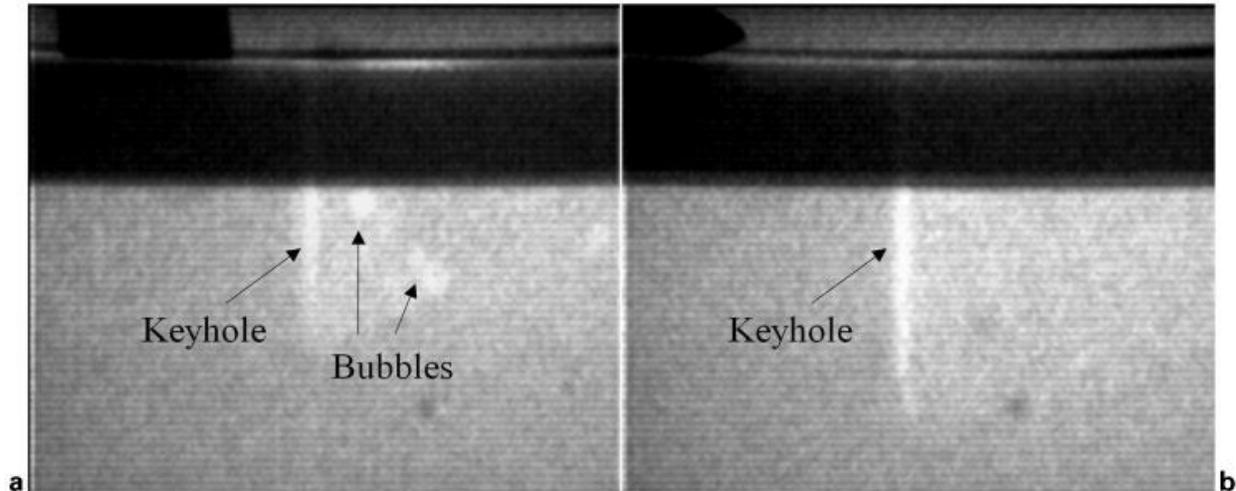
Figure 29: Laser welds made (a) without and (b) with 10% O2 added to the helium shielding gas [20].

Zhao et al. [20] sought to understand the stabilizing effect of O_2 on the keyhole. Two possible causes include the formation of CO as an opening pressure or the reduction of surface tension as a closing pressure. Carbon monoxide evolution results from the reaction of dissolved carbon and oxygen in the liquid metal, e.g. $[\underline{C}] + [\underline{O}] \Rightarrow CO_{(g)}$. The authors confirmed the formation of CO by measuring the carbon content in the steel before and after welding. When welded in the presence of 20% O_2-He, the carbon content dropped from 0.16 wt.% to 0.14%. To test if surface tension was the primary factor, the authors varied the sulfur content in the base metal from 60 ppm to 1500 ppm. X-ray images of the porosity are shown in Figure 30. Increasing the sulfur content does not affect the generation of bubbles and the formation of porosity, so the authors concluded that the primary benefit of oxygen in the shielding gas was the generation of CO.

Adding oxygen to the shielding gas is another strategy for reducing keyhole porosity. However, carbon must be present in the base metal at appropriate quantities. In the previously discussed study, carbon content was on the order of 0.16 wt. %. If, the carbon content is lower, the porosity suppressing effect of oxygen-rich shielding gas is lower [20]. This strategy also affects the composition of the final weld because carbon will be removed and oxygen will be added, so for welds with strict composition controls, oxygen-rich shielding gases are not applicable.

Sulphur content	Fibre laser welding (X-ray radiograph taken from top)
60 ppm	
150 ppm	
560 ppm	
770 ppm	
1010 ppm	
1500 ppm	
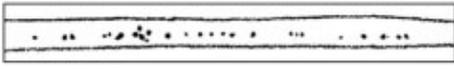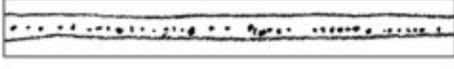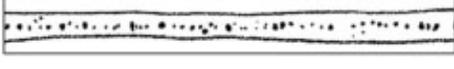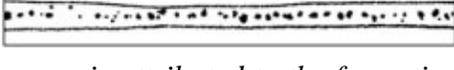
Figure 30: The low porosity from oxygen is attributed to the formation of CO, not the reduction in surface tension that would be similar to adding S to the weld [20].

2.3.6 Welding with a Laser and an Arc

When an arc, with or without a consumable electrode, is added to the laser weld, a hybrid laser-arc process is created. Several researchers have investigated the effect of hybrid welding on keyhole porosity with mixed results [20,43]. Zhao et al. [20] used a fiber laser and a pulsed arc with a consumable electrode on plain carbon steel. They found a noticeable increase in porosity during hybrid laser-arc welding compared to laser welding. Power modulation of the laser did not improve the porosity during hybrid welding, however, oxygen in the shielding gas did reduce the porosity amount. The researchers attributed the higher porosity to the pulsed arc, which dominated the weld pool oscillation and could not be compensated with the laser power modulation.

Katayama et al. [43] investigated the use of a non-consumable electrode arc (e.g. gas tungsten arc, GTA) during hybrid laser-arc welding of 304 stainless steel. Arc current was varied from 0 (laser weld) to 200 A. At 0 A and 100 A, severe porosity was observed. Porosity was eliminated with an arc current of 200 A. The reduction in porosity was attributed to lower formation frequency of bubbles in the molten pool as observed in X-ray videography. While evidence of reduced porosity during hybrid welding is mixed, parameter sets exist for very low

porosity in hybrid welds. For example, Zhang et al. [44] optimized a low alloy steel hybrid welding process with a consumable electrode. They found that of the sampled parameters, the highest laser power, lowest welding speed, and the greatest positive beam defocus produced the welds with the least porosity. These parameters contrast sharply with the trends presented earlier in the chapter, namely increasing power and decreasing welding are expected to produce more porosity, according to Kawihito et al. [25,26]. Studies by other authors show that positive defocus increases porosity during laser welding [30].

Hybrid welding has a number of advantages for thick section, large component fabrication, such as large gap-bridging and deep penetration. And, the process can be optimized for low keyhole porosity, however, the mechanism is not well understood and may vary based on whether the electrode is consumable. In addition, the trends in process parameters for reducing porosity are opposite the trends observed in laser welding. If these mechanisms are understood, the process does not suffer from some of the downsides of the other porosity reduction techniques, such as alloy impurity contamination and expensive additional capital equipment.

2.4 Summary of Keyhole Porosity

The origin and heat and pressure balances governing the geometry of the keyhole have been discussed. The inherent instability of the keyhole has been presented through previous research and the calculation of the pressure balance of a known keyhole geometry under three different conditions, including normal, low ambient pressure, and low surface tension. From a review of the literature, techniques for reducing porosity have been reviewed, and the mechanism for low porosity has been identified for each technique. Table 2 is a review of the techniques with the advantages, disadvantages, and porosity reduction mechanism included.

Table 2: The strategies for reducing porosity are listed with the advantages, disadvantages, and mechanism of porosity reduction.

Porosity Reduction Strategy	Advantages	Disadvantages	Pressure Balance Mechanism
Laser Power	easily adjustable	low porosity associated with low power, which lowers penetration and productivtiy	unknown, higher powers restrict the effectiveness of faster weld speeds
Welding Speed	easily adjustable	low porosity associated with high speed, which lowers penetration and productivtiy	elongation of the keyhole, reduction in P_s
Power Modulation	easily adjustable	frequency, duty cycle, peak power, min power, and waveform become variables, mechanism not well understood	unknown, probably related to constantly growing/shrinking keyhole, e.g. no steady-state pressure balance established
Low Ambient Pressure	virtually no porosity below 4 mbar ambient	vacuum chamber required, limited processing volume for large components	low P_0
Nitrogen-Rich Shielding Gas	easily implementable	weld metal may pick up N	low P_s
Oxygen-Rich Shielding Gas	easily implementable	alloy must contain C, weld metal may pick up O	low P_s and addition of P_{gas}
Hybrid Laser-Arc Process	easily implementable	mechanism unknown, does not fit the existing mechanism framework	unknown, probably not related to pressure balance

2.5 Root Defect Characteristics and Origin

In partial penetration welds, keyhole porosity is a common defect. However, in full penetration welds, where the keyhole and weld pool extend through the thickness of the plate and melting occurs on the bottom of the plate, very small amounts of keyhole porosity, if any, are typically observed. While keyhole porosity is uncommon, full penetration welding introduces defects along the root of the weld, which are not present in partial penetration welds. These types of defects are shown in Figure 31. Large bulges form at the bottom surface and solidify as the heat source passes. These large bulges remove metal from the joint, reducing weld strength and producing a rejectable defect. The defects are typically found during welding of thick plates. For example, in Figure 31 a and b [45,46], the plate thicknesses are 6 and 16 mm, respectively.

In practice these defects are mostly observed after the weld is complete. However, some research has attempted to observe this dynamic process of defect origination and evolution, using high speed videography. During laser welding of 8 mm thick 304 stainless steel, Ilar et al. [47]

(a)

(b)

Figure 31: Examples of (a) a root defect on the root side of a weld [45] and (b) a transverse cross-section of a weld with a root defect [46].

used a high speed camera, mirror, and laser illumination to image the bottom of the weld from a side angle. Images captured every 2 ms for a total of 16 ms are shown in Figure 32. The laser is moving left to right and travels 0.1 mm between frames. The white square markers are 1 mm in length. While a bulge in the liquid metal is present for the first 12 ms, solidification does not start until 14 or 16 ms. The bulge does not form at the keyhole exit but appears to start one-half to two-thirds back along the length of the weld pool.
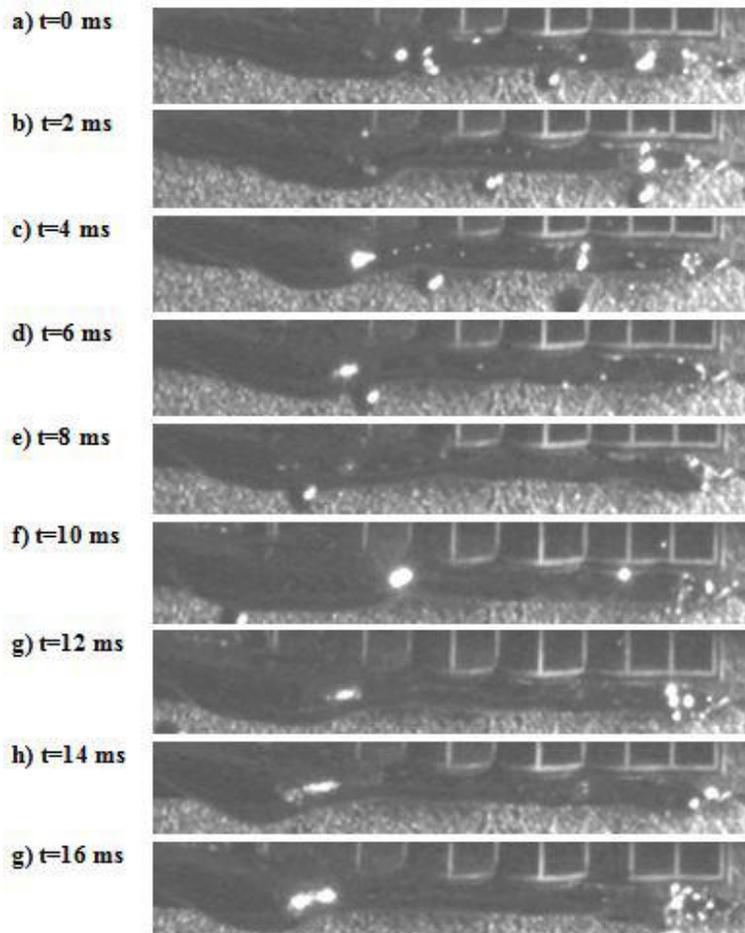
Figure 32: A frame from a high speed video experiment of hybrid laser-arc welding of structural steel. Two bulges can be observed and will eventually form root defects [47].

Frostevarg and Haeussermann [48] published the results of a high speed imaging experiment during hybrid laser-arc welding of structural steel. The researchers used a mirror to image the bottom surface, where the laser was traveling from right to left. Figure 33 shows a frame from one of the videos. Clearly, the dynamics are different during hybrid laser-arc welding compared to laser welding. Besides the large "hose" of liquid metal extending from the pool near the keyhole, the image clearly shows that the pool solidifies between globules, which solidify later. This solidified melt channel and cooling droplet are highlighted in the figure. Since multiple
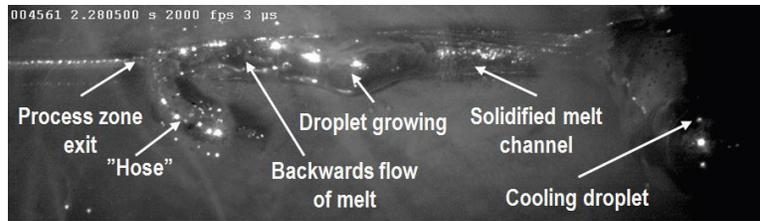
Figure 33: Frame from high speed imaging of laser weld shows the origin and evolution of root defects [48].

frames are not available, it is unclear where the droplet started or if the growing droplet in the figure will grow and be pinched off from the rest of the pool.

2.6 Root Defect Modes and Formation Modeling

From high speed imaging experiments and welding trials, where laser power and travel speed are varied, the effect of laser power is understood to a certain extent. Frostevarg [49] lays out the effect of increasing laser power in Figure 34, which shows schematics of the weld pool and final morphology as the laser power increases. At the lowest heat input, only partial penetration occurs, the bottom of the plate never melts, and there is no chance of root defects forming. With
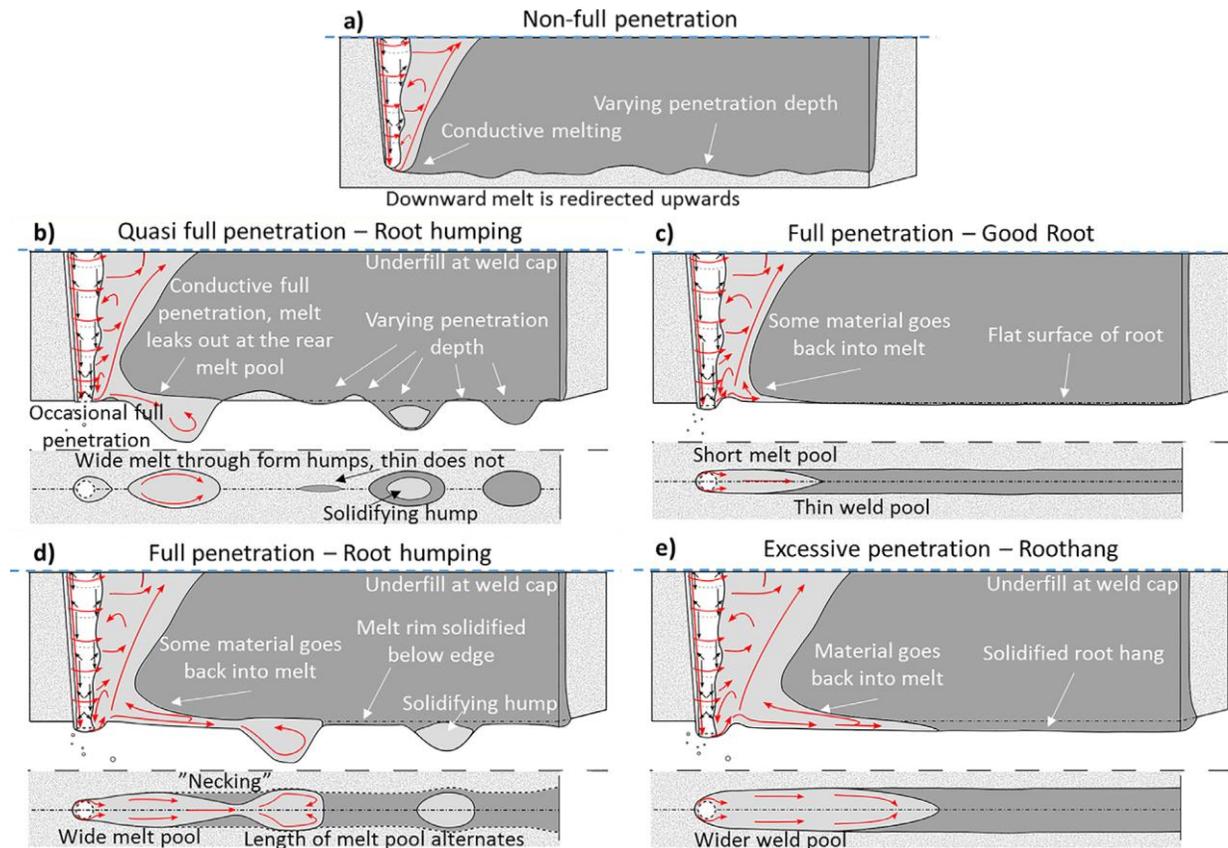
Figure 34: The varied morphologies of weld roots with increasing laser power [49].

48

increasing power, the bottom of the plate will sporadically melt (e.g. consistent full penetration is not achieved) and root defects will form. At the third lowest power, a full penetration weld with a defect-free root is formed. When the second highest power is used, root defects form with consistent penetration. At the highest power, root defects cease to form, but the root sags excessively, resulting in another form of root defects, which would disqualify the weld.

Some attention has been paid to the theoretical modeling of the formation of root defects. Most of the work has been carried out to evaluate the effectiveness of electromagnetic support of the liquid metal [50-52]. These models considered heat transfer and fluid flow to calculate the temperature and fluid velocity fields and then used these data to compute the variables related to root defects. In the formulation considered by previous researchers, the formation of root defects depends on the competition of two forces, liquid metal weight and surface tension, expressed in units of pressure. The weight force can be expressed as

$$p_w(z) = \rho g_0 (h - z) \tag{9}$$

where ρ is liquid metal density, g_0 is acceleration due to gravity, h is plate thickness, and z is the distance from the bottom of the plate. The variables h, g_0, and z are shown schematically in Figure 35, which depicts the root defect in a transverse cross-section. The surface tension force is calculated as

$$p_s = 2\gamma\kappa = \gamma\left(\frac{1}{R_x} + \frac{1}{R_y}\right) \tag{10}$$

where γ is surface tension of the liquid metal, and κ is the curvature of the liquid metal bulge at the bottom of the pool. The product 2κ can be expressed as the sum of the reciprocals of the radii of curvature in the x and y axes. With this force balance, the importance of alloy and plate thickness selection is clear. Less dense alloys with high surface tensions (i.e. low alloy and impurity content) are less likely to form root defects, and thinner plates are better than thicker plates. The curvature of the weld pool at the root depends on the combination of welding parameters and thermophysical properties of the alloy, but selection of those parameters and properties should produce a narrow, shortened bottom pool surface to lower the chance of forming root defects.
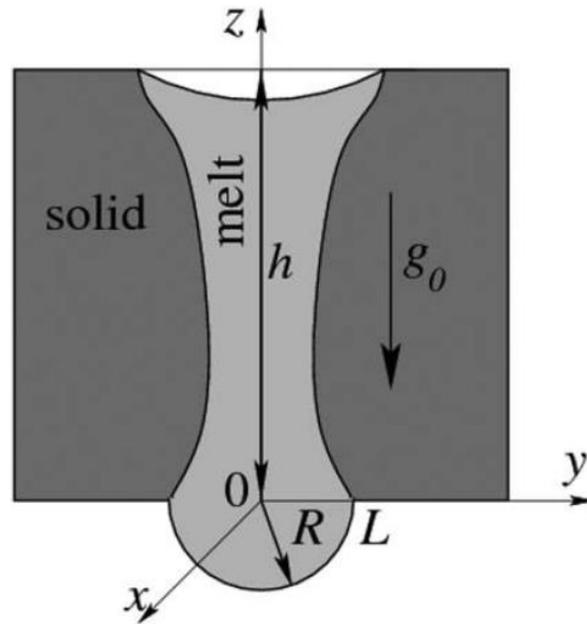
Figure 35: Diagram [50] of the important parameters affecting root defect formation during full penetration laser welds.

The previous research was only interested in single values of the weight force and surface tension force because a single electromagnetic force value had to be selected. But, during welding, there is a spatially varying 3D temperature field, and the competing forces are affected by that field via the temperature dependent variables density and surface tension. With an increasing temperature in the absence of any surface active species, the surface tension and density will decrease in a linear manner, complicating the simple picture shown in Figure 35. In theory, the force balance will vary with position at the bottom of the weld pool. In addition, other forces could be considered such as recoil pressure from evaporation, hydrodynamic forces due to fluid flow, and electromagnetic force in the case of hybrid laser-arc welding. None of these forces has been considered in previous research. In the case of recoil pressure and hydrodynamic forces, these forces would affect both sides of the force balance. For example, a recoil force can be calculated at both the bottom and the top surfaces of the weld pool, but presumably, the recoil force would be a net root defect promoter because the average surface temperature is higher at the top surface.

2.7 Root Defect Mitigation Strategies

While understanding the mechanism for root defect formation is important, the process engineer on the shop floor or in the field requires a tool box of mitigation strategies. The crudest method is to employ a backing plate, which can be fabricated from a variety of materials [53] and is fixtured or tack-welded to the joint prior to the weld as shown in Figure 36. This backing plate keeps the liquid metal from falling from the molten pool if the material and design are properly selected [53]. However, if the backing plate geometry is not designed well, the weld metal might spill from the bottom and solidify on the bottom surface without a metallurgical bond. In this case, a crevice between the weld metal and plate forms and creates a crack initiation feature [53]. The strategies that follow are better alternatives with varying difficulty in implementation.
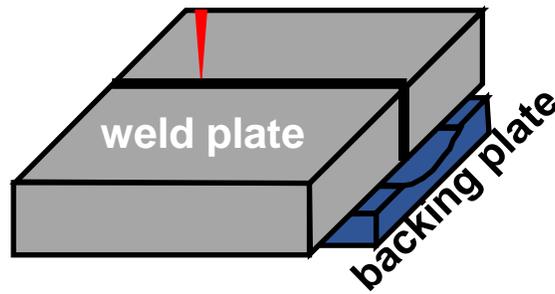
Figure 36: A backing plate below a welding plate produces the easiest solution to root defect formation. The backing plate keeps the weld metal attached to the weld bead. Adapted from [53].

2.7.1 Process Parameter Selection

The primary variable most proven to reduce defects is welding speed, which, along with laser power, is one of the most straightforward parameters to change in many laser welding arrangements [49,50,54]. Zhang et al. [54] produced laser welds in 12 mm thick 304 stainless steel plates. Laser power remained constant at 10 kW, and weld speed varied from 10 to 45 mm/s. The seven welds are shown in Figure 37. At the extreme low end of welding speed, clear root defects did not form, but significant sagging of the root was observed. At the maximum 45 mm/s, consistent full penetration was not achieved. Within the intermediate speeds, a clear transition was observed when the welding speed increased from 25 mm/s to 30 mm/s. At the lower speed, a very large defect formed with a width greater than the root width. When the weld speed increased, no large defects formed, except at the end of the weld, where a root bulge occurred in every other weld. With this power and speed combination, the resulting weld width at the top is only 2.0 mm, so tight fit up of the plates would be required during production. Increasing the weld speed produces a narrower weld pool, a greater potential curvature, and a higher retaining surface tension force.
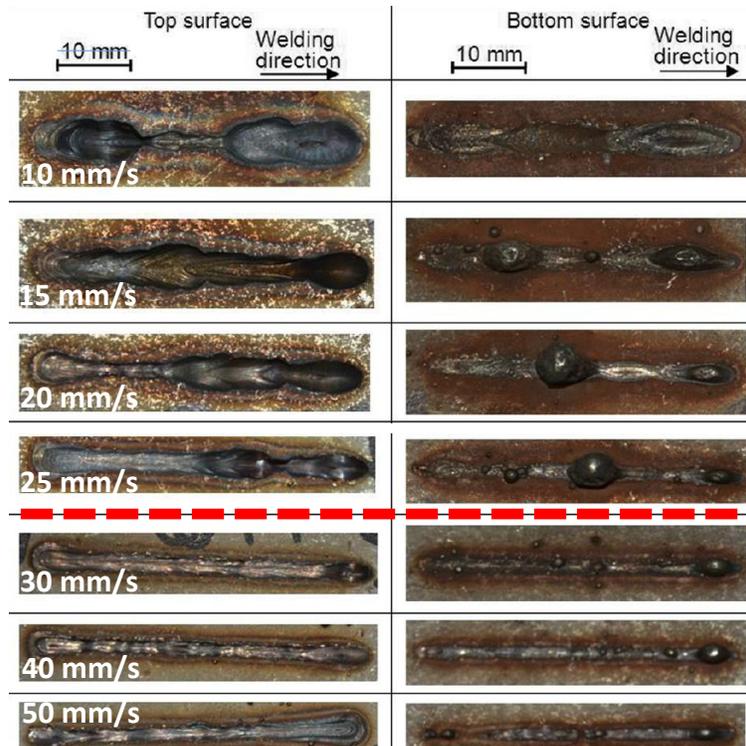
Figure 37: The effect of welding speed on the formation of root defects was investigated. A transition from root defects to defect free was observed after 25 mm/s [54].

Other laser and hybrid laser-arc welding experiments can be investigated from the perspective of linear heat input, i.e. not the adjustment of a single variable. Frostevarg tested 26 combinations of heat input for laser and hybrid laser-arc welding by primarily varying the laser power, although weld speed and plate gap width were also modified slightly between some welds [49]. The welds joined 12 mm thick structural steel plates, and the hybrid welds employed a matching filler metal. For all the parameter combinations that produced some penetration, the different morphologies were recorded and sorted into the categories shown in Figure 34.

The heat inputs defined as the total laser and arc power input divided by the weld speed are plotted in Figure 38, along with the characterization of the root condition. The heat inputs observed in this experiment vary from 270 J/mm for one of the partial penetration welds to 1000 J/mm, which formed a sagging or hanging root. The two parameter sets that produce defect free welds have heat inputs of 300 and 330 J/mm, which are the 2nd lowest and 3rd lowest heat inputs of all the welds that produced full penetration. Another important feature is the small range over which the different root morphologies occur during laser welding. Varying heat input from 280 J/mm to 380 J/mm produces a wide range of root conditions. This process window is very small for critical, structural joints and complicated by the fact that within this heat input range, partial penetration welds are possible. Figure 38 captures the difficulty in producing defect free full
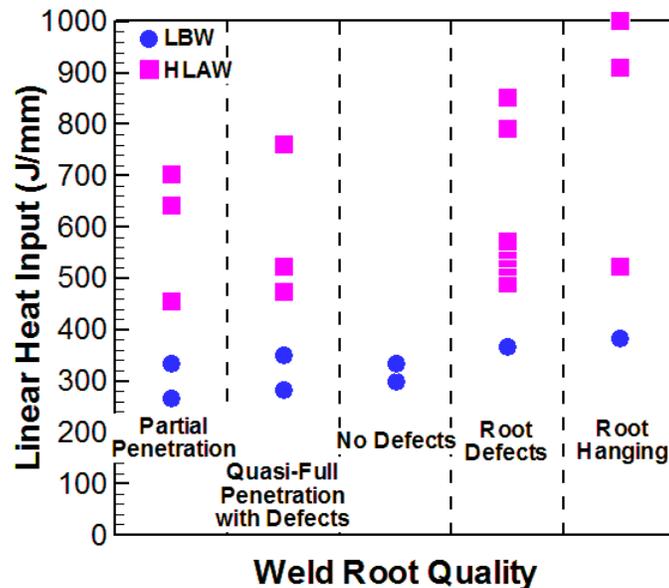
Figure 38: The heat input and root characteristic data from [49] are plotted to show that root defects are a high heat input defect.

penetration welds (hybrid welding produce zero acceptable welds) and explains why researchers have looked to strategies beyond parameter optimization.

2.7.2 Re-melting Weld Roots

The process window for defect free weld roots is very narrow, and parameter optimization may not be an attractive or necessary option. So, repair or prevention by methods other than a backing plate are attractive. Repair of the weld root and defects after welding is a possible option if the weld root is accessible. One solution for repair is to use the same process laser, but defocused, to re-melt the weld root and defects, producing a smoother surface, similar to an initially defect free weld root. This solution was explored by Frostevarg et al. and Powell et al. [55,56] during hybrid-laser arc welding of 12 mm thick structural steel plates. The welds were fabricated normally, and then the weld roots were re-melted (or re-welded) with same laser beam defocused 45 mm from the plate, while the power was maintained at 9 kW. This defocus enlarged the beam from 0.4 mm during welding to 5.0 mm for the re-melting. Examples of the starting and ending roots are shown in Figure 39. The remelting clearly flattens the root, significantly reducing any bulges. This technique shows promise for reducing defects, however it can only be employed in very particular circumstances where the root is accessible and the weldment can be manipulated so the root can be welded. In a situation where the component is very large, manipulation may not possible, or in the case of welding of smaller diameter tubing or piping, the root may not be reachable. Another complication is the metal lost to the defect nuggets, reducing the thickness of
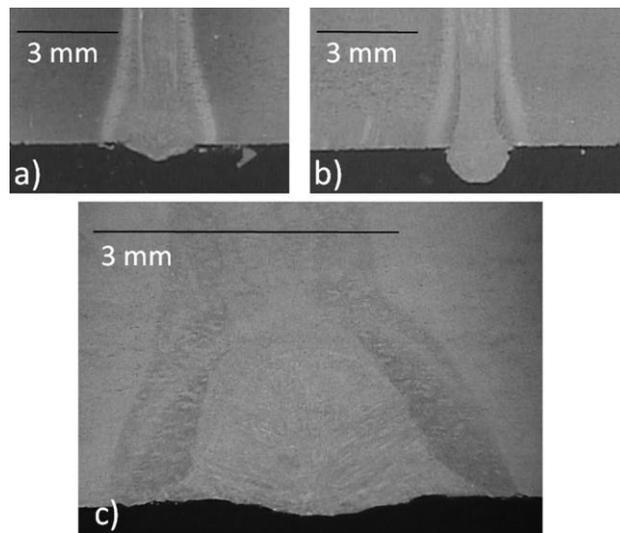
Figure 39: The variety of root morphologies is shown in a) and b). The re-melted root is shown in c) [56].
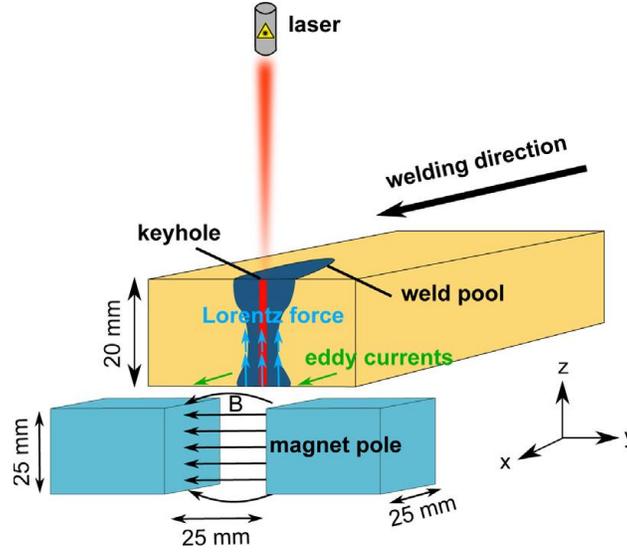
Figure 40: Schematic of the experimental setup to support the weld root with electromagnetic forces [52].

the joint (see Figure 31b). Since re-welding only melts the nuggets, the technique will not work if there is significant metal loss after the first weld.

2.7.3 Electromagnetic Root Support

Unlike the remelting of a defective weld root, another technique reduces the chances of root defects forming during welding by adding a second term to the root defect mitigation side of the force balance, described in equations 9 and 10. In this case, the weld root is supported by an electromagnetic force, which acts against gravity and in support of surface tension [50-52]. The technology has been employed in Al-Mg alloys and stainless steel with plate thicknesses up to 30 mm [50]. A schematic of the experimental setup is shown in Figure 40. Essentially, an electromagnet was placed below the plate, which is able to travel relative the stationary beam and keep the weld pool above the magnet. The electromagnetic force term in units of pressure is expressed as [50]

$$p_{EM}(z) = \frac{B_0^2}{4\mu_0} \exp\left(-2z\sqrt{\pi\mu_0 \sigma f}\right)$$

(11)

where B_0 is the amplitude of the AC magnetic field, μ_0 is the permeability constant, σ is the temperature dependent electrical conductivity of the liquid metal, and f is the AC frequency. The variables B_0 and f are not alloy dependent or constants and must be optimized for every welding setup. These values will vary based on alloy and plate thickness, however given the relationship

Alloy	Plate Thickness (mm)	B_0 (mT)	f (Hz)	Ref.
AlMg3	20	77	459	46
AlMg3	30	98	452	46
304 S.S.	10	205	2500	48
304 S.S.	15	220	2650	48
304 S.S. + 1015 steel	20	234	2575	48

of $F_{EM} \propto B_0^2\sqrt{(f)}$, the magnetic field has a much stronger influence on the electromagnetic force. Example values of B_0 and f that successfully prevented root defects in experiments are shown in Table 3. As expected the aluminum alloy required less support than a combination of stainless steel and plain carbon steel. Unexpectedly, the variation in B_0 with plate thickness is greater in aluminum compared to steel, while the opposite is true for AC frequency. This complex behavior probably reflects the volumetric nature of the electromagnetic force and the effect of the alloy conductivity on decay of the force in the alloy.

The results of electromagnetic support applied to 10 mm thick 304 stainless steel plates is shown in Figure 41. With no magnetic field, large root defects form. As the field strength is increased to 165 mT, the defects become smaller and less metal is removed from the top of the weld. Under near optimal field strength of 208 mT, the weld root is nearly flat or maintains only
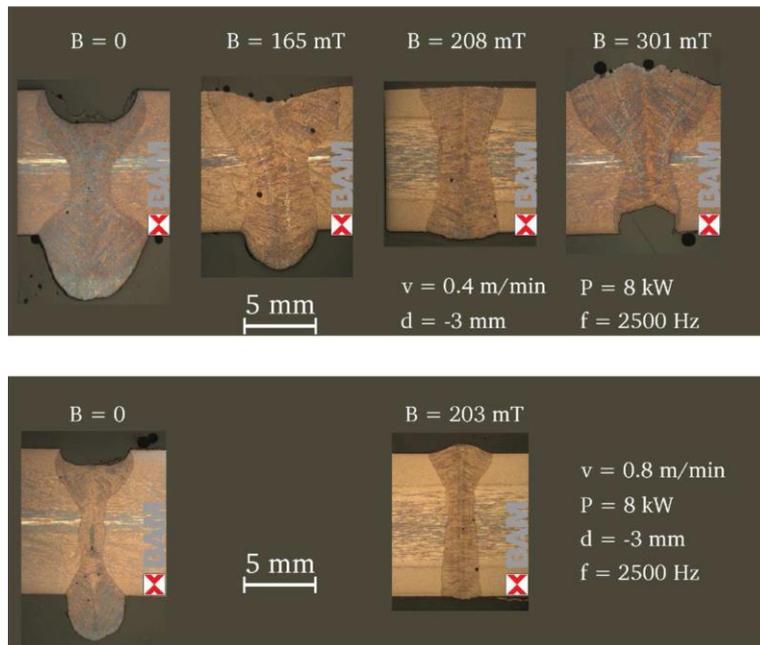
Figure 41: The weld roots under different magnetic field strengths [52].

a slight convexity. As the field strength increases, the weld metal starts to get pushed out of the weld with severe concavity at the root and a very large crown. Bachmann et al. [52] was able to model the process and predict the field strength necessary to keep the weld from forming root defects. The welds fabricated with an optimized electromagnetic force exhibit nearly flat roots, suggesting a surface tension force of near zero and that the electromagnetic force is the primary restraining force. While the technique is novel, the technology is not yet mature enough to deploy for high value welds in thicker plates. Even if the technology was mature, the technique requires more equipment and is limited to flat welding geometries. It is unclear if this technique would work with hybrid laser-arc welding.

2.8 Summary

Keyhole porosity in partial penetration welding and root defects during full penetration welds are common defects during laser and hybrid laser-arc welding. Both defects limit the deployment of high power lasers for thick section welding. In the case of keyhole porosity, intense study over many decades has illuminated many of the mechanisms and produced effective strategies to limit these defects. For many applications, defect free welds can be fabricated, but may require special equipment or introduce detrimental impurity elements. Some of the promising techniques, such as hybrid welding, have not been fully explored, and mechanisms remain poorly understood. While power modulation has long been identified as a porosity reduction technique, a method for selecting appropriate parameters, such as frequency, peak and minimum powers, and duty cycle, is not available. Mathematical modeling of the transient keyhole geometry may be the key to selecting the parameters because a growing keyhole is not expected to produce defects, so using a frequency that never allows the keyhole to reach a steady state depth may be an important factor.

Root defects, on the other hand, have only recently attracted the attention of researchers in the last decade due to the proliferation of less expensive, high power fiber lasers capable of joining thick metal plates. The surface tension and liquid metal weight force balance is mostly understood, however it has not been rigorously incorporated into a welding model to understand the experimentally observed trends with different processing parameters. Other potential forces, such as recoil pressure and hydrodynamic pressure, have not been considered at all. Given this progress, there is still debate on whether root defects are a low heat input or high heat input defect (i.e. the

57

effect of laser power and welding speed is not completely understood). The surface tension term of the force balance suggests a narrow pool (i.e. low heat input and small pool) will reduce the risk of forming root defects. The research shows that the processing window for defect free welds is very small with 5% to 17% off nominal heat inputs producing defects [49,54]. With such a narrow window, there needs to be clarity on whether increasing or decreasing heat input will lead to fewer root defects.

2.9 References

[1] Ribic, B., Palmer, T.A., and DebRoy, T. 2009. Problems and issues in laser-arc hybrid welding. *Int. Mater. Rev.* 54 (4): 223-244.

[2] Bagger, C. and Olsen, F.O. 2005. Review of laser hybrid welding. *J. Laser Appl.* 17 (1): 2-14.

[3] Assuncao, E., Williams, S., and Yapp, D. 2012. Interaction time and beam diameter effects on the conduction mode limit. *Opt. Lasers Eng.* 50 (6): 823-828.

[4] Kaplan, A. 1994. A model of deep penetration laser welding based on calculation of the keyhole profile. *J. Phys. D: Appl. Phys.* 27 (9): 1805-1814.

[5] Ki, H., Mohanty, S.M., and Mazumder, J. 2002. Multiple reflection and its influence on keyhole evolution. *J. Laser Appl.* 14 (1): 39-45.

[6] Solana, P. and Negro, G. 1997. A study of the effect of multiple reflections on the shape of the keyhole in the laser processing of materials. *J. Phys. D: Appl. Phys* 30 (23): 3216-3222.

[7] Jin, X. 2008. A three-dimensional model of multiple reflections for high-speed deep penetration laser welding based on an actual keyhole. *Opt. Laser Eng*. 46 (1): 83-93.

[8] Wang, H., Nakanishi, M., and Kawahito, Y. 2017. Effects of welding speed on absorption rate in partial and full penetration welding of stainless steel with high brightness and high power laser. *J. Mater. Process. Tech*. 249:193-201.

[9] Trapp, J., Rubenchik, A.M., Guss, G., Matthews, M.J. 2017. In situ absorptivity measurements of metallic powders during laser powder-bed fusion additive manufacturing. *Appl. Mater. Today*. 9 (12) 341-349.

[10] Kawahito, Y., Kinoshita, K., Matsumoto, N., Mizutani, M., and Katayama, S. 2008. Effect of weakly ionized plasma on penetration of stainless steel weld produced with ultra high power density fibre laser. *Sci. Technol. Weld. Joining* 13 (8): 749-753.

[11] Locke, E.V., Hoag, E.D., and Hella, R.A. 1972. Deep penetration welding with high-power CO_2 lasers. *IEEE J. Quantum Electron*. QE-8 (2): 132-135.

[12] Seto, N., Katayama, S., and Matsunawa, A. 2000. High-speed simultaneous observation of plasma and keyhole behavior during high power CO_2 laser welding: Effect of shielding gas on porosity. *J. Laser Appl.* 12 (6): 245-250.

[13] Kroos, J., Gratzke, U., and Simon, G. 1993. Towards a self-consistent model of the keyhole in penetration laser beam welding. *J. Phys. D: Appl. Phys.* 26 (3): 474-480.

[14] Rai. R, Elmer, J.W., Palmer, T.A., and DebRoy, T. 2007. Heat transfer and fluid flow during keyhole mode laser welding of tantalum, Ti-6Al-4V, 304L stainless steel and vanadium. *J. Phys. D: Appl. Phys.* 40 (18): 5753-5766.

[15] Volpp, J. and Vollertsen, F. 2016. Keyhole stability during laser welding – part I: modeling and evaluation. *Prod. Eng. Res. Develop.* 10 (4-5): 443-457.

[16] Matsunawa, A. and Semak, V. The simulation of front keyhole wall dynamics during laser welding. *J. Phys. D: Appl. Phys.* 30 (5): 798-809.

[17] Ki, H., Mohanty, P.S., and Mazumder, J. Modeling of laser keyhole welding: part I. mathematical modeling, numerical methodology, role of recoil pressure, multiple reflections, and free surface evolution. *Metall. Mater. Trans. A.* 33A (6): 1817-1830.

[18] Ribic, B., Tsukamoto, S., Rai, R., and DebRoy, T. 2011. Role of surface-active elements during keyhole-mode laser welding. *J. Phys. D: Appl. Phys.* 44 (48): 485203.

[19] Landau, L.D. and Lifshitz, E.M. 1972. Fluid Mechanics, 2nd Ed. Pergamon Press New York: 22.

[20] Zhao, L., Tsukamoto, S., Arakane, G., and Sugino, T. 2014. Prevention of porosity by oxygen addition in fibre laser and fibre laser-GMA hybrid welding. *Sci. Technol. Weld. Joining* 19 (2): 91-97.

[21] Collur, M.M., Paul, A., and DebRoy, T. 1987. Mechanism of alloying element vaporization during laser welding. *Metall. Trans. B.-Process Metall.* 18 (4): 733-740.

[22] Sahoo, P., Collur, M.M., and DebRoy, T. 1988. Effects of oxygen and sulfur on alloying element vaporization rates during laser welding. *Metall. Trans. B.-Process Metall.* 19 (6): 967-972.

[23] Zhao, H. and DebRoy, T. 2003. Macroporosity free aluminum alloy weldments through numerical simulation of keyhole mode laser welding. *J. Appl. Phys.* 93: 10089.

[24] Matsunawa, A., Kim, J.-D., Seto, N., Mizutani, M., and Katayama, S. 1998. Dynamics of keyhole and molten pool in laser welding. *J. Laser Appl.* 10 (6): 247-254.

[25] Kawahito, Y., Mizutani, M, and Katayama, S. 2009. High quality welding of stainless steel with 10 kW high power fibre laser. *Sci. Technol. Weld. Joining* 14 (4): 288-294.

[26] Kawahito, Y., Mizutani, M., and Katayama, S. 2007. Elucidation of high-power fibre laser welding phenomena of stainless steel and effect of factors on weld geometry. *J. Phys. D: Appl. Phys.* 40 (19): 5854 to 5859.

[27] Katayama, S., Kobayashi, Y., Mizutani, M., and Matsunawa, A. 2001. Effect of vacuum on penetration and defects in laser welding. *J. Laser Appl.* 13 (5): 187–192.

[28] Semak, V. and Matsunawa, A. 1997. The recoil pressure in energy balance during laser materials processing. *J. Phys. D: Appl. Phys.* 30 (18): 2541-2552.

[29] Gao, M., Kawahito, Y., and Kajii, S. 2017. Observation and understanding in laser welding of pure titanium at subatmospheric pressure. *Opt. Express*. 25 (12): 13539.

[30] Tucker, J.D., Nolan, T.K., Martin, A.J., and Young, G.A. 2012. Effect of travel speed and beam focus on porosity in Alloy 690 laser welds. *JOM*, 64 (12): 1409-1417.

[31] Kuo, T.-Y. 2005. Effects of pulsed and continuous Nd-YAG laser beam waves on welding of Inconel alloy. *Sci. Technol. Weld. Joining*. 10 (5): 557-565.

[32] Jiang, Z., Tao, W., Yu, K., Tan, C., Chen, Y., Li, L., and Li, Z. 2016. Comparative study on fiber laser welding of GH3535 superalloy in continuous and pulsed waves. *Mater. Des.* 110: 728-739.

[33] Blackburn, J.E., Allen, C.M., Hilton, P.A., Li, L., Hoque, M.I., and Khan, A.H. Modulated Nd : YAG laser welding of Ti-6Al-4V. *Sci. Technol. Weld. Joining*. 15 (5): 433-439.

[34] Elmer, J.W., Vaja, J., and Carlton, H.D. 2016. The effect of reduced pressure on keyhole weld porosity and weld geometry in commercially pure titanium and nickel. *Weld. J.* 95 (11): 419s-430s.

[35] Elmer, J.W., Vaja, J., Carlton, H.D., and Pong, R. 2015. The effect of Ar and N_2 shielding gas on laser weld porosity in steel, stainless steel, and nickel. *Weld. J.* 94 (10): 313s-325s.

[36] Sun. J, Nie, P., Lu, F., Huang, J., Feng, K., Li, Z., Guo, B., Jiang, E., and Zhang, W. 2017. The characteristics and reduction of porosity in high-power laser welds of thick AISI 304 plate. *Int. J. Adv. Manuf. Technol.* 93 (9-12): 3517-3530.

[37] Kuo, T.-Y. and Lin, Y.-D. 2007. Effects of different shielding gases and power waveforms on penetration characteristics and porosity formation in laser welding of Inconel 690 alloy. *Mater. Trans.* 48 (2): 219-226.

[38] Zhao, L., Tsukamoto, S., Arakane, G., Sugino, T., and DebRoy, T. 2011. Influence of oxygen on weld geometry in fibre laser and fibre-laser GMA hybrid welding. *Sci. Technol. Weld. Joining*. 16 (2): 166-173.

[39] Panwisawas, C., Perumal, B., Ward, R.M., Turner, N., Turner, R.P., Brooks, J.W., and Basoalto, H.C. 2017. Keyhole formation and thermal fluid flow-induced porosity during laser fusion welding in titanium alloys: experimental and modelling. *Acta Mater.* 126: 251-263.

[40] Moosavy, H.N., Aboutalebi, M.-R., Seyedein, S.H., Goodarzi, M., Khodabakhshi, M., Mapelli, C., and Barella, S. 2014. Modern fiber laser beam welding of the newly-designed precipitation-strengthened nickel-base superalloys. *Opt. Lasers Technol.* 57 (SI): 12-20.

[41] Kumar, A. and DebRoy, T. 2006. Toward a unified model to prevent humping defects in gas tungsten arc welding. *Weld. J.* 85 (12): 292s-304s.

[42] Sciaky Large Chamber EB Welding Systems. < http://www.sciaky.com/eb-welding-systems/large-chamber-systems>

[43] Katayama, S., Naito, Y., Uchiumi, S., and Mizutani, M. 2007. Laser-arc hybrid welding. *Solid State Phenom.* 127: 295-300.

[44] Zhang, Y., Chen, G., Mao, S., Zhou, C., and Chen, F. 2017. Optimization of hybrid laser arc welding of 42CrMo steel to suppress pore formation. *Appl. Phys. A*. 123 (6): 389.

[45] Salminen, A., Piili, H., and Purtonen, T. 2010. The characteristics of high power fibre laser welding. *Proc. Inst. Mech. Eng. C: J. Mech. Eng. Sci.*, 224 (C5): 1019-1029.

[46] Kaplan, A. and Wiklund, G. 2009. Advanced welding analysis methods applied to heavy section welding with 15 kW fibre laser. *Weld. World*. 53: 295-300.

[47] Ilar, T., Eriksson, I., Powell, J., and Kaplan, A. 2012. Root humping in laser welding – an investigation based on high speed imaging. 7th *Conf. Laser Assist. Net Shape Eng./Int. Conf. Photonic Eng.* eds. M. Schmidt, F. Vollertsen, and M. Geiger, pp. 27-32. Elsevier Sci.

[48] Frostevarg, J. and Haeussermann, T. 2015. Dropout formation in thick steel plates during laser welding. *IIW International Conference – High-Strength Materials – Challenges and Applications.* 2-3 July 2015, Helsinki, Finland.

[49] Frostevarg, J. 2018. Factors affecting weld root morphology in laser keyhole welding. *Opt. Lasers Eng.* 101: 89-98.

[50] Avilov, V. V., Gumenyuk, A., Lammers, M., and Rethmeier, M. 2012. PA position full penetration high power laser beam welding of up to 30 mm thick AlMg3 plates using electromagnetic weld pool support. *Sci. Technol. Weld. Joining* 17 (2): 128 to 133.

[51] Bachmann, M., Avilov, V., Gumenyuk, A., and Rethmeier, M. 2012. Numerical simulation of full penetration laser beam welding of thick aluminium plates with inductive support. *J. Phys. D: Appl. Phys* 45 (3): 035201.

[52] Bachmann, M., Avilov, V., Gumenyuk, A., and Rethmeier, M. 2014. Experimental and numerical investigation of an electromagnetic weld pool support system for high power laser beam welding of austenitic stainless steel. *J. Mater. Process. Technol.* 214 (3): 578-591

[53] Wahba, M., Mizutani, M., and Katayama, S. 2016. Single pass hybrid laser-arc welding of 25 mm thick square groove butt joints. *Mater. Des.* 97: 1-6.

[54] Zhang, M., Chen, G., Zhou, Y., and Liao, S. 2014. Optimization of deep penetration laser welding of thick stainless steel with a 10 kW fiber laser. *Mater. Des.* 53: 568-576.

[55] Powell, J., Ilar, T., Frostevarg, J., Torkamany, M.J., Na, S.-J., and Petring, D. 2015. Weld root instabilities in fiber laser welding. *J. Laser Appl.* 27 (S2): 9008.

[56] Frostevarg, J., Torkamany, M.J., Powell, J., and Kaplan, A.F.H. 2014. Improving weld quality by laser re-melting. *J. Laser Appl.* 26 (4): 41502.

Chapter 3 – Mapping Solidification during Laser Welding of Alloy 690

3.1 Solidification Related Welding Defects in Alloy 690

During conventional arc welding of Ni-Cr-Fe alloys, process-limiting defects, such as ductility dip cracking and solidification cracking, form primarily in the weld fusion zone. An example of a common solidification microstructure formed during multi-pass arc welding of Alloy 690 is shown Figure 42 [1]. Common characteristics of the fusion zone, such as solidification morphology and straight grain boundaries, can be observed. The primary solidification morphology is a mix of cells and very fine columnar dendrites. In the reheated regions, mostly straight grain boundaries are observed with less defined dendrites and cells.
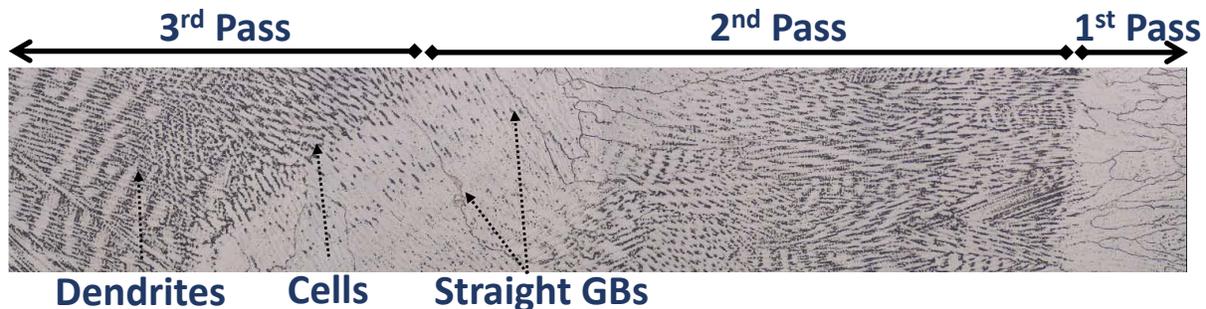
Figure 42: Conventional arc welded joint for thick sections of Alloy 690. The reheated second and first passes can be observed. Courtesy of EPRI [1].

During the solidification of the weld pool, grains tend to grow in the direction opposite of heat flow, which does not change dramatically (e.g. abrupt 90°), resulting in mostly straight grain boundaries. These straight grain boundaries, which become straighter in reheated region due to diffusion of segregated alloy elements, are one of the necessary conditions for ductility dip cracking (DDC). Reheating regions of straight grain boundaries below the melting point with successive weld passes results in the formation of stresses and grain boundary sliding that can lead to tiny ductility dip cracks at grain triple points. In addition to DDC, solidification cracking can occur with some welding wire compositions designed to prevent DDC by promoting the formation of tortuous grain boundaries, which are believed to limit DDC susceptibility.

Solidification cracking occurs when the remaining liquid in the mushy zone cannot accommodate the solidification and cooling strains [2]. Alloys with greater melting temperature ranges (i.e. the difference between liquidus and solidus temperatures) show a greater susceptibility to solidification cracking because the mushy zone is larger, resulting in a greater volume of the

weld that is susceptible to cracking [2]. There is also a wetted area effect, where the alloys that show lower wetted surface during solidification have a greater resistance to solidification cracking. By limiting the thin film of liquid separating grains, there are discrete areas of liquid globules that do not significantly affect the strength of the solid [2].

3.2 The Role of the Temperature Field on Solidification

Solidification characteristics are influenced by heat transfer and fluid flow and can be described quantitatively at a given position by the temperature gradient (G), solidification rate (R), cooling rate (GR), and morphology parameter (G/R) [2]. The relationship between G and R is shown in Figure 43 [2]. With G on the vertical axis and R on the horizontal axis, constant cooling rates (GR) are shown as G(R)=(cooling rate)/R curves. Cooling rate affects the coarsening of solidification structures, with lower cooling rates leading to coarser microstructures.
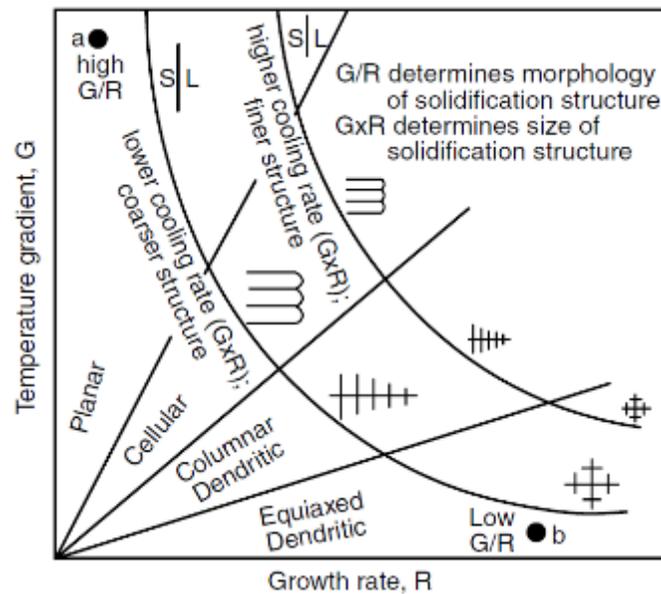
Figure 43: the solidification map shows the effects of G and R in the combined forms of cooling rate (GR) and the morphology parameter (G/R) [2].

The positive sloping lines in Figure 43 indicate constant G/R values and generally mark the boundaries between the solidification morphologies. At the onset of solidification for a very short time, planar structures predominate because G/R is very high, but soon after, instabilities on the solidification front and a relatively wide mushy zone lead to the breakdown of the planar front and the formation of cells and columnar dendrites [2]. Cells form at higher values of G/R than columnar dendrites.   At the lowest values of G/R, equiaxed solidification is possible with nucleation and growth of small grains in the mushy zone. Under typical welding conditions,

including arc and laser welding, equiaxed dendrites only form due to heterogeneous nucleation in the presence of insoluble particles, such as TiB_2, with a melting temperature of 3488 K (pure) in 6000 series aluminum welds [2]. The solidification parameters, G and R, can be calculated directly with the temperatures in and around the weld pool. Similar to other weld characteristics, such as weld pool dimensions, these parameters are significantly influenced by the process parameters, such as laser power and welding speed.

Since most of the defects found in Alloy 690 welds occur in the fusion zone or reheated weld metal (i.e. a previous fusion zone), deployment of laser and hybrid laser-arc welding technology requires a quantitative understanding of solidification characteristics under these new circumstances. For example, a process engineer will need to understand the expected solidification differences between the different welding processes and the impact of those differences on defect formation.

The objective of this chapter[1] is to quantitatively understand the solidification characteristics of Ni-base Inconel® Alloy 690 under laser welding conditions. Several laser welds were fabricated and the resulting fusion zone characterized in terms of solidification structure and scale. In order to produce a range of solidification structures without the complications of a spatially varying alloy composition, autogenous laser welds were fabricated in plates of alloy 690. With the calculated temperature fields from a three-dimensional heat transfer and fluid flow model, which is validated by comparing the fusion zone shapes and sizes, the solidification parameters are calculated for a range of laser welding conditions. The cell and dendrite arm spacings in experimental laser welds are correlated to calculated cooling rates. The general morphology (cell or dendrite) at various positions in the welds was also correlated to calculated morphology parameters. The results of this research were combined into a solidification map describing the scale and morphology of the solidification structure produced under varying temperature gradients and solidification rates.

---

[1]Portions of this chapter are directly excerpted from J.J. Blecher, T.A. Palmer, and T. DebRoy, 'Solidification Map of a Ni-base Alloy', Met. Mater. Trans. A, **45A**, 2014, 2142-2151.

3.3 Experiments and Model Development

3.3.1 Laser Welding Parameters Development

Autogenous bead on plate welds were made on 12.7 mm thick Inconel® Alloy 690 plate with an IPG Photonics® YLR-12000-L ytterbium fiber laser. The 1070 to 1080 nm wavelength laser light was delivered to the YW50 Precitec® welding head by a 200 μm process fiber. The transmissive optics included a 200 mm focal length collimating lens to provide a constant beam size to the 200 mm focal length focusing lenses. The welding head was attached to a multi-axis gantry robot for lateral movement of the beam. Plates were mechanically fastened to a workbench before welding.

Beam characterization was performed with a PRIMES® Focus Monitor and confirmed a 200 mm focus length from the welding head reference, a 300 μm beam diameter at focus, and a divergence angle of 150 mrad. The focus plane of the laser beam was positioned at the surface of the workpiece with no offset. Laser power was varied between 1.0 kW and 5.6 kW, and travel speed was held constant at 34 mm/s. As power progresses to above 4.7 kW, the welding process starts transitioning to cutting as shown at 5.6 kW.

Standard metallographic techniques were used to prepare transverse sections of the laser welds. Electrolytic etching between 4 and 8 V in 10 wt.% oxalic acid for several seconds revealed the microstructure of the fusion zone and base metal. A Nikon® Epiphot microscope was used to image the microstructures at various magnifications, and a Nikon® DS-Fi2 camera and Nikon® NIS Elements software were used to capture micrographs. Series of 10 to 30 images at the same magnification were stitched together using Adobe® Photoshop CS5 to provide full images of the fusion zones with a high resolution for the correlation of solidification morphology with solidification parameters GR and G/R.
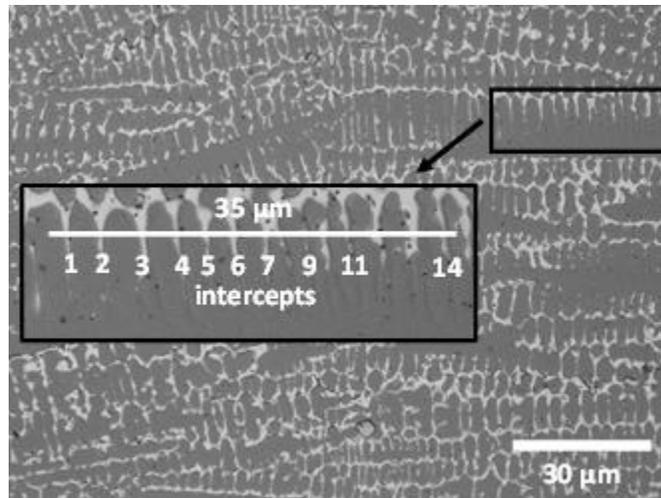
Figure 44: The linear intercept method for measuring dendrite arm spacings is illustrated

Dendrite arm spacing, cell spacing, and morphology area measurements were performed with ImageJ® software. The linear intercept method was used to measure the dendrite arm spacings and cell spacings. The method used to measure dendrite arm and cell spacings is shown in Figure 44. In this particular example, a 35 μm line is drawn across 15 dendrite arms, and the line crosses the interdendritic region 14 times. So, the measurement in this example yields a dendrite arm spacing measurement of 35 μm/14, or 2.5 μm. Four measurements per micrograph at a higher magnification were used to determine cell spacings for each location and corresponding cooling rate. If one cell spacing measurement fell outside one standard deviation from the mean, it was not included in the reported mean. The reported dendrite arm spacings are an average of three or more measurements in one 1000x magnification micrograph. Each dendrite used in the measurement had a minimum of seven arms.

3.3.2 Mathematical Modeling and Solidification Calculations

The molten pool sizes involved in this study are on the order of several millimeters in terms of weld width and depth, and the dendrite arm and cell spacings are only a few microns. Experimental temperature field measurements on this scale during welding are prohibitively difficult, and thermocouple measurements at several points would not provide the necessary resolution to accurately calculate location-specific temperature gradients and solidification rates, which control the solidification scale and morphology.   Other means of determining the temperature fields are, therefore, required. Physics based models, incorporating heat transfer and

fluid flow, commonly have been used to calculate these temperature and fluid flow velocity fields in a variety of welding conditions [3-9].

The three dimensional (3D) finite difference based heat transfer and fluid flow model used in this paper has been documented elsewhere in the literature [3-9]. The model can be broken down into two parts, calculation of the keyhole geometry followed by calculation of the velocity and temperature fields for the overall weldment. Calculation of the keyhole profile is done before the heat transfer and fluid flow calculations and is based on the method proposed by Kaplan [10], which performs a point by point heat balance at the keyhole wall. The profile and resulting heat flux at the keyhole wall are then incorporated into the heat transfer and fluid flow model as a heat source.

In the second part, the equations for the conservation of mass, momentum, and energy are solved for enthalpy and fluid velocity. The conservation of mass, or continuity, equation is

$$\frac{\partial(\rho u_i)}{\partial x_i} = 0 \tag{1}$$

where ρ is density, u_i is the velocity in the ith orthogonal direction ($i = 1, 2, 3$), and x_i is the length in the ith direction. The conservation of momentum equation is defined as

$$\rho\frac{\partial u_j}{\partial t} + \rho\frac{\partial(u_i u_j)}{\partial x_i} = \frac{\partial}{\partial x_i}\left(\mu\frac{\partial u_j}{\partial x_i}\right) + S_j \tag{2}$$

where t is time, μ is viscosity, u_j is the velocity in the jth direction, and S_j is the source term in the jth momentum equation. All of the modeling experiments described in this dissertation were conducted for a steady state, i.e. not transient or time varying, so the first term in equation 2 would not be considered. The momentum equation source term considers the pressure field, flow through the mushy zone, buoyancy driven flow, and the motion of the heat source relative to the workpiece and is defined as

$$S_j = -\frac{\partial p}{\partial x_j} + \frac{\partial}{\partial x_i}\left(\mu\frac{\partial u_i}{\partial x_j}\right) - C\left(\frac{(1-f_L)^2}{f_L^3 + B}\right)u_j + \rho g\beta(T - T_{ref}) - \rho U\frac{\partial u_j}{\partial x_1} \tag{3}$$

where p is pressure, C is a constant accounting for the morphology of the mushy zone, f_L is the fraction of liquid, B is a small constant to avoid division by zero, g is acceleration due to gravity,

β is the volume expansion coefficient, and U is the welding speed. The final governing equation is the energy equation and is defined as

$$\rho \frac{\partial h}{\partial t} + \rho \frac{\partial (u_i h)}{\partial x_i} = \frac{\partial}{\partial x_i}\left(\frac{k}{C_p}\frac{\partial h}{\partial x_i}\right) + S_h \tag{4}$$

where h is enthalpy, k is thermal conductivity, C_p is the specific heat, and S_h is the source term. The energy equation source term considers the latent heat and the welding velocity and is defined as

$$S_h = -\rho \frac{\partial (\Delta H)}{\partial t} - \rho \frac{\partial (u_i \Delta H)}{\partial x_i} - \rho U \frac{\partial h}{\partial x_1} - \rho U \frac{\partial \Delta H}{\partial x_1} \tag{5}$$

where ΔH is the latent heat. The total enthalpy, H, is $H = h + \Delta H$, where h is the sensible heat. In this way, the model incorporates the solid $\leftrightarrow$ liquid phase transition.
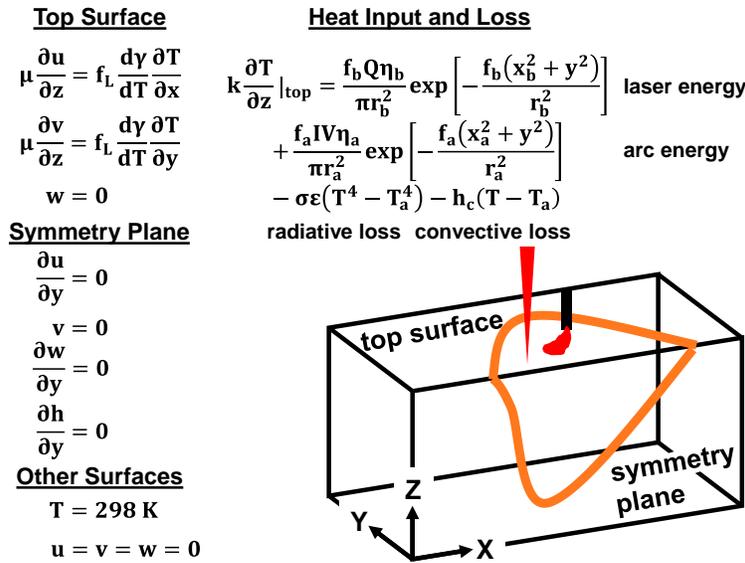
Figure 45: The boundary conditions for the solution of the governing equations are shown.

The boundary conditions for solution of the governing equations at each face of the computational domain are defined as shown in Figure 45. At the top surface, flow is driven by the differences in surface tension due to the temperature gradient, also known as the Marangoni effect. In these equations, u, v, and w are the x, y, and z components of velocity, and $d\gamma/dT$ is the temperature gradient of surface tension, which is a constant value for most alloys. All of the energy input and loss occurs at the top surface as well, as shown by the relevant section in Figure 45, where f_b and f_a are the laser and arc power distribution factors, respectively, Q is the laser power,

η_b and η_a are the laser absorption coefficient and arc efficiency, respectively, r_b and r_a are the laser beam radius and arc radius, respectively, x_b and x_a are the distances relative to the center of the laser beam and arc, respectively, I is the arc current, V is the arc voltage, σ is the Stefan-Boltzmann constant, ε is emissivity, h_c is the heat transfer coefficient, and T_a is the ambient temperature. The model only considers one-half of the weld due to symmetry. So, there is no heat or mass transfer across the symmetry plane, and the y-component of velocity, v, is set to zero. There are also no energy or velocity gradients across the symmetry plane. At the other four surfaces, the temperature is set to ambient, and the velocity is zero. The governing equations with the boundary conditions are solved using the tri-diagonal matrix algorithm (TDMA). The resulting temperature fields are used to determine the solidification parameters. The Alloy 690 material properties used for these calculations are shown in Table 4.

The heat transfer and fluid flow model has been extensively evaluated and validated for keyhole mode laser beam welding of a variety of materials, including aluminum, stainless steel, tantalum, titanium, vanadium, and structural steel alloys [3-5]. In addition to accurately predicting the experimental weld pool dimensions for various welding powers, speeds, and laser beam profiles, the model calculates temperature and velocity fields across the computational domain. This output from the heat transfer and fluid flow model can then be used to calculate the

Table 4: The material properties used for the heat transfer and fluid flow modeling is shown.

Material Property	Value	Reference
Absorptivity of liquid	0.313	[11]
Density of liquid at the melting point (kg/m3)	7500	[12]
Density of liquid at the boiling point (kg/m3)	6100	[12]
Viscosity of liquid (kg/m-s)	0.0051	[12]
Solidus temperature (K)	1616	[13]
Liquidus temperature (K)	1650	[13]
Enthalpy of solid at solidus (kJ/kg)	879	[14]
Enthalpy of liquid at liquidus (kJ/kg)	1200	[14]
Specific heat of solid (J/kg-K)	665	[14]
Specific heat of liquid (J/kg-K)	673	[14]
Thermal conductivity of solid (J/m-s-K)	33	[15]
Thermal conductivity of liquid (J/m-s-K)	46	[12]
Thermal conductivity of liquid at boiling point (J/m-s-K)	47	[12]
Coefficient of thermal expansion (1/K)	1.0 E-06	[12]
Temperature coefficient of surface tension (mN/m-K)	-0.37	[12]

solidification parameters G, R, GR, and G/R [4]. The combined forms of G and R include the cooling rate (GR) and the solidification morphology parameter (G/R).

The temperature gradient (G) and solidification growth rate (R) are calculated from the temperature field for every position along the solidification front, which is a three dimensional surface from which the two dimensional transverse cross-section is extracted. A few studies [16-19] have calculated the solidification parameters during conduction mode laser welding of single crystal Ni-base alloys. These studies concluded that the solidification parameters could be employed to accurately calculate the growth directions, and since the experiments were conducted on single crystals, only solidification in six discrete <100> directions is possible in a (100) oriented plate with a face centered cubic crystal structure. The major conclusions of these studies involved the formation of stray grains, which occur under some processing conditions and result in a non-single crystal weld. In this study, the workpiece is a polycrystalline metal, and one of the goals is to correlate solidification structure size to calculated cooling rates, not just computation of solidification direction. The model has also been employed to quantitatively study the solidification of austenitic stainless steels [20] and the effect of cooling rate on the primary solidification phase. The calculated and measured thermal cycles and cooling rates agreed, which allowed for the establishment of relations between cooling rates (1000 to 10000 K/s) and spacings of dendrites and dendrite arms.

In order to calculate G and R at each location along the solid-liquid boundary, the direction of heat flow at the liquidus temperature must be known. This direction is the gradient of the temperature field (∇T) and can be determined using:

$$\nabla T = \frac{\partial T}{\partial x} i + \frac{\partial T}{\partial y} j + \frac{\partial T}{\partial z} k \tag{6}$$

where T is temperature and i, j, and k are unit vectors in the x, y, and z directions, respectively. The heat flow direction at a certain position in space is expected to be normal to the three dimensional liquidus surface. The temperature gradient, G, which is simply the magnitude of the vector, is calculated using the relationship below:

$$G = \|\nabla T\| = \sqrt{\left(\frac{\partial T}{\partial x}\right)^2 + \left(\frac{\partial T}{\partial y}\right)^2 + \left(\frac{\partial T}{\partial z}\right)^2} \tag{7}$$
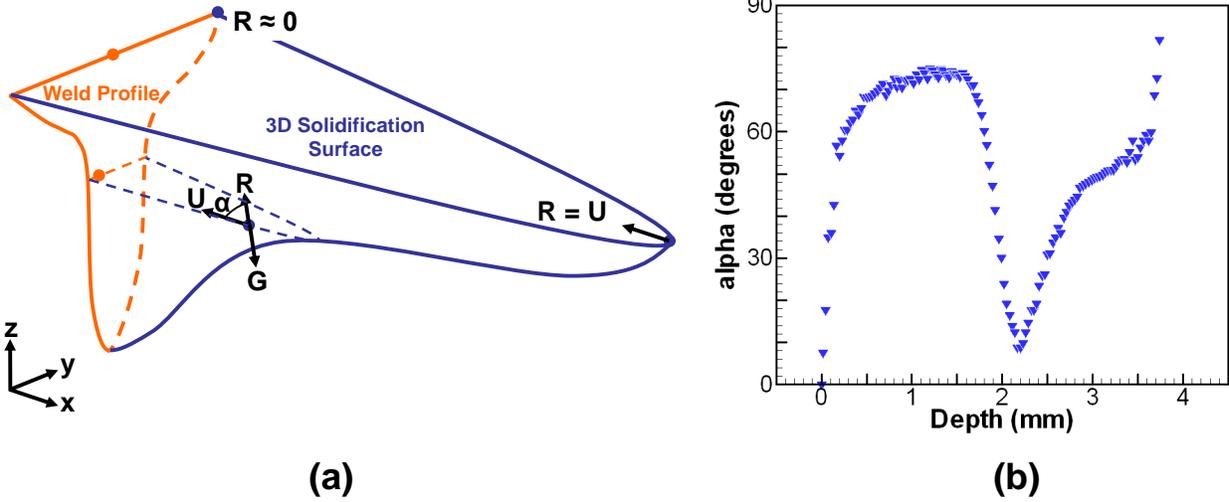
Figure 46: The 3D solidification surface and resulting weld profile, (a), and variation of the angle α with depth along the central longitudinal plane for a 2.8 kW weld, (b) are shown. Also shown is the relationship between the welding speed, U, and the solidification rate, R, and angle between the two vectors, α.

In Figure 46, the direction of G is shown relative to the 3D solidification surface, and the i,j,k components of G are used to determine the solidification direction (α) and solidification rate (R). The relationship between the solidification location in 3D and the location observed in the transverse weld section is also shown in Figure 46. This solidification direction is assumed to be aligned opposite to the heat transfer direction, as described in the relationship below:

$$\cos \alpha = \frac{-\frac{\partial T}{\partial x}}{\|\nabla T\|} \tag{8}$$

where α is the angle between the welding direction and solidification growth direction. In order for the assumption to be valid, the orientation of the easy growth direction, <100>, of the pre-existing grain must be parallel to the solidification direction. In polycrystalline materials with randomly oriented grains, this condition is not usually met. However, with mean grain sizes much smaller than the dimensions of the weld, competitive growth will quickly select the best orientation during solidification [2]. In general, the angle, α, varies across the weld from zero to almost 90°, and variation of α along the weld centerline of a laser weld is shown in Figure 46b. In this figure, the angle achieves a local maximum and minimum around the mid-depth of the weld.

The other primary solidification parameter, the solidification rate, R, is defined by the following relationship:

$$R = U \cos \alpha \tag{9}$$

where U is the welding speed. This equation contains two special simplifications for the top surface of the weld pool. Along the centerline at the end of the pool, the angle is zero, so the solidification rate is equal to the welding speed. At the maximum width of the pool, the solidification rate is near zero because the angle is 90°. Both of these cases are shown in Figure 46a. It should be noted that R is also a function of the angle between the easy growth direction of the grain and the welding direction. However, this angle, β, is typically neglected for the case of polycrystalline materials.

3.4 Weld Dimensions, Temperature Field Calculations, and Solidification Structures

3.4.1 Evaluating Effect of Power on Laser Weld Penetration

In order to provide validation for the modeling efforts, autogenous laser welds were made on Alloy 690 plates at travel speeds of 34 mm/s and powers ranging from 1.0 to 5.6 kW. The combination of laser power and welding speed resulted in the formation of a keyhole in each weld. The transverse weld profiles are shown in Figure 47. The wineglass shape of the fusion zone characteristic of keyhole mode welding is observable in all the welds. Maximum weld depths and widths varied from 2.0 to 5.5 mm and 1.5 to 3.5 mm, respectively, with all welds displaying an aspect ratio (depth/width) greater than 1, which is also a common feature of keyhole mode welds.
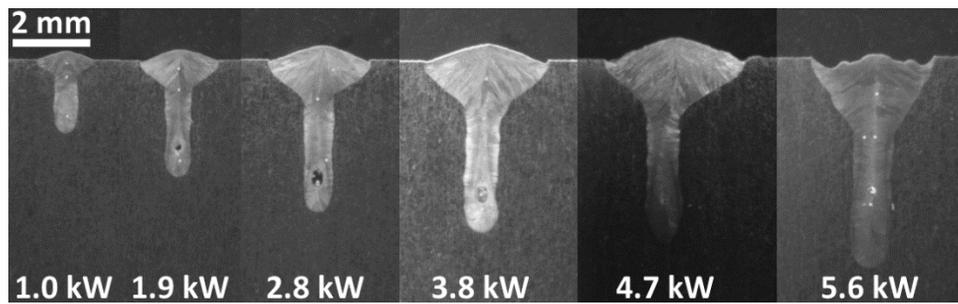
Figure 47: Lasers welds in Alloy 690 with increasing power.

Calculated temperature and fluid velocity fields are shown in Figure 48 for powers of 1.0, 2.8, and 4.7 kW. The boiling (3085 K), liquidus (1687 K), and solidus (1650 K) temperature
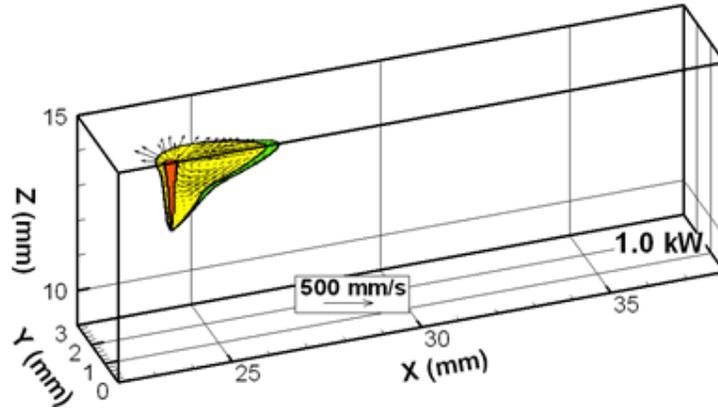
(a)
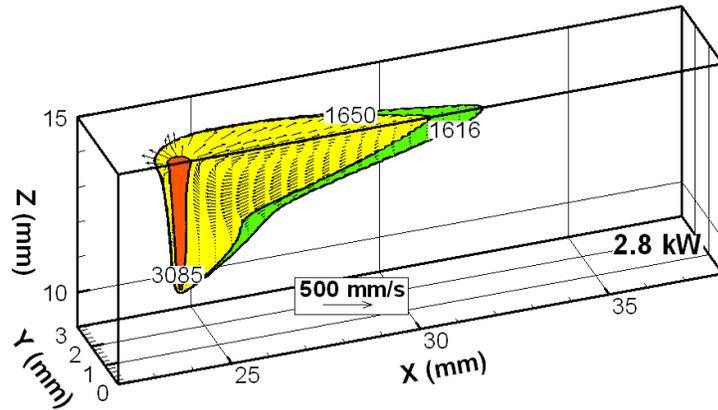
(b)
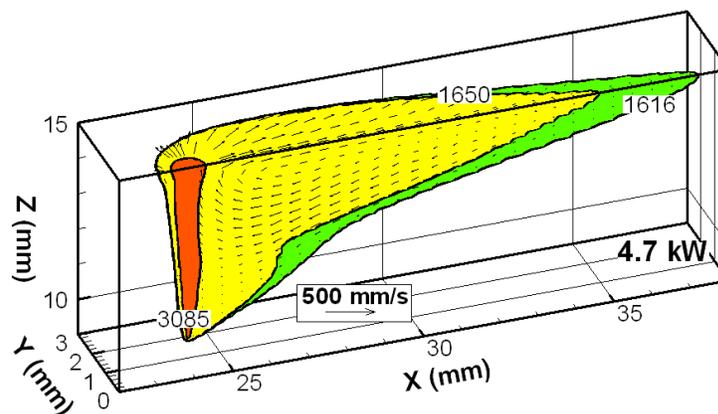
(c)

Figure 48: The calculated molten pool profiles during keyhole mode laser welding are shown at different laser powers, (a) 1.0 kW, (b) 2.8 kW, and (c) 4.7 kW. The boiling point, liquidus temperature, and solidus temperatures are 3085 K, 1650 K, and 1616 K, respectively.
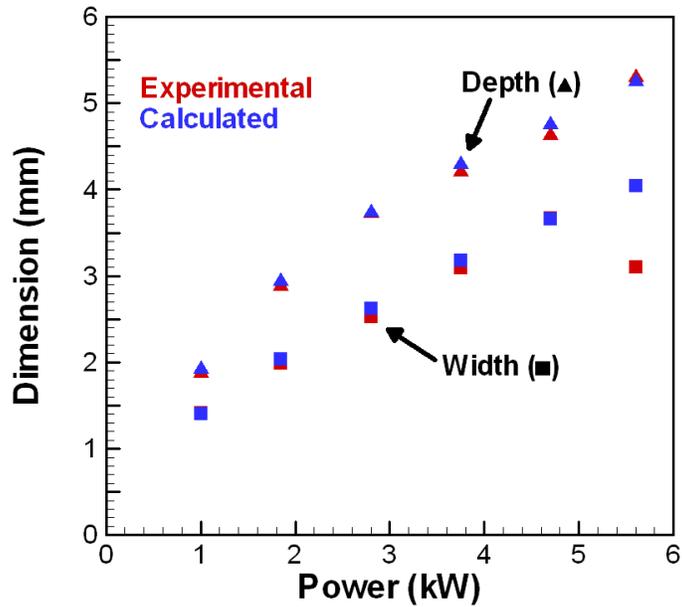
Figure 49: The calculated and experimental molten pool dimensions are shown as a function of laser power for a travel speed of 34 m/s. The experimental and calculated molten pool widths and depths show good agreement.

contours are plotted, allowing for the keyhole and molten pool sizes to be more easily identified. The characteristic high depth to width ratio of keyhole mode laser weld pools is observed as well as the Marangoni effect driven fluid flow, which drives molten metal to the edges of the pool. As expected, an increase in the laser power produces a larger pool overall. The width of the two phase mushy region also increases, which suggests different thermal cycles along the solidification front.

A comparison of the experimental and calculated weld pool dimensions is shown in Figure 49. Good agreement is observed between both sets of values, for laser powers up to 5.6 kW width. At powers exceeding 5.6 kW and up to 10.6 kW, significant liquid metal expulsion occurred,
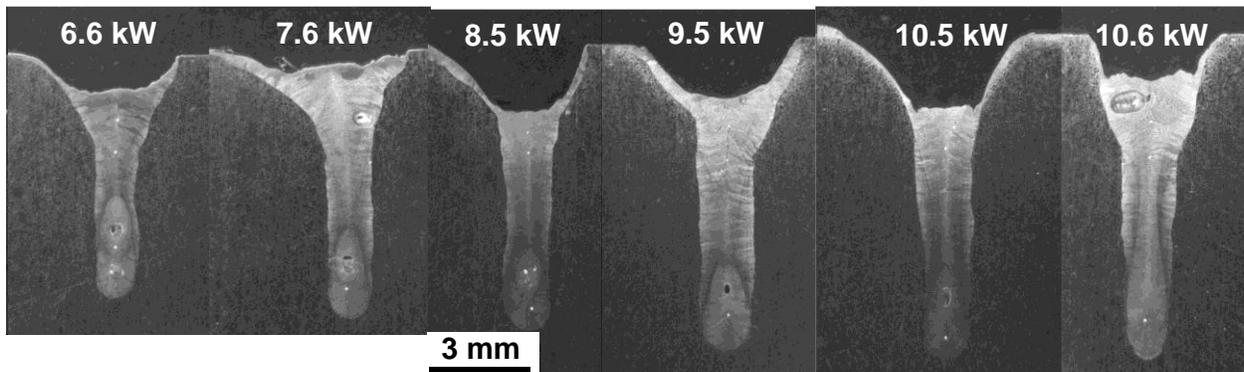
Figure 50: The transition from keyhole mode welding to drilling is observed at powers exceeding 6 kW.

76

indicating that the laser-material interaction mode may have transitioned from welding to a mixed welding/drilling mode, as shown in Figure 50. The heat transfer and fluid flow model assumes conservation of mass and energy, which is mostly met during keyhole mode welding with the exception of liquid metal evaporation that is too small to significantly affect the results. In the case of drilling, significant amounts of hot liquid metal is expelled from the molten pool. This expelled metal contains a significant amount of energy and mass that is unaccounted for in the current model, so the model cannot accurately calculate the temperature fields during drilling.

3.4.2 Fusion Zone Morphology and Scale

While understanding the effects of welding parameters on the general shape of the molten pool is important, all of the weld defects specific to Alloy 690 are found within the fusion zone. For example, ductility dip cracking has been tied to the final structure of the grains in the fusion zone. Grain boundary structure is influenced by the initial solidification morphology, which may provide some of the tortuousness necessary to avoid DDC. For instance, a fusion zone of mostly dendrites would have a more tortuous grain boundary structure compared to a weld with a mostly cellular fusion zone. Therefore, it is important to understand how the welding parameters influence the final solidification structure scale and morphology. The heat transfer and fluid flow model provides the 3D information across the fusion zone that can be used to determine features at a small enough scale to capture grain evolution.

Examination of the fusion zone microstructure revealed two distinct morphologies consisting of cells and columnar dendrites, which exist over a range of size scales. Figure 51 shows representative micrographs of cells and columnar dendrites at different locations in the transverse fusion zone of the autogenous laser weld produced with a laser power of 3.8 kW. The cells, shown in Figure 51c, are located near the root of the weld, where the relatively high cooling rates are experienced, with the cell spacing measured to be about 3 μm. At this location, cell growth occurs in a variety of directions, and the elongated cells reach lengths of 60 μm or more. On the other hand, columnar dendrites, shown in Figure 51b, are located near the center of the weld finger and are much coarser than the cells, with dendrite arm sizes of 4 to 5 μm. Well-developed columnar dendrites are observable in most of Figure 51b, while tertiary dendrites are observed in the region adjacent to the weld centerline.
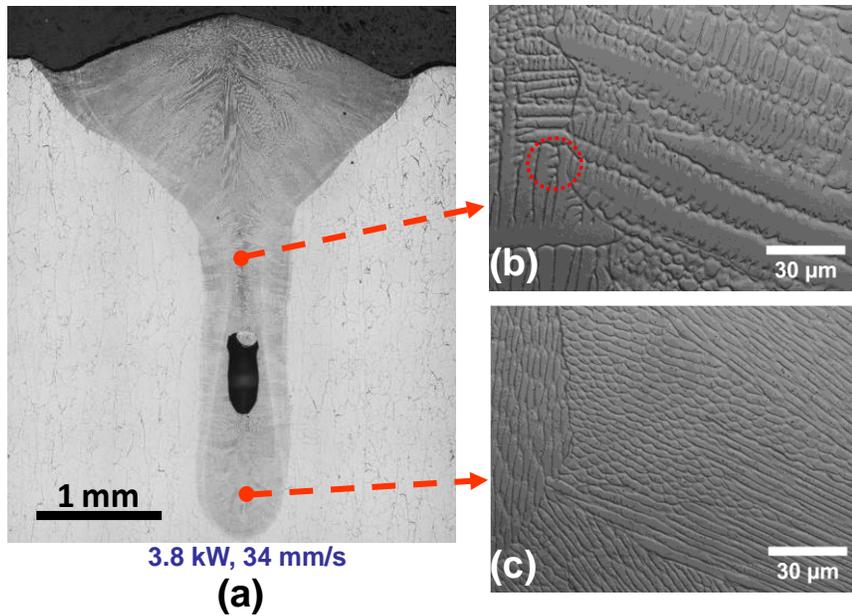
Figure 51: The fusion zone and local solidification morphologies and scales are shown for the laser weld fabricated with 3.8 kW laser power.

Cells and dendrites are observed in different sections of the weld because the different areas experience different solidification conditions. The G/R morphology parameter is relatively higher at locations where the cells are located at the bottom along the longitudinal center plane of the weld. For dendrites to form, the value of G is relatively lower, and that for R is relatively higher, making the morphology parameter G/R lower. The cooling rate differences are apparent in the microstructure shown in Figure 51. The cells in Figure 51c are much finer than the dendrites and dendrite arms in Figure 51b, indicating higher cooling rates at the bottom of the weld in Figure 51c compared to the middle.

A broader overview of the 2.8 kW weld fusion zone along with the calculated solidification direction is given in Figure 52. This smaller weld is chosen in order to show a higher level of solidification direction detail in the stitched image of the full fusion zone. Overall, the general wineglass shape of keyhole mode laser welds is observed as well as some porosity near the bottom of the weld due to keyhole instability. In terms of cell, dendrite, and grain orientation, the growth direction is a function of position in the weld. The calculated temperature gradient vectors, which determine solidification direction and final orientation of cells and dendrites, are shown as unit vectors, so that in three dimensions, the vectors have the same length and magnitude. Mathematically, the unit vectors are the fractional x, y, and z components after $\nabla T/G$. Small

vectors indicate significant growth in the x-direction, perpendicular to the page. In the middle part of the weld finger, mainly horizontal growth dominates. Outside of the middle of the weld finger, the solidification structures generally grow vertically towards the top surface of the workpiece. At the top of the weld, growth is at 45° to the horizontal, while at the weld root, growth is almost vertical. Qualitatively, the observed and calculated growth directions described in Figure 52 agree well, indicating that the experimental and calculated heat transfer directions are quite close.

The large variations in size and morphology of solidification structures across the fusion zone from the top of the weld to the bottom are illustrated in Figure 52a, b, and c, respectively. In
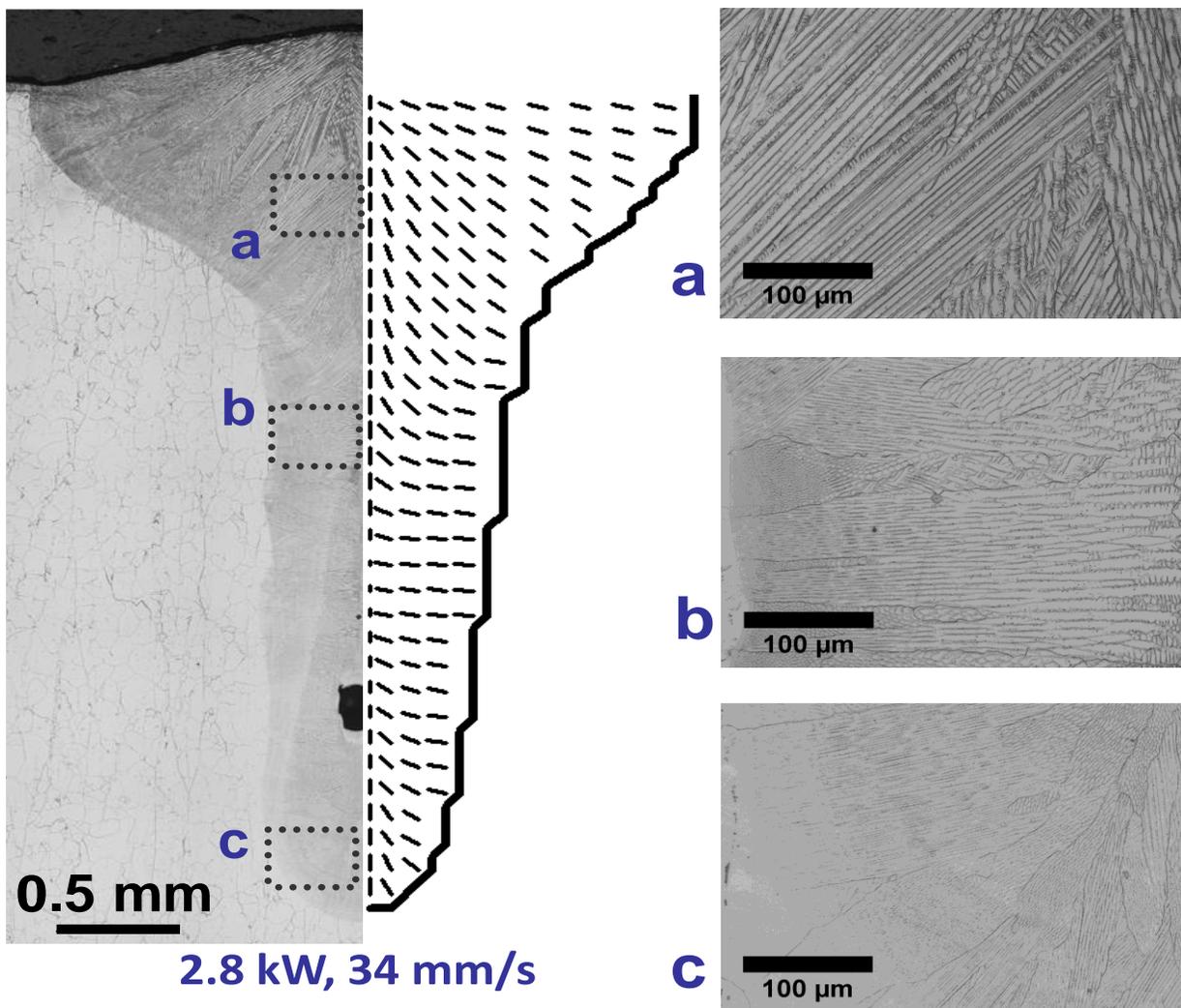
Figure 52: The scale, mode, and orientation of solidification varies across the transverse section of the 2.8 kW weld. In the general profile (left), the positions of (a), (b), and (c) are highlighted with rectangles. The calculated orientation of the solidifying cells, dendrites, and grains are shown at left based on the direction of heat flow at those positions.

Figure 52b, cells and dendrites exist together near the mid-depth of the weld. This spatial variation indicates that the morphology parameter G/R is decreasing across the weld pool width from the edge to the center. The growth orientation becomes steeper from the fusion line to the center of the weld. Figure 52c also shows both cells and dendrites at the weld root, but the variation in scale is clear. Individual cells are barely resolved at the fusion line, while relatively large dendrite arms are present at the centerline. This observation indicates that the cooling rate has decreased dramatically from the fusion line to the centerline. Compared to Figure 51a, which contained mostly cells and dendrites growing at angles greater than 45° from horizontal, significant horizontal columnar dendrite growth is shown in Figure 52b, near the mid-depth. Only fine cells growing in a nearly vertical direction are observed in Figure 52c at the root. This observation indicates relatively high values of GR and G/R are expected at this location.

While observation of the fusion zone indicates that G/R varied enough to produce cells and columnar dendrites, the variation only produced trivial or non-existent amounts of the other solidification morphologies, such as equiaxed dendrites and planar solidification. No equiaxed dendrites were observed in the fusion zones of any of the welds, and this observation is consistent with solidification in fusion welding processes, where equiaxed dendrites are only observed in the presence of grain refining particles [16,21]. A very thin section of planar solidification, 3 μm thick, is observable just at the edge of the fusion zone in Figure 52b. Unlike the other morphologies, a minimum G/R value for planar solidification can be estimated from known thermophysical values of the alloy [16] and is on the order of 7000 K-s/mm^2. So, based on experimental observations, G/R is at least 7000 K-s/mm^2 at the edge of the fusion zone, but at all other locations, the value is lower. It is not possible to predict G/R values for cells or dendrites in the same fashion. Some mixture of experiments and modeling is required.

3.4.3 Calculation of Solidification Characteristics during Laser Welding

Figure 53 illustrates the calculated variation of G and R as a function of depth along the liquidus contour in the central x-z plane in a 2.8 kW weld. The weld pool profile along the central longitudinal plane is shown as well in order to demonstrate how the shape of the solidification front affects the solidification parameters. The direction of heat transfer, which is aligned to the solidification direction, can be discerned by the slope of the liquidus contour (1650 K). A more vertical slope (i.e. the surface normal is closer aligned to the weld direction) produces a higher solidification rate. If the slope is close to zero, or the liquidus contour is nearly horizontal, the solidification rate is low. The magnitude of the temperature gradient (G) is qualitatively represented by how close the solidus and liquidus lines are to one another, or, alternatively, the width of the mushy zone. A larger mushy zone is associated with a lower temperature gradient.

In Figure 53, the slope of the liquidus contour and the width of the mushy zone decrease from the top to half the weld depth, which is represented by the increase in the temperature gradient and decrease in solidification rate. This behavior is typically observed in ellipsoidal weld pools produced by arcs and low intensity lasers [16,22]. However, due to the nature of the keyhole heat source, which extends through the depth of the weld pool, the liquidus contour becomes nearly
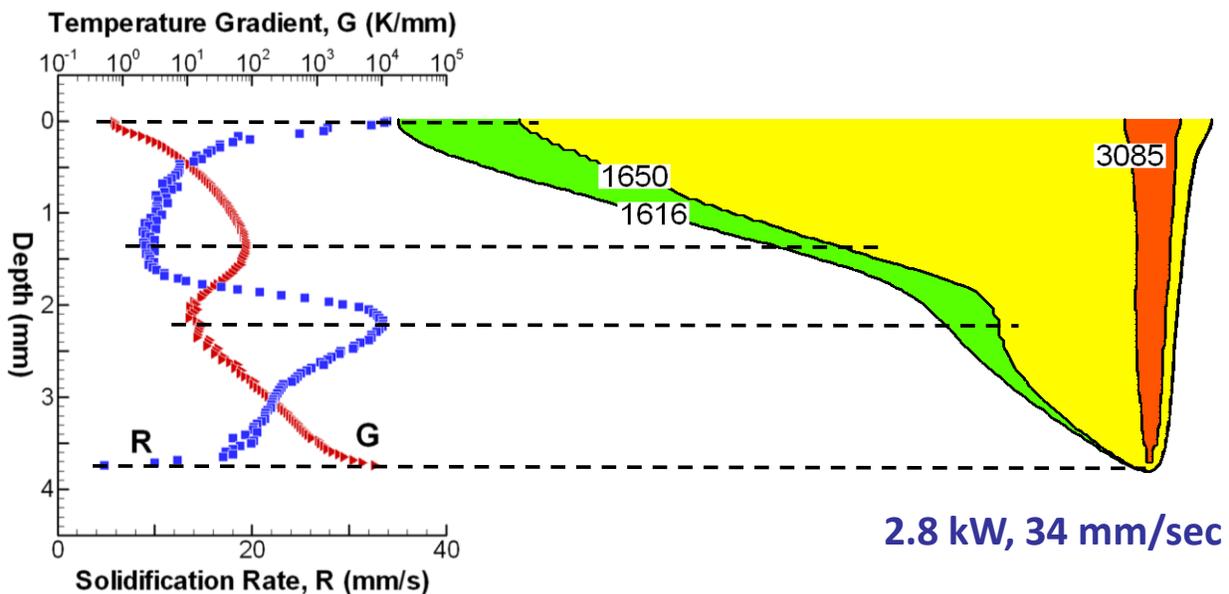
Figure 53: The behavior of G and R as a function of depth along the central longitudinal plane for a 2.8 kW weld. The slope of the liquidus contour represents the solidification rate (i.e. larger absolute slope, greater R), and the distance between the solidus and liquidus contours corresponds to the temperature gradient (i.e. larger distance, lower G).

vertical, and the width of the mushy zone increases sharply at the mid-depth along the weld centerline. This change results in a decrease of G and an increase of R. The mushy zone width and liquidus contour slope then decrease again as the liquidus contour approaches the bottom of the keyhole. Along the central x-z plane, the temperature gradient varies over four orders of magnitude from the top of the weld to the bottom, and the shapes of these two curves will impact the combined forms of G and R.

Changes in the processing conditions also impact these solidification parameters. The temperature gradient (G) and solidification rate (R) along the central x-z plane and two dimensional contour plots of G and R for powers of 1.0, 2.8, and 4.7 kW and a travel speed of 34 mm/s are shown in Figure 54. The curves are determined in the same way as Figure 53 while the contour plots are determined from the 3D liquidus surface. Each G curve exhibits a local minimum and maximum along the depth, and an increase in power tends to shift the curve down and increase the range over which G varies. For example, in the case of the 1 kW weld, G varies over a range of three orders of magnitude, from 10 to 10000 K/mm, but for the 4.7 kW weld, G varies over four orders of magnitude from 0.2 K/mm at the top of the weld pool to 5000 K/mm near the bottom of the keyhole. A review of the temperature gradient plots inset in Figure 54a shows that increasing the power does not simply result in a larger weld profile with similar contours. At higher powers, lower temperature gradients and a higher degree of spatial variation are observed throughout the weld.

In Figure 54b, the solidification rate, R, varies from 4 mm/s to 34 mm/s (the welding speed). Across the powers tested in this study, power does not appear to have a significant effect
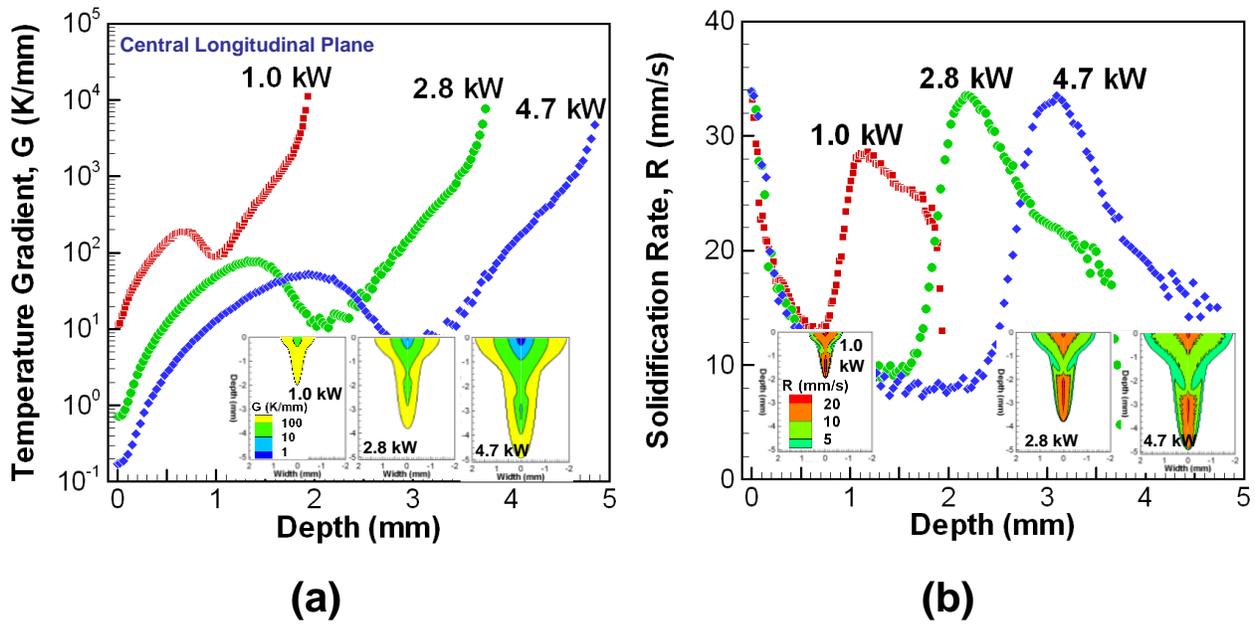
Figure 54: The solidification parameters, (a) temperature gradient (G) and (b) solidification rate (R), are plotted as a function of depth along the central x-z plane and in 2D contour plots for various powers.

on R at the central longitudinal plane. Similar to the G plots, a local minimum and maximum are observed. However in the two-dimensional R plots, relatively lower solidification rates are observed at higher powers. In the 4.7 kW weld, R is mostly 5 mm/s or more at the top half, while decreasing the power to 1.0 kW results in a value of R at 20 mm/s or more. Along the cross-section, R decreases from the center of the weld to the fusion line because the surface normal vector becomes increasingly misaligned with the travel direction.

Both G and R exhibit a high degree of spatial variability along the solidification front, which will lead to variability in the parameters that control solidification structure scale and morphology. Figure 55 shows GR and G/R as a function of depth along the central x-z axis and cross-sections for laser powers of 1.0, 2.8, and 4.7 kW. The shapes of the curves are similar to the previous plots of G and R with a local minimum and maximum near the half depth of the weld, and the curves tend to shift to lower values with increasing power. However, the values of GR and G/R are varying over 4 to 5 orders of magnitude. For a weld power of 4.7 kW, the cooling rate varies from 6 to 40000 K/s, and G/R varies from 0.005 to 600 K-s/mm^2. The large spatial variation in cooling rates and G/R values explains the variation in scale and morphology of solidification structures observed in Figure 52.
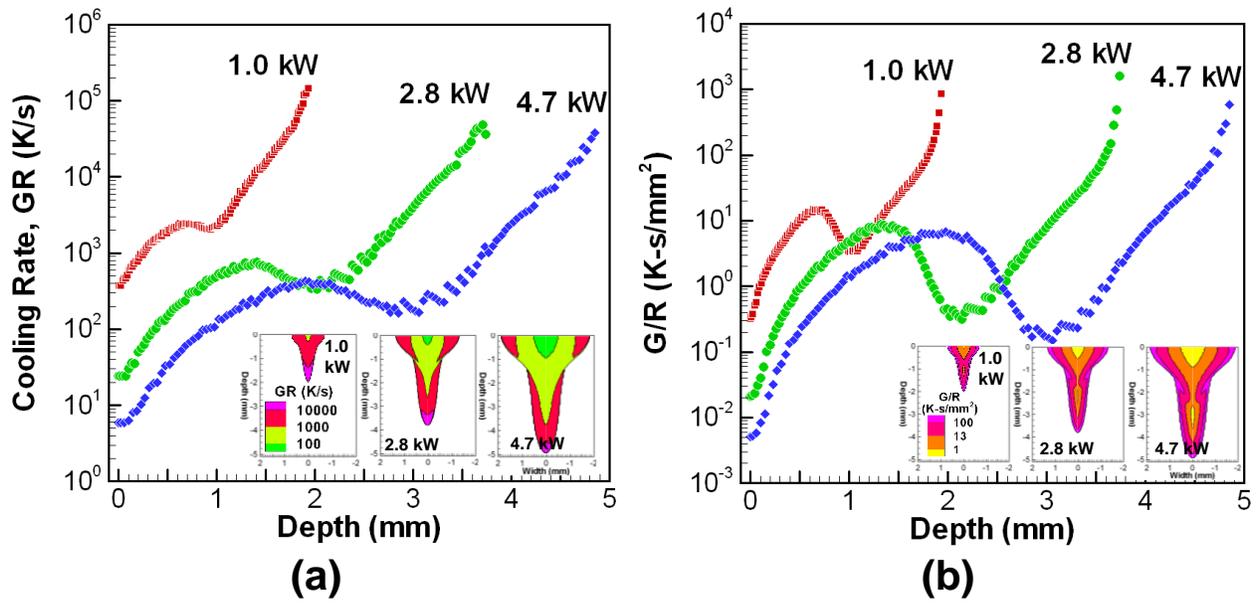
Figure 55: The combined forms of solidification rate and temperature gradient, (a) cooling rate (GR) and (b) morphology parameter (G/R), are plotted as a function of depth along the central x-z plane and in 2D contour plots for various powers.

The effect of laser power on the cooling rate can be observed in the inset contour plots in Figure 55a. At 1.0 kW most of the weld is cooling at rates above 1000 K/s, but as the power increases, significant parts of the weld are cooling at rates lower than 1000 K/s. At the highest power, a large section of the top of the weld is cooling at a rate below 100 K/s. The 2D G/R plots in Figure 55b also show the effects of power on the distribution of the solidification structure morphology. The G/R contour of 13 K-s/mm^2 is chosen because it is close to the experimentally observed transition value from cellular to columnar dendritic morphologies. As power increases, the amount of the weld enclosed by the transition value contour increases, resulting in an increase in the area of the fusion zone containing dendritic structures. Another observation of the same contour shows that it is not continuous along the depth for the 1 kW fusion weld, indicating that transitions from dendrites to cells to dendrites may be observable at the center of the zone.

3.4.4 Scale of the Solidification Structures

The size and scale of cells and dendrites are known to vary as a function of cooling rate [16]. The cooling rate varied significantly over the range of laser powers investigated. This relation is well established in the study of dendrite arm spacings and is based on the solidification time being inversely proportional to the cooling rate [16]. A more detailed description by Kurz and Fisher [23], which uses a similar relation, assumes competing growth between two cylinders
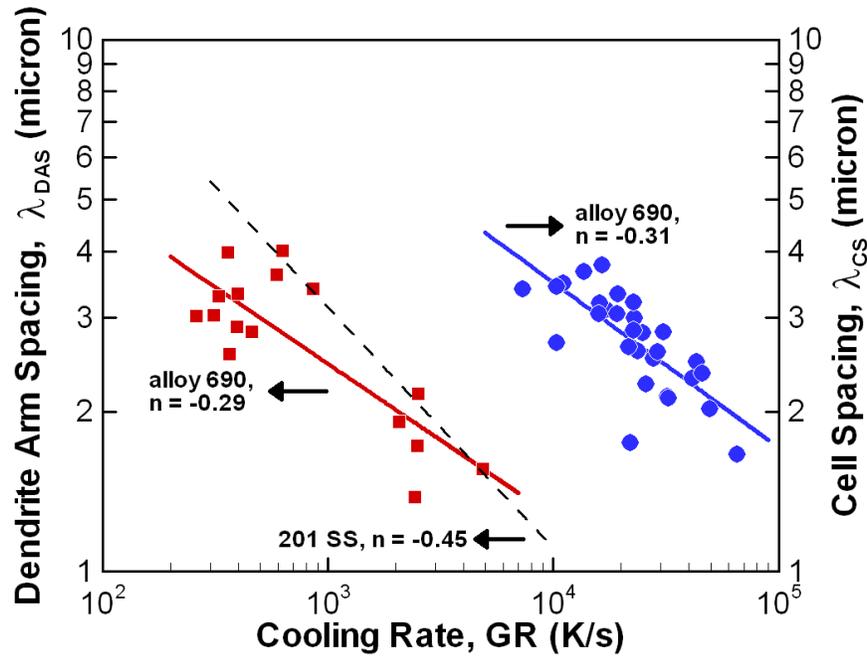
Figure 56: The measured cell spacing (circles) and dendrite arm spacing (squares) are shown as a function of calculated cooling rate. The 201 stainless steel [24] system is shown for comparison.

(i.e. dendrite arms). The measured cell and dendrite arm spacings were correlated to the calculated cooling rates (GR) at various positions in the weld cross-section. Figure 56 shows the effect of the calculated cooling rate on experimental cell spacing and dendrite arm spacing. The fitted lines are of the form

log(spacing)=n log(GR)   (10)

where spacing is the dendrite arm or cell spacing and n is an exponent with a theoretical value of 1/3. In Figure 56, the measured cell spacing ranges from 3.9 µm at a GR value of 8000 K/s to 1.7 µm at a GR value of 90000 K/s. The dendrite arm spacing varies from 4.0 µm at 200 K/s to 1.4 µm at 7000 K/s. The data compare well to similar measurements made on 201 stainless steel welds [24]. Additionally, the measured cell and dendrite arm spacings from the literature for Alloy 690 showed cell and dendrite arm spacings of about 4 µm for comparable heat inputs [25,26]. The data points shown in Figure 56 represent a combination of 87 and 58 linear intercept measurements for cells and dendrite arms, respectively. The standard deviations for the measurements vary from 0.06 to 1.01 µm, with median values in that range of 0.35 µm and 0.28 µm for cell and dendrite arm spacings, respectively. These standard deviations are comparable to the standard deviations of similarly sized stainless steel spacing measurements [16].

The following relations give the size of the solidification structures in microns as a function of cooling rate (K/s) in the general form $\lambda = b(GR)^n$, based on the fitted lines in Figure 56

$$\lambda_{CS} = 60.6(GR)^{-0.31}$$

(11)

$$\lambda_{DAS} = 17.9(GR)^{-0.29}$$

(12)

where λ_{CS} is the cell spacing and λ_{DAS} is the dendrite arm spacing. These cooling rate relations are much more precise than any general heat input relations since, as demonstrated previously, the cooling rate can vary significantly as a function of position in a weld pool for any given heat input. These data are not limited to laser welding and can be applied to various processes that require or incorporate solidification processing, including casting, conventional arc welding, and other high energy beam processes.

3.4.5 Morphology of the Solidification Structures

The G/R parameter, which determines the morphology of the solidification structure, can be calculated and correlated to the experimental microstructure in the fusion zone. In the fusion zone, the solidification structure consisted of cells and columnar dendrites and, the area fractions of cells and columnar dendrites were measured by optical microscopy. G/R values were then correlated with the observed solidification structures in the fusion zone. Computed G/R values were 13 K-s/mm^2 or lower in all areas where columnar dendrites were observed. Similarly, the computed G/R values were 21 K-s/mm^2 or higher where cellular structure was observed. The transition between columnar dendrites and cellular structure can then be assumed to occur between 13 and 21 K-s/mm^2. By using the G/R values that correspond to the cells and columnar dendrites, the area fractions of the two solidification structures in the transverse cross-section of the weld can be calculated.

C ≡ cell area
D ≡ dendrite area
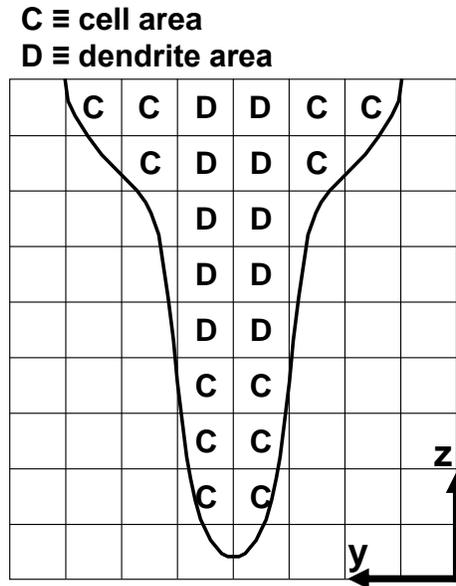
Figure 57: A schematic of the calculated fusion zone shows how the area fractions of cells and dendrites are calculated. If the calculated G/R value of a given control volume is greater than the critical value, then the area of the y-z face is assigned to the cell area fraction. Otherwise, the area is added to the dendrite area fraction.

A transverse cross section schematic of the fusion zone is shown in Figure 57. If the G/R value is lower than the critical value for the transition from dendrites to cells, then the y-z face of the control volume is assigned to the dendrite area, or 'D' in the schematic. In this way, the total area of cells and dendrites can be determined. The area fractions are the areas of cells or dendrites divided by the total area. Figure 58 shows the experimental and calculated fusion zone area fractions of columnar dendrites with two different critical G/R values. Only the fraction of cells and columnar dendrites are considered, since significant amounts of equiaxed dendrites and planar solidification were not observed. For the conditions examined in this study, the area fraction of columnar dendrites barely exceeds 0.5 for a laser power of 4.7 kW. The model calculations and experimental measurements agree. While the overall fractions agree, the relative location of the transition from cells to dendrites can also be observed. Figure 59 shows the transition in a microgragh along with a G/R contour plot. The transition is not as sharp as the contour plot indicates, but in 150 μm the solidification morphology clearly changes from cells to dendrites.
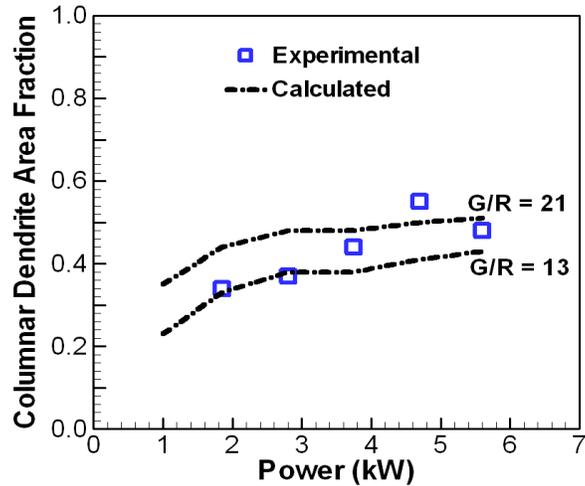
Figure 58: A comparison between the calculated and experimental area fractions of columnar dendrites shows good agreement. The different G/R values represent the lowest value at which cells were observed (G/R =21 K-s/mm2) and greatest value where columnar dendrites were observed (G/R = 13 K-s/mm2).

The size and morphology of the solidification structures within the experimental welds have been correlated to calculated solidification parameters. A solidification map for Alloy 690 can now be constructed to predict the solidification morphology and the scale of the structure. This map is shown in Figure 60. The solid straight line delineates the cellular and columnar dendritic regions of the map. Cooling rates are represented by the dashed curved lines and show the cell spacings and dendrite arm spacings calculated from Equations 11 and 12, respectively.

This map has a number of practical applications. For any given set of welding parameters, the minimum size of dendrite arm spacings as a function of welding speed can be determined immediately since the solidification rate cannot exceed the welding speed. For example, if the
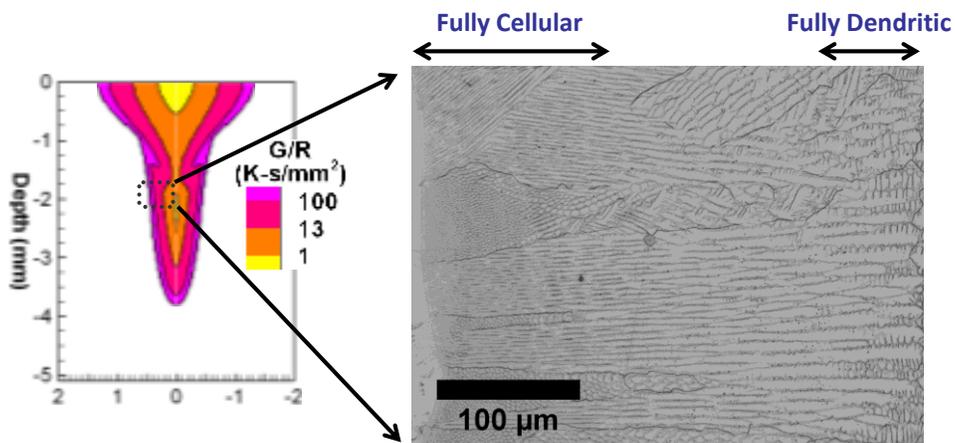
Figure 59: The transition from cellular to dendritic is shown in the micrograph.
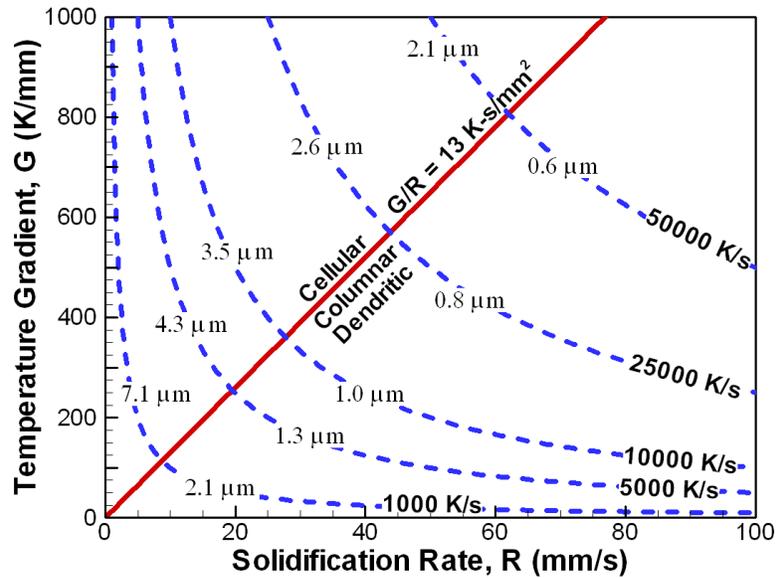
Figure 60: The solidification map shows the transition from cellular to columnar dendritic morphology with various cooling rates. Along each cooling rate is the cell spacing (λ_{CS}) and dendrite arm spacing (λ_{DAS}), which are determined from Eqs. 11 and 12. With this map the scale and morphology of the solidification structures can be predicted quantitatively.

welding speed is set to 25 mm/s, then a dendrite arm spacing of 1.3 µm is possible, while a value of 1.0 µm is not. On the other hand, cell spacings greater than 2.6 µm would be expected for most of the weld, where the temperature gradient is 1000 K/mm or less. Spacings less than 2.6 µm would be confined to high temperature gradient and cooling rate regions, such as the root of the weld and near the fusion line. In addition, the wide range of G and R values makes the map applicable to any process, where solidification processing of Alloy 690 is necessary.

3.5 Summary and Conclusions

The solidification parameters of Inconel® Alloy 690 during keyhole mode laser welding have been calculated using a mathematical heat transfer and fluid flow model. The calculated parameters, temperature gradient (G), solidification rate (R), cooling rate (GR), and solidification parameter (G/R), were used to describe the observed microstructure in the welding experiments. The large variation in the solidification parameter values in the molten pool of the laser welds allowed for the construction of a solidification map that describes the scale and morphology of the solidification structures for given values of G and R.

(1)   Due to the keyhole heat source, which extends into the depth of the weld, a large spatial variation of the calculated solidification parameters was observed. Along the central

longitudinal plane, the G/R value could vary up to 5 orders of magnitude. In both the transverse cross section and the central longitudinal plane, increases in laser power lead to a significant increase in the spatial variation of the solidification parameters.

(2)   The measured cell and dendrite arm spacings were correlated to the calculated solidification parameters and expressed as functions of cooling rate in the form $\lambda = b(GR)^n$. These expressions can be applied for a variety of welding processes and conditions. G/R values of 13 and 21 K-s/mm^2, which are associated with the transition from cellular to columnar dendritic solidification structures, were used to calculate the dendrite area fractions, which agreed with the measured values.

(3)   A map of solidification scales and morphologies for Alloy 690 was constructed based on the data presented in this work. The cell and dendrite arm sizes and the cellular and dendritic morphology regions are plotted as a function of the temperature gradient, G, and the solidification rate, R. The utility of the map was highlighted by describing how minimum dendrite arm spacings can be selected based on the welding speed. Due to the large range of G and R values captured in these keyhole mode laser welds, the map has very wide applicability to a range of materials processes from casting to arc and laser welding.

3.6 References

[1]   Willis, E. Electric Power Research Institute (EPRI). 1 December 2011. Private communication.

[2] Kou S. 2013. Welding Metallurgy, second ed. Hoboken: John Wiley & Sons, Inc.

[3] Rai, R., Roy, G.G., and DebRoy, T. 2007. A computationally efficient model of convective heat transfer and solidification characteristics during keyhole mode laser welding. *J. Appl. Phys.* 101 (5): 054909.

[4] Rai, R., Elmer, J.W., Palmer, T.A., and DebRoy, T. 2007. Heat transfer and fluid flow during keyhole mode laser welding of tantalum, Ti-6Al-4V, 304L stainless steel and vanadium. *J. Phys. D: Appl. Phys.* 40 (18): 5753-5766.

[5]   Rai, R., Kelly, S.M., Martukanitz, R.P., and DebRoy, T. 2008. A convective heat-transfer model for partial and full penetration keyhole mode laser welding of a structural steel. *Metall. Mater. Trans. A* 39A (1): 98-112.

[6]   Zhang, W., Kim, C.-H., and DebRoy, T. 2004. Heat and fluid flow in complex joints during gas metal arc welding - Part I: Numerical model of fillet welding. *J. Appl. Phys.* 95 (9): 5210-5219.

[7]   Zhao, H. and DebRoy, T. 2003. Macroporosity free aluminum alloy weldments through numerical simulation of keyhole mode laser welding. *J. Appl. Phys.* 93 (12): 10089-10096.

[8]   Ribic, B., Rai, R., and DebRoy, T. 2008. Numerical simulation of heat transfer and fluid flow in GTA/Laser hybrid welding. *Sci. Technol. Weld. Joining* 13 (8): 683-693.

[9]   Ribic, B., Tsukamoto, S., Rai, R., and DebRoy, T. 2011. Role of surface-active elements during keyhole-mode laser welding. *J. Phys. D: Appl. Phys.* 44 (48): 485203.

[10]   Kaplan, A. 1994. A model of deep penetration laser-welding based on calculation of the keyhole profile. *J. Phys. D: Appl. Phys.* 27 (9): 1805-1814.

[11] Krishnan, S. and Nordine, P.C. 1996. Spectral emissivities in the visible and infrared of liquid Zr, Ni, and nickel-based binary alloys. *J. Appl. Phys.* 80 (3): 1735-1742.

[12]   Gale, W.F. and Totemeier, T.C. 2004. Smithells Metals Reference Book, eighth ed. Burlington: Elsevier Butterworth-Heinemann.

[13] Special Metals Corporation, INCONEL® Alloy 690 Data Sheet, Publication Number SMC-079 (2009). Accessed 9 July 2013.

<http://www.specialmetals.com/documents/Inconel%20alloy%20690.pdf>

[14]   Pakratz, L.B. 1982. Thermodynamic Properties of Elements and Oxides. District of Columbia: U.S. Dept. of the Interior, Bureau of Mines.

[15] Glagoleva, Y.V., Pushkareva, N.B., Lapshova, Y.E., Sadyreva, O.V., Polev, V.R., Gorbatov, V.I., Taluts, S.G., and Korshunov, I.G. 2006. Thermophysical and transport properties of nickel-chromium alloys at high temperatures. *Phys. Met. Metallography* 102 (1): 48-54.

[16]   Liu, W. and Dupont, J.N. 2004. Effects of melt-pool geometry on crystal growth and microstructure development in laser surface-melted superalloy single crystals. Mathematical modeling of single crystal growth in a melt pool (part I). *Acta Mater.* 52 (16): 4833-4847.

[17] Liu, W. and DuPont, J.N. 2005. Effects of substrate crystallographic orientations on crystal growth and microstructure development in laser surface-melted superalloy single crystals. Mathematical modeling of single-crystal growth in melt pool (Part II). *Acta Mater.* 53 (5): 1545-1558.

[18] Anderson, T.D., DuPont, J.N., and DebRoy, T. 2010. Stray grain formation in welds of single-crystal Ni-base superalloy CMSX-4. *Metall. Mater. Trans. A* 41A (1): 181-193.

[19] Anderson, T.D., DuPont, J.N., and DebRoy, T. 2010. Origin of stray grain formation in single-crystal superalloy weld pools from heat transfer and fluid flow modeling. *Acta Mater.* 58 (4): 1441-1454.

[20]   Valiente-Bermejo, M.A., Karlsson, L., and DebRoy T. 2013. Influence of low energy laser welding on solidification and microstructure of austenitic stainless steel welds. *14th Nordic Laser Materials Processing Conference*: 1-12.

[21] Schempp, P., Cross, C.E., Pittner, A., Oder, G., Neumann, R.S., Rooch, H., Dorfel, I., Osterle, W., and Rethmeier, M. 2014. Solidification of GTA aluminum weld metal: Part I – grain morphology dependent upon alloy composition and grain refiner content. *Weld. J.* 93 (2): 53s-59s.

[22]   Vitek, J.M. 2005. The effect of welding conditions on stray grain formation in single crystal welds - theoretical analysis. *Acta Mater.* 53 (1): 53-67.

[23]   Kurz W. and Fisher, D.J. Fundamentals of Solidification, third ed. Brookfield: Trans Tech Publications; 1989.

[24]   Paul, A. and DebRoy, T. 1988. Free-surface flow and heat-transfer in conduction mode laser-welding. *Metall. Trans. B* 19B (6): 851-858.

[25]   Abraham, G.J., Bhambroo, R., Kain, V., Dey, G.K., and Raja, V.S. 2013. Comparing Reactivation Behavior of TIG and Laser Beam Welded Alloy 690. *J. Mater. Eng. Perform.* 22 (2): 427-432.

[26]   Lee, H.T. and Wu, J.L. 2009. The effects of peak temperature and cooling rate on the susceptibility to intergranular corrosion of alloy 690 by laser beam and gas tungsten arc welding. *Corros. Sci.* 51 (3): 439-445.

Chapter 4 – Formation of Root Defects

4.1 Root Defects in Complete Penetration Welds

High power laser and hybrid laser-arc welding processes [1-5] offer a range of advantages, such as faster welding speeds, lower heat inputs, and deeper penetration, over traditional arc welding processes. Given these attractive properties, these laser based process have found applications in a range of different construction and fabrication industries [6]. However, these processes are also susceptible to unique defects associated with their high aspect ratio and deep penetration. Two of the most common of these defects include porosity from keyhole instability in partial penetration welds [7-9] and root defects in full penetration welding. These root defects have also been called chain of pearls [10], dropping [11], and root humping [12] and are characterized by the formation of weld metal spheroids at the bottom surface of a full penetration weld. An example of these root defects in a DH36 steel hybrid laser-arc weld is shown in Figure 61. As higher laser powers become available and deeper penetrations are obtained, these defects will become more problematic, and a deeper understanding of the mechanisms driving these defects will be necessary to take advantage of these high laser powers.

Figure 61: The typical weld root defects formed during hybrid laser-gas metal arc welding with a laser power, welding speed, and filler wire feed rate of 5 kW, 30 mm/s, and 229 mm/s, respectively.

Root defects have been characterized at both high [13-16] and low [11,13,17,18] heat inputs, making it difficult to identify the predominant mechanism for their formation or a single means for preventing their formation. For example, in 304 stainless steel, Zhang et al. [14] and Kaplan and Wiklund [16] found that root defects occur at lower welding speeds (i.e. higher heat input) during the laser welding of 12 mm and 16 mm thick plates, respectively. In other cases, increasing the heat input leads to acceptable welds. Havrilla et al. [11] increased the laser power by 1 kW from 7.75 kW to 8.75 kW at a constant welding speed to eliminate root defects in 12 mm thick steel. Ilar et al. [12] employed high speed imaging to study the formation of root defects in real time during the laser welding of 8 mm thick 304 stainless steel plate. The high speed videos showed the initiation of bulges immediately behind the keyhole, and these bulges would occasionally build up and solidify as root defects. Ilar et al. [12] concluded that gravity, surface tension, and melt availability play a role in the formation of root defects.

One method for avoiding root defects is supporting the weld pool from the bottom through the use of electro-magnetic forces from an oscillating magnetic field [15,19,20]. Bachmann et al. [15,20] complemented physical experiments by utilizing a 3D numerical heat transfer and fluid flow model to calculate the electromagnetic (EM) forces necessary to balance the hydrostatic pressure and prevent the formation of root defects in 10 mm thick steel and 20 mm thick aluminum plates. However, the predicted EM force values were slightly lower than the experimental values necessary to hold the liquid in place, since only the weight of the liquid metal column above the bottom pool surface was taken into account. While EM support can be used to weld thick sections, utilizing the process in a production environment may not be practical, and the application of EM forces can change the fluid flow patterns during welding [20]. Therefore, it is necessary to develop a deeper understanding of the conditions that promote root defect formation in order to intelligently select welding parameters that suppress it.

In this chapter[2], the formation of root defects is investigated for laser and hybrid laser-arc welding under a variety of welding conditions. For the first time, the three dimensional (3D) internal structure of the root defect nuggets in a structural steel plate weld was characterized by X-ray computed tomography (CT) and was found to depend on the welding process employed. The melt volume and the surface tension of the molten DH36 steel were independently varied to determine the effect of each on root defect formation. Melt volume was varied by changing the heat input of the welds, and surface tension was altered by removing the oxide scale on the bottom surface of the plate prior to welding. Increasing melt volume or decreasing surface tension led to root defects being formed. In order to quantify each effect, a force balance considering the weight of the liquid steel and the surface tension at the weld root is developed for an idealized weld pool and used to determine the conditions for the formation of root defects. Process maps for defect free full penetration laser welds, for which substantial experimental results have been reported, and selected hybrid laser-arc welds were developed for low carbon steel and 304 stainless steel.

---

[2]Portions of this chapter are directly excerpted from J.J. Blecher, T.A. Palmer, and T. DebRoy, 'Mitigation of Root Defect in Laser and Hybrid Laser-Arc Welding', Weld. J., **94**, 2015, 73s-82s.

4.2 Welding Experiments and Characterization Details

Bead on plate laser and hybrid laser-arc welds were performed on 4.8 and 9.8 mm thick DH36 steel plate, using an IPG Photonics® YLR-12000-L ytterbium fiber laser with a Precitec® YW50 welding head. The optics system utilizes collimating and focusing lenses with 200 mm and 500 mm focal lengths, respectively. The 1 μm laser wavelength is transported to the welding head through a 200 μm diameter process fiber. The focused spot size and full divergence angle were measured with a Primes® Focus Monitor and are 0.52 mm and 64 mrad, respectively. A Lincoln Electric® Power Wave 455 M/STT power source with a Binzel® WH 455D water cooled welding gun was used with ER 70S-6 welding wire for the hybrid welding experiments.

In both the laser and hybrid laser-arc welds on a 4.8 mm thick plate, a laser power of 5kW, laser-arc separation distance of 3 mm, and arc voltage of 31 V were maintained constant, while wire feed speed, arc current and travel speed were varied as shown in Table 5. A positive 8 mm defocus, indicating that the position of focus is above the plate, was also used. When welding on a 9.8 mm thick plate, a laser power of 7 kW with zero defocus, or the laser focused on the substrate surface, was selected. Additionally, to test the effect of the oxide presence on the bottom surface, two configurations of plate were used, one with only the top surface of the plate sand blasted to remove the oxide. The other plate had the oxide removed on both sides. A summary of the welding parameters are given in Table 5 for both laser beam welding (LBW) and hybrid laser-arc welding (HLAW). Oxide removed refers to whether the oxide scale was removed on both sides prior to welding.

Table 5: Welding conditions for the laser beam (LBW) and hybrid laser-GMA (HLAW) welds used in this study. 'Oxide Removed' refers to the bottom surface oxide scale being removed.

Weld Number	Oxide Removed	Welding Process	Plate Thickness (mm)	Root Defects	Weld Speed (mm/s)	WFS (mm/s)
1	no	LBW	4.8	no	30	…
2	no	LBW	4.8	no	40	…
3	no	LBW	9.5	yes	15	…
4	no	HLAW	4.8	yes	30	127
5	no	HLAW	4.8	yes	30	152
6	no	HLAW	4.8	yes	30	229
7	yes	HLAW	4.8	no	40	127
8	no	HLAW	4.8	yes	40	127
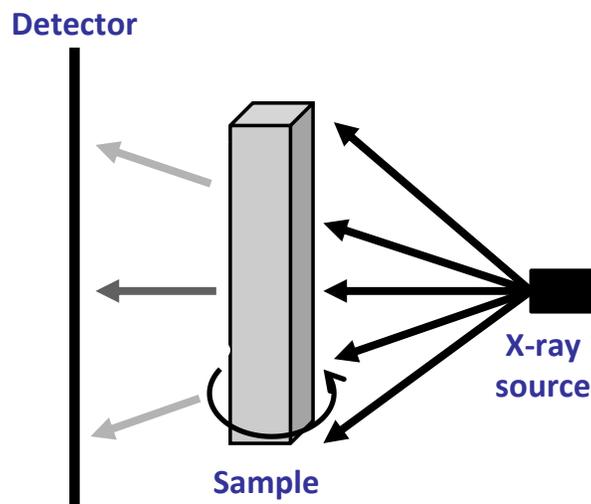
Figure 62: The general operation of a X-ray CT imaging system.

Metallographic specimens were removed from the welds using an abrasive saw. In order to leave large, mostly whole welds for X-ray CT, transverse cross-section samples were taken from the ends of the welds, but still within the steady-state region of the weld. These cross-section specimens were mounted, polished, and etched with a 3% nital solution, and optical microscopy was performed using the same equipment described previously[3].

Unique pore structures were found in the root defects during the initial optical microscopy. In order to characterize the 3D structure of these pores, X-ray computed tomography (CT) imaging was used. The general operation of X-ray CT imaging is shown schematically in Figure 62. The sample is positioned in front of a source of polychromatic X-rays, which are generated from an electron beam incident on a metal target. The X-ray intensity after transmission through the part is captured by a detector as an image. Several hundred images are captured at different angles as the part is rotated.

X-ray CT images were captured with a General Electric® v|tome|x CT system. The accelerating voltage and current for each scan were 280 kV and 180 μA, respectively. The voxel (i.e. 3D pixel) size with a magnification of 20x was 50 μm. DatosX® software handled the reconstruction of the individual X-ray images to produce the 3D image. The defect detection

---

[3]The description of the optical microscopy equipment and software is described in section 3.3.1.

module in the Volume Graphics® VGStudio Max software was used to examine the internal pore structure of the weld defects.

4.3 Root Defect Formation and Characterization

Based on previous research [12,15,19,20], several forces are expected to play a role in root defect formation and include the weight of the liquid metal, the arc force, and the surface tension force. These forces are shown schematically in Figure 63. The weight of the liquid metal is primarily a function of the plate thickness. The arc force varies with the current, and the surface tension force is affected by the surface tension of the liquid metal and the maximum degree of convexity, which can be approximated by the weld pool dimensions at the bottom of the weld. The arc force varies as the square of the arc current but also depends on the arc radius, which is constant with current [21]. While an expression can be derived for arc force, extrapolations of direct measurements are used in this work [21]. The equations for weight force (F_g), surface tension force (F_s), and arc force (F_a) are shown below

$$\frac{F_g}{A_{unit}} = \rho g t \tag{13}$$

$$\frac{F_s}{A_{unit}} = 2\sigma\left(\frac{1}{w} + \frac{1}{l}\right) \tag{14}$$

$$\frac{F_a}{A_{unit}} = \frac{\mu_0 I^2}{4\pi^2 r_a^2} \tag{15}$$
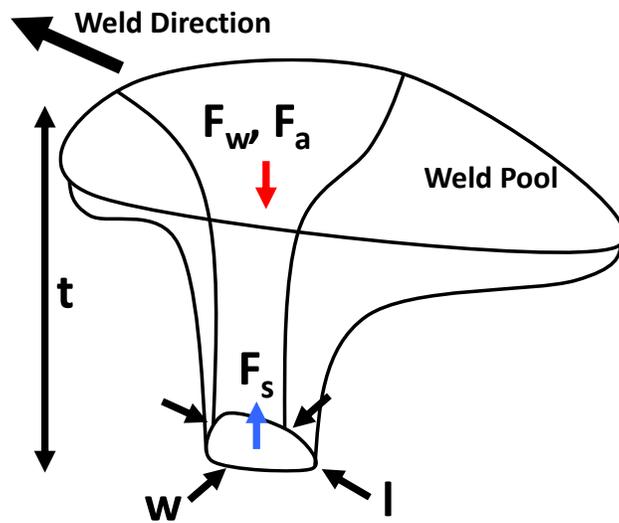
Figure 63: At the weld pool, the arc and weight force act to promote root defects. The surface tension force acts to prevent defects.

where ρ is the liquid metal density, g is acceleration due to gravity, t is plate thickness, σ is the surface tension, w is the pool width at the bottom of the plate, l is the pool length at the bottom of the plate, μ_0 is vacuum permeability, I is the arc current, r_a is the arc radius, and A_{unit} is a unit area. Typically the length of the pool is several times greater than the width, and since the maximum possible curvature is inversely proportional to the pool dimensions, the length of the pool has a smaller effect on surface tension than the lower magnitude width. For most of the cases in this chapter, the length of the pool can be dropped from equation 14 because it will have only a small effect on the surface tension force. If $F_g + F_a > F_s$, then defects are expected to form.

During the welding trials, plate thickness, arc force, and the surface tension force were all varied by using a different plate, adding an arc heat source for hybrid laser arc welding, increasing/decreasing heat input to change the pool dimensions, and keeping/removing the oxide scale, as shown in Table 5. This section of the chapter describes the qualitative results of the welding experiments after one or more variables is changed. Typically, these parameters cannot be varied independently. For example, increasing the plate thickness will require a different combination of laser power and welding speed to achieve a full penetration weld, and these adjustments may result in different pool dimensions and, therefore, a different surface tension force.

In the case of plate thickness, welds 1 and 2 represented laser welds at two different welding speeds that produced defect free welds in a 4.8 mm thick plate. Weld 3, another laser weld, was fabricated with a 9.5 mm thick plate, which is double the plate thickness of welds 1 and 2. In addition to a greater weight force driven by a doubling of the plate thickness, weld 3 was also about 1 mm wider at the bottom compared to welds 1 and 2, which were both about 1.5 mm wide. As a result, the weight force doubled and the surface tension force decreased by 40%. From the force balance, F_g increased and F_s decreased, leading to the formation of root defects as predicted by the force balance.

The effect of arc force during hybrid laser-arc welding was tested next. Hybrid welds 4, 5, and 6 can be compared to laser weld 1 because these welds were all fabricated with a welding speed of 30 mm/s. The hybrid welds 4, 5, and 6 were fabricated with increasing wire feed speeds of 127, 152, and 229 mm/s, respectively. As wire feed speed increases, arc current, heat input, and arc force increase, and the bottom pool width would also be expected to increase. Welds 1

and 4 have the same welding speed, and weld 4 was the lowest heat input (e.g. lowest arc force) hybrid weld and least likely of the hybrid welds to form root defects. These welds are shown in Figure 64. The addition of an arc lead to the formation of root defects and a more prominent weld crown due to the addition of filler material. From the images, the arc clearly increased the weld dimensions, including the bottom width of the pool from 1.6 mm to 2.5 mm, which would have decreased the surface tension force by 40%. The arc force in weld 4 is expected to be on the order of 99% of the surface tension force, and the plate thicknesses and, therefore, the weight forces are identical. In summary, F_g is the same for both welds, F_s is 40% lower in the hybrid weld, and F_a = F_s in the hybrid weld. From the force balance, the hybrid weld would be expected to be more susceptible to root defect formation compared to laser weld.

The presence of oxygen in molten iron has a significant effect on the surface tension. At high oxygen contents between 0.06 and 0.1 wt.%, the surface tension of liquid iron is lowered by 50% or more [22] compared to its oxygen free value of 1.91 N/m [23]. The maximum oxygen dissolvable by liquid iron at the melting point is 0.16 wt. % [24]. Oxide scale is expected to deliver most of the oxygen to the weld pool. This scale would have developed naturally on the steel plates
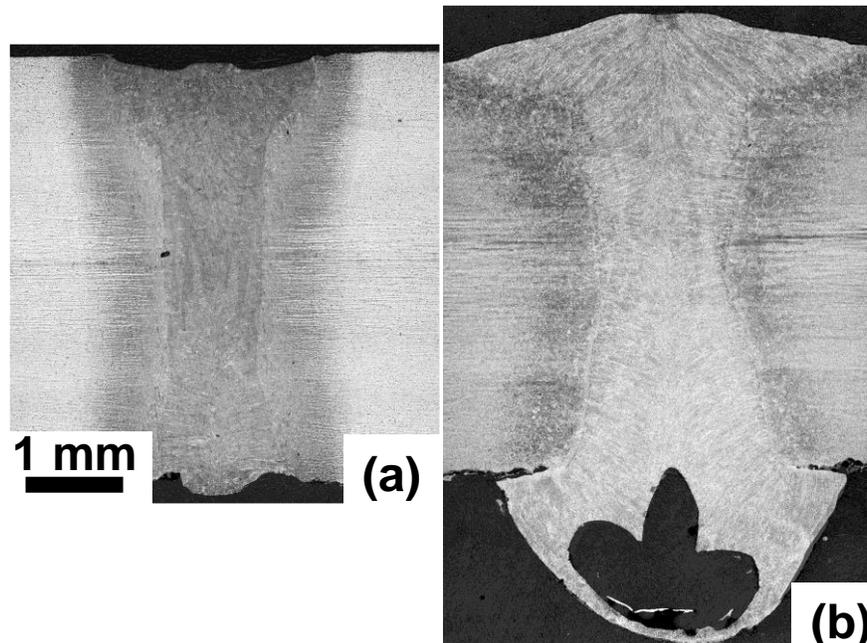
Figure 64: The transverse weld cross-sections for (a) a laser weld (weld 1) and (b) a hybrid weld (4) are shown. The laser conditions are the same, but the hybrid weld has increased heat input, larger amount of melted volume, and greater weight that must be supported by the surface tension force.
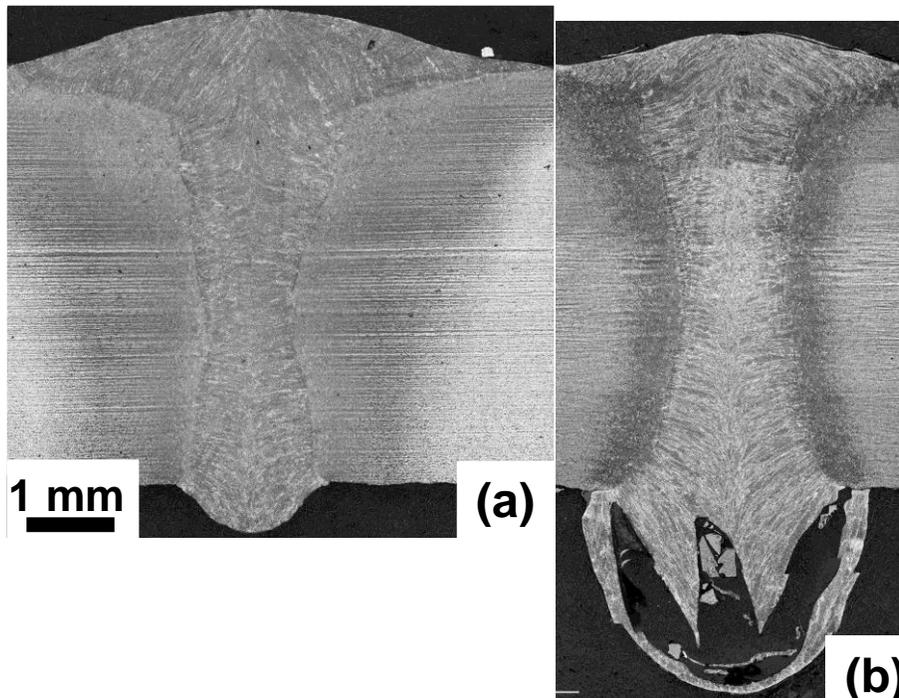
Figure 65: A comparison of the transverse hybrid weld (7 and 8) cross-sections with identical welding conditions with the exception of bottom surface oxide scale, which was not present in (a) and present in (b). The sizes of the welds are similar, suggesting that the weight of the liquid metal is similar and that the reduction in surface tension in (b) due to the oxide scale presence led to the root defects.

during storage. While not exactly identical to scale that formed during storage, mill scale has been extensively studied and the measured oxygen content in that scale exceeds 20 wt. % [25]. This scale during welding provides a rich source of oxygen for the liquid steel to dissolve. It can also be assumed that rapid convection in the weld pool produces a well-mixed pool, so the introduction of oxygen to either surface would quickly diffuse, mix with the flow, and distribute to the rest of the pool.

During the welding experiments, oxygen levels were controlled by selectively removing the oxide scale. In all cases, the scale on the top surface was removed with an angle grinder. For one hybrid weld, the oxide scale was removed from the bottom surface as well, with the expectation that the weld pool would have less dissolved oxygen and a higher surface tension. In examining the effect of surface tension, hybrid welds (welds 7 and 8) were made using the same processing parameters, with the exception of the presence of an oxide scale on the bottom surface on one of the welds (8). The weld with scale (8) formed root defects. On the other hand, the weld without scale (7) formed no root defects. A comparison of the transverse weld cross-sections and

bottom surfaces are shown in Figure 65 and Figure 66, respectively. In Figure 66, irregularly spaced root defects can be observed in the weld with bottom surface oxide scale (8). While the weld without scale contains some re-enforcement on the bottom surface, there are no observable defects (7).

In terms of the forces acting to promote and restrict the formation of root defects, the weight force and arc force are expected to be similar due to identical plate thicknesses and welding conditions. As shown in the transverse cross sections in Figure 65, the weld widths are about equal with the weld without the bottom oxide scale (7) having a width 10% larger. In the absence of a lowered surface tension from oxide scale, this weld would have surface tension force that is 10% less than the weld with bottom surface oxide scale. However, with the oxide scale, the surface tension (σ) is expected to drop from 1.91 N/m to 0.88 N/m. With this updated surface tension, the weld with scale (8) would have a surface tension force approximately 49% lower than the weld without scale (7). In summary, F_g and F_a are identical for both welds, and F_s in the weld with bottom surface oxide scale is 49% of the force in the other weld. So, defects would be expected to form in weld with bottom surface oxide scale.
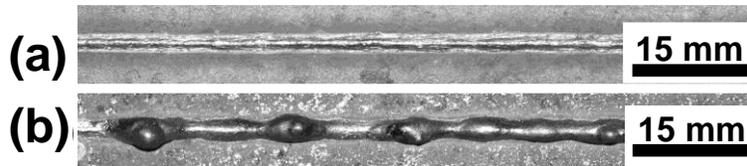
Figure 66: The bottoms of weld beads (a) 7 without oxide and (b) 8 with oxide scale show the effect of surface tension on the formation of root defects.

4.4 Root Defect Structure Characterization

Analysis of micrographs, specifically Figure 64b and Figure 65b, revealed complex porosity structures in the root defect nuggets. The porosity did not appear to be related to keyhole collapse, and some porosity was linked to the surface, observable after welding. In order to understand the internal structure of the defects, the root defect nuggets were characterized using X-ray CT, which non-destructively evaluates internal defects by differentiating regions by density. Within a metal structure, pores appear brighter since fewer X-rays are absorbed. Typical internal structures of root defects formed during hybrid laser-arc welding and laser welding are shown in Figure 67. The porosity is represented by the yellow colored shapes within the defects. The large pore in the hybrid weld is fully interconnected. Eight arms start at the edges of the weld and extend

(a)   **(b)**
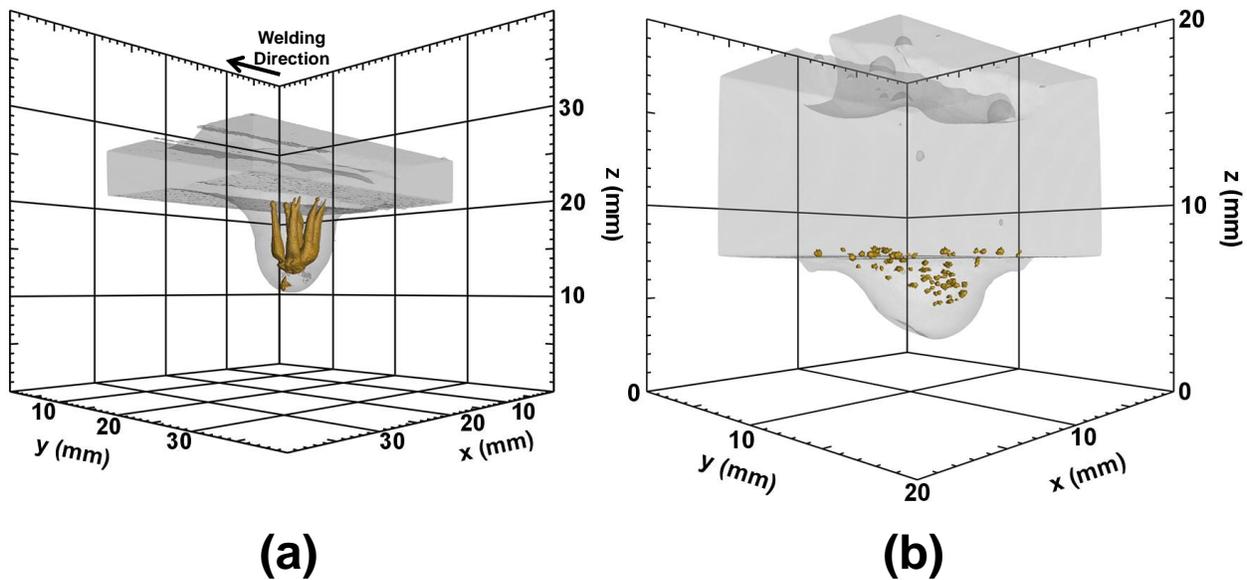
Figure 67: The internal structure of root defects in (a) hybrid laser-gas metal arc weld in 4.8 mm thick plate (weld 6) and (b) laser weld in 9.5 mm thick plate (weld 3) as determined by X-ray computed tomography. The direction of welding is indicated by the arrow in (a). The strands of porosity that stretch from the bottom of the plate and connect in the center of the defect as shown in (a) were common in all the hybrid welds where root defects formed. In (b) only individual pores are observed. Evidence of gouging due to material loss to root defects can be observed at the top of the plate.

down to the bottom of the root defect nugget where they connect to a large central pore. This interconnected porosity contrasts with pores shown in Figure 67b for a laser weld fabricated in thicker plate of 9.5 mm plate compared to the 4.8 mm plate used in the hybrid weld. In the laser weld, there is a dispersion of smaller spherical pores, which are only present in the top half of the defect. Large gouges in the top surface resulting from the loss of material to the defect are also visible in Figure 67.

Clearly, the laser and hybrid welding processes produced different pore shapes and sizes within the weld defects. Typically, in laser welding processes, where large spherical pores are present, keyhole collapse [7] results in pores centered on the laser beam axis. However, several characteristics do not support the proposition that keyhole dynamics cause root defects. These characteristics include video evidence of root defects forming and growing along the length of the pool away from the keyhole [12], X-ray CT images of complex pore networks, and different structures for different welding processes. The most likely explanation is that the additional forces in arc welding, such as the arc pressure and droplet impact force, led to the network of pores observed in Figure 67a.

4.5 Mechanism of Root Defect Formation

The formation of weld root defects can be viewed as a force balance between the weight force, the surface tension force, and the arc force, with the weight and arc forces acting in the same direction. The values for weight force and surface tension force can be estimated from Eq. 1 and Eq. 2. The calculations for Eq. 1 are straightforward. For Eq. 2, the length and width of the pool at the bottom surface must be known. For the calculations here, the length, which cannot be directly measured, is assumed to be twice the width, which can be measured directly from the weld. Because the reciprocal of each value is used for the surface tension calculation, the selection of the length values are not as important as accurate measurement of the widths, which are given in Table 5.

For the purposes of calculating a force balance, the available maximum curvature of the pool for surface tension is expected to be defined by the length and width of the molten pool at the bottom surface. If the curvature of the pool exceeds the maximum (i.e. the term in parentheses in Eq. 14), the weld is expected to form root defects. The arc pressure cannot be directly calculated like the other two forces. Experiments have been performed to measure the force, and the results have been reported. The maximum arc pressure for currents between 100 A and 220 A is expected to be between 1040 N/m^2 and 1920 N/m^2, based on the work by Lin and Eager [21]. The values for arc force estimated from the literature are shown in Table 6 [21].

The results of the force balance between weight and arc force and surface tension are shown in Figure 68. The numbers next to each point indicate which weld is plotted. Error bars represent

Table 6: Average and standard deviations of width of the pool at the bottom and the estimated arc force are listed.

Weld Number	w (mm)	Arc Force (N/m^2)
1	1.6 ± 0.2	0
2	1.5 ± 0.1	0
3	2.5 ± 0.1	0
4	2.5 ± 0.1	1040
5	2.6 ± 0.3	1260
6	3.3 ± 0.4	1920
7	2.2 ± 0.3	1040
8	2.0 ± 0.2	1040

the spread in values calculated with the uncertainty for each measured dimension given in Table 5. The force balance, $F_g = F_s$, line defines the boundary between regions where root defects will and will not occur. The formation of root defects is predicted correctly in seven out of eight welds. The assumptions do not entirely capture the effect of increasing the plate thickness from 4.8 mm to 9.5 mm (i.e. weld 3). While the forces promoting root defects increase compared to the other two laser welds (welds 1 and 2) and the surface tension force decreases compared to the same welds, the combined effect is not enough to move the weld into the root defect region.

Because there is no arc force in the laser welds, these welds (1,2, and 3) have the lowest forces promoting the formation of root defects (i.e. points closest to the x-axis). The forces due to gravity did not exceed 340 N/m^2 for the 4.8 mm thick plate and 670 N/m^2 for the 9.5 mm thick plate, while the calculated surface tension forces varied from 1060 N/m^2 and 1760 N/m^2. According to the model used in Figure 68, this surface tension variation is high enough to retain the liquid metal weight and not form defects, with the exception of weld 3, which did form defects during experimental welds.
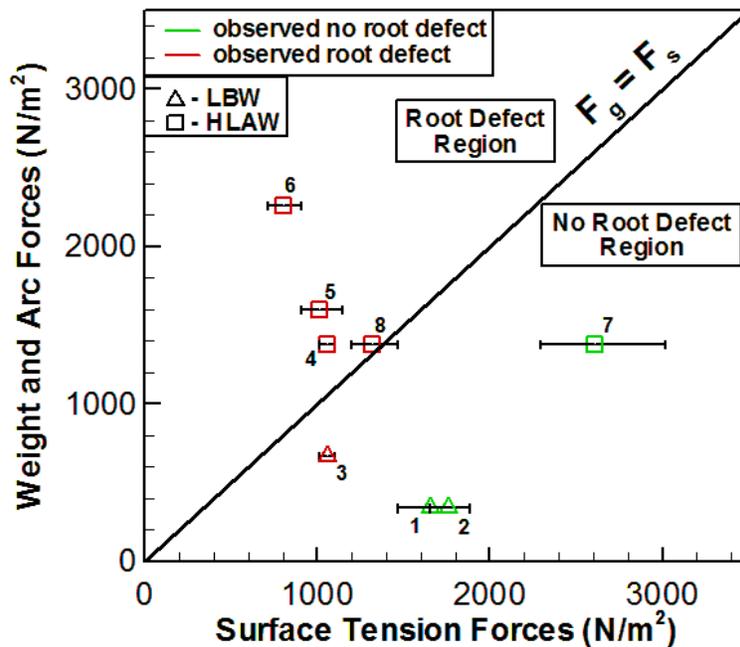
Figure 68: The comparison of surface tension force and weight force for the experimental welds considered is shown. The numbers next to each weld indicate the processing conditions as shown in Table 1. Compared to experimental results all the welds are found to be on the correct side of the $F_g = F_s$ line.

For the laser and hybrid laser-arc welds with the same 30 mm/s welding speed (1, 4, 5, 6), the model predicts increasing defect-promoting forces, arc and weight forces, from 340 N/m^2 to 2260 N/m^2 due to increasing heat input, and the surface tension decreases by a factor of two from 1650 to 800 N/m^2. The model predictions for these welds agree with the experimental observations. The force balance also captures the differences in welds on plates with and without bottom surface oxide and identical process conditions (7 and 8) with identical defect promoting forces of 1380 N/m^2. With the presence of the oxide scale, though, weld 8 possesses only 50% of the surface tension force of weld 7, which had no oxide scale. These results indicate that representation of the root defect formation phenomenon as a quantitative force balance between weight and arc forces and surface tension allows for a qualitative prediction of an important welding defect.

Figure 68 assumes a constant temperature near the melting point and, therefore, a constant liquid metal density and surface tension. In reality, the temperature (and density and surface tension) varies spatially in three dimensions, creating a much more complicated problem that cannot be fully captured with this analysis. In addition, the net recoil pressure (i.e. from the top
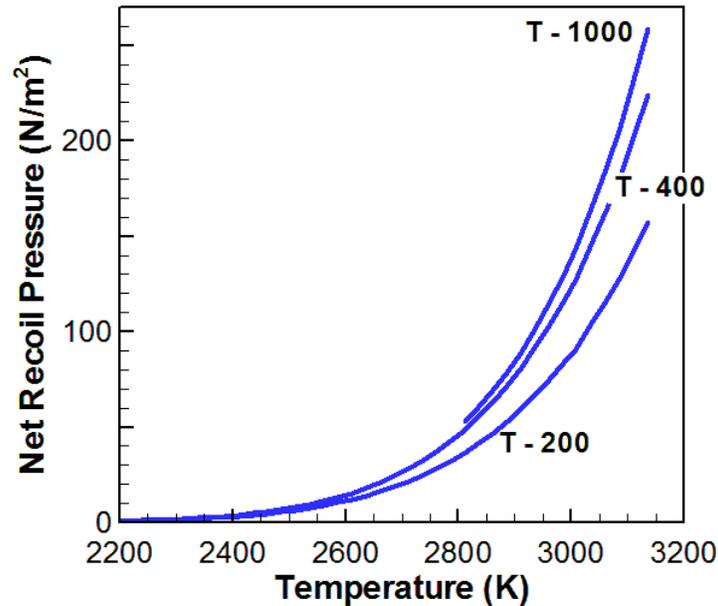
Figure 69: The net recoil pressure is calculated from the difference experienced by the liquid metal at the top and bottom of a liquid column. The top surface temperature is shown on the x-axis, and the bottom surface temperatures are shown in the plot.

and bottom surfaces of the pool) from the evaporating liquid metal has not been accounted for and varies, as shown in Figure 69. The recoil pressure is calculated as

$$P_r = J_v^2 / \rho_v \tag{3}$$

where J_v is the evaporation flux and ρ_v is the density of the evaporating gas. The evaporation flux can be calculated as

$$J_v = P_v(T)\sqrt{\frac{M}{2\pi RT}} \tag{4}$$

where P_v is the vapor pressure at temperature T and M is the molar mass. The temperature at a given x-y location on the top surface (z_t) of the pool is generally higher than the same x-y position at the bottom surface (z_b) of the pool [26]. This difference results in a higher recoil pressure at the top surface and an additional force acting to promote defects. Including this force into Figure 68 would move weld 3 vertically up and significantly closer to $F_g = F_s$ line, indicating that the inclusion of additional forces could improve the predictive value of the force balance model.

4.6 Process Maps for Full Penetration Laser Welding

The results described above indicate that both heat input and plate thickness affect the formation of root defects in DH36 steel and are expected to play a role in other alloys. For given laser welding parameters, material properties, and plate thicknesses, however, the developed model cannot provide a broader predictive capability of root defect formation. Additionally, the process parameters that produce defect free full penetration welds are bounded by other laser-material interaction modes, such as cutting and partial penetration laser welding. In order to address these additional complexities, process maps that tie together laser welding parameters, material properties, heat input, plate thickness, and laser-material interaction modes are constructed for different alloy systems. Comparison of process maps for different alloys should show where similarities exist and what conclusions apply across material types.

Process maps have been constructed for laser processing of low carbon steels and 304 stainless steel. The non-dimensional heat input per unit length, which is similar to that used by De and DebRoy [27] includes laser welding parameters and material properties and is defined as

$$H^* = \frac{\frac{\eta P}{U}}{\rho(h+\Delta H_v)\pi r_b^2} \tag{5}$$

where η is absorptivity, P is laser power, r_b is the laser beam radius at focus, U is the welding speed, ρ is the liquid metal density, h is the enthalpy of the liquid at the boiling point, and ΔH_v is the heat of vaporization. Both the numerator and denominator have units of energy per unit length, J/m. Equation 5 compares the amount of energy absorbed from the laser per unit length in the numerator to the amount of energy per unit length necessary to heat the alloy from room temperature to the boiling point (denominator). For the experiments considered here, H* is typically greater than one, indicating that absorbed laser energy is a multiple of the energy to heat the alloy to the boiling point. The material property values that were used to calculate H* for each alloy are given in Table 7. Estimated resistivities [24] were used to calculate absorptivity [28], and density, enthalpy, and heat of vaporization were obtained from available references [24,29].

Table 7: The values listed below were used to construct the process maps. Absorptivity, η, depends on the wavelength of the laser beam.

Alloy	η - 1μm	η - 1.3 μm	η - 10.6 μm	ρ (kg/m3)	h (kJ/kg)	ΔH_v (kJ/kg)
steel	0.34	0.31	0.12	7030	2390	6260
304 SS	0.34	0.31	0.12	7070	2290	6330
Ti-6Al-4V	0.35	0.32	0.13	3970	2860	8810
AM50	0.17	0.15	0.06	1540	1730	5550
AM60	0.17	0.15	0.06	1540	1730	5580
AZ31	0.17	0.15	0.06	1560	1720	5450
AZ61	0.17	0.15	0.06	1600	1730	5640
AZ91	0.17	0.15	0.06	1600	1740	5830

When H* is plotted as a function of plate thickness, four regions defining cutting, full penetration welding without defects, full penetration welding with defects, and partial penetration welding can be identified. In the case of cutting low carbon steel or stainless steel in the presence of oxygen gas, laser energy accounts for approximately half of the total energy input into the system with oxidation of liquid iron accounting for the other half [30,31]. Other processes, such as hybrid laser-arc welding, are not considered in these maps, but as shown previously, the addition of another heat source can increase the probability of root defect formation.

The process maps for the laser welding of low carbon steel [18,30,32-56], 304 stainless steel [14-16,42,43,57-73], Ti-6Al-4V [74-84], and Mg-Al alloys [1,85-100] are shown in Figure 70. The Mg-Al alloys contain between 3 and 9 wt.% Al and combined amounts of Zn and Mn up to 1.3 wt.%. Experimental H* data for cutting, full penetration welds without root defects, and partial penetration welds are determined by macrographs of the welds or explicit statements in the text and plotted for every material type. Root defects reported in the literature are assumed to form because of the competition between the surface tension and the weight of the liquid metal and not
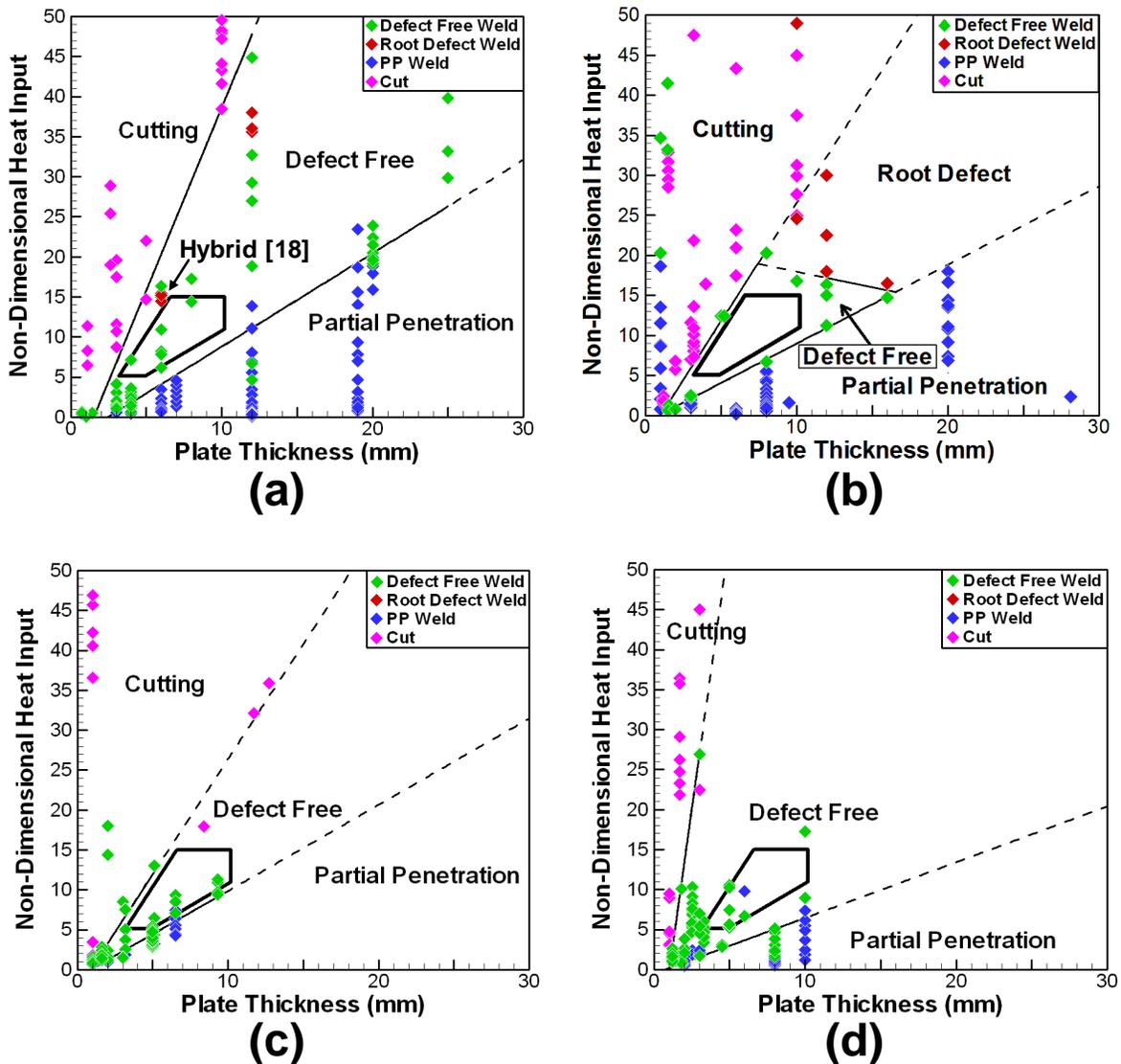
Figure 70: Process maps for (a) low carbon steels, (b) 304 stainless steel, (c) Ti-6Al-4V, and (d) Mg-Al-Zn-Mn alloys were constructed from available reports of laser welding and cutting experiments. The maps indicate with what processing conditions acceptable full penetration welds can be made with respect to other interaction modes.

other phenomena, such as keyhole instability, which leads to macroporosity. The lines defining each region are fit to the full penetration laser welding data, except in the case of the Ti-6Al-4V cutting line, which is fit to cutting data points for titanium [83]. All the conditions shown are for a laser only, except as indicated in Figure 70a, where a set of hybrid laser-GMAW conditions [18] is used to show another case of root defects in low-carbon steel.

The points indicating root defect formation for low carbon steel in 12 mm thick plate [34] are situated close to the cutting/full penetration transition line, and, therefore, it is difficult to determine the exact defect/defect-free transition line for full penetration welds . On the other hand, in the case of 304 stainless steel, which has more data available, a line indicating the transition from defect free welds to welds with root defects can be drawn and fully encloses the full penetration laser welding space for the alloy. According to the process map, the laser welding parameters for full penetration welds in excess of 16 mm are very limited, so only careful selection of processing parameters can produce a defect free weld. For the same space in low carbon steel, relatively thick plates of 25 mm can be welded at non-dimensional heat inputs of 40 or less.

Comparison of the process maps shows relatively similar behaviors at lower heat inputs and plate thicknesses. This similarity across process maps is highlighted by the thick solid black line, which encloses an identical process space in the defect free zone, and can be used to produce defect free full penetration welds for each alloy. For example, process parameters yielding an H* of 12 will produce a defect free weld in 8 mm thick plate of low carbon steel, 304 stainless steel, Ti-6Al-4V, and Mg-Al alloys. Identical H* values for plate thicknesses between 3.5 mm and 10 mm can be used across alloy systems. The parameters shown in Figure 70 can speed process parameter development, especially in thick plates, where greater heat inputs lead to longer cooling times between trial welds. For example, if laser optics are fixed (i.e. minimum laser beam radius cannot change), then welding engineers can quickly select non-dimensional heat input from Figure 70 for a given plate thickness and use Eq. 5 to calculate the laser powers and welding speeds that will produce defect free, full penetration welds.

At higher heat inputs and plate thicknesses, the behaviors of each alloy diverge. A very small defect free full penetration process space is observed in 304 stainless steel, and the same space in Ti-6Al-4V is highly constrained between the cutting and partial penetration regions. The opposite is observed in low carbon steels and Mg-Al alloys with the latter having the widest

process space for full penetration welds. The process maps indicate that two conditions are necessary before root defects can form during laser welding. First, the plate thickness must be 10 mm or greater. Second, the non-dimensional heat input must be greater than 16, which is also a minimum value associated with root defects. Once these two conditions are met, root defects are likely to form. However, as shown in the process maps, satisfying the conditions does not guarantee root defect formation. For example, the mean average H* value for root defect formation in low carbon steel and 304 stainless steel laser welds is 33, so the chances of forming root defects increases as the heat input increases. The only time these conditions stated above were met for Ti-6Al-4V and Mg-Al alloys was for 10 mm thick AZ31 plate [84] and an H* value of 17. In this case, these conditions produced a defect free full penetration weld.

From the process maps, 304 stainless steel is more susceptible to root defect formation than low carbon steel. The reason is the difference in surface tension, which is 1.91 N/m [23] and 1.17 N/m [101] for steel and stainless steel, respectively. The density of liquid steel is 7030 kg/m^3 and 7070 kg/m^3 for 304 stainless steel [24]. Both surface tension and density should affect the formation of root defects, and only surface tension is very different between the two alloys.

Close inspection of Figure 70 indicates that root defects are associated with relatively higher heat inputs. For low carbon steel, the root defects in both laser and hybrid welding conditions are close to the cutting transition line, indicating high heat input. In the case of 304 stainless steel, all the heat inputs associated with root defects are greater than the defect free heat inputs for the same plate thicknesses, 10, 12 and 16 mm. Some researchers have concluded that the root defects are associated with low heat input [11,18,34]. However, the data compiled in Figure 70 suggest that the opposite is true. In cases where lower heat inputs certainly led to root defect formation in a single study, it appears that the researchers were already operating at a high heat input. For example, for 12 mm thick low carbon steel plate [34] and non-dimensional heat inputs between 35 and 40, defects formed, but at lower heat inputs of 29 and 33 and higher heat inputs of 45 and 50 root defects did not form. Additionally, all of these heat inputs are relatively high because full penetration defect free welds were made at non-dimensional heat inputs as low as 5 and 7 [34]. By considering the whole range of process parameters captured in the non-dimensional heat input parameter, the fact that root defects are a high heat input phenomenon becomes clear and unambiguous.

4.7 Summary and Conclusions

The formation of root defects in full penetration laser and hybrid laser-arc welding has been experimentally and theoretically investigated. Welding parameters, plate preparation, and plate size were varied to produce welds with and without root defects. Optical microscopy and X-ray CT were used to characterize the internal structure of the defect nuggets for different welding processes. A force balance between the weight of the liquid metal and the surface tension was developed to describe the competing forces driving the onset of defect formation. Process maps for four alloy systems have been constructed based on the experimental welding and cutting parameters reported in the literature. The conclusions of this work are listed below.

1. The qualitative effect of surface tension and weight of liquid metal on the formation of root defects was determined by varying the welding parameters. A decrease in surface tension due to the presence of oxide scale on the bottom plate surface led to the defect formation while no defects formed for the same conditions on a plate with the oxide scale removed. Larger weld pools were formed either by increasing heat input with the addition of an arc or laser welding on 9.5 mm thick plate. The larger pools led to root defects, while the laser welds on 4.8 mm thick plate formed smaller pools and did not result in root defects.

2. With the use of X-ray CT, the internal structure of defect nuggets formed during hybrid laser-arc and laser welding were found to be different. In hybrid welding, the structure consisted of a network of large pore strands that stretched from the edge of the bottom weld bead to the center of the defect nugget. On the other hand, defect nuggets resulting from a laser weld showed a dispersion of small spherical pores. The additional arc pressure and droplet impact forces in hybrid welding are the likely factors for the difference in porosity structure.

3. Based on the observations of surface tension and weight of liquid metal, a force balance between the two was developed for an idealized weld pool and applied to the experimental conditions used in the study. The force balance calculations matched the experimental observations in terms of root defect formation for all of the cases considered. The results showed that the force balance has utility for predicting the defect formation, assuming the pool geometry is known or can be calculated.

4. The process maps for low carbon steel and 304 stainless steel revealed that H* values between 5 and 15 can be used to fabricate defect free welds in plate thicknesses between 3.5 and 10 mm for the two alloys considered.

5. The compiled data showed that two conditions, plate thicknesses greater than 10 mm and H* values greater than 15, must be met before root defects can form. Consideration of the heat inputs necessary to form root defects in low carbon steel and stainless steel demonstrated that root defects are a high heat input phenomenon, so in most cases, reducing heat input will eliminate defect formation.

<u>4.8 References</u>

[1] Zhang, J., Shan, J. G., Ren, J.L, and Wen, P. 2013. Reducing the porosity in die-cast magnesium alloys during laser welding. *Weld. J.* 92 (4): 101-s to 109-s.

[2] Roepke, C., Liu, S., Kelly, S., and Martukanitz, R. 2010. Hybrid laser arc welding process evaluation on DH36 and EH36 steel. *Weld. J.* 89 (7): 140-s to 150-s.

[3] Sachez-Amaya, J. M., Boukha, Z., Amaya-Vazquez, M. R. and Botana, F. J. 2012. Weldability of aluminum alloys with high-power diode laser. *Weld. J.* 91 (5): 155-s to 161-s.

[4] Victor, B., Farson, D. F., Ream, S., and Walters, C. T. 2011. Custom beam shaping for high-power fiber laser welding. *Weld. J.* 90 (6): 113-s to 120-s.

[5] Wu, S. C., Yu, X., Zuo, R. Z., Zhang, W. H., Xie, H. L., and Jiang, J. Z. 2013. Porosity, element loss, and strength model on softening behavior of hybrid laser arc welded Al-Zn-Mg-Cu alloy with synchrotron radiation analysis. *Weld. J.* 92 (3): 64-s to 71-s.

[6] Ribic, B., Palmer, T. A., and DebRoy, T. 2009. Problems and issues in laser-arc hybrid welding. *Int. Mater. Rev.* 54 (4): 223 to 244.

[7] Matsunawa, A., Kim, J.-D., Seto, N., Mizutani, M., and Katayama, S. 1998. Dynamics of keyhole and molten pool in laser welding. *J. Laser Appl.* 10 (6): 247 to 254.

[8] Tucker, J. D., Nolan, T. K., Martin, A. J., and Young, G. A. 2012. Effect of travel speed and beam focus on porosity in alloy 690 laser welds. *JOM* 64 (12): 1409 to 1417.

[9] Madison, J. D., and Aagesen, L. K. 2012. Quantitative characterization of porosity in laser welds of stainless steel. *Scripta Mater.* 67 (9): 783 to 786.

[10] Salminen, A., Piili, H., and Purtonen, T. 2010. The characteristics of high power fibre laser welding. *Proc. IMechE, Part C J. Mech. Eng. Sci.* 224 (C5): 1019 to 1029.

[11] Havrilla, D., Rominger, V., Holzer, M., Harrer, T., and Andreev, A. 2013. Advanced welding techniques with optimized accessories for high brightness 1 μm lasers. *Proc. SPIE 8603, High-Power Laser Mater. Process.: Lasers, Beam Deliv., Diagn., and Appl. II.* ed. F. Dorsch, 86030N. SPIE.

[12] Ilar, T., Eriksson, I., Powell, J., and Kaplan, A. 2012. Root humping in laser welding – an investigation based on high speed imaging. *7th Conf. Laser Assist. Net Shape Eng./Int. Conf. Photonic Eng.* eds. M. Schmidt, F. Vollertsen, and M. Geiger, pp. 27-32. Elsevier Sci.

[13] Punkari, A., Weckman, D. C., and Kerr, H. W. 2003. Effects of magnesium content on dual beam Nd:YAG laser welding of Al-Mg alloys. *Sci. Technol. Weld. Joining* 8 (4): 269 to 281.

[14] Zhang, M., Chen, G., Zhou, Y., and Liao, S. 2014. Optimization of deep penetration laser welding of thick stainless steel with a 10 kW fiber laser. *Mater. Des.* 53: 568-576.

[15] Bachmann, M., Avilov, V., Gumenyuk, A., and Rethmeier, M. 2014. Experimental and numerical investigation of an electromagnetic weld pool support system for high power laser beam welding of austenitic stainless steel. *J. Mater. Process. Technol.* 214 (3): 578-591.

[16] Kaplan, A. F. H., and Wiklund, G. 2011. Advanced welding analysis methods applied to heavy section welding with a 15 kW fibre laser. *Weld. World* 53: 295 to 300.

[17] Ohnishi, T., Kawahito, Y., Mizutani, M., and Katayama, S. 2013. Butt welding of thick, high strength steel plate with a high power laser and hot wire to improve tolerance to gap variance and control weld metal oxygen content. *Sci. Technol. Weld. Joining* 18 (4): 314 to 322.

[18] Piili, H., Salminen, A., Harkko, P., and Lehtinen, J. 2008. Study of phenomenon of fibre-laser-mig/mag-hybrid-welding. *ICALEO 2008 – 27th Int. Congr. Appl. Lasers Electro-Opt.* pp. 506-515. Laser Inst. of America.

[19] Avilov, V. V., Gumenyuk, A., Lammers, M., and Rethmeier, M. 2012. PA position full penetration high power laser beam welding of up to 30 mm thick AlMg3 plates using electromagnetic weld pool support. *Sci. Technol. Weld. Joining* 17 (2): 128 to 133.

[20] Bachmann, M., Avilov, V., Gumenyuk, A., and Rethmeier, M. 2012. Numerical simulation of full penetration laser beam welding of thick aluminium plates with inductive support. *J. Phys. D: Appl. Phys* 45 (3): 035201.

[21] Lin, L., and Eager, T. W. 1986. Pressures produced by gas tungsten arcs. *Metall. Trans. B.* 17B (3): 601 to 607.

[22] Keene, B. J. 1988. Review of data for the surface tension of iron and its binary alloys. *Int. Mater. Rev.* 33 (1): 1 to 37.

[23] Keene, B. J. 1993. Review of data for the surface tension of pure metals. *Int. Mater. Rev.* 38 (4): 157 to 192.

[24] Gale, W. F. 2004. *Smithells metals reference book, 8th Edn.* Burlington, MA, Elsevier Butterworth-Heinemann.

[25] M.C. Bagatini, V. Zymla, E. Osorio, and A.C.F. Vilela, 'Characterization and Reduction Behavior of Mill Scale', ISIJ Int. 51 (7): 1072 to 1079

[26] H.L. Wei, J.J. Blecher, T.A. Palmer, and T. DebRoy, 'Fusion zone microstructure and geometry in complete-joint-penetration laser-arc hybrid welding of low-alloy steel,' Weld. J., 94 (4) 2015, 135s-144s.

[27] De, A., and DebRoy, T. 2004. A smart model to estimate effective thermal conductivity and viscosity in the weld pool. *J. Appl. Phys.* 95 (9): 5230-5240.

[28] Dowden, J., and Phiroze, K. 1995 A mathematical investigation of the penetration depth in the keyhole welding with continuous CO2 lasers. *J. Phys. D: Appl. Phys.* 28 (11): 2252 to 2261.

[29] Pakratz, L. B. 1982. *Thermodynamic properties of elements and oxides.* U.S. Dept. of the Interior, Bureau of Mines, District of Columbia.

[30] Hsu M. J., and Molian, P. A. 1994. Thermochemical modeling in CO_2 laser cutting of carbon steel. *J. Mater. Sci.* 29 (21): 5607-5611.

[31] Ivarson, A., Powell, J., and Magnusson, C. 1991. The role of oxidation in laser cutting stainless and mild steel. J. Laser Appl. 3 (3): 41 to 45.

[32] Krasnoperov, M. Y., Pieters, R. R. G. M., and Richardson, I. M. 2004. Weld pool geometry during keyhole laser welding of thin steel sheets. *Sci. Technol. Weld. Joining* 9 (6): 501-506.

[33] Sokolov, M., Salminen, A., Kuznetsov, M., and Tsibulskiy, I. 2011. Laser welding and weld hardness analysis of thick section S355 structural steel. *Mater. Des.* 32 (10): 5127-5131.

[34] Rominger, V., Haug, P., Speker, N., and Holzer, M. 2013. High-power full penetration welding behavior. *Laser Tech. J.* 10 (3): 36 to 40.

[35] Assuncao, E., Ganguly, S., Yapp, D., Williams, S., and Paradowska, A. 2011. Characterisation of residual stress state in laser welded low carbon mild steel plates produced in keyhole and conduction mode. *Sci. Technol. Weld. Joining* 16 (3): 239 to 243.

[36] Cui, C., Hu, J., Gao, K., Pang, S., Yang, Y., Wang, H., and Guo, Z. 2008. Effects of process parameters on weld metal keyhole characteristics with CO2 laser butt welding. *Lasers Eng.* 18 (5-6): 319 to 327.

[37] Hamatani, H., Miyazaki, Y., Otani, T., and Ohkita, S. 2006. Minimization of heat-affected zone size in welded ultra-fined grained steel under cooling by liquid nitrogen during laser welding. *Mater. Sci. Eng. A* 426 (1-2): 21 to 30.

[38] Ion, J. C., Salminen, A. S., and Sun, Z. 1996. Process diagrams for laser beam welding of carbon manganese steels. *Weld. J.* 75 (7): 225-s to 232-s.

[39] Oefele, F., Musiol, J., Zaeh, M. F. 2008. Influence of remote-laser-welding parameters for an 8 kW fibre laser on the seam quality of steels. *ICALEO 2008 – 27th Int. Congr. Appl. Lasers Electro-Opt.* pp. 399-405. Laser Inst. of America.

[40] Mori K., and Miyamoto, I. 1997. In-process monitoring of laser welding by the analysis of ripples in the plasma emission. *J. Laser Appl.* 9 (3): 155 to 159.

[41] Vollertsen, F., Grunenwald, S., Rethmeier, M., Gumenyuk, A., Reisgen, U., Olschok, S. 2010. Welding thick steel plates with fibre lasers and GMAW. *Weld. World* 54 (3-4): R62 to R70.

[42] Brown, R. T. 2008. Keyhole welding studies with a moderate-power, high-brightness fiber laser. *J. Laser Appl.* 20 (4): 201 to 208.

[43] Nakamura, S., Sakurai, M., Kamimuki, K., Inoue, T., and Ito, Y. 2000. Detection technique for transition between deep penetration mode and shallow penetration mode and shallow penetration mode in CO_2 laser welding of metals. *J. Phys. D: Appl. Phys.* 33 (22): 2941-2948.

[44] Kumar, N., Kataria, S., Shanmugarajan, B., Dash, S., Tyagi, A. K., Padmananbham, G., and Raj, B. 2010. Contact mechanical studies on continuous wave CO2 laser beam weld of mild steel with ambient and under water medium. *Mater. Des.* 31 (8): 3610-3617.

[45] Miranda, R., Quintino, L., Willams, S., and Yapp, D. 2010. Welding with high power fiber laser API5L-X100 pipeline steel. *5th Int. Mater. Symp./14th Conf. Soc.-Port.-Mater.* eds. L. G. Rosa and F. Margarido, pp. 592-596. Trans Tech Publ.

[46] Quintino, L., Costa, A., Miranda, R., Yapp, D., Kumar, V., and Kong, C. J. 2007. Welding with high power fiber lasers – a preliminary study. *Mater. Des.* 28 (4): 1231 to 1237.

[47] Suder, W. J., and Williams, S. 2014. Power factor model for selection of welding parameters in CW laser welding. *Opt. Laser. Technol.* 56: 223 to 229.

[48] Chen, S.-L. 1998. The effect of gas composition on the CO_2 laser cutting of mild steel. *J. Mater. Process. Technol.* 73 (1-3): 147 to 159.

[49] Lo, K. H. 2012. A comparative study on Nd:YAG laser cutting of steel and stainless steel using continuous, square, and sine waveforms. *J. Mater. Eng. Perform.* 21 (6): 907 to 914.

[50] Malikov, A. G., Orishich, A. M., and Shulyat'ev, V. B. 2009. Experimental optimization of the gas-assisted laser cutting of thick steel sheets. *Quantum Electron.* 39 (6): 547 to 551.

[51] O'Neill, W., and Steen, W. M. 1995. A three-dimensional analysis of gas entrainment operating during the laser-cutting process. *J. Phys. D: Appl. Phys.* 28 (12): 12 to 18.

[52] Powell, J., Al-Mashikhi, S. O., Kaplan, A. F. H., and Voisey, K. T. 2011. Fibre laser cutting of thin section mild steel: an explanation of the 'striation free' effect. *Opt. Lasers Eng.* 49 (8): 1069 to 1075.

[53] Shariff, S. M., Sundararajan, G., and Joshi, S. V. 1999. Parametric influence on cut quality attributes and generation of processing maps for laser cutting. *J. Laser Appl.* 11 (2): 54 to 63.

[54] Sobih, M., Crouse, P. L., and Li, L. 2007. Elimination of striation in laser cutting of mild steel. *J. Phys. D: Appl. Phys.* 40 (22): 6908 to 6916.

[55] Wandera, C., Kujanpaa, V., and Salminen, A. 2010. Laser power requirement for cutting thick-section steel and effects of processing parameters on mild steel cut quality. *Proc. IMechE Part B: J. Eng. Manuf.* 225 (B5): 651 to 661.

[56] Zaied, M., Miraoui, I., Boujelbene, M., and Bayraktar, E. 2013. Analysis of heat affected zone obtained by CO_2 laser cutting of low carbon steel (S235). *3rd Int. Congr. Adv. Appl. Phys. Mater. Sci.* eds. A. Y. Oral, Z. B. Bahsi, and A. Sonmez, pp. 323-326. Amer. Inst. Phys.

[57] Nath, A. K., Sridhar, R., Ganesh, P., and Kaul, R. 2002. Laser power coupling efficiency in conduction and keyhole welding of austenitic stainless steel. *Sadhana* 27: 383-292.

[58] Bhargava, P., Paul, C. P., Mundra, G., Premsingh, C. H., Mishra, S. K., Nagpure, D., Kumar, A., and Kukreja, L. M. 2014. Study on weld bead surface profile and angular distortion in 6 mm thick butt weld joints on SS304 using fiber laser. *Opt. Laser Eng.* 53: 152 to 157.

[59] Nakabayashi, T., Wani, F., Hayakawa, A., Suzuki, S., and Yasuda, K. 2003. Thick plate welding with Nd:YAG laser and COIL. *1st Int. Symp. High-Power Laser Macroprocess.* eds. I. Miyamoto, K. F. Kobayashi, K. Sugioka, R. Poprawe, H. Helvajian, pp. 416-421. SPIE.

[60] Panstar, H., Salminen, A., Jansson, A., and Kujanpaa, V. 2004. Quality and costs analysis of laser welded all steel sandwich panels. *J. Laser Appl.* 16 (2): 66 to 72.

[61] Kawahito, Y., Mizutani, M., and Katayama, S. 2007. Elucidation of high-power fibre laser welding phenomena of stainless steel and effect of factors on weld geometry. *J. Phys. D: Appl. Phys.* 40 (19): 5854 to 5859.

[62] Ghany, K. A., and Newishy, M. 2005. Cutting of 1.2 mm thick austenitic stainless steel sheet using pulsed and CW Nd:YAG laser. *J. Mater. Process. Technol.* 168 (3): 438-447.

[63] Hsu, M. J., and Molian, P. A. 1995. Off-axial, gas-jet-assisted, laser cutting of 6.35-mm thick stainless steel. *Trans. ASME* 117 (2): 272 to 276.

[64] Ilavarasan, P. M., and Molian, P. A. 1995. Laser cutting of thick sectioned steels using gas flow impingement on the erosion front. *J. Laser Appl.* 7 (4): 199 to 209.

[65] Purtonen, T., and Salminen, A. 2014. A study on the effect of cutting position on performance of fiber laser cutting of stainless steel tubes. *Weld. World* 58 (2): 193 to 204.

[66] Sheng, P. S., and Joshi, V. S. 1995. Analysis of heat-affected zone formation for laser cutting of stainless steel. *J. Mater. Process. Technol.* 53 (3-4): 879 to 892.

[67] Sparkes, M., Gross, M., Celotto, S., Zhang, T., and O'Neill, W. 2008. Practical and theoretical investigations into inert gas cutting of 304 stainless steel using a high brightness fiber laser. *J. Laser Appl.* 20 (1): 59 to 67.

[68] Stelzer, S., Mahrle, A., Wetzig, A., and Beyer, E. 2013. Experimental investigations on fusion cutting stainless steel with fiber and CO_2 laser beams. *7th Int. WLT Conf. Lasers Manuf.* eds. C. Emmelmann, M. F. Zaeh, T. Graf, and M. Schmidt, pp. 392-397. Elsevier Sci. BV.

[69] Wandera, C., Salminen, A., and Kujanpaa, V. 2009. Inert gas cutting of thick-section stainless steel and medium-section aluminum using a high power fiber laser. *J. Laser Appl.* 21 (3): 154 to 161.

[70] Kuo, T. Y., and Jeng, S. L. 2005. Porosity reduction in Nd-YAG laser welding of stainless steel and inconel alloy by using a pulsed wave. *J. Phys. D: Appl. Phys.* 38 (5): 722 to 728.

[71] Rizzi, D., Sibillano, T., Calabrese, P. P., Ancona, A., and Lugara, P. M. 2011. Spectroscopic, energetic and metallographic investigations of the laser lap welding of AISI 304 using the response surface methodology. *Opt. Lasers Eng.* 49 (7): 892 to 898.

[72] Hartwig, L., Ebert, R., Kloetzer, S., Weinhold, S., Dreschel, J., Peuckert, F., Schille, J., and Exner, H. 2010. Material processing with a 3kW single mode fibre laser. *J. Laser Micro/Nanoeng.* 5 (2): 128 to 133.

[73] Kawahito, Y., Mizutani, M., Katayama, S. 2009. High quality welding of stainless steel with 10 kW high power fibre laser. *Sci. Technol. Weld. Joining* 14 (4): 288 to 294.

[74] Caiazzo, F., Alfieri, V., Cardaropoli, F., and Sergi, V. 2013. Butt autogenous laser welding of AA 2024 aluminium alloy thin sheets with a Yb:YAG disk laser. *Int. J. Adv. Manuf. Technol.* 67 (9-12): 2157 to 2169.

[75] Cao, X., and Jahazi, M. 2009. Effect of welding speed on butt joint quality of Ti-6Al-4V alloy welded using a high-power Nd:YAG laser. *Opt. Lasers Eng.* 47 (11): 1231 to 1241.

[76] Cao, X., Kabir, A. S. H., Wanjara, P., Gholipour, J., Birur, A., Cuddy, J., and Medraj, M. 2014. Global and local mechanical properties of autogenously laser welded Ti-6Al-4V. *Metall. Mater. Trans. A* 45A (3): 1258 to 1272.

[77] Costa, A., Miranda, R., Quintino, L., and Yapp, D. 2007. Analysis of beam material interaction in welding of titanium with fiber lasers. *Mater. Manuf. Process.* 22 (7-8): 798-803.

[78] Lisiecki, A. 2012. Welding of titanium alloy by different types of lasers. *Mater. Manuf. Process.* 58 (2): 209 to 218.

[79] Liu, H., Nakata, K., Yamamoto, N., and Liao, J. 2012. Microstructural characteristics and mechanical properties in laser beam welds of Ti6Al4V alloy. *J. Mater. Sci.* 47 (3): 1460 to 1470.

[80] Squillace, A., Prisco, U., Ciliberto, S., and Astarita, A. 2012. Effect of welding parameters on morphology and mechanical properties of Ti-6Al-4V laser beam welded butt joints. *J. Mater. Process. Technol.* 212 (2): 427 to 436.

[81] Hilton, P., Blackburn, J., and Chong, P. 2007. Welding of Ti-6Al-4V with fibre delivered laser beams. *26th Int. Congr. Appl. Lasers Electro-Opt., ICALEO 2007*. 1607. Laser Inst. America.

[82] Astarita, A., Genna, S., Leone, C., Memola Capece Minutolo, F., Paradiso, V., and Squillace, A. 2013. Ti-6Al-4V cutting by 100 W fibre laser in both CW and modulated regime. *16th ESAFORM Conf. Mater. Form., ESAFORM 2013*, pp. 1835-1844. Trans Tech Publ.

[83] Kar, A., Carroll, D. L., Latham, W. P., and Rothenflue, J. A. 1999. Cutting performance of a chemical oxygen-iodine laser on aerospace and industrial materials. *J. Laser Appl.* 11 (3): 119-127.

[84] Scintilla, L. D., Sorgente, D., and Tricarico, L. 2011. Experimental investigation on fiber laser cutting of Ti6Al4V thin sheet. *Int. Conf. Adv. Mater. Process. Technol.* eds. M. S. J. Hashmi, S. Mridha, and S. Naher, pp. 1281-1286. Trans Tech Publ.

[85] Belhadj, A., Bessrour, J., Masse, J.-E., Bouhafs, M., and Barrallier, L. 2010. Finite element simulation of magnesium alloys laser beam welding. *J. Mater. Process. Technol.* 210 (9): 1131 to 1137.

[86] Quan, Y., Chen, Z., Yu, Z., Gong, X., and Li, M. 2008. Characteristics of laser welded wrought Mg-Al-Mn alloy. *Mater. Charact.* 59 (12): 1799 to 1804.

[87] Kim, J.-D., Lee, J.-H., and Kim, J.-S. 2010. Characteristics of butt-welded joints on AZ31 magnesium alloy using a Nd:YAG laser. *Int. J. Prec. Eng. Manuf.* 11 (3): 369 to 373.

[88] Sanders, P. G., Keske, J. S., Leong, K. H., and Kornecki, G. 1999. High power Nd:YAG and CO_2 laser welding of magnesium. *J. Laser Appl.* 11 (2): 96 to 103.

[89] Wang, Z., Gao, M., Tang, H., and Zeng, X. 2011. Characterization of AZ31B wrought magnesium alloy joints welded by high power fiber laser. *Mater. Charact.* 62 (10): 943 to 951.

[90] Weisheit, A., Galun, R., and Mordike, B. L. 1998. CO_2 laser beam welding of magnesium-based alloys. *Weld. J.* 77 (4): 149-s to 154-s.

[91] Dhahri, M., Masse, J. E., Mathieu, J. F., Barreau, G., and Autric, M. 2001. Laser welding of AZ91 and WE43 magnesium alloys for automotive and aerospace industries. *Adv. Eng. Mater.* 3 (7): 504 to 507.

[92] Harooni, M., Carlson, B., and Kovacevic, R. 2014. Detection of defects in laser welding of AZ31B magnesium alloy in zero-gap lap joint configuration by a real-time spectroscopic analysis. *Opt. Laser Eng.* 56 (): 54 to 66.

[93] Abderrazak, K., Salem, W. B., Mhiri, H., Bournot, P., and Autric, M. 2009. Nd:YAG laser welding of AZ91 magnesium alloy for aerospace industries. *Metall. Mater. Trans. B* 40B (1): 54 to 61.

[94] Scintilla, L. D., and Tricarico, L. 2013. Experimental investigation on fiber and CO_2 inert gas fusion cutting of AZ31 magnesium alloy sheets. *Opt. Laser Technol.* 46: 42 to 52.

[95] Kratky, A., Schuocker, D., and Liedl, G. 2009. Processing with kW fibre lasers – advantages and limits. 17th *Int. Symp. Gas Flow, Chem. Lasers, High-Power Lasers.* eds. R. Vilar, O. Conde, M. Fajardo, L. O. Silva, M. Pires, and A. Utkin, 71311X. SPIE.

[96] Marya, M., and Edwards, G. R. 2001. Factors controlling the magnesium weld morphology in deep penetration welding by a CO_2 laser. *J. Mater. Eng. Perform.* 10 (4): 435 to 443.

[97] Kolodziejczak, P., and Kalita, W. 2009. Properties of CO_2 laser-welded butt joints of dissimilar magnesium alloys. *J. Mater. Process. Technol.* 209 (2): 1122 to 1128.

[98] Sorgente, D., Palumbo, G., Scintilla, L. D., and Tricarico, L. 2013. Evaluation of the strain behavior of butt joints on AZ31 magnesium alloy thin sheets welded by Nd:YAG laser. *Int. J. Adv. Manuf. Technol.* 67 (9-12): 2753 to 2763.

[99] Lehner, C., Reinhart, G., and Schaller, L. 1999. Welding of die-casted magnesium alloys for production. *J. Laser Appl.* 11 (5): 206 to 210.

[100] Scintilla, L. D., Tricarico, L., Brandizzi, M., and Satriano, A. A. 2010. Nd:YAG laser weldability and mechanical properties of AZ31 magnesium alloy butt joints. *J. Mater. Process. Technol.* 210 (15): 2206-2214.

[101] He, X., Norris, J. T., Fuerschbach, P.W., and DebRoy, T. 2006. Liquid metal expulsion during laser spot welding of 304 stainless steel. *J. Phys. D: Appl. Phys.* 39 (3): 525 to 534.

Chapter 5 – Porosity in Thick Section Alloy 690 Laser and Hybrid Laser-Arc Welds

5.1 Porosity during Laser Welding of Alloy 690

While laser and hybrid laser-arc welding are faster and can potentially overcome many of the defects that arise with conventional welding processes, these laser processes are not a panacea and introduce their own unique problems. Besides root defects in full penetration welds, porosity during partial penetration welding is another potential source of catastrophic defects. In general, there are three possible types of porosity that can form in the weld pool during welding. One type of porosity results from the solubility of monatomic and diatomic oxygen, nitrogen, and hydrogen in molten metal and their corresponding low solubility in the solid metal [1]. During solidification, the solubility decreases, gas evolution occurs, and the bubbles become trapped as pores. The susceptibility of different alloys to gas evolution pores depends on the initial solubility of the gas in the weld pool. Not all alloys dissolve sufficient quantities of atmospheric gases to pose a porosity problem. Smaller pores can also coalesce during welding and form larger voids [2]. This behavior is observed in base metals with high pre-existing levels of porosity, such as die-cast magnesium alloys. For example, Zhao and DebRoy [2] found an increase in porosity compared to the base metal during laser welding of die-cast Mg due to the expansion and coalescence of pre-existing pores during laser welding.

Porosity is also produced by keyhole instability, where the bottom tip of the keyhole fluctuates during welding, and the vapor column collapses, producing large bubbles, which can be trapped in the solidifying metal. Keyhole porosity is limited to high energy beam welding processes [3] and is by far the most common cause of macroporosity in laser and hybrid laser-arc welding [4-7]. Several researchers have investigated the effects of laser welding on Alloy 690 weld geometry [8-10, 11-13] and porosity [11-13]. These previous studies have been limited to laser powers of 5.5 kW or less and resulted in full penetration welds with a maximum depth of 3 mm and partial penetration welds with depths of 6 mm or less. These low power laser welds in Alloy 690 have a high depth to width ratio [8-10, 11-13] similar to that observed in the laser welding of other common structural alloys [14,15]. In terms of porosity, Kuo et al. [11] found Alloy 690 to be more susceptible to the formation of keyhole porosity than AISI 304 stainless steel during pulsed laser welding. Tucker et al. [10] found that porosity could only be minimized through the selection of laser defocus and welding speed but not entirely avoided.

Equilibrium vapor pressure-temperature relations [16,17], such as those shown previously in Figure 7 (Ch. 1) may explain why Alloy 690 is more prone to keyhole porosity. Since only the relative differences are a concern, an ideal solution is assumed for the calculation of vapor pressure, which is the sum of the product of the mole fraction of the alloying element and the equilibrium vapor pressure for the pure substance (i.e. Fe, Cr, Ni, Ti, Al, and V) at each temperature. Near the boiling point at 1 atmosphere, the temperature gradient of vapor pressure is higher for Alloy 690 as compared to other common structural alloys. As a result, small changes in keyhole wall temperature, which will be near the boiling point, will produce larger changes in pressure, resulting in more instability and porosity. Power modulation [9], a defocused beam, and increased welding speeds have been shown to help to reduce porosity levels in laser welded Alloy 690, but there is no generally accepted methodology for eliminating keyhole porosity.

The objective of this chapter[4] is to identify and implement methods to eliminate porosity in Alloy 690 welds with a combined experimental and modeling analysis of the process, detailing the complex interactions occurring in the weld. X-ray computed tomography (CT) has been used to characterize the size and location of pores in the laser and hybrid laser-arc welds. A well tested, three dimensional (3D) heat transfer and fluid flow numerical model [18-21] is used to calculate the temperature and fluid velocity fields during laser and hybrid welding. Utilizing an analytical model [18, 22-24], the dimensions of the filler metal-molten pool mixing region can be estimated, and its effect on bubble escape analyzed. The mechanism controlling high porosity in hybrid welds is linked to the consumable filler metal electrode entering the molten weld pool at high speeds greater than 1 m/s. When combined with low laser powers and shallow weld pools, the filler metal addition inhibits the upward motion of bubbles and results in high levels of porosity. At higher laser powers, the pool is deeper and larger, in general, compared to the region where filler metal is entering the pool, so bubbles avoid being trapped in the advancing solid-liquid interface due to the increased pool size and available liquid metal below the filler metal-molten pool mixing region.

---

[4]Portions of this chapter are directly excerpted from J.J. Blecher, T.A. Palmer, and T. DebRoy, 'Porosity in thick section alloy 690 welds – experiments, modeling, mechanism, and remedy', Weld. J., **95**, 2016, 17s-26s.

5.2 Experimental Methods

Bead on plate laser and hybrid laser-GMA welds were made on 12.7 mm thick Alloy 690 plate. For both the laser and hybrid welds examined here, the same combinations of laser welding conditions were used. The laser parameters, including the laser, optics combination, and final beam focus diameter and divergence angle, were the same as previously described[5] in Chapter 4. The focus position was placed 8 mm below the top plate surface, so the beam diameter at the top surface was 0.73 mm. Consistent with beam characterization studies [25], the beam profile near focus took on a top hat distribution, while at one Rayleigh length (8.1 mm in this case) or more from focus, the beam profile took on a Gaussian shape. The welding speed and laser power were varied between 10 and 20 mm/s and 2 and 6 kW, respectively.

For the hybrid welds, a Lincoln Electric® Power Wave 455 M/STT power source with a Binzel® WH 455D water cooled welding gun was used as the GMA source. The torch angle was maintained at 15˚ from vertical. A gas mixture of Ar-25% He shielded the weld from the atmosphere at a flow rate of 2.7 m^3/hr. Inconel® Filler Metal (FM) 52 wire, which is compositionally identical to Alloy 690, as shown in Table 8, with a diameter of 1.1 mm was used as the consumable electrode. The wire feed speed was set to 121 mm/s. The laser-arc separation distance was held constant at 3 mm with the laser leading. The arc voltage was set to 32 V, and the current was estimated as 200 A based on the instantaneous values displayed on the power source, the wire feed speed, and the diameter of the filler metal wire. Standard metallographic techniques were used to prepare and analyze transverse cross-section samples removed from locations in each weld where steady state processes are expected. The samples were electrolytically etched in a 10 wt.% oxalic acid solution.

A General Electric® v|tome|x X-ray computed tomography (CT) system was used to inspect and characterize the internal porosity in each weld. X-ray CT provides a high degree of

Table 8: Composition of the Alloy 690 base metal and filler metal 52.

	Ni	Cr	Fe	Mn	Si	Ti	Al	Cu	C
Alloy 690	59.80	29.63	9.65	0.28	0.36	0	0	0.25	0.03
FM 52	60.88	29.22	8.65	0.24	0.14	0.38	0.4	0.01	0.02

[5]See Chapter 4 for a description of the laser beam propagation parameters and optics combinations used.

spatial resolution for the precise location and size of internal defects, such as pores [26]. An accelerating voltage of 250 kV and current of 200 µA were used to image the laser welds. Because the hybrid welds were approximately 10 mm wider at the top surface of the weld than the relatively narrow laser welds, the voltage and current were increased to 285 kV and 230 µA, respectively, during imaging of the hybrid welds. Using these combinations of accelerating voltage and current, the resolution in all directions was 50 µm and 66 µm for the laser and hybrid welds, respectively. DatosX® software reconstructed the individual X-ray images into a 3D representation. Volume Graphics® VGStudio Max software with the defect detection module was used to measure the sizes and locations of individual pores within the welds.

5.3 Experimental Weld Morphology and Size

The fusion zone geometry is an important characteristic for comparing partial penetration laser and hybrid welds. For example, the depth of the weld is related to the maximum weldable plate thickness in a single pass, and the width is related to the plate gap bridgeability, which allows for higher tolerances during plate fit-up before welding. Generally, hybrid welds have a greater width and a similar depth as laser welds. Transverse weld profiles obtained from a series of laser and hybrid welds produced here are shown in Figure 71. The linear heat input during laser welding
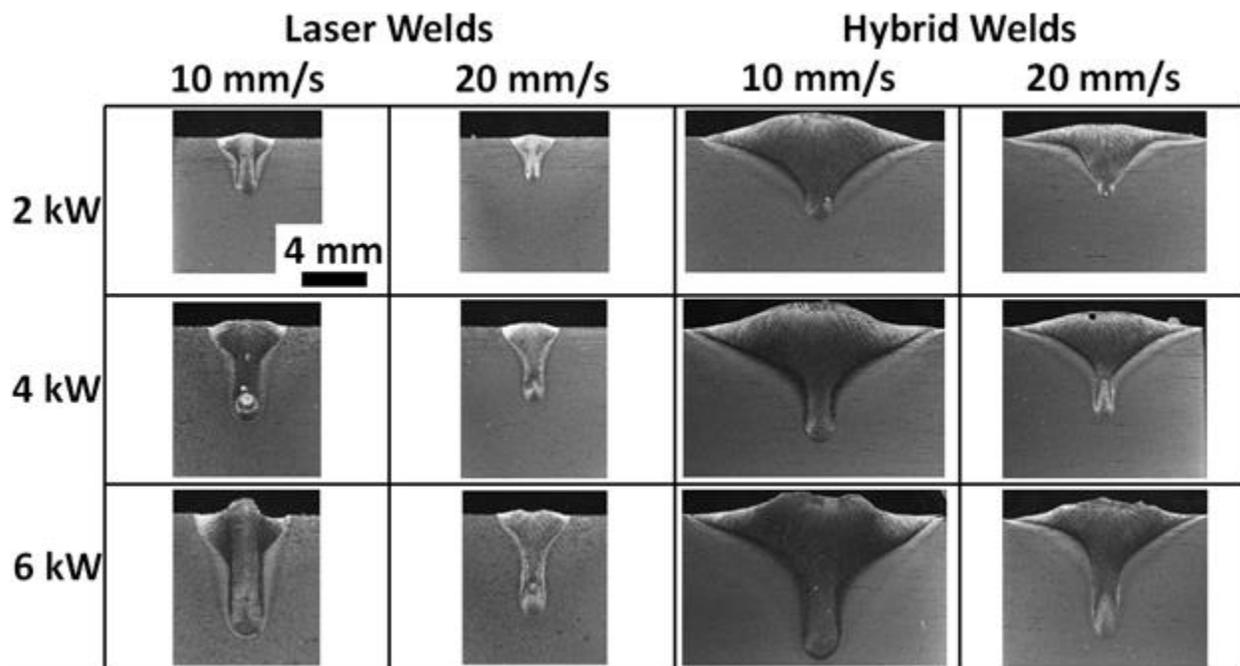
Figure 71: Laser and hybrid laser-weld transverse cross-sections of Alloy 690 are shown. The additional heat source in the hybrid welds produces much larger welds with lower aspect ratios.

was varied between 100 W/mm and 600 W/mm. On the other hand, the heat input during hybrid laser-arc welding was higher with the addition of the arc and ranged between 400 W/mm and 1200 W/mm. Alloy 690 does not exhibit a distinct fusion zone similar to steels since the nickel base alloy does not undergo a phase transformation below the melting point and is provided in the annealed state with relatively large grains. Some grain growth can be observed near the fusion zone boundary in Figure 71, especially at high heat inputs.

The measured weld pool widths and depths are shown in Table 9. For the laser welds, the width and depth increase steadily with laser power, with a maximum width and depth of 5.9 and 7.6 mm, respectively, for a weld made at a laser power of 6 kW and a welding speed of 10 mm/s. Hybrid weld depth increases with power, achieving a depth of 9.1 mm at a laser power of 6 kW, but the width does not increase significantly and ranges from 11.2 to 15.2 mm across the power range from 2 kW to 6 kW. The hybrid weld widths are significantly greater than the laser weld widths due to the addition of the arc, which acts as a broad heat source. The difference between the laser and hybrid welds in width is 5 mm or more in most cases, while the depth of the hybrid welds are about 1 to 2 mm deeper than the laser welds under identical laser powers and welding speeds.

Due to the addition of the arc and the resulting increase in heat input, the hybrid welds also display a much larger cross-sectional area than the laser welds. At laser powers of 2 kW, the influence of the arc on the hybrid weld pool shape is evident and dominates the characteristics of the weld pool. For example, the characteristic finger penetration shape of a typical GMA weld [27] is obvious at a welding speed of 20 mm/s, while at the very bottom of the weld, the finger

Table 9: Summary of weld widths and depths as a function of laser power, welding speed, and welding technique.

Power (kW)	Speed (mm/s)	Width (mm)		Depth (mm)	
		Laser	Hybrid	Laser	Hybrid
2	10	3.7	13.6	3.5	4.7
4	10	4.5	15.1	5.7	7.0
6	10	5.9	15.2	7.6	9.1
2	20	2.7	12.4	2.7	3.5
4	20	3.6	11.2	4.7	5.8
6	20	4.4	11.6	6.2	7.6

penetration representative of a laser weld can also be observed. Since the arc parameters are 31 V and about 200 A, the arc power is on the order of 6 kW, as compared to 2 kW for the laser. At higher laser powers of 4 and 6 kW, the influence of the arc on the weld pool shape is diminished due to the parity in the arc and laser powers with only the increased weld width produced by the arc being evident.

5.4 Analysis of Macroporosity

Large pores in the solidified weld metal are formed when bubbles from the bottom of the keyhole become trapped by the advancing solid-liquid interface [3]. The keyhole tip near the bottom of the weld pool fluctuates rapidly and will pinch off regularly, creating bubbles in the liquid. While the role of the laser induced keyhole in the formation of porosity in laser welding is understood, the effects of the addition of an arc in the hybrid laser-arc welding process are not. Using AISI 304 stainless steel as the base metal, Naito et al. [28] found that keyhole induced
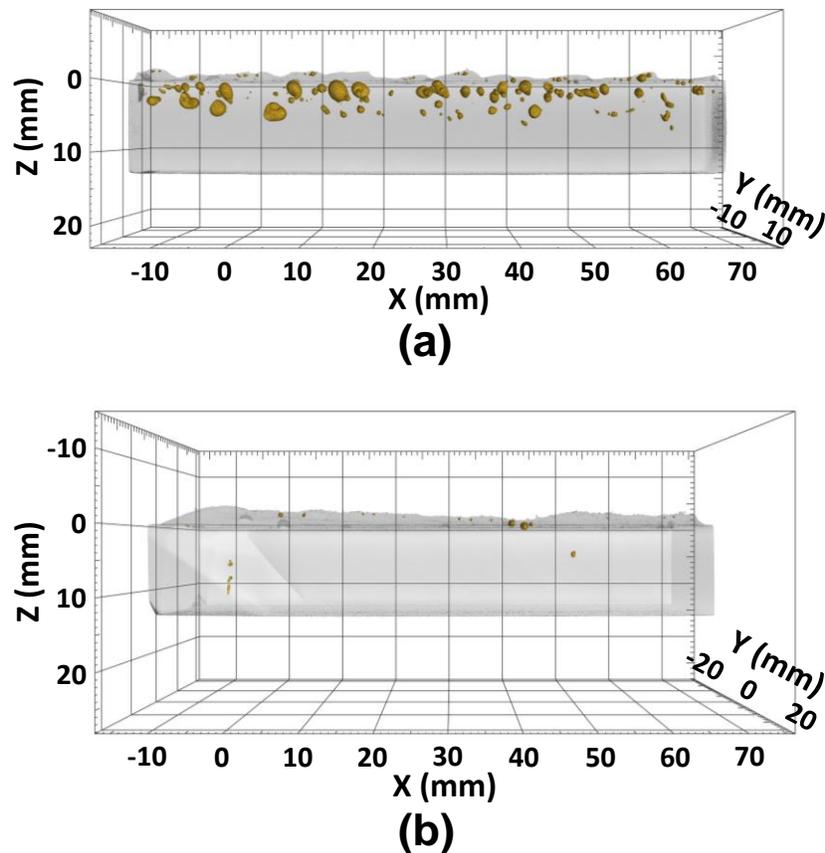
Figure 72: X-ray CT scans reveal the porosity in 6 kW 10 mm/s (a) laser weld and (b) hybrid weld. Hybrid welding significantly reduces the amount of porosity in the weld. The solid metal regions appear grey, while the pores are shown in a yellow color.

porosity is reduced but not entirely eliminated in hybrid laser-GTA welding compared to laser welding. This same relationship in Alloy 690 is explored here, using a consumable electrode rather than a tungsten electrode. A similar behavior compared to AISI 304 stainless steel is expected because the alloys have similar properties, including density, viscosity, melting and boiling points, and surface tension values. The primary difference is that Alloy 690 is more susceptible to porosity than stainless steel [29].

A comparison of porosity measured using X-ray CT scanning technologies in Alloy 690 laser and hybrid laser-arc welds fabricated using the same laser power and welding speed (6 kW, 10 mm/s) is shown in Figure 72. For the laser weld, the level of porosity detected in the laser weld is much higher than that observed in the hybrid weld. For example, 103 pores were identified in the X-ray CT scan with a median pore volume of 0.14 mm^3, while only 17 pores were detected in the hybrid weld with a median pore volume of 0.02 mm^3. In the hybrid welds, the locations of the detected pores is also important. For example, outside the start of the weld and the weld reinforcement, there is only one pore in the entire hybrid weld. This location on the weld can be
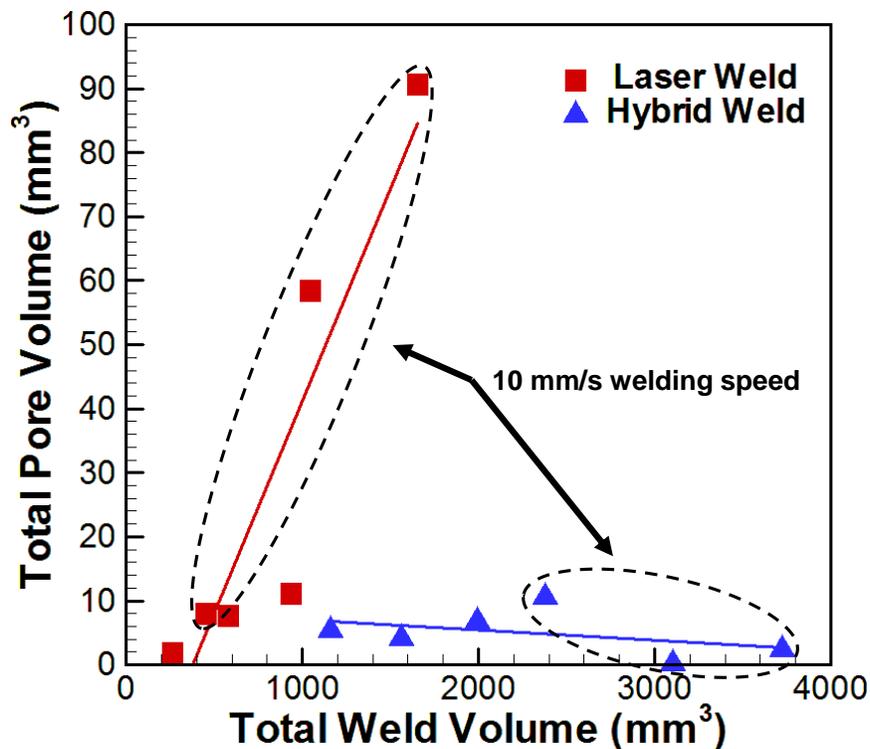
Figure 73: Total pore volume increases with the total weld volume in the laser welds, and the opposite relation is observed in the hybrid welds. Similarly, the low speed laser welds had very high pore volume, while the same hybrid welds had relatively lower pore volume.

separated from the weld region of interest by adding a 'run-on/run-off tab' that can be removed in a production environment.

The relationships between the total weld volume and the total pore volume over a 70 mm length of the laser and hybrid welds are shown in Figure 73. In the laser welds, an increase in the total weld volume leads to an increase in pore volume. The hybrid welds, in general, exhibit a decrease in total pore volume as the welds become larger. In addition, the lower speed welds in each welding technique lead to different pore characteristics. Comparing the two types of welds,
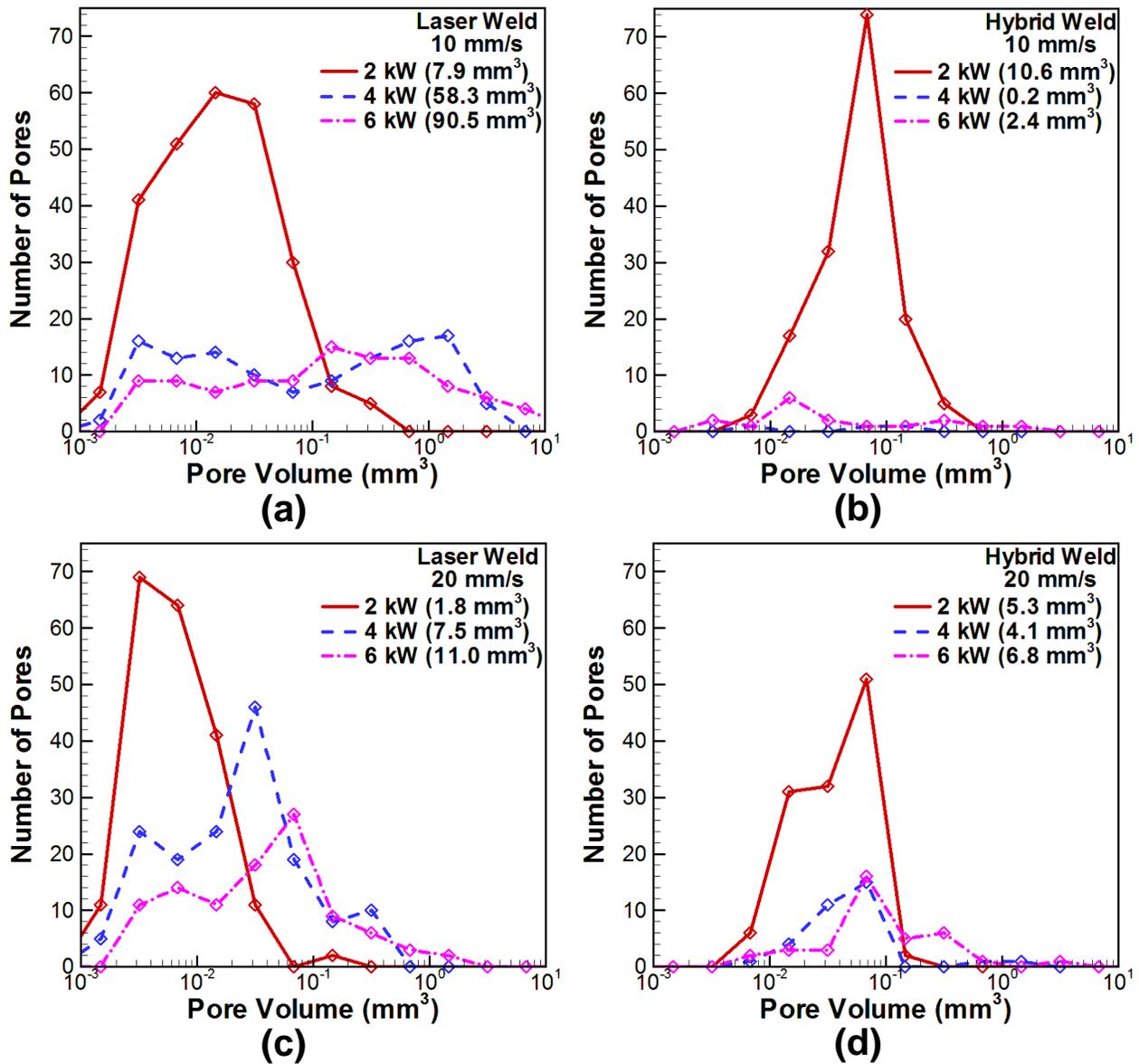
Figure 74: The pore size distributions for (a and c) laser welds and (b and d) hybrid welds and the total porosity volumes in parentheses are shown. The number of pores for almost all sizes decrease when going from laser to hybrid welding at laser powers of 4 and 6 kW.

the porosity-weld volume relationships are opposite, indicating a clear reduction in porosity with a change from laser welding to hybrid laser-arc welding. The lowest pore volumes are found in the low speed hybrid welds, while the highest pore volumes are found in the low speed laser welds.

Total pore volume and pore size distributions are important for understanding mechanisms driving porosity formation in both laser and hybrid welds. Comparisons between the pore volume and pore size distributions in laser and hybrid welds produced under a variety of conditions are shown in Figure 74. In the 4 kW and 6 kW cases, porosity decreased when transitioning from laser to hybrid welding. Clearly, the two highest heat input hybrid welds (i.e. 4 and 6 kW and 10 mm/s) have the lowest porosity values. In fact, the 4 kW weld has only 3 pores with two of those located in the weld reinforcement. The laser welds with the same laser power and welding speed conditions show much higher overall porosity levels, which are up to 90.5 mm^3 in 1600 mm^3 of weld metal. These porosity levels are many times higher than the hybrid welds, which can have porosity values as low as 0.2 mm^3 in 3000 mm^3 of weld metal.

5.5 Mechanism of Low Porosity in Higher Power Laser-Arc Hybrid Welds

However, the trends of decreasing porosity in hybrid welds do not hold constant at lower powers. For example, the 2 kW, 10 mm/s hybrid weld does not show the same low levels of porosity as the 4 kW and 6 kW hybrid welds and, in fact, has a higher porosity level than the laser weld made with the same conditions. The same is true in the hybrid welds made at this same power but a more rapid welding speed of 20 mm/s. This difference in behavior with changes in power may be traced to a combination of filler metal addition and small weld pool volume in the low power (2 kW) hybrid welds. The filler metal is entering the molten pool at a relatively high rate of speed, on the order of 1.5 m/s or faster [22]. Bubbles that form near the bottom of the keyhole need to move towards the top of the weld pool to escape. This mobility towards the top is likely hindered by the filler metal entering the pool at a high velocity. In addition, the weld pool volume is relatively small compared to the higher laser power welds, further limiting the bubble mobility towards the top of the pool. The decrease in pore volume in the laser welds with increasing welding speed is consistent with previously reported experiments [5, 30].

For similar processing conditions, the differences in porosity between the laser and hybrid welds are related to the harmful or beneficial effects of the arc and impinging filler metal depending on the selected laser power. The size of the filler metal-weld pool interaction region

can be estimated, using a cylindrical volumetric heat source (VHS) model [18]. A detailed description of the VHS model is available in the literature [23, 24], and the equations necessary for the calculations performed here are available in Appendix A. The model assumes that liquid droplets are accelerated from the end of the consumable electrode, strike the molten pool, and transfer heat and momentum to the weld. The height, depth, and energy intensity of the VHS can be calculated based on the material properties and welding parameters.

Knowledge of the relationship between the arc current and droplet detachment frequency is an important component of the calculations. Especially important is the transition from globular to spray transfer. However, most studies of droplet detachment have focused on mild steel electrodes with little attention paid to other filler metals, such as FM 52. The welding recommendations for spray transfer mode from the FM 52 manufacturer have been used to estimate the transition currents [31]. The transition current for mild steel is around 290 A, so a current of 300 A or greater will lead to spray transfer mode. The recommended parameters for FM 52 suggest the transition current varies between 150 A and 225 A, depending on the electrode diameter. The factors affecting the transition current magnitude include several thermophysical properties of the liquid and solid filler metal, the shielding gas composition, and the thickness of the wire. Since the value is influenced by several parameters, typically, the filler metal manufacturer recommendation is used, or a set of optimization experiments, where all values except current are held constant, is undertaken.

Using the experimental welding parameters and material properties, the VHS height and width can be computed. The height and diameter, which are identical for all hybrid welding cases,
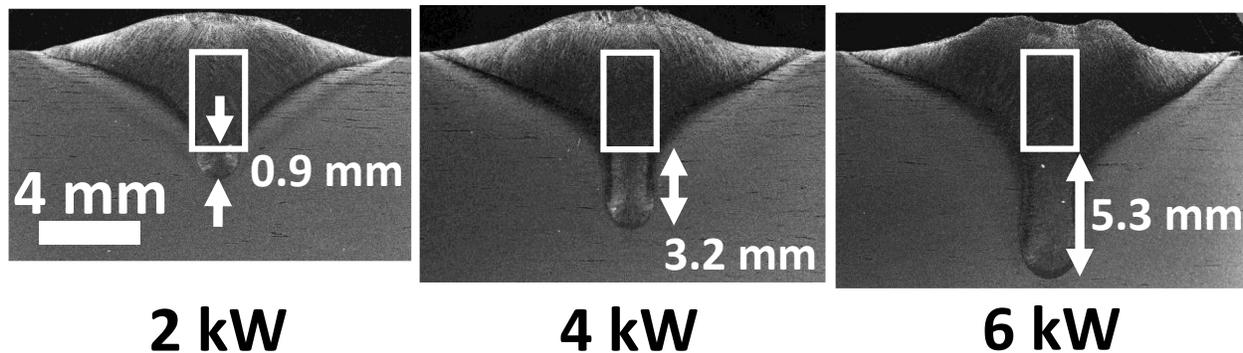
Figure 75: The calculated cylindrical volumetric heat source outline is overlaid on the 10 mm/s hybrid welds. The gap between the bottom of the heat source and weld bottom grows with laser power. The larger gap combined with a larger of weld volume behind the gap led to more pores escaping in the 4 and 6 kW welds.

132

are calculated as 3.8 and 2.1 mm, respectively. The VHS profile has been overlaid on the transverse cross-sections of the 10 mm/s welding speed hybrid welds in Figure 75 over the power range evaluated here. As the power increases, the gap between the bottom of the VHS and the bottom of the weld increases from 1 mm to more than 5 mm. The impinging droplet velocity, which is expected to interrupt pore motion through high fluid velocity turbulence, has a value of 1.6 m/s. The maximum calculated fluid flow velocity in a recent study of hybrid welding of steel was less than 0.3 m/s [32], so the high velocity of the impinging droplets would have a significant impact on fluid flow in the weld pool and would interrupt the upward pore motion in the pool and potentially trap pores within the solidifying weld pool.

The evidence for this low mobility model can be extracted from Figure 74, which shows a shift to higher pore sizes when going from laser to hybrid welding. This behavior is only seen in the 2 kW welds and suggests that bubbles stay trapped at the bottom of the weld and combine to form larger bubbles before they are entrapped as pores by the advancing solidification front. In addition, the bubbles in the hybrid welds should be trapped in the bottom part of the weld and not show a great deal of variation in location distributions if the combination of the filler metal addition
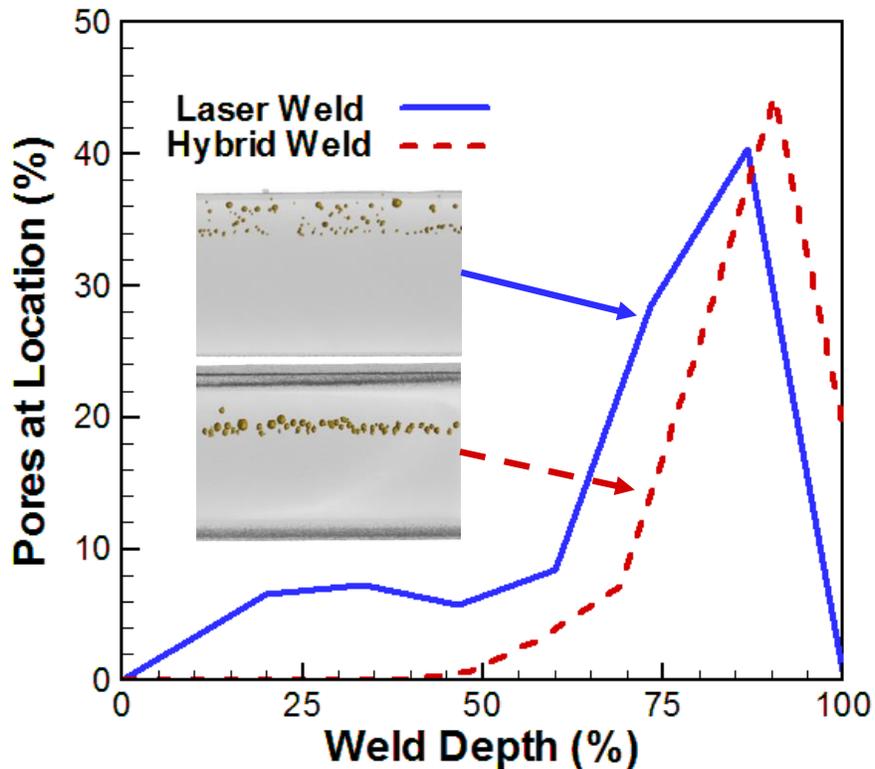
Figure 76: The pore location distributions in laser and hybrid welds for 2 kW of laser power and 10 mm/s welding speed are shown. The roots of the welds are at 100% weld depth.

and small pool volume are limiting mobility. Figure 76 shows the pore location distributions as a percentage of the total depth in the 2 kW, 10 mm/s laser and hybrid welds along with pertinent portions of the relevant X-ray CT images. In both welds, more pores are located near the bottom of the weld pool. In the laser weld, the top third of the weld contains 16% of the total number of the pores, but in the hybrid weld, zero pores are found in the same third of the weld.

5.6 Modeling Low Bubble Mobility in Low Power Hybrid Welds

While comparing the weld transverse cross-sections and the VHS dimensions provides some insight into how bubbles move through the weld pool, a more complete picture can be provided by calculating the 3D weld pool dimensions. Heat transfer and fluid flow modeling, which calculates the temperature and fluid velocity fields during welding, has been used successfully to simulate spot welding [19, 33], arc welding [18], and laser and hybrid laser arc welding for a variety of materials [20, 21, 34, 35]. The same model used recently to simulate laser welding of Alloy 690 and hybrid laser-arc welding of steel has been utilized here to calculate the temperature and velocity fields during hybrid laser-GMA welding of Alloy 690 [13, 32]. The numerical model solves the equations of conservation of mass, momentum, and energy in three dimensions (3D) for enthalpy and fluid velocities. The keyhole heat source geometry is calculated using a point by point heat balance at the keyhole wall, which is then integrated into the 3D model. The addition of filler metal is taken into account as a volumetric heat source, while the arc is considered to have a Gaussian distribution on the surface. A comparison of the experimental and
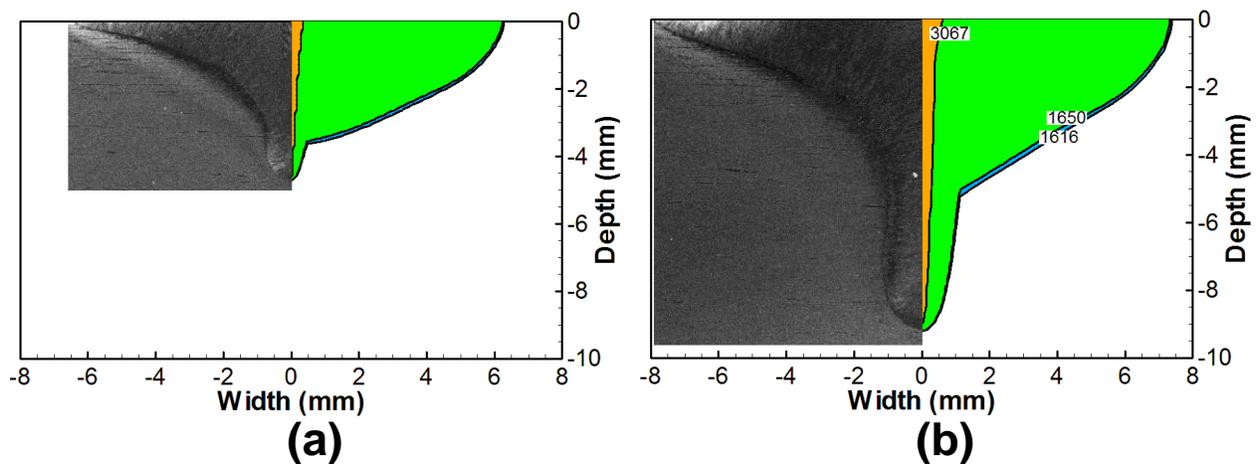
Figure 77: The experimental and calculated weld profiles for the (a) 2 kW and (b) 6 kW hybrid welds made at 10 mm/s welding speed show reasonable agreement. The temperature contours are in Kelvin.
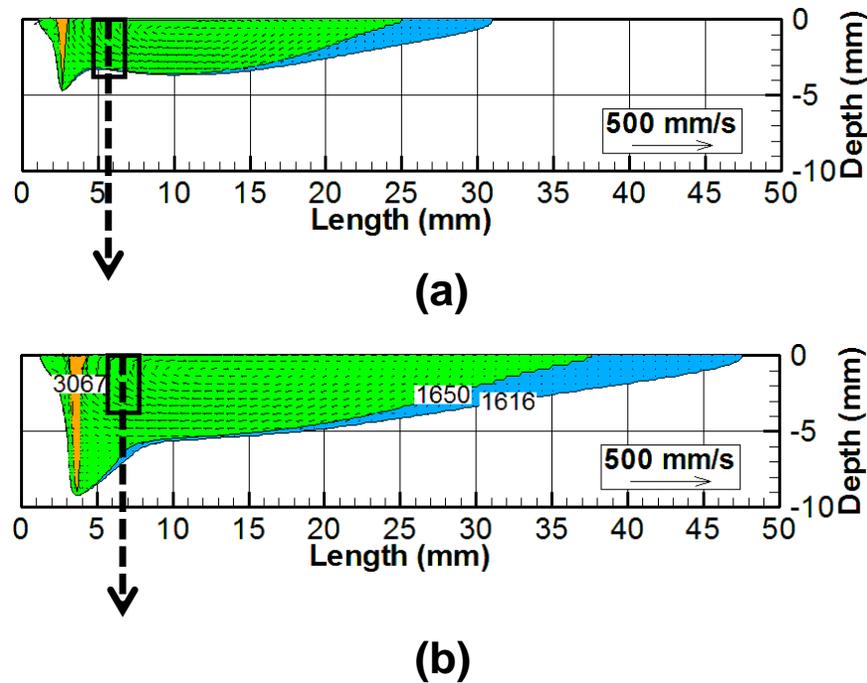
Figure 78: Calculated temperature and fluid velocity fields for the (a) 2 kW and (b) 6 kW welds hybrid laser-arc welds with 10 mm/s welding speed. The outline of the volumetric heat source and the to-scale velocity vector of the impinging metal droplets is also shown.

calculated fusion zone profiles for the hybrid welds made at 2 kW and 6 kW laser power and 10 mm/s weld speed is shown in Figure 77. The defocus in the 6 kW has been decreased to 2 mm to account for possible thermal lensing in the laser optics [25]. Once the defocus is adjusted slightly for the 6kW weld, there is good agreement between the two values.

Figure 78 shows the central longitudinal plane of the 2 and 6 kW hybrid welds with 10 mm/s welding speed. The geometry of the VHS is outlined, and the large downward pointing arrow is the to-scale velocity vector of the impinging metal droplets from the consumable electrode. In the 2 kW weld, which had a high degree of porosity, the VHS height is approximately the depth of the pool 3 mm behind the laser beam. If a bubble forms near the bottom of the keyhole, it could easily be trapped in the advancing solid-liquid interface before it has a chance to escape. In the 6 kW weld, the minimum space between the bottom of the VHS and the pool below is 1.7 mm, which allowed for most bubbles to escape the pool and not be trapped in the solid as a pore.

Laser welds had a much greater amount of porosity compared to the hybrid welds, especially at high laser powers and low welding speeds. One reason for this difference in porosity content could be the relatively low volume of the laser welds, as shown in Figure 79. The figure
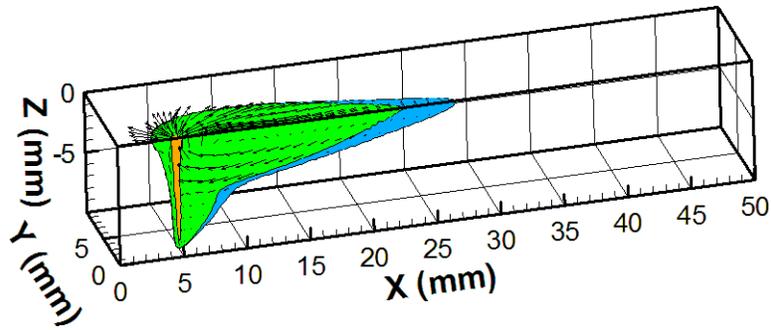
(a)
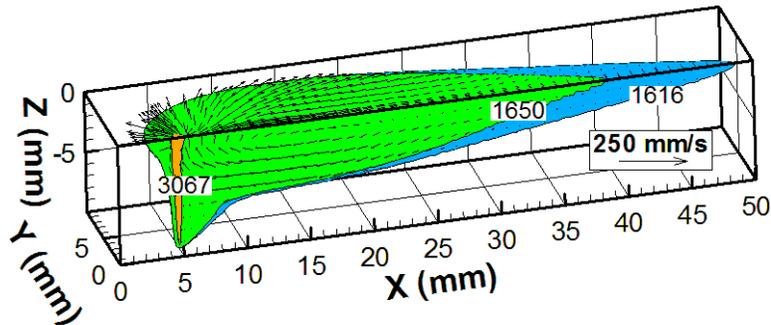
(b)

Figure 79: The 6 kW, 10 mm/s (a) laser and (b) hybrid welds are shown for comparison. In the larger hybrid weld, pores have a greater chance to escape the weld.

shows the calculated temperature and fluid velocity fields in the 6 kW, 10 mm/s laser and hybrid welds. Due to the arc, the hybrid weld is not only wider but also longer by more than 20 mm. The low weld volume leading to high porosity in laser welds is similar to the low volume and filler metal addition leading to high porosity in the low laser power hybrid welds.

5.7 Process Maps for Low Porosity Hybrid Welds

Since the likelihood of low porosity in the hybrid welds can be related to the distance between the bottom of the VHS and the bottom of the weld, the weld depth and VHS height are two dimensions which can be related to porosity. Arc current, FM 52 electrode diameter, and linear laser heat input are easily selectable welding parameters affecting these two important dimensions. Figure 80 shows the combined effect of different combinations of the welding parameters in the form of a process map with wire feed speed increased linearly with current for calculation purposes. The three non-solid lines represent the effect of the current and electrode diameter on VHS height on the left y-axis. The three regions predict linear laser heat inputs for all electrode diameters that will lead to gaps between the bottom of the VHS and the weld pool,

136

corresponding to the gaps observed in the experimental welds shown in Figure 75 (i.e. 0.9, 3.2, and 5.3 mm). Heat inputs in the lower region result in gaps of 0.9 mm, which was experimentally shown to have a high degree of porosity. VHS height-weld depth gaps of 3.2 and 5.3 mm in the middle and top heat input regions, respectively, are expected to have a low degree of porosity. The
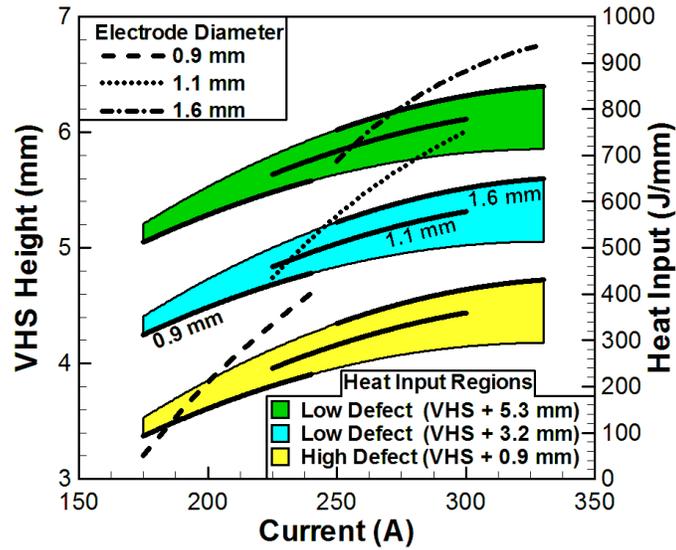
(a)
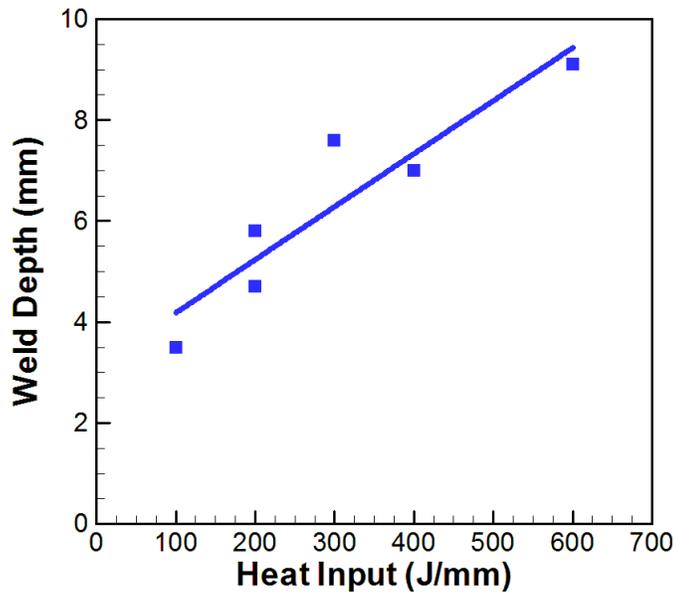
(b)

Figure 80: The volumetric heat source height for different arc currents and electrode diameters are shown in (a). The laser heat inputs to provide different porosity values is also shown in (a). The relation between weld depth and laser heat input used in (a) is shown in (b).

solid lines in each heat input region designate the exact electrode diameter dependent heat inputs. The weld depth-heat input relationship from the experimental welds is shown in Figure 80b.

The process map in Figure 80a covers the range of electrode diameters and arc currents suggested for FM 52 [32]. For a given arc current and electrode diameter, a linear laser heat input is suggested to avoid porosity. For example, if a 1.6 mm electrode diameter and arc current of 300 A is selected, then the VHS height is predicted to be 6.5 mm. According to the top two regions, a laser heat input between 630 and 830 J/mm would produce a weld depth between 9.7 and 11.8 mm and weld depth-VHS height differences between 3.2 and 5.3 mm, which have been shown experimentally to lead to low porosity. On the other hand, a heat input of 410 J/mm yields a weld depth of 7.4 mm with only a 0.9 mm difference between the VHS height and weld depth. Based on experiments, this small difference is expected to lead to a high porosity content. A spacing of 0.9 mm provides too little space for bubbles to escape the pool, and these bubbles become trapped as pores.

As shown in Figure 80, VHS height increases with both current and electrode diameter. According to the graph, the minimum heat input from the laser for low porosity increases with both arc current and electrode diameter. The minimum heat input for the 1.1 mm diameter filler metal is 460 J/mm. For the 0.9 and 1.6 mm diameter electrodes, the minimum heat inputs are 310 and 550 J/mm, respectively. For a 10 mm/s welding speed, reasonable laser powers of 5 to 6 kW can be used to fabricate low porosity welds up to 9.0 mm in depth with any FM 52 electrode diameter. However, if greater productivity is desired in terms of welding speed or penetration depth, much higher powers will be required. For example, an increase of the welding speed to 20 mm/s would require 11 kW laser power to make pore free welds with 1.6 mm diameter electrodes.

5.8 Summary and Conclusions

The characteristics of laser and hybrid laser-gas metal arc welded Alloy 690 with a compositionally identical filler metal have been analyzed for several welding conditions experimentally and theoretically. Experimental characterization of total porosity amounts was performed with X-ray computed tomography. Transverse fusion zone geometries and porosity resulting from keyhole collapse for both laser and hybrid welds have been compared and found to have significant differences, thus affecting the choice of a suitable welding process. The following conclusions were drawn from this work.

1. An analysis of Alloy 690 vapor pressure at various temperatures show that the equilibrium vapor pressures are very sensitive to small changes in temperature making Alloy 690 susceptible to macroporosity due to keyhole fluctuations during high power laser welding. X-ray computed tomography data revealed significant levels of macroporosity in keyhole mode laser welds for a wide variety of welding conditions.

2. The addition of an arc to a laser beam significantly reduced porosity levels in the high power welds. The lowest levels of porosity were observed in the hybrid welds at powers of 4 kW and 6 kW and a welding speed of 10 mm/s. A minimum porosity total of 0.2 mm^3 in a total weld volume of 3000 mm^3 was found in a hybrid weld with 4 kW laser power and 10 mm/s welding speed. In contrast, a laser weld made at a power of 6 kW and a travel speed of 10 mm/s displayed a porosity volume of 90.5 mm^3 in 1600 mm^3 of weld metal.

3. A transition from high levels of porosity to virtually no porosity was observed in the hybrid welds as power increased above 2 kW. The combination of the experimental weld characterization, calculations of the filler metal-molten pool mixing region dimensions, and three dimensional heat transfer and fluid flow modeling suggests that the mechanism of this high porosity is linked to the relative sizes of the molten pool and filler metal-molten pool mixing region. Filler metal transfer and low weld pool volume at 2 kW laser power limit upward bubble mobility out of the pool by impeding bubble motion and restricting the regions in which the bubbles can move. As the power increases, the size of the filler metal mixing region relative to the weld pool decreases, allowing the bubbles to more easily escape.

4. Experimental evidence of this mechanism included a shift in the pore size distribution to larger pores when going from laser to hybrid welding and more pores located at the bottom of the pool in hybrid welding compared to laser welding. In addition, three dimensional heat transfer and fluid flow modeling showed no gap between the bottom of the filler metal-molten pool mixing region and the bottom of the weld pool, while at higher powers, this gap increases to 2 mm and allows easy escape of the bubbles during welding. The 2 mm wide gap is larger than most, approximately 97 %, of the observed pore diameters.

5. A minimum spacing between the weld depth and filler metal-weld pool mixing region ensures a weld with low porosity. Calculations, accounting for the volumetric heat source dimensions, weld depths, and filler metal 52 electrode dimensions were incorporated into a process map to establish the combinations of arc current, linear laser heat input, and filler metal wire

diameter needed to produce low porosity hybrid laser-arc welds. The minimum heat input varied between 240 and 490 J/mm with greater heat inputs required for larger electrode diameters. With welding speeds of 10 mm/s or less, no more than 5 kW laser power would be required to produce pore free welds with every electrode diameter. Increasing welding speed or current to improve productivity or filler metal deposition would require higher laser powers.

Based on the results of this study, hybrid welding is recommended for welding thick sections of Alloy 690, especially at laser powers above 2 kW. The large amounts of porosity in the laser welds are mostly eliminated when transitioning to hybrid laser-GMA welding processes and the arc is appropriately added to the process using the proposed heat input ranges defined by process map. With optimized process parameters, macroporosity free thick section welds could be produced by hybrid welding.

5.10 References

[1] Kou, S. 2003. *Welding Metallurgy*. 2nd ed. Hoboken, NJ: John Wiley & Sons, Inc.

[2] Zhao, H. and DebRoy, T. 2001. Pore Formation during Laser Beam Welding of Die-Cast Magnesium Alloy AM60B — Mechanism and Remedy. *Weld. J.* 80 (8): 204–210.

[3] Matsunawa, A., Kim, J.-D., Seto, N., Mizutani, M., and Katayama, S. 1998. Dynamics of keyhole and molten pool in laser welding. *J. Laser Appl.* 10 (6): 247–254.

[4] Katayama, S., Kobayashi, Y., Mizutani, M., and Matsunawa, A. 2001. Effect of vacuum on penetration and defects in laser welding. *J. Laser Appl.* 13 (5): 187–192.

[5] Kawahito, Y., Mizutani, M., and Katayama, S. 2007. Elucidation of high-power fibre laser welding phenomena of stainless steel and effect of factors on weld geometry. *J. Phys. D. Appl. Phys.* 40 (19): 5854–5859.

[6] Zhao, H., Martukanitz, R. P., and Debroy, T. 1999. Porosity, Underfill and Magnesium Loss during Continuous Wave Nd : YAG Laser Welding of Thin Plates of Aluminum Alloys 5182 and 5754. *Weld. J.* 78 (6): 207–216.

[7] Zhao, H. and DebRoy, T. 2003. Macroporosity free aluminum alloy weldments through numerical simulation of keyhole mode laser welding. *J. Appl. Phys.* 93 (12): 10089–10096.

[8] Kuo, T.-Y. 2005. Effects of pulsed and continuous Nd–YAG laser beam waves on welding of Inconel alloy. *Sci. Technol. Weld. Join.* 10 (5): 557–565.

[9] Kuo, T.-Y. and Lin, Y.-D. 2007. Effects of Different Shielding Gases and Power Waveforms on Penetration Characteristics and Porosity Formation in Laser Welding of Inconel 690 Alloy. *Mater. Trans.* 48 (2): 219–226.

[10] Tucker, J. D., Nolan, T. K., Martin, A. J., and Young, G. a. 2012. Effect of travel speed and beam focus on porosity in alloy 690 laser welds. *JOM* 64 (12): 1409–1417.

[11] Blecher, J. J., Galbraith, C. M., Van Vlack, C., Palmer, T. A., Fraser, J. M., Webster, P. J. L., and DebRoy, T. 2014. Real time monitoring of laser beam welding keyhole depth by laser interferometry. *Sci. Technol. Weld. Join.* 19 (7): 560–564.

[12] Lee, H. T., Chen, C. T., and Wu, J. L. 2010. 3D numerical study of effects of temperature field on sensitisation of Alloy 690 butt welds fabricated by gas tungsten arc welding and laser beam welding. *Sci. Technol. Weld. Join.* 15 (7): 605–612.

[13] Blecher, J. J., Palmer, T. A., and DebRoy, T. 2013. Solidification Map of a Nickel-Base Alloy. *Metall. Mater. Trans. A* 45 (4): 2142–2151.

[14] Suder, W. J. and Williams, S. 2014. Power factor model for selection of welding parameters in CW laser welding. *Opt. Laser Technol.* 56 223–229.

[15] Quintino, L., Costa, A., Miranda, R., Yapp, D., Kumar, V., and Kong, C. J. 2007. Welding with high power fiber lasers - A preliminary study. *Mater. Des.* 28 (4): 1231–1237.

[16] Smithells, C. 2004. *Smithells metals reference book.* 8th ed. Boston: Elsevier Butterworth-Heinemann.

[17] Yaws, C. L. 2007. *The Yaws handbook of vapor pressure : Antoine coefficients.* Houston: Gulf Publishing Company.

[18] Kim, C. H., Zhang, W., and DebRoy, T. 2003. Modeling of temperature field and solidified surface profile during gas-metal arc fillet welding. *J. Appl. Phys.* 94 (4): 2667–2679.

[19] Zhang, W., Roy, G. G., Elmer, J. W., and DebRoy, T. 2003. Modeling of heat transfer and fluid flow during gas tungsten arc spot welding of low carbon steel. *J. Appl. Phys.* 93 (5): 3022–3033.

[20] Rai, R., Elmer, J. W., Palmer, T. A., and DebRoy, T. 2007. Heat transfer and fluid flow during keyhole mode laser welding of tantalum, Ti–6Al–4V, 304L stainless steel and vanadium. *J. Phys. D. Appl. Phys.* 40 (18): 5753–5766.

[21] Ribic, B., Rai, R., and DebRoy, T. 2008. Numerical simulation of heat transfer and fluid flow in GTA/Laser hybrid welding. *Sci. Technol. Weld. Join.* 13 (8): 683–693.

[22] Jones, L. A., Eagar, T. W., and Lang, J. H. 1999. A dynamic model of drops detaching from a gas metal arc welding electrode. *J. Phys. D. Appl. Phys.* 31 (1): 107–123.

[23] Lancaster, J. F. 1986. *The physics of welding*. 2nd ed. Oxford: Pergamon.

[24] Kumar, S. and Bhaduri, S. 1994. Three-dimensional finite element modeling of gas metal-arc welding. *Metall. Mater. Trans. B* 25 (3): 435–441.

[25] Blecher, J., Palmer, T. A., Kelly, S. M., and Martukanitz, R. P. 2012. Identifying Performance Differences in Transmissive and Reflective Laser Optics Using Beam Diagnostic Tools. *Weld. J.* 91 (7): 204–214.

[26] Madison, J. D. and Aagesen, L. K. 2012. Quantitative characterization of porosity in laser welds of stainless steel. *Scr. Mater.* 67 (9): 783–786.

[27] Yang, Z. and Debroy, T. 1999. Modeling Macro-and Microstructures of Gas-Metal-Arc Welded HSLA-100 Steel. *Metall. Mater. Trans. B-Process Metall. Mater. Process. Sci.* 30 (3): 483–493.

[28] Naito, Y., Katayama, S., and Matsunawa, A. 2003. Keyhole behavior and liquid flow in molten pool during laser-arc hybrid welding. *Proc. SPIE* 4831 357–362.

[29] T.Y. Kuo and S.L. Jeng, 'Porosity reduction in Nd-YAG laser welding of stainless steel and Inconel alloy by using a pulsed wave,' J. Phys. D: Appl. Phys., **38** (5), 722-728 (2005).

[30] Kawahito, Y., Mizutani, M, and Katayama, S. 2009. High quality welding of stainless steel with 10 kW high power fibre laser. *Sci. Technol. Weld. Joining* 14 (4): 288-294.

[31]   Special Metals Corporation, "Joining", accessed 30 April 2015, pg. 9, <www.specialmetalswelding.com>.

[32]   Wei, H. L., Blecher, J. J., Palmer, T. A., and DebRoy, T. 2015. Fusion Zone Microstructure and Geometry in Complete-Joint-Penetration Laser-Arc Hybrid Welding of Low-Alloy Steel. *Weld. J.* 94 (4): 135–144.

[33]   He, X., Fuerschbach, P. W., and DebRoy, T. 2003. Heat transfer and fluid flow during laser spot welding of 304 stainless steel. *J. Phys. D. Appl. Phys.* 36 (12): 1388–1398.

[34]   Rai, R., Roy, G. G., and Debroy, T. 2007. A computationally efficient model of convective heat transfer and solidification characteristics during keyhole mode laser welding. *J. Appl. Phys.* 101 (5): 054909.

[35]   Rai, R., Kelly, S. M., Martukanitz, R. P., and DebRoy, T. 2008. A convective heat-transfer model for partial and full penetration keyhole mode laser welding of a structural steel. *Metall. Mater. Trans. A Phys. Metall. Mater. Sci.* 39 (1): 98–112.

[36]   Rhee, S. and Kannatey-Asibu, E. 1992. Observation of metal transfer during gas metal arc welding. *Weld. J.* 71 (10): 381–386.

[37]   Kim, G.-H. and Na, S.-J. 2001. A study of an arc sensor model for gas metal arc welding with rotating arc Part 1: dynamic simulation of wire melting. *Proc. Inst. Mech. Eng. Part B J. Eng. Manuf.* 215 (9): 1271–1279.

[38]   Waszink, J. H. and Van Den Heuvel, G. J. P. M. 1982. Heat Generation and Heat Flow in the Filler in GMA Welding. *Weld. J.* 61 (8): 269–280.

Chapter 6 – Probing Keyhole Mode Welding

6.1 Barriers to Effective Keyhole Monitoring

The ability of lasers to produce defect free deep penetration welds with depths of 20 mm and more depends on the formation of a stable keyhole [1-5]. However, keyhole stability, in terms of constant depth with respect to time, is difficult to achieve. Commonly, this lack of stability can lead to the formation of defects as the bottom of the keyhole separates from the rest, forms bubbles in the weld pool, and becomes trapped as pores in solidifying metal. This behavior has been observed many times during X-ray videography of keyhole mode welds [5-7]. Given that changes in keyhole geometry, specifically depth, are known to coincide with the formation of defects, there is strong interest in the ability to monitor the depth during welding.

The spatial and temporal characteristics of the keyhole complicates depth monitoring. Typically, the keyhole opening is only as wide as the process laser beam, which is on the order of 0.5 mm, so visualizing the keyhole through the opening is very difficult. Besides the small opening, large amounts of visible and infrared emissions radiate from the weld pool near the keyhole, requiring complex filtering and lighting arrangements. High velocity (0.5 to 1.0 mach) vapors exiting the keyhole are also a barrier to direct optical measurement. The keyhole also has a temporal component, which manifests as a constantly fluctuating geometry that can produce hundreds of bubbles and eventual pores in only a few inches of welds. The frequency of bubble formation has not been measured directly, but estimating from X-ray videography yields 14 Hz for aluminum alloy [6]. If a bubble forms each time the keyhole geometry fluctuates, then data from Ch. 5 yields a frequency between 15 and 57 Hz for Alloy 690 under laser welding conditions of 2 to 6 kW laser power and 10 to 20 mm/s welding speed. Due to these complexities, various monitoring technologies rely on indirect observation of the keyhole.

6.2 Current Techniques for Keyhole Monitoring

At present there is no accepted technique for the real time measurement of keyhole depth during laser welding. Weld quality, which describes widely varying qualitative characteristics, such as complete penetration, weld defects, and constant welding parameters, is more often measured. Popular methods for monitoring weld quality can be classified as indirect and include capturing the optical [8,9] and acoustic [10,11] signals produced by vapor escaping the keyhole

[12,13]. Other techniques include measuring plasma charge [14], viewing the weld pool with cameras [9,15,16], or utilizing a combination of sensors [9,16]. In limited cases, where there is motivation to develop a neural network and multiple regression framework to match acoustic signals with weld depth, the error rate for predicted weld depth is still 5 to 10% [11]. However, indirect measurements are subject to numerous difficulties, requiring additional calibration each time a process or material parameter changes. A need exists for a direct measurement of keyhole depth.

Much of the existing knowledge of keyhole dynamics has been obtained using X-ray videography, which views the keyhole directly in plates thin enough to allow X-ray transmission [6]. While the technology has a capture rate of 5000 Hz and is fast enough to characterize keyhole collapse and bubble formation in a variety of alloys [5-7], there are severe limitations that impact the process flexibility. The process is not easily implementable due restrictions to thin plates and the availability and mobility of X-ray generators.

6.3 Application of Inline Coherent Imaging

An alternative to interpretation of indirect measurements and X-ray videography, inline coherent imaging (ICI) has recently been developed and measures the keyhole depth directly and with a high degree of process flexibility [17-19]. ICI is an interferometric technique that directs a probe beam coaxially with the process beam into the keyhole. As long as a reflective surface is present, ICI can directly measure the keyhole depth in any partial penetration weld regardless of other process parameters. Because the probe laser runs coaxially with the process laser, integration complexity is not significant, and ICI can used in a variety of laser processes. The technique has already been used during laser machining to automatically control the drill hole depths in ferrous alloys [17,18] and the shape of fresh and dry cortical bone [20]. Another application includes characterization of the longitudinal molten pool shape during powder bed fusion additive manufacturing by deflecting the probe beam along the length of the pool [21]. Similar to the other applications, employing ICI for keyhole geometry characterization is still in its early stages, demonstrating accurate keyhole depth measurements during constant power and power cycling in mild low carbon steel [19]. The ability of ICI to measure keyhole depth for broad classes of engineering alloys and to provide novel insight into keyhole dynamics has not yet been tested.

In this chapter[6], the utility of ICI to provide real-time measurements of keyhole depth is demonstrated in DH36 steel, 304 stainless steel, Inconel® Alloy 690, Ti-6Al-4V, and 2219 aluminum alloys. These alloys are selected because they represent broad classes of typical engineering alloys, have a large composition variation, and include a range of properties that impact keyhole dynamics, such as laser energy absorptivity, density, heat of vaporization, thermal conductivity, and melting point. Keyhole depth measurements are performed for each alloy and compared with metallographic cross-sections. To demonstrate the ability of ICI to capture novel keyhole dynamics, the initiation and growth of the keyhole at the beginning of welding for the five alloys are captured. These data allow direct measurement of the keyhole growth rates in the first 5 ms of welding with unprecedented temporal resolutions on the order of 5 μs. The keyhole growth rates are estimated using an energy balance between the laser energy and the energy necessary to evaporate the liquid metal. An order of magnitude agreement between the measured and theoretical rates indicates that the measured growth rates are realistic.

6.4 ICI Technology Background

ICI utilizes a Michelson interferometer construction. Using a superluminescent diode (SLD) with a wavelength of 843 nm and FWHM of 20 nm as the light source, a reference beam is set along a path of known distance with appropriate dispersion matching optics. The probe beam is directed through the same optics as the high power process beam and into the keyhole, where the probe beam reflects off surfaces along its path. The two beams are recombined and directed to a spectrometer, which collects the interference pattern, or interferogram, at a measured integration time of 1.5 μs, giving the system a total temporal resolution of 5 μs. From the spectral interference pattern, the scattering surface positions along laser axis are measured with a resolution of 22 μm. A schematic of the process is shown in Figure 81 [19]. After sampling of the interference pattern at 200 kHz over the length of the weld, the keyhole depth as a function of position is extracted.

---

[6]Portions of this chapter are directly excerpted from J.J. Blecher, C.M. Galbraith, C. Van Vlack, T.A. Palmer, J.M. Fraser, P.J.L. Webster, and T. DebRoy, "Real time monitoring of laser beam welding keyhole depth by laser interferometry", Sci. Technol. Weld. Joining, **19**, 2014, 560-564.
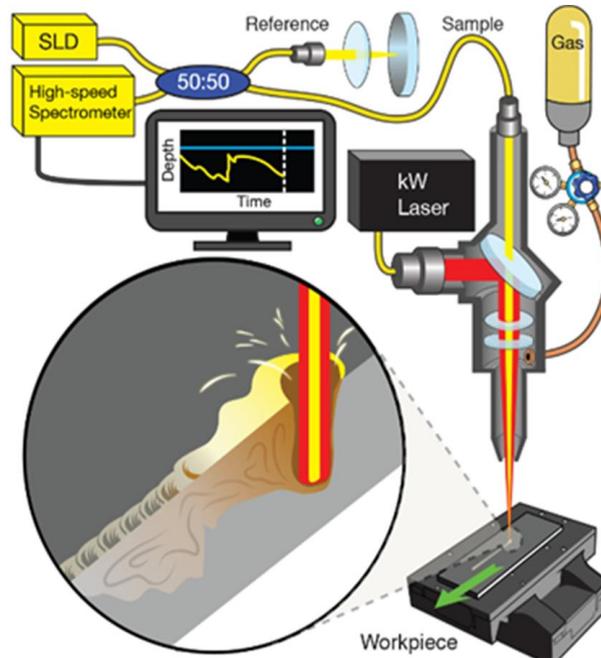
Figure 81: The elements of the inline coherent imaging system are shown [19].

One method of visualizing the data is shown in Figure 82. The first narrow pane indicates the surface determination prior to welding and is captured by traversing the probe beam across the plate without power to the process laser. These data are needed for precise calculation of the keyhole depth relative to the surface. The faint signal around 2400 μm depth in the pre-scan is due to an imaging artifact and does not represent a real scattering surface. In the center pane, all of the reflecting surfaces during welding are shown. The strongest signals are as dark as the un-melted surface in the pre-weld scan. These data are covered by the blue dots, which represent the ICI measured keyhole depth as determined by a depth-tracking algorithm.

The data in Figure 82 are taken from an Inconel® Alloy 690 weld and are typical of most welds in terms of appearance and structure. At the start of the weld in Figure 82, the laser weld starts, and the keyhole depth increases to 2.3 mm after 4 mm of weld length has been completed. Over the course of the weld, the ICI measured keyhole depth fluctuates between extremes of 2.1 and 2.8 mm, which represent a maximum change of 22% in the measured depth of the weld, which was independently measured from three metallographic cross-sections. At the end of the weld, a small section of the unmelted surface is captured.
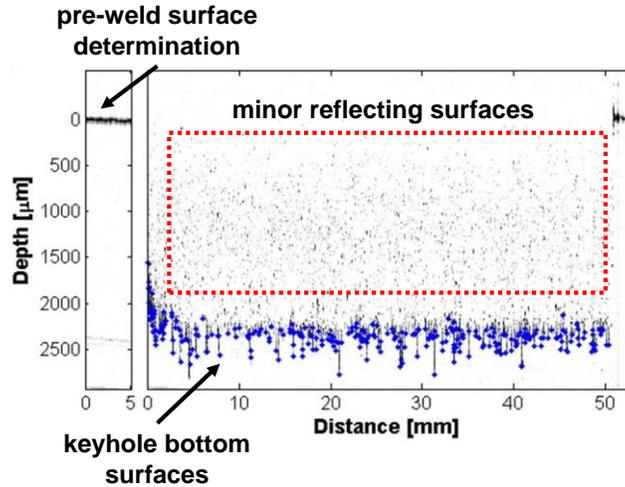
Figure 82: An ICI image of a weld in Alloy 690 is presented. The left panel shows the height of plate surface determined from the pre-scan measurement. The large pane shows the raw ICI data (dark spots) and the keyhole depth (blue dots). Minor reflecting surfaces represent depths above the bottom of the keyhole that reflected a small amount of probe laser light.

6.5 Laser Welding Experiments

An IPG Photonics® YLS-1000-IC laser with a 100 μm core process fiber coupled to a Laser Mechanisms AccuFiber head with a 60 mm focal length collimator and a 150 mm focal length lens was used to produce a series of autogenous welds on DH36 steel, 304 stainless steel, Inconel® Alloy 690, Ti-6Al-4V, and 2219 aluminum alloy substrates. The nominal compositions of the selected alloys are given in Table 10. A laser power and welding speed of 1.1 kW and 25 mm/s, respectively, was used with coaxial argon shielding gas for all of the welds produced here. The focus of the process beam, which was determined in prior characterization activities, was located at the surface of the material for all experiments. During welding, ICI data were collected in real-time. After welding, six transverse cross-sections were extracted from each weld and prepared for optical microscopy using standard metallographic techniques. A Nikon® DS-Fi2

Table 10: The compositions (wt.%) of the various alloys that were welded in this study are given.

Alloy	Fe	C	Mn	Si	Cr	Ni	Ti	Al	V	Cu
DH36	Balance	0.18	1.25	0.30	0.25	0.40	…	…	0.10	0.35
304	Balance	0.08	1.50	2.00	20.00	10.00	…	…	…	…
Alloy 690	10.00	0.03	0.19	0.08	30.00	Balance	…	…	…	…
Ti-6Al-4V	0.30	0.10	…	…	…	…	Balance	6.00	4.00	…
AA 2219	…	…	0.30	…	…	…	0.06	Balance	0.10	6.30

camera attached to a Nikon® Epiphot microscope and Nikon® NIS Elements software captured micrographs of the welds.

6.6 Testing ICI Accuracy in Five Alloys

Representative metallographic cross-sections for each weld are shown in Figure 83. Keyhole mode welding is achieved for each alloy, and with the exception of the high thermal conductivity aluminum alloy, the typical wineglass shape is apparent. The dimensions for each weld are provided in Table 11. The weld depths in DH36 steel, 304 stainless steel, Alloy 690, and Ti-6Al-4V appear to be very similar. On the other hand, the aluminum weld is 26% shallower than the other welds. In terms of top surface width, aluminum alloy 2219 and Ti-6Al-4V are 18% and 35% are wider, respectively, than the Fe-base and Ni-base alloys. These differences are much
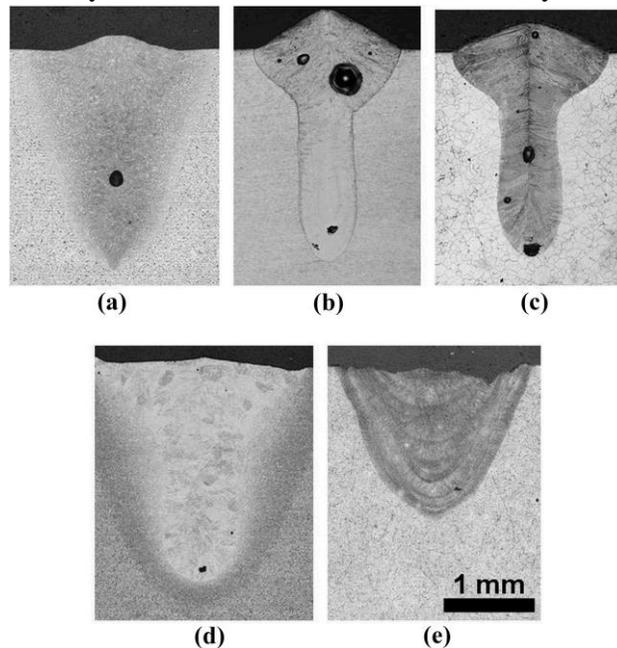
Figure 83: The metallographic cross-sections of (a) DH36 steel, (b) 304 stainless steel, (c) Alloy 690, (d) Ti-6Al-4V, and (e) 2219 aluminum are shown. Each weld was created with a laser power of 1.1 kW and welding speed of 25 mm/s.

Table 11: The depth and two widths are measured for each weld. Width two is measured at half the depth of the weld pool.

Alloy	Depth (mm)	Width 1 (mm)	Width 2 (mm)	Dimensions Diagram
DH36	2.3	1.7	0.68	
304 S.S.	2.5	1.6	0.62	
Alloy 690	2.3	1.7	0.64	
Ti-6Al-4V	2.3	2.3	0.89	
AA 2219	1.7	2.0	1.55	

more pronounced at the half depth of the weld. The Al-base alloy and Ti-base alloy welds are 140% and 38% wider, respectively, compared to the other three alloys. Among other thermophysical properties, such as melting and boiling points, the differences in the thermal conductivity and laser absorption coefficient for each alloy determine the differences in weld pool dimensions and should also affect the keyhole dynamics.

An important issue in any new technique is the accuracy of the measurements. Figure 84 shows a comparison of the average ICI depth measurements and weld depths determined by transverse metallographic cross-sections. The metallographic depths shown in this figure are taken from an average of six measurements at different positions in the weld. For the ICI data set, the black bars are given by the standard deviation of measurements taken over the length of the weld and are representative of real variation in the keyhole depth. The precision of an instantaneous ICI keyhole depth measurement is limited by the axial resolution of the system, which at 22 μm, is an order of magnitude smaller than the observed keyhole depth fluctuations. The standard deviations are relatively close, however, the standard deviations determined by the measured cross sections are smaller than those measured by ICI, suggesting that six cross-sectional measurements of weld depth is not enough to reproduce the keyhole depth variability observed with ICI measurements.
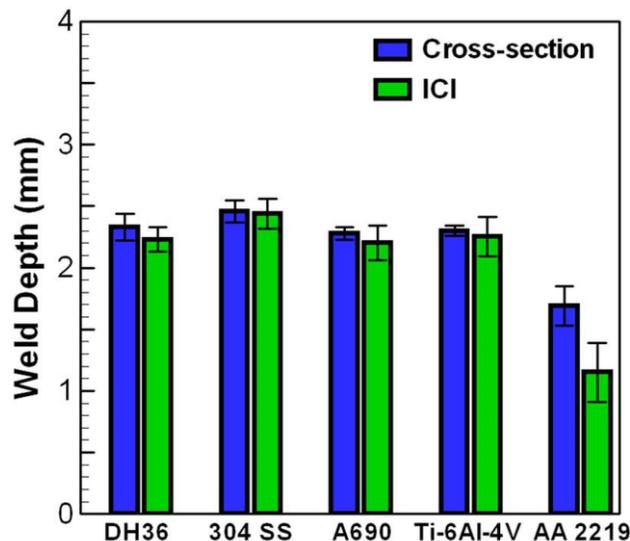
Figure 84: A comparison of ICI depth measurements and depths from metallographic cross-sections is shown. The ICI weld depth was averaged from the depth tracking algorithm across the entire weld region. Black bars represent the standard deviation of the depths measured by each technique. The two sets of measurements agree except in the case of AA 2219.

150

In every case, the measured keyhole depth (ICI) is slightly smaller than the measured weld depth (metallographic cross-section), which agrees with modeling results showing that the weld depth is always slightly greater than the keyhole depth [22,23]. With the exception of the 2219 aluminum alloy, very good agreement is observed between the ICI and the metallographic measurements across a wide alloy composition range, indicating that inline coherent imaging can be used as a real-time process monitoring tool for capturing keyhole depths. To give a consistent comparison, the same experimental imaging parameters were used for all five alloys. In the case of aluminum, the high melt reflectivity resulted in intermittent saturation of the ICI system. When combined with the large and rapid fluctuations in keyhole depth characteristic of this alloy, the averaged ICI depth measurements were biased toward artificially shallow values. Optimization of imaging parameters, such as reducing probe laser intensity, and algorithmic interpretation of the ICI data, tuned for rapid depth fluctuations, is expected to improve the accuracy in aluminum weld depths.

6.7 Probing Keyhole Dynamics

ICI has proven to accurately measure the keyhole depth in most alloys. To leverage the novel spatial and temporal resolutions of the technique, the initial formation and growth of keyholes are compiled in Figure 85. At time zero, the laser beam turns on, and processing begins. In aluminum, there is a 1.6 ms delay between the beam turning on and a rapid increase in depth at a rate of 0.56 m/s. The observed delay is consistent with the relatively high reflectivity and thermal conductivity of aluminum. In the other alloys during the initial 1 ms of welding, the keyholes
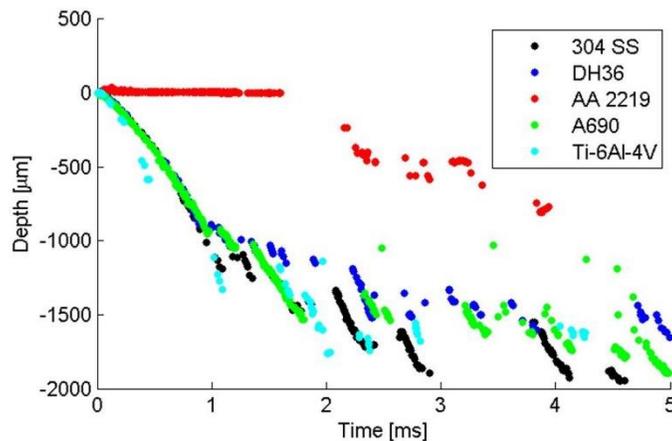
Figure 85: The ICI measured keyhole depths during the first 5 ms, or 0.125 mm, of welding show how fast the keyhole initiates and grows for each alloy. Aluminum 2219 is the slowest to initiate and grow a keyhole, while Ti-6Al-4V is the fastest.

151

grew at rates between 0.91 and 1.11 m/s. At least two studies measured initial growth rates with X-ray transmission videography, which has temporal resolutions of 200 µs [24,25], compared to the 5 µs achieved here. These studies include: (1) a 1.50 m/s keyhole growth rate in in 304 stainless steel with 2.3 kW laser power, 10 mm/s welding speed, and 1.1 mm beam diameter [24] and (2) a 0.66 m/s growth rate in Ti-6Al-4V with 8.7 kW laser power and 0.45 mm beam diameter (spot weld) [25]. The difference in temporal resolution is important for providing a more accurate determination of the onset of keyhole formation for the aluminum alloy and differentiating the growth rates in the other four alloys. With X-ray transmission videography, the growth rates in steel, stainless steel, Alloy 690, and Ti-6Al-4V would have appeared the same. Unfortunately, the accuracy of the X-ray and ICI keyhole depth measurement techniques cannot be compared since this information was not given in the studies of X-ray transmission videography.

Order of magnitude keyhole growth rates can be estimated by equating the laser energy absorbed by the workpiece and the energy necessary to evaporate the liquid metal at any point on the vaporizing surface. This theoretical growth rate is defined in the following relationship

$$u = \frac{\eta I_L}{\rho \Delta H_v} \tag{1}$$

where η is the absorptivity of the liquid metal, I_L is the peak intensity of the laser, approximately 130 kW/mm^2 in this case, ρ is the density of the liquid metal, and ΔH_v is the latent heat of vaporization. The necessary material properties and the measured and calculated growth rates are shown in Table 12. The order of magnitude estimates agree with the ICI measured keyhole growth rates in DH36 steel, 304 stainless steel, Alloy 690, and Ti-6Al-4V, indicating that the scale analysis can be used to estimate the keyhole growth rates in these alloys when the relevant process parameters and material properties are known. In the case of aluminum alloy 2219, the ICI

Table 12: The material properties used in the heat balance and the measured and calculated keyhole growth rates are given.

	DH36	304 S.S.	A690	Ti-6Al-4V	AA2219
Absorptivity, η	0.33	0.32	0.29	0.31	0.19
Density, ρ (kg/m^3)	7050	7070	7480	3970	2560
Heat of Vaporization, ΔH_v (kJ/kg)	6260	6330	6450	8810	10720
Measured Growth Rate, u (m/s)	0.91	1.09	0.98	1.11	0.56
Calculated Growth Rate, u (m/s)	0.97	0.93	0.78	1.15	0.90

measured keyhole growth rate was lower than that estimated by scale analysis assuming no heat loss. The comparison shows considerable heat loss by conduction in the alloy.

6.8 Summary and Conclusion

The application of inline coherent imaging to keyhole depth monitoring in laser welding has been demonstrated in DH 36 steel, 304 stainless steel, Inconel® Alloy 690, Ti-6Al-4V, and aluminum alloy 2219. The accuracy of ICI has been tested, and the application of the technique to keyhole growth rate has been explored. The findings from this chapter are listed below.

(1) Real-time keyhole depth measurements from autogenous bead on plate welds of five alloys were compared to depths from metallographic transverse cross-sections. The two sets of data show good agreement, indicating that the technique can be applied to a wide range of different alloys and maintain the ability to measure the keyhole depth in real-time.

(2) The initiation and growth of the keyholes was investigated with real-time measurements. The observed keyhole growth rates between 0.56 and 1.11 m/s compare well to previous measurements, which used X-ray videography. The initial keyhole growth rates measured by the inline coherent imaging technique agree well with the corresponding values estimated by scale analysis.

6.9 References

[1] You, D. Y., Gao, X. D., and Katayama, S. 2014. Review of laser welding monitoring. *Sci. Technol. Weld. Joining* 19 (3): 181-201.

[2] Coniglio, N. and Patry, M. 2013. Measuring laser weldability of aluminium alloys using controlled restraint weldability test. *Sci. Technol. Weld. Joining* 18 (7): 573-580.

[3] Assuncao, E., Ganguly, S., Yapp, D., Williams, S., and Paradowska, A. 2011. Characterisation of residual stress state in laser welded low carbon mild steel plates produced in keyhole and conduction mode. *Sci. Technol. Weld. Joining* 16 (3): 239-243.

[4] Blackburn, J. E., Allen, C. M., Hilton, P. A., Li, L., Hoque, M. I., and Khan, A. H. 2010. Modulated Nd:YAG laser welding of Ti-6Al-4V. *Sci. Technol. Weld. Joining* 15 (5): 433-439.

[5] Kawahito, Y., Mizutani, M., and Katayama, S. 2009. High quality welding of stainless steel with 10 kW high power fibre laser. *Sci. Technol. Weld. Joining* 14 (4): 588-594.

[6] Matsunawa, A., Kim, J. D., Seto, N., Mizutani, M., and Katayama, S. 1998. Dynamics of keyhole and molten pool in laser welding. *J. Laser Appl.* 10 (6): 247-254.

[7] Kawahito, Y., Mizutani, M., and Katayama, S. 2007. Elucidation of high-power fibre laser welding phenomena of stainless steel and effect of factors on weld geometry. *J. Phys. D: Appl. Phys.* 40 (19): 5854 to 5859.

[8] Ancona, A., Spagnolo, V., Lugara, P. M., and Ferrara, M. 2001. Optical sensor for real-time monitoring of CO_2 laser welding process. *Appl. Opt.* 40 (33): 6019-6025.

[9] You, D., Gao, X., and Katayama, S. 2013. Multiple-optics sensing of high-brightness disk laser welding process. *NDT&E Int.* 60: 32-39.

[10] Huang, W. and Kovacevic, R. 2009. Feasibility study of using acoustic signals for online monitoring of the depth of weld in the laser welding of high-strength steels. *Proc. IMechE Part B: J. Eng. Manuf.* 223 (4): 343-361.

[11] Huang, W. and Kovacevic, R. 2011. A neural network and multiple regression method for the characterization of the depth of weld penetration in laser welding based on acoustic signatures. *J. Intell. Manuf.* 922 (2): 131-143.

[12] Farson, D. F. and Kim, K. R. 1999. Generation of optical and acoustic emissions in laser weld plumes. *J. Appl. Phys.* 85 (3): 1329-1336.

[13] Farson, D., Ali, A., and Sang, Y. 1998. Relationship of optical and acoustic emissions to laser weld penetration. *Weld. J.* 77 (4): 142s-148s.

[14] Li, L., Brookfield, D. J., and Steen, W. M. 1996. Plasma charge sensor for in-process, non-contact monitoring of the laser welding process. *Meas. Sci. Technol.* 7 (4): 615-626.

[15] Kim, C.-H. and Ahn, D.-C. 2012 Coaxial monitoring of keyhole during Yb:YAG laser welding. *Opt. Laser Technol.* 44 (6): 1874-1880.

[16] Kawahito, Y., Ohnishi, T., and Katayama, S. 2009. In-process monitoring and feedback control for stable production of full-penetration weld in continuous wave fibre laser welding. *J. Phys. D: Appl. Phys.* 42 (8): 085501.

[17] Webster, P. J. L., Leung, B. Y. C., Yu, J. X. Z., Anderson, M. D., Hoult, T. P., and Fraser, J. M. 2010. Coaxial real-time metrology and gas assisted laser micromachining: process development, stochastic behavior and feedback control. *Proc. SPIE* **7590**: 003.

[18] Webster, P. J. L., Wright, L. G., Mortimer, K. D., Leung, B. Y., Yu, J. X. Z., and Fraser, J. M. 2011. Automatic real-time guidance of laser machining with inline coherent imaging. *J. Laser Appl.* 23 (2): 022001.

[19] Webster, P. J. L., Wright, L. G., Ji, Y., Galbraith, C. M., Kinross, A. W., Van Vlack, C., and Fraser, J. M. 2014. Fully-automatic laser welding and micro-sculpting with universal in situ inline coherent imaging. *arXiv*: 1404.4419.

[20] Yin, C., Ruzzante, S.W., and Fraser, J.M. 2016. Automated 3D bone ablation with 1070 nm Yb-doped fiber laser enabled by inline coherent imaging. *Lasers Surg. Med.* 48 (3): 288-298.

[21] Kanko, J.A., Sibley, A.P., and Fraser, J.M. 2016. In situ morphology-based defect detection of selective laser melting through inline coherent imaging. *J. Mater. Process. Technol.* 231: 488-500.

[22] Rai, R., Roy, G. G., and DebRoy, T. 2007. A computationally efficient model of convective heat transfer and solidification characteristics during keyhole mode laser welding. *J. Appl. Phys.* 101 (5): 054909.

[23] Rai, R., Elmer, J. W., Palmer, T. A., and DebRoy, T. 2007. Heat transfer and fluid flow during keyhole mode laser welding of tantalum, Ti-6Al-4V, 304L stainless steel and vanadium. *J. Phys. D: Appl. Phys.* 40 (18): 5753-5766.

[24] Fujinaga, S., Takenaka, H., Narikiyo, T., Katayama, S., and Matsunawa A. 2000. Direct observation of keyhole behaviour during pulse modulated high-power Nd:YAG laser irradiation. *J. Phys. D: Appl. Phys.* 33 (5): 492-497.

[25] Perret, O., Bizouard, M., Naudy, Ph., Pascal, G., Nore, D., Horde, Y., and Delaisse, Y. 2001. Characterization of the keyhole formed during pulsed Nd-YAG laser interaction with a Ti-6Al-4V metallic target. *J. Appl. Phys.* 90 (1): 27-30.

Chapter 7 – Concluding Remarks

7.1 – Summary and Conclusions

Laser and, especially, hybrid laser-arc welding offer an attractive alternative for joining Inconel Alloy 690, which is typically done with conventional arc welding. While the benefits include the usual characteristics of hybrid welding compared to arc welding, such as good gap bridgeability, deeper penetration depths, and faster weld speeds and higher productivity, the unique defects found in Alloy 690 welds may be avoided entirely during single pass hybrid-laser arc welding. Ductility dip cracking (DDC) and solidification cracking (due to alloy additions to avoid DDC) are the two novel defects that originate in the fusion zone solidification microstructure and can be avoided with laser and hybrid welding. These laser based techniques reduce the likelihood of DDC and solidification cracking, but understanding the fusion zone evolution during deep penetration welding of Alloy 690 is still important due to its role in defects during conventional arc welding.

To investigate the solidification behavior of during laser welding of Alloy 690, a combined experimental and theoretical strategy was employed. A series of laser welds with different laser powers were fabricated in Alloy 690. The fusion zone was characterized in terms of solidification morphology (e.g. either cells or columnar dendrites) and cell spacing or secondary dendrite arm spacing. In order to correlate the morphology and spacings to quantitative solidification parameters, a three dimensional (3D) heat transfer and fluid flow model calculated the temperature fields and fluid velocity fields for every welding case. The solidification parameters temperature gradient (G), solidification rate (R), cooling rate (GR), and morphology parameter (G/R) were calculated at every position along the solidification interface, or the liquidus temperature contour. The model was validated quantitatively with experimental weld geometry and qualitatively by comparing the local calculated temperature gradient with the local direction of solidification in the micrographs of the weld fusion zone. The major findings include:

(1)   A large spatial variation in solidification morphology and scale exists in deep penetration welds due to the keyhole, which as a heat source extends through the thickness of the weld. The calculated solidification parameters reflect this reality, and the G/R value can vary by

5 orders of magnitude along the central longitudinal plane. This variation is dependent on the process parameters and increases with increases in laser power.

(2)   Relations in the form of $\lambda=b(GR)^n$ were determined from the correlated measured cell and dendrite arm spacings and calculated solidification parameters. The relations are applicable across a variety of welding processes and conditions. The values of G/R associated with the transition from cellular to columnar dendritic solidification structures were determined to be between 13 and 21 K-s/mm^2. Dendrite area fractions were computed with these values and agreed with measured values.

(3)   Using the cooling rate-spacing relations and the cell-to-dendrite transition morphology parameter, a solidification map was constructed with axes of temperature gradient and solidification rate. Curves of constant cooling rate and solidification morphology regions are included in the map. Using the map, a welding engineer could predict the minimum dendrite arm spacing from the welding speed. The map captures the full range of G and R observed in the weld pool and is expected to have utility in a variety of materials processes from casting to arc and laser welding.

Laser and hybrid laser-arc welding creates a spatially variable solidification microstructure but avoids the defects found in conventional arc welding. However, deep penetration laser welding techniques can lead to their own novel defects, which include root defects and keyhole porosity. Root defects form during full penetration welding when liquid metal drops out of the weld pool but does not detach from the bottom of the plate and solidifies as nuggets. While root defects have been observed previously, there has been limited studies on the effect of process parameters, welding techniques, and thermo-physical properties of the alloy.

In order to study the formation of root defects during laser and hybrid laser-arc welding, low alloy steel plates with plate thicknesses between 4.8 and 9.5 mm were welded with various processing conditions and different plate bottom surface condition. A matching filler metal was used for hybrid welding, and the oxide scale on the bottom of the plate was either left as is to reduce surface tension or removed to maintain the typical surface tension of low alloy steel. A force balance was developed, accounting for the weight of the liquid metal and the surface tension force at the bottom of the pool, and applied to the experimental welds. The internal structure of the defect nugget internal structure was characterized with optical microscopy and X-ray CT. To

further extend the utility of these experiments and provide a tool for engineers, process maps, showing regions of partial penetration, quality welds, cutting, and root defects, were constructed for low alloy steel, stainless steel, Ti-6Al-4V, and magnesium-aluminum alloys.

(1)   By varying the welding process parameters, the surface tension and liquid metal weight could be varied independently, and the qualitative effect of each on the formation of root defects was examined. With the oxide scale present on the bottom plate surface and the resulting low surface tension, root defects formed, while when the scale was removed, the same welding parameters produced no defects. By welding with an arc in a hybrid welding setup or using a larger plate, the effect of larger pools and greater liquid metal weight was tested. Larger weld pools produced defects, and welding with a just a laser and with smaller plates produced no defects.

(2)   The internal structure of the defects was characterized by X-ray CT and found to be different for the laser weld in 9.5 mm thick plate and the hybrid weld in 4.8 mm thick plate. The defects in the laser weld were solid with a dispersion of small spherical pores. On the other hand, in the hybrid welds, the defect structure contained a complex network of porosity with a large pore at the bottom of the nugget and porosity strands stretching from the bottom of the defect up to the bottom of the plate. The additional forces during hybrid laser-arc welding, such as arc pressure and droplet impact force, are probably responsible for the difference in defect structure.

(3)   Since the surface tension and liquid metal weight appeared to control the formation of root defects in the experimental welds, a force balance was developed, using an idealized weld pool shape for estimating unknown weld pool dimensions. For all the cases except one, the force balance successfully predicted the formation of root defects. The results of the force balance prove the importance of surface tension and liquid metal weight on the formation of root defects.

(4)   The process maps for low carbon steel, 304 stainless steel, Ti-6Al-4V, and magnesium-aluminum alloys revealed that identical H* values between 5 and 15 can be used to fabricate defect free welds in plate thicknesses between 3.5 and 10 mm for the four alloys considered. Most observed root defects to date have mainly been observed in stainless steel.

(5)   The compiled data in the process maps show that two conditions, plate thicknesses greater than 10 mm and H* values greater than 15, are required before defects can form. However, these two conditions do not guarantee the formation of root defects as shown in the process maps for the

lower density alloys. The process maps clearly show that root defects are the result of high heat inputs, so, in most cases, reducing heat input will reduce the chances of forming root defects.

The other novel defect associated with laser and hybrid laser-arc welding is keyhole porosity, which forms when the unstable keyhole periodically collapses and forms a bubble in the liquid metal. This bubble becomes trapped in the solidification front and remains in the weld as a pore. To examine keyhole porosity in Inconel Alloy 690 during laser and hybrid welding, a series of welds with three different laser powers and two different welding speeds were fabricated. The porosity characteristics of each weld were characterized with X-ray CT in terms of size and location. A 3D heat transfer and fluid flow model and a model of the volumetric heat source (e.g. the zone where filler metal enters the pool) were employed to examine the differences in porosity characteristics.

(1)   In the high power laser power welds, the addition of an arc significantly reduced porosity. The hybrid welds with process parameters of 4 and 6 kW laser power and a welding speed of 10 mm/s produced welds with the lowest levels of porosity. In the case of the 4 kW laser power hybrid weld, the lowest porosity of 2 mm^3 in a total weld volume of 3000 mm^3 was found. On the other hand, the laser weld at 6 kW laser power and 10 mm/s speed produced porosity of 90.5 mm^3 in 1600 mm^3 of weld metal.

(2)   In the hybrid welds as the power increased above 2 kW, a transition from high levels of porosity to virtually no porosity was observed above 2 kW. Based on the available evidence, the mechanism for the high to low porosity transition is linked to the relative sizes of the molten pool and filler metal-molten pool mixing region. At the lower laser power, the filler metal transfer and low weld pool volume restricts the space for bubble motion. As the power increases, the space below the filler metal mixing region increases, allowing bubbles to escape from the bottom of the keyhole to the surface of the weld pool.

(3)   The experimental evidence of this mechanism included observation of larger pores and more concentrated at the bottom of the weld in the hybrid welds compared to the laser welds. From the 3D heat transfer and fluid flow model, no gap was observed between the filler metal mixing region and the bottom of the pool at 2 kW laser power. At higher powers, that gap increased to 2 mm, which is larger than 97% of the observed pore sizes, allowing enough space for bubbles to escape.

(4)   A process map was constructed based on the proposed method of porosity reduction in hybrid laser-arc welds and accounted for volumetric heat source dimensions, weld depth, filler metal electrode dimensions, arc current, and linear laser heat input. To create a gap large enough for bubble escape required heat inputs between 240 and 490 J/mm, with larger electrodes requiring greater heat inputs. For the electrode diameters considered, only 5 kW laser power is required to produce pore free welds if the welding speed is 10 mm/s or less.

The repeated collapse of the keyhole, formation of a bubble, and re-formation of the keyhole during laser and hybrid welding is a dynamic process with a rapidly changing keyhole geometry. Monitoring or characterizing and controlling this dynamic process offer the possibility of fabricating a pore free laser weld. However, no such monitoring technique is available, and there is a trade-off between direct observation of the keyhole geometry (e.g. X-ray videography) and applicability of the technique outside of a laboratory environment, such as indirect acoustic or emission monitoring. A relatively new technique, inline coherent imaging (ICI), has been applied to accurately measuring laser welding depth and laser machining hole depth and may be applicable to characterizing keyhole dynamics in various structural alloys. In order to determine this possibility, ICI was employed during welding four structural alloys, including DH 36 steel, 304 stainless steel, Inconel® Alloy 690, Ti-6Al-4V, and aluminum alloy 2219. The major findings of those welding experiments include:

(1)   The average real-time measured keyhole depths and the weld depths measured through metallography agreed well with the exception of aluminum alloy. These findings suggest that the technique can be applied to a wide range of alloys.

(2)   The keyhole depth at the very start of the weld was characterized with ICI. The measured keyhole growth rates varied from 0.56 to 1.11 m/s, which is within the range of previously measured growth rates. The growth rates compared well with an order of magnitude scale analysis.

7.2 – Future Work

The primary force balance impacting the formation of root defects is well known and shown to predict the formation of root defects in this work. The mechanism has been distilled to a few mathematical expressions that can be implemented into a 3D heat transfer and fluid flow models. While this has been done previously, the utility was limited to only electromagnetic support of the weld pool. Generally, there are a number of open questions:

1. The effect of alloy composition has not been adequately addressed. Currently, low alloy steel up to at least 25 mm plate thickness can be laser welded with no root defects. On the other hand, stainless steel plates above 10 mm are all most impossible to weld without forming defects. There is very little understanding on the formation of root defects in thick aluminum alloy and titanium alloy plates.

2. This work started to explore the effect of hybrid laser-arc welding on root defect formation in low alloy steel from a simple force balance model. Applying a 3D heat transfer and fluid flow model to hybrid welding of steel, stainless steel, and Alloy 690 can build a better understanding of the technique with respect to alloys vulnerable to root defect formation.

3. A 3D heat transfer and fluid flow model will also be able to account for temperature dependent properties, such as liquid metal density and surface tension. Additional terms, such as recoil pressure at both surfaces of the weld pool and the hydrodynamic forces within the weld pool, could be evaluated.

Despite the results of this work, keyhole porosity in laser and hybrid laser-arc welds is still a major issue. Laser power modulation is the most versatile method for eliminating keyhole porosity. The major roadblocks to this method were the inability to monitor the keyhole response to power modulation and the lack of a well-tested transient keyhole model to test strategies before fabricating real welds. So, in the past, power modulation research was limited to trial and error experiments. Currently, most fiber lasers can be easily programmed to modulate laser power during welding at frequencies up to 50 kHz, and inline coherent imaging technology has been productized and can be implemented with most laser welding setups. Two of the three necessary technologies to make serious progress towards power modulation laser welding research are in place. The only remaining technology is a transient keyhole model.

Appendix A: Calculation of Volumetric Heat Source Dimensions

The volumetric heat source (VHS) calculation assumes a cylindrical shape with dimensions of diameter and height. The VHS is commonly used to model consumable electrode heat transfer during gas-metal arc welding [1,2]. In these experiments, spray metal transfer, where small droplets form at the end of the electrode and accelerate into the molten pool, is expected. Several variables are required for the calculation, including material properties, welding parameters, and droplet frequency.

The height of the VHS is given as

$$d = h_v - x_v + D_d \tag{1}$$

where h_v is height of the cavity formed by the impinging droplets, x_v is the distance traveled in the cavity by each droplet before the arrival of the next impinging droplet, and D_d is the droplet diameter. The cavity height is

$$h_v = \left(-\frac{2\gamma}{D_d \rho g} + \sqrt{\left[\left(\frac{2\gamma}{D_d \rho g} \right)^2 + \frac{D_d v_d^2}{6g} \right]} \right) \tag{2}$$

where γ is surface tension of the liquid metal, ρ is the liquid metal density, g is acceleration due to gravity, and v_d is the droplet impingement velocity. The surface tension and density of FM 52 were taken as 1.1 N/m and 6500 kg/m^3, respectively. These values and others are also recorded in Table A1. The distance traveled by each droplet is defined as

$$x_v = \left(h_v + \frac{2\gamma}{D_d \rho g} \right) \left\{ 1 - \cos\left[\left(\frac{g}{h_v} \right)^{1/2} \Delta t \right] \right\} \tag{3}$$

Table A1: The variables, their symbols, and the magnitudes for the calculations in this appendix are shown.

Parameter	Symbol	Value
liquid metal surface tension	γ	1.1 N/m
liquid metal density	ρ	6500 kg/m^3
transition current (1.1 mm wire)	I_t	200 A
transition current (0.9 mm wire)	I_t	150 A
transition current (1.6 mm wire)	I_t	225 A
plasma density	ρ_g	0.06 kg/m^3
constant coefficient	k_t	0.25 m/s-A
kinetic viscosity	v_k	3.4 x 10^{-4} m^2/s

where Δt is the time interval between the impingement of two droplets and can be defined as Δt = 1/f. The frequency of droplets, f, is

$$f = \frac{-243.44}{1+exp\left(\frac{I-I_t}{6.06437}\right)} + 323.506 - 0.874I + 0.0025I^2 \tag{4}$$

where I (A) is current and I_t is the transition current from globular to spray transfer. The transition current for FM 52 has been estimated based on the suggested process parameters by the electrode manufacturer [3]. The frequency current relations are shown in Figure A1 for three FM 52 electrode diameters and, for reference [4, 5], a fitted line to experimental data for mild steel. The droplet shape is assumed to be spherical, and the radius of the sphere is expressed as

$$r_d = \sqrt[3]{\frac{3}{4}r_w^2 w_f/f} \tag{5}$$

where r_w is the radius of the filler metal wire and w_f is the wire feed speed. The VHS diameter is four times the droplet radius. The droplet velocity is
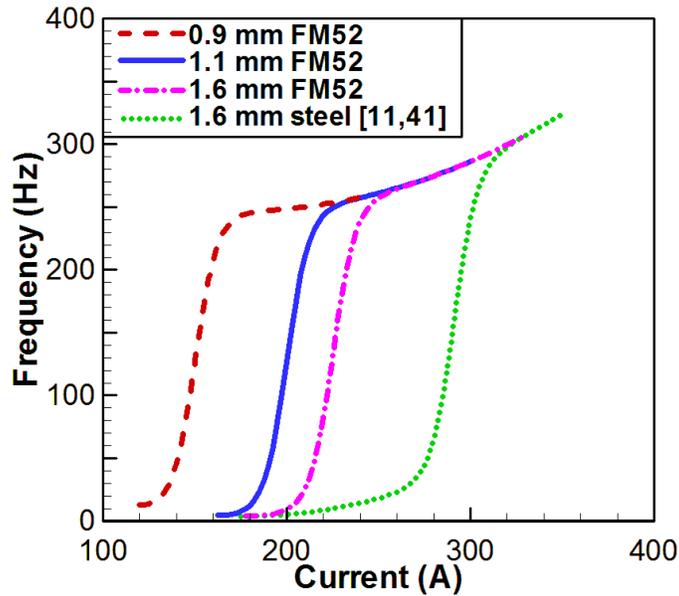
$$v_d = \sqrt{v_0^2 + 2aL_a} \tag{6}$$

Figure A1: *The current-droplet detachment frequencies for filler metal 52 are not experimentally known. Based on suggested currents, voltages, shielding gases, and wire feed speeds for different electrode diameters from the manufactures, the relations have been estimated. The fit line for experimental data for steel in Ar-5%CO2 shielding gas is shown for reference.*

where v_0 is the initial velocity, a is the droplet acceleration, and L_a is the arc length. The calculation for the arc length [6] and measured electrode extension length [7], which is required for the arc length calculation, are available in the literature. Acceleration is taken as

$$a = \frac{3}{8}\frac{v_g^3 \rho_g}{r_d \rho}C_d + g \tag{7}$$

where v_g is the velocity of the plasma, ρ_g is the density of the plasma, and C_d is the drag coefficient. The plasma density was taken as 0.06 kg/m^3. The velocity of the plasma is estimated with the effective velocity (in m/s), which is

$$v_{eff} = k_1 \times I \tag{8}$$

where k_1 is a constant coefficient of ¼. The drag coefficient is

$$C_d = -242.74 Re^{-2} + 59.67 Re^{-1} + 0.44793 \tag{9}$$

where Re is the Reynolds number, which is defined as

$$Re = \frac{r_d v_{eff}}{v_k} \tag{10}$$

The variable v_k is kinetic viscosity and is 3.4 x 10^{-3} m^2/s. The initial velocity is calculated as

$$v_0 = \sqrt{-0.33692 + 0.00854(I/D_d)} \tag{11}$$

References

[1] Kim, C. H., Zhang, W., and DebRoy, T. 2003. Modeling of temperature field and solidified surface profile during gas-metal arc fillet welding. *J. Appl. Phys.* 94 (4): 2667–2679.

[2] Kumar, S. and Bhaduri, S. 1994. Three-dimensional finite element modeling of gas metal-arc welding. *Metall. Mater. Trans. B* 25 (3): 435–441.

[3] Special Metals Corporation, "Joining", accessed 30 April 2015, pg. 9, <www.specialmetalswelding.com>.

[4] Jones, L. A., Eagar, T. W., and Lang, J. H. 1999. A dynamic model of drops detaching from a gas metal arc welding electrode. *J. Phys. D. Appl. Phys.* 31 (1): 107–123.

[5] Rhee, S. and Kannatey-Asibu, E. 1992. Observation of metal transfer during gas metal arc welding. *Weld. J.* 71 (10): 381–386.

[6]   Kim, G.-H. and Na, S.-J. 2001. A study of an arc sensor model for gas metal arc welding with rotating arc Part 1: dynamic simulation of wire melting. *Proc. Inst. Mech. Eng. Part B J. Eng. Manuf.* 215 (9): 1271–1279.

[7]   Waszink, J. H. and Van Den Heuvel, G. J. P. M. 1982. Heat Generation and Heat Flow in the Filler in GMA Welding. *Weld. J.* 61 (8): 269–280.

Vita

Jared J. Blecher

Jared completed a Bachelor of Science degree in Materials Science and Engineering at The Pennsylvania State University in 2010 and completed a Master of Science in the same department and university in 2012. In July 2015, he joined 3D Systems Corporation as an Aerospace and Defense engineer working in the Corporate Research department. A list of publications is shown below.

1. *J.J. Blecher*, T.A. Palmer, and T. DebRoy, 'Porosity in Thick Section Alloy 690 Welds – Experiments, Modeling, Mechanism, and Remedy', *Welding Journal*, in press (2015).
2. H.L. Wei, *J.J. Blecher*, T.A. Palmer, and T. DebRoy, 'Fusion Zone Microstructure and Geometry in Full Penetration Laser-Arc Hybrid Welding of Low Alloy Steel', *Welding Journal*, **94**, 135s-144s (2015).
3. *J.J. Blecher*, T.A. Palmer, and T. DebRoy, 'Mitigation of Root Defect in Laser and Hybrid Laser-Arc Welding', *Welding Journal*, **94**, 73s-82s (2015).
4. *J.J. Blecher*, C.M. Galbraith, C. Van Vlack, T.A. Palmer, J.M. Fraser, P.J.L. Webster, and T. DebRoy, 'Real Time Monitoring of Laser Beam Welding Keyhole Depth by Laser Interferometry,' *Science and Technology of Welding and Joining*, **19**, 560-564 (2014).
5. *J.J. Blecher*, T.A. Palmer, and T. DebRoy, 'Solidification Map of a Nickel Base Alloy,' *Metallurgical and Materials Transactions A*, **45A**, 2142-2151 (2014).
6. *J.J. Blecher*, T.A. Palmer, E.W. Reutzel, and T. DebRoy, 'Laser-Silicon Interaction for Selective Emitter Formation in Photovoltaics. II. Model Applications,' *Journal of Applied Physics*, **112**, 114907 (2012).
7. *J.J. Blecher*, T.A. Palmer, and T. DebRoy, 'Laser-Silicon Interaction for Selective Emitter Formation in Photovoltaics. I. Numerical Model and Validation,' *Journal of Applied Physics*, **112**, 114906 (2012).
8. *J.J. Blecher*, T.A. Palmer, S.M. Kelly, and R.P. Martukanitz, 'Identifying Performance Differences in Transmissive and Reflective Laser Optics Using Beam Diagnostic Tools,' *Welding Journal*, **91,** 204S-214s (2012).